31st conference with international participation

COMPUTATIONAL MECHANICS 2015

BOOK OF EXTENDED ABSTRACTS

November 9 - 11, 2015

HOTEL HORIZONT, ŠPIČÁK
CZECH REPUBLIC

BOOK OF EXTENDED ABSTRACTS
31st conference with international participation **Computational Mechanics 2015**

ISBN 978-80-261-0568-8

Published by
University of West Bohemia, Univerzitní 8, 306 14 Plzeň, Czech Republic, IC 49777513

Edited by
Vítězslav Adámek
Martin Zajíček
Alena Jonášová

Conference secretariat
Petra Pechmanová
Department of Mechanics
Faculty of Applied Sciences
University of West Bohemia
Univerzitní 8
306 14 Plzeň
Czech Republic

phone: +420 377 634 736
e-mail: vm@kme.zcu.cz

Copyright © 2015 University of West Bohemia, Plzeň, Czech Republic

PREFACE

The Book of Extended Abstracts contains 69 two-page abstracts presented at the 31st conference **Computational Mechanics 2015**, which was held at the Hotel Horizont in Špičák, Czech Republic, on November 9 – 11, 2015. This annual conference, which was attended by nearly ninety participants from the Czech Republic, Slovakia and from abroad, was organised by the Department of Mechanics, Faculty of Applied Sciences of the University of West Bohemia under the auspices of

- Miroslav Lávička, the Dean of the Faculty of Applied Sciences,
- Jiří Struček, the Vice-President of the Pilsen Region for Education, Sport, Culture and Tourism,
- Czech Society for Mechanics,
- Czech National Committee of IFToMM,
- Central European Association for Computational Mechanics.

The main objective of this traditional conference is to bring together academicians, researchers and industrial partners interested in relevant disciplines of mechanics including

- solid mechanics,
- dynamics of mechanical systems,
- mechatronics and vibrations,
- reliability and durability of structures,
- fracture mechanics,
- mechanics in civil engineering,
- fluid mechanics and fluid-structure interaction,
- thermodynamics,
- biomechanics,
- heterogeneous media and multiscale problems,
- experimental methods in mechanics,

to create an opportunity for meeting, discussion and collaboration among the participants. As in the previous years, the three best papers presented at this conference were awarded the Czech Society for Mechanics Award for young researchers under 35 years of age.

To all conference participants, we offer the possibility to publish their peer-reviewed full papers in the international journal **Applied and Computational Mechanics**, which has been published by the University of West Bohemia since 2007 (see http://www.kme.zcu.cz/acm/).

We would like to express our gratitude to all the invited speakers for their significant contribution to the conference and the time and effort they put. Considerable acknowledgement belongs also to the members of the Organising Committee for their important work.

We strongly believe that all participants of the CM2015 enjoyed their stay in the beautiful nature of the Šumava region in a meaningful way. Finally, we want to invite you all to come to the next conference CM2016.

Jan Vimmr
University of West Bohemia
Chairman of the Scientific Committee

Vítězslav Adámek
University of West Bohemia
Chairman of the Organising Committee

SCIENTIFIC COMMITTEE

Chairman:

Jan Vimmr
University of West of West Bohemia, Faculty of Applied Sciences, Czech Republic

Members:

Miroslav Balda
Research and Testing Institute Plzeň, Czech Republic

Jan Dupal
University of West of West Bohemia, Faculty of Applied Sciences, Czech Republic

Miroslav Holeček
University of West Bohemia, Czech Republic

Jaromír Horáček
Institute Thermomechanics, Czech Academy of Sciences, Czech Republic

Jiří Křen
University of West Bohemia, Faculty of Applied Sciences, Czech Republic

Vladislav Laš
University of West Bohemia, Faculty of Applied Sciences, Czech Republic

Eduard Malenovský
Brno University of Technology, Faculty of Mechanical Engineering, Czech Republic

Milan Naď
Slovak University of Technology in Bratislava, Faculty of Materials Science and Technology in Trnava, Slovak Republic

Jiří Náprstek
Institute of Theoretical and Applied Mechanics, Czech Academy of Sciences, Czech Republic

Miloslav Okrouhlík
Institute of Thermomechanics, Czech Academy of Sciences, Czech Republic

Pavel Polach
Research and Testing Institute Plzeň, Czech Republic

Josef Rosenberg
University of West Bohemia, Faculty of Applied Sciences, Czech Republic

Milan Růžička
Czech Technical University in Prague, Faculty of Mechanical Engineering, Czech Republic

Milan Sága
University of Žilina, Faculty of Mechanical Engineering, Slovak Republic

Eugeniusz Switonski
Silesian University of Technology, Faculty of Mechanical Engineering, Poland

Michael Valášek
Czech Technical University in Prague, Faculty of Mechanical Engineering, Czech Republic

Jaroslav Zapoměl
VŠB - Technical University of Ostrava, Faculty of Mechanical Engineering, Czech Republic

Vladimír Zeman
University of West Bohemia, Faculty of Applied Sciences, Czech Republic

Table of Contents

Adámek V., Valeš F.: *Analytical solution for transient waves in layered orthotropic viscoelastic strip* 1

Balázsová M., Feistauer M., Horáček J., Sváček P.: *Discontinuous Galerkin method for compressible flow with low Mach numbers* 3

Balda M.: *A new way for estimating fatigue damage of prestressed material* 5

Bauma V., Valášek M.: *Synthesis of theoretical cam profile with non-constant angular velocity* 7

Beneš P., Šika Z., Polach P., Valášek M., Zavřel J., Volech J.: *Kinematic analysis of possible concepts of multi-level mechanisms combining active structures and cable-driven mechanisms* 9

Blekta J.: *Verification of algorithm for automatic chute motion control* 11

Bońkowski T., Hajžman M., Kottner R., Görner T., Hubík L., Vychytil J., Hynčík L.: *Contact forces on motorcycle rider overall during high speed low side sliding accident* . . 13

Brůha J., Zeman V.: *Modelling of a blade couple with contact in shrouding by means of Rayleigh beam finite elements* 15

Bublík O., Vimmr J., Pecka A., Jonášová A.: *A parallel implementation of the implicit discontinuous Galerkin finite element method for fluid flow problems* 17

Burša J.: *Constitutive models of materials showing large elastic strain* 19

Cimrman R., Novák M., Kolman R., Vackář J.: *Real-space ab-initio electronic structure calculations using SfePy* 21

Denk P., Steinbauer P., Šika Z., Macek J., Morkus J.: *Discretisation and parameterization of route description for velocity profile optimization of vehicle* 23

Dupal J., Byrtus M.: *Methodology of behaviour simulation of cable-driven manipulators with varying cable lengths* 25

Fišer M., Bublík O., Vimmr J.: *Novel limiting process of the discontinuous Galerkin method applied to shallow water equations* 27

Hajžman M., Červená O., Mrštík J., Balda M.: *On the unbalance estimation for large turbine dynamic models from a run-down* 29

Heczko J., Kottner R.: *Modelling fatigue damage using finite elements and time homogenization* 31

Hokeš F.: *Comparison of suitability of selected material models of concrete for inverse identification of parameters with the aid of optimization algorithms* 33

Hora P.: *The root-finding of dispersion curves in a bar impact problem* 35

Horáček J., Feistauer M., Sváček P.: *Numerical modelling of flutter instability of the NACA 0012 profile in turbulent and laminar flow* 37

Hračov S., Macháček M.: *Combined effect of passive damping element and soil-structure interaction on dynamic behaviour of tall slender structure* 39

Hrubý P., Hokeš F., Krňávek O., Nevařil A.: *Numerical analysis of the process of repairing defects in lamellar flange and its influence on the local stress state* 41

Hynčík L., Špička J., Baierl P.: *Discrete element method for simulation of dynamical behaviour of crowd of people reacting on external loading* 43

Janoušek J., Holmström S., Pohja R.: *Cyclic softening of tempered ferritic-martensitic steel P91* 45

Kepka M., Kepka M., Bartoň L., Žlábek P.: *Fatigue life calculation and testing in Regional Technological Institute – current state and vision* 47

Kerkoub Y., Merabti L., Benzaoui A.: *Mass and heat transfer in the wheel of desiccant cooling system using solar energy* 49

Klouček V.: *Control of hydraulic hexapod with 6 DOF* 51

Kolman R., Berezovski A., Cho S., Okrouhlík M., Kopačka J., Gabriel D., Tamm K., Plešek J., Park K.: *Comparison of finite difference method, finite element method, isogeometric analysis and finite volume method in one-dimensional discontinuous elastic wave propagation* 53

Král R., Náprstek J.: *Finite element solution of the nonlinear 2DOFs dynamic system under random Gaussian excitation using the Fokker-Planck equation* 55

Jansová M., Křen J., Lobovský L., Votápek P., Koudela K., Hynčík L.: *Load in total hip arthoplasty during a golf swing* 57

Kulíšek V., Růžička M., Kašpárková T., Poul R.: *Modelling of composite spindle rams* . 59

Lalaoua A., Chaieb Z., Aouli M.: *On the stability of Taylor vortex flow in a cylindrical annulus for different working fluids* 61

Lobovský L., Hartlová J., Salášek M., Krystek J., Jansová M., Votápek P., Tupý R., Ferda J., Pavelka T., Křen J.: *Comparison of sacral bone fixation techniques* 63

Lukeš V., Rohan E.: *Optimization of perforated structures based on two-scale homogenization* 65

Machů T., Fialová S., Říha Z., Pochylý F.: *Study of a pump based on the pulsatile flow principle* 67

Matyska M., Růžička M.: *Probabilistic assessment of the propeller blade failure based on the fatigue tests and the vibratory stress survey* 69

Náprstek J., Hračov S.: *Dynamics of beam pair coupled by visco-elastic interlayer* 71

Nováková N., Dobšáková L., Habán V., Hudec M.: *Effect of liquid film on rotor dynamics* 73

Očenášek J., Voldřich J.: *One-dimensional mathematical model of the whole process in a continuous screw press* 75

Padovec Z., Růžička M., Král M., Sedláček R., Růžička P.: *Computation of thermo-elastic characteristics of plates randomly reinforced with pellets using image processing methods and statistics* 77

Pecka A., Bublík O., Vimmr J.: *An implicit discontinuous Galerkin scheme for a numerical solution of transonic flow problems* 79

Pečínka L., Švrček M.: *Parametric oscillations of the coolant in PWR primary circuit* . . 81

Phamová L.: *Microphone arrays and their algorithms - short review* 83

Plánička S., Vimmr J.: *Convective flux schemes for numerical solution of two-phase flows* 85

Poduška J., Hutař P., Kučera J., Sadílek J., Náhlík L.: *A simple method of assessing residual stress distribution in PE pipes* 87

Pokorný P., Náhlík L., Hutař P.: *Influence of mean stress on residual fatigue lifetime of railway axles* 89

Polach P., Byrtus M., Dupal J., Hajžman M., Šika Z.: *Alternative modelling of cables of varying length* 91

Půst L., Pešek L., Radolfová A.: *Negative stiffness in gear contact* 93

Rosenberg J., Byrtus M.: *Bifurcation of co-dimension 2 in the Cajal-like cell model dynamics* 95

Smolík L., Hyrát J.: *Experimental identification of modal properties of turbine generator foundations* 97

Steinbauer P., Stojan R., Šika Z.: *Simulation study of vehicle stream with coordinated control* 99

Stulík P., Hanuš J., Bém M.: *Initial evaluation of possible resonance vibration consequences due to parametric flow oscillation* 101

Sváček P.: *Extended finite element method for free-surface flows* 103

Svoboda J., Kraus V.: *Vibration tests of 15T tram chassis cover* 105

Šafařík P.: *Data reduction method as an investigation tool in the field of internal aerodynamics* 107

Šedlbauer D.: *Heterogeneous material modelling via optimized wang tiles* 109

Šika Z., Volech J., Plecháček J., Mráz L., Valášek M., Beneš P.: *Synthesis of computed torques control of flexible robot with additional sensors* 111

Špička J.: *Application of Euler parameters for the development of MBS human body model* 113

Štegnerová K., Náhlík L., Hutař P.: *Crack propagation study in layered alumina-zirconia ceramic composite* 115

Štigler J.: *Improved formula for fully developed mean flow velocity profile for both laminar and turbulent flow in tube* 117

Turjanicová J., Rohan E.: *Modelling of ionic transport in cortical bone porous structure* . 119

Valášek M., Bauma V., Vampola T.: *Simulation and experimental calibration of mechatronic flexible joint* 121

Vampola T., Horáček J.: *Numerical reconstruction of the videokymography records – sensitivity of the computational model* 123

Volech J., Šika Z., Skopec T., Valášek M.: *Adaptive calibration of measurement model of flexible robot end-effector position using internal sensors* 125

Vrána T., Bradáč J., Kovanda J.: *Study of wheel geometrical parameters for single-axle suspension by using elasto-kinematic model* 127

Vychytil J., Čechová H., Maňas J.: *Mechanical response of neck in virtual human body model VIRTHUMAN* 129

Zapoměl J., Ferfecki P., Dekýš V., Žmindák M.: *Modelling and investigations of influence of material damping on vibrations of flexible rotors* 131

Zavřel J., Šika Z., Valášek M., Beneš P., Dupal J.: *Optimization of mechanical properties of active structure and choice and placement of sensors and actuators* 133

Zeman V., Dyk Š.: *Impact vibrations of guide thimbles in nuclear fuel assembly* 135

Žák J., Lukášová V.: *Model of binding point in comparison with a real fabric* 137

COMPUTATIONAL MECHANICS 2015
31st conference with international participation
Špičák
November 9 - 11, 2015

Analytical solution for transient waves in layered orthotropic viscoelastic strip

V. Adámek[a], F. Valeš[b]

[a] NTIS – New Technologies for the Information Society, University of West Bohemia, Univerzitní 8, 306 14 Pilsen, Czech Republic
[b] Institute of Thermomechanics AS CR, v.v.i., Veleslavínova 11, 301 14 Pilsen, Czech Republic

Wave propagation in heterogeneous media like composites is a subject of considerable interest for many years. Contrary to most of studies dealing with such problems using numerical or experimental techniques, this work presents the analytical solution of a particular transient 2D plane-stress problem.

Let us assume an infinite thin strip which is composed of two viscoelastic layers of the same height d. Further, let both the layers have special orthotropic properties, i.e. the material and geometric axes coincide in both cases. The coordinate system $x_1 - x_2$ with respect to which the problem will be solved, is chosen in such a way that both axes are the axes of problem symmetry and that the horizontal axis x_1 coincides with the interface of the layers. Finally, we will assume that the strip is loaded on its upper edge in the direction of x_2 by a pressure load the amplitude of which is described by an even function of x_1. The bottom edge will be free.

Transient wave phenomena in each layer are described by a system of two partial integro-differential equations which are similar to those presented in [1] where the problem of a viscoelastic orthotropic strip is solved. Based on this analogy and taking into account the zero initial conditions of the problem, the Laplace transforms $U_{1,n}(x_1, x_2, p)$, $U_{2,n}(x_1, x_2, p)$ of the displacement component $u_{1,n}(x_1, x_2, t)$, $u_{2,n}(x_1, x_2, t)$ which represent the unknown functions of the problem can be expressed as

$$U_{1,n} = \frac{1}{\pi}\int_0^\infty [P_n(\omega,p)\sinh(x_2\Lambda_{1,n}(\omega,p)) + Q_n(\omega,p)\cosh(x_2\Lambda_{1,n}(\omega,p)) + R_n(\omega,p)\sinh(x_2\Lambda_{2,n}(\omega,p)) + S_n(\omega,p)\cosh(x_2\Lambda_{2,n}(\omega,p))]\sin(\omega x_1)d\omega, \quad (1)$$

$$U_{2,n} = \frac{1}{\pi}\int_0^\infty [(P_n(\omega,p)\cosh(x_2\Lambda_{1,n}(\omega,p)) + Q_n(\omega,p)\sinh(x_2\Lambda_{1,n}(\omega,p)))L_{1,n}(\omega,p) + (R_n(\omega,p)\cosh(x_2\Lambda_{2,n}(\omega,p)) + S_n(\omega,p)\sinh(x_2\Lambda_{2,n}(\omega,p)))L_{2,n}(\omega,p)]\cos(\omega x_1)d\omega, \quad (2)$$

where $p \in C$ is the variable of Laplace transform and the subscript n denotes the number of the layer ($n = 1$ corresponds to the bottom layer, $n = 2$ denotes the upper layer). The meaning and the formulas for complex functions $\Lambda_{1,n}$, $\Lambda_{2,n}$, $L_{1,n}$ and $L_{2,n}$ can be deduced from the relations stated in [1]. The remaining functions in (1)-(2), i.e. P_n, Q_n, R_n, S_n, have to be determined using the boundary conditions of the problem. If the boundary conditions on both edges of the strip and at the interface of the strip layers are formulated, one obtains a system of eight algebraic equations. Finding its solution leads to final formulas for the Laplace transforms of

required displacement components. Using these functions it is then easy to derive the Laplace transforms of other mechanical quantities.

The inversion from the Laplace domain back to the time domain can be then done either analytically or numerically. A numerical procedure was used in this work. As in our previous works dealing with analytical solutions of wave problems, we used a method which is based on FFT and Wynn's epsilon algorithm (for more details about this procedure see e.g. [2]). The evaluation of derived analytical formulas was made in Matlab environment. It was considered that the strip consists of two layers with $d = 20\mathrm{mm}$ and of the same properties as in [1]. The fibers were oriented horizontally and vertically in the first ($n = 1$) and the second ($n = 2$) layer, respectively. The transient response to a pressure load which was nonzero only for $x_1 \in \langle -2,\ 2\rangle\,\mathrm{mm}$ and which was described by Heaviside function in time was studied. The change of pressure amplitude $1\,\mathrm{MPa}$ was given by a cosine function.

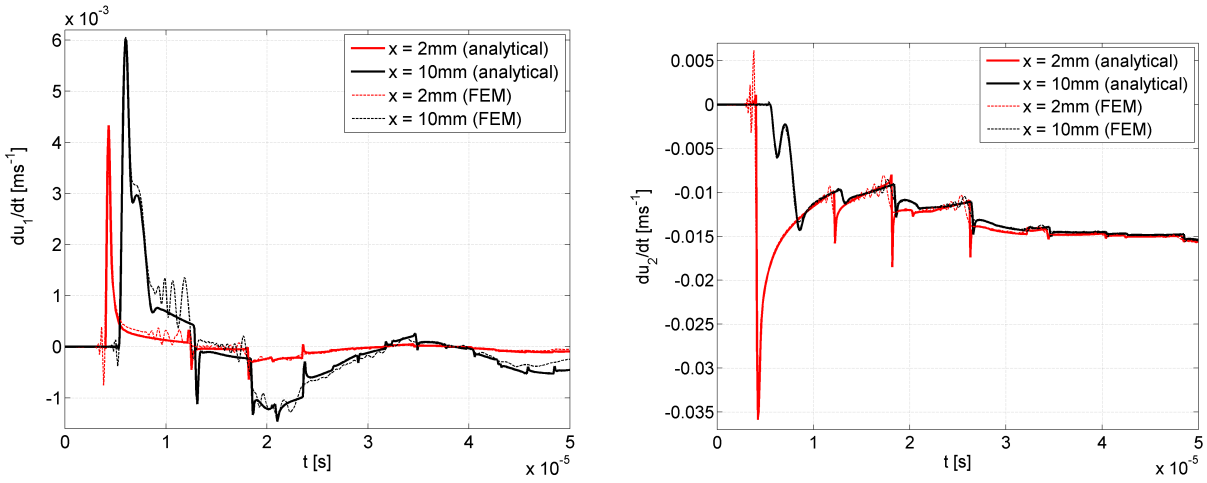

(a) (b)

Fig. 1. Comparison of analytical (*thick lines*) and numerical (*thin lines*) results for $x_2 = 0\,\mathrm{mm}$ and for different values of x_1: (a) the horizontal velocity du_1/dt, (b) the vertical velocity du_2/dt

Fig. 1(a)-(b) show the histories of horizontal and vertical velocities at the interface of the layers for $x_1 = \{2, 10\}\,\mathrm{mm}$ obtained from formulas derived (thick lines). With respect to the complexity of the process of the analytical solution derivation and of its evaluation, numerical simulation of the problem solved has been carried out by a finite element software, as well, to verify the analytical procedure. A very good agreement between numerical and analytical results confirms the correctness of the used procedure. The analytical solution can now be used for studying of wave phenomena in layered strips. Moreover, it is a good starting point for the derivation of analytical solution for transient response of multilayered strips and strips made of functionally graded materials.

Acknowledgements

This publication was supported by the project LO1506 of the Czech Ministry of Education, Youth and Sports and by the project GA CR P101/12/2315.

References

[1] Adámek, V., Valeš, F., Červ, J., Problem of non-stationary waves in viscoelastic orthotropic strip solved using analytical method, Proceedings of the 5th ECCOMAS Thematic Conference on Computational Methods in Structural Dynamics and Earthquake Engineering, Crete, 2015.

[2] Brančík L., Programs for fast numerical inversion of Laplace transforms in Matlab language environment, Proceedings of MATLAB Conference 1999, Prague, 1999.

COMPUTATIONAL MECHANICS 2015
31st conference with international participation
Špičák
November 9 - 11, 2015

Discontinuous Galerkin method for compressible flow with low Mach numbers

M. Balázsová[a,b], M. Feistauer[a], J. Horáček[b], P. Sváček[c]

[a] Faculty of Mathematics and Physics, Charles University in Prague, Sokolovská 83, 186 75 Prague 8, Czech Republic
[b] Institute of Termomechanics, Academy of Sciences of the Czech Republic, Dolejškova 5, 182 00 Prague 8, Czech Republic
[c] Faculty of Mechanical Engineering, Czech Technical University, Karlovo náměstí 13, 121 35 Prague 2, Czech Republic

We will deal with compressible viscous flow in a bounded domain $\Omega \subset \mathbb{R}^2$, which can be described by the system of the Navier-Stokes equations:

$$\frac{\partial \mathbf{w}}{\partial t} + \sum_{s=1}^{2} \frac{\partial \mathbf{f}_s}{\partial x_s} = \sum_{s=1}^{2} \frac{\partial \mathbf{R}_s(\mathbf{w}, \nabla \mathbf{w})}{\partial x_s}, \tag{1}$$

$$\mathbf{w}(x,0) = \mathbf{w}^0(x), \quad x \in \Omega, \tag{2}$$

where $\mathbf{w}$ is the so called state vector, defined as $\mathbf{w} = (w_1, w_2, w_3, w_4)^T = (\rho, \rho v_1, \rho v_2, E)^T \in \mathbb{R}^4$ and $\mathbf{w}^0(x)$ is the initial condition. Functions

$$\mathbf{f}_s(\mathbf{w}) = (\rho v_s, \rho v_1 v_s + \delta_{1,s}\rho p, \rho v_2 v_s + \delta_{2,s}\rho p, (E+p)v_s)^T,$$

$$\mathbf{R}_s(\mathbf{w}, \nabla \mathbf{w}) = \left(0, \tau^V_{s,1}, \tau^V_{s,2}, \tau^V_{s,1} v_1 + \tau^V_{s,2} v_2 + \frac{\gamma k}{Re\, Pr} \frac{\partial \theta}{\partial x_s}\right)^T$$

represent the inviscid ad the viscous terms, respectively. We use the following notation: ρ - density, $v = (v_1, v_2)$ - velocity, p - pressure, E - total energy, θ - absolute temperature, $\tau = \{\tau_{ij}\}$ - stress tensor, $\tau^V = \{\tau^V_{ij}\}$ - viscous part of the stress tensor, k - heat conductivity, $\gamma > 1$ - Poisson adiabatic constant.

For discretization we employ the discontinuous Galerkin method (DGM). Let $\mathcal{T}_h$ be a partition of the domain $\overline{\Omega}$ into finite number of closed triangles K. Furthermore, we consider a partition $0 = t_0 < \ldots < t_r = T$ of the time interval $[0, T]$ and set $\tau_k = t_k - t_{k-1}, k = 1, \ldots, r$. Over $\mathcal{T}_h$ we define the broken Sobolev space

$$\mathbf{H}^2(\Omega, \mathcal{T}_h) = (H^2(\Omega, \mathcal{T}_h))^4, \quad \text{where} \quad H^2(\Omega, \mathcal{T}_h) = \{v : \Omega \to \mathbb{R}; v|_K \in H^2(K)\, \forall K \in \mathcal{T}_h\}.$$

The approximate solution is sought in the space of piecewise polynomial functions

$$\mathbf{S}_{hp} = (S_{hp})^4, \quad \text{where} \quad S_{hp} = \{v \in L^2(\Omega); v|_K \in P^p(K)\, \forall K \in \mathcal{T}_h\}.$$

To derive the space semidiscrete problem, we multiply (1) by a test function $\boldsymbol{\varphi}_h \in \mathbf{H}^2(\Omega, \mathcal{T}_h)$, integrate over an element $K \in \mathcal{T}_h$, apply Green's theorem and sum over all elements. To discretize the inviscid term, we use the so-called numerical flux. In the discretization of the viscous term we add appropriate stabilization and interior and boundary penalization forms. In the time discretization we use the n-step backward difference formula (BDF) with coefficients $\alpha_{n,l}, l = 0, \ldots, n$, which depend on time steps $\tau_{k-l}, l = 0, \ldots, n$. For more details see [1].

We say that the finite sequence of functions $\mathbf{w}_h^k = \mathbf{w}_h(t_k),\ k = 0, \ldots, r$ is the approximate solution of (1)–(2) computed by the BDF-DGM, if the following conditions are satisfied:

$$\mathbf{w}_h^0 = \Pi_h \mathbf{w}^0, \quad \mathbf{w}_h^k \in \mathbf{S}_{hp},\ k = 0, 1, \ldots, r, \tag{3}$$

$$\frac{1}{\tau_k}\left(\sum_{l=0}^{n} \alpha_{n,l} \mathbf{w}_h^{k-l}, \boldsymbol{\varphi}_h\right) + \mathbf{c}_h(\mathbf{w}_h^k, \boldsymbol{\varphi}_h) = 0 \quad \forall \boldsymbol{\varphi}_h \in \mathbf{S}_{hp},\ k = n, \ldots, r, \tag{4}$$

$\mathbf{w}_h^l \in \mathbf{S}_{hp},\ l = 1, \ldots, n-1$ are determined by a suitable q-step method with $q < n$ or by an explicit Runge-Kutta method. (5)

It is well-known that compressible flow with very low Mach number is very close to incompressible flow. In our numerical experiments we consider a channel with two bumps, which represent a simplified model of vocal folds. We prescribed the following data: the fluid viscosity $\mu = 18 \times 10^{-6}\,\mathrm{kg\,m^{-1}\,s^{-1}}$, the inlet density $\rho_{in} = 1.225\,\mathrm{kg\,m^{-3}}$, the outlet pressure $p_{out} = 97\,611\,\mathrm{Pa}$, heat conduction coefficient $k = 2.428 \times 10^{-2}\,\mathrm{kg\,m\,s^{-2}\,K^{-1}}$ and three different values of the inlet velocity $v_{in} = 4\,\mathrm{m\,s^{-1}}$, $v_{in} = 0.4\,\mathrm{m\,s^{-1}}$ and $v_{in} = 0.04\,\mathrm{m\,s^{-1}}$. The evolution of the velocity for the first two cases at the same time instant $t = 0.162\,\mathrm{s}$ computed by the BDF-DGM for compressible flow can be seen in Figs. 1 and 2 below. The results concerning the comparison of the compressible and incompressible flow will be presented at the conference.

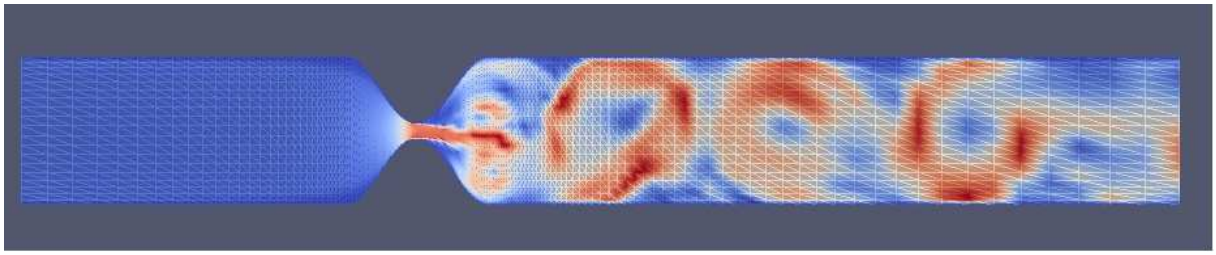

Fig. 1. Evolution of the velocity for $v_{in} = 4\,\mathrm{m\,s^{-1}}$ at the time instant $t = 0.162\,\mathrm{s}$

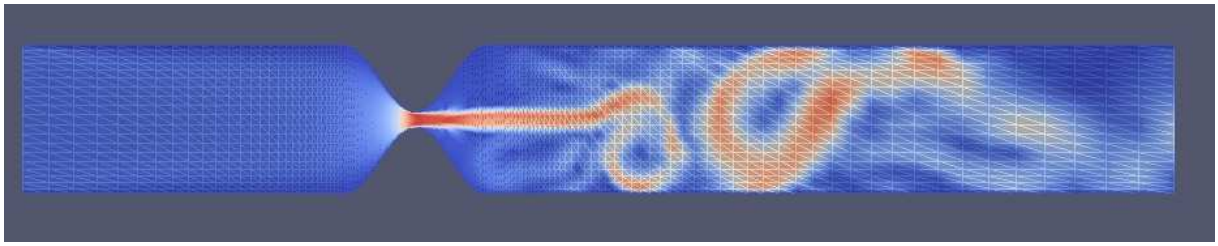

Fig. 2. Evolution of the velocity for $v_{in} = 0.4\,\mathrm{m\,s^{-1}}$ at the time instant $t = 0.162\,\mathrm{s}$

Acknowledgement

The work of P. Sváček was supported by the grant GACR P101/11/0207.

References

[1] Dolejší, V., Feistauer, M., Discontinuous Galerkin method – Analysis and applications to compressible flow, Springer, 2015.

COMPUTATIONAL MECHANICS 2015
31st conference with international participation
Špičák
November 9 - 11, 2015

A new way for estimating fatigue damage of prestressed material

M. Balda[a]

[a]*Research and Testing Institute Plzeň Ltd., Tylova 46, 301 00 Plzeň, Czech Republic*

A common way of assessing a safe load of a machine part exposed not only to a static stress σ_m, but also a dynamic stress with amplitude σ_a, is based on an application of the Haigh diagram, which documents how a mean stress lowers fatigue limit σ_c of applied material to $\sigma_c(\sigma_m) = \sigma_{cm}$. It is a kind of safe-life evaluation [1]. As far as the actual stress $\sigma_{am} = [\sigma_a,\, \sigma_m]$ lies below the ultimate line of the Haigh diagram, there is no danger of a fatigue damage.

Years ago, the author of this contribution attempted years ago to exploit the information on the lowered fatigue limit σ_{cm} even for fatigue life estimate [2], when he expressed elementary damage caused by a single loading cycle as

$$d_{am} = \frac{1}{N_{am}} = \frac{1}{N_a}\, g_m\, h_m^w\,, \tag{1}$$

where N_a is a number of cycles up to a total damage of an object loaded by σ_a, while $\sigma_m = 0$, w is the exponent of Woehler's curve, and g_m and h_m are functions of σ_m. While formula $h_m = (1 - \sigma_m/R_m)^{k_H}$, where k_H is a suitable material-dependent value, well fits experimental data, the chosen form of $g_m = 1 - (\sigma_m/R_m)^2$ appears now inappropriate.

In recent time, old experimental data $[\sigma_{am}, N_{am}]$ for constant σ_m were found [3]. Since an attempt to identify both approaches for estimating damages collapsed due to the wrong form of g_m, the way of estimating damage according to Eq. (1) must be refused. The old measurements yielded data of two S-N curves for T671 material of the Böhler Company, namely for prestresses $\sigma_m = 450\,\text{MPa}$ and $\sigma_m = 600\,\text{MPa}$. Unfortunately, those measurements were not

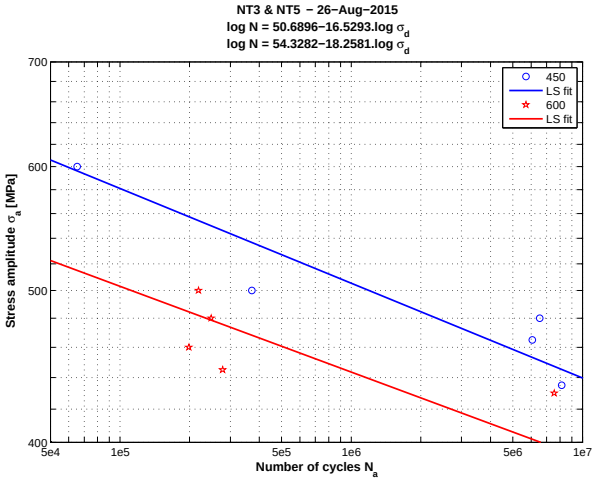

Fig. 1. Crossed S-N curves

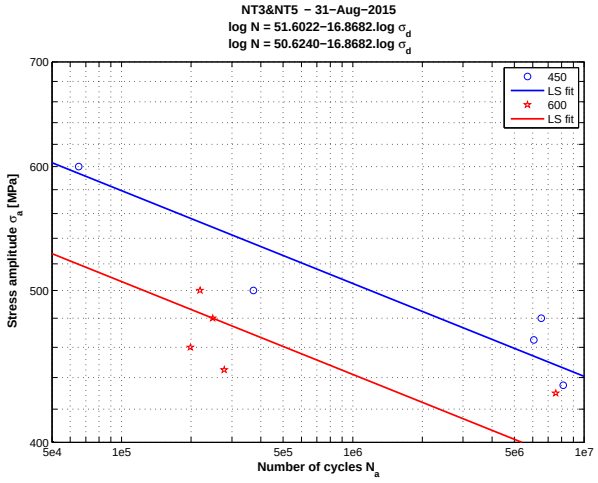

Fig. 2. Parallel S-N curves

too precise, and thus, depicted in log-log diagram, they have a big range of variance. However, when processed by linear regression due to the relation $N_{am} = A_m\, \sigma_{am}^{B_m}$, transformed into

$$\log N_{am} = \log A_m + B_m\, \log \sigma_{am}\,, \tag{2}$$

it returned results drawn in Fig. 1. It is obvious that both regression lines are almost parallel. Hence, both data were processed together into two parallel lines with $B_{m_1} = B_{m_2} = -w$, without any noticeable line changes of line positions towards the measured points (see Fig. 2). The only bigger differences occurred in logarithms A_m. If both S-N lines were lengthen up to $N_{am} = 0.5$, the fictive amplitudes $\sigma_{am_1,05} = 1\,193.95\,\text{MPa}$ and $\sigma_{am_2,05} = 1\,044.71\,\text{MPa}$ would be obtained for prestresses $\sigma_{m_1} = 450\,\text{MPa}$ and $\sigma_{m_2} = 600\,\text{MPa}$, respectively. It is quite interesting, that their difference is $\Delta\sigma_{am,05} = 149.24 \approx 150\,\text{MPa}$.

Having this result, we may conclude that the fictive amplitude of any S-N curve of prestressed material might be evaluated as

$$\sigma_{am,05} = \sigma_{a0,05} - \sigma_m\,, \tag{3}$$

where $\sigma_{a0,05}$ is the fictive amplitude of the Wöhler curve (with $\sigma_m = 0$) on $N = 0.5$. This situation is depicted in Fig. 3. Then, an elementary damage is evaluated as $d_{am} = 1/N_{am}$, where N_{am} is found from Eq. (2) for particular σ_m.

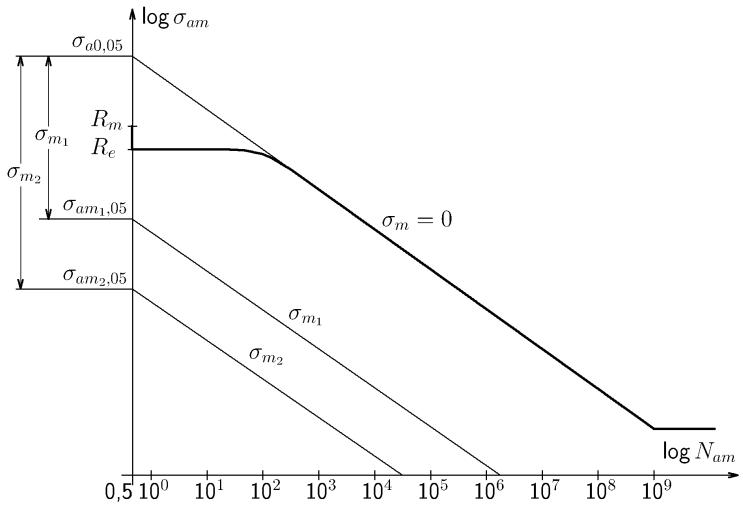

Fig. 3. A construction of S-N curves with prestress

Acknowledgement

The contribution has originated in the Research and Testing Institute Plzeň in the framework of works on the project "Center of Research and Experimental Development of Reliable Energy Production" sponsored by the Technological Agency of the Czech Republic.

References

[1] Balda, M., Červená, O., Determination of fatigue life of turbine blades in service, Proceedings of the 4th conference Turbostroje 2015, TechSoft Engineering, Praha, 2015. (in Czech)

[2] Balda, M., Svoboda, J., Fröhlich, V., Using hypotheses for calculating fatigue lives of parts exposed to combined random loads, Proceedings of the conference Engineering Mechanics, Svratka, 2003.

[3] Chvojan, J., Testing protocol No. 846/2003, Test of T671 high cycle fatigue, Testing laboratory of Škoda Research, Plzeň, Czech Republic, 2003. (in Czech)

COMPUTATIONAL MECHANICS 2015
31st conference with international participation
Špičák
November 9 - 11, 2015

Synthesis of theoretical cam profile with non-constant angular velocity

V. Bauma [a], M. Valášek [a]

[a] *Department of Mechanics, Biomechanics and Mechatronics, Faculty of Mechanical Engineering, Czech Technical University in Prague, Technická 4, 16607 Praha 6, Czech Republic*

For testing belts, child safety seats and other safety devices in the automotive industry deceleration simulators are used. Newly are for tests designed acceleration simulators (Fig 1.), which allow the same process of acceleration. One type of these mechanisms is based on cam mechanisms. In the conventional proposal of theoretical cam profile the constant angular velocity is assumed. The paper deals with the analytic synthesis of theoretical cam profile for given motion of the follower, when the angular velocity of the cam isn't constant.

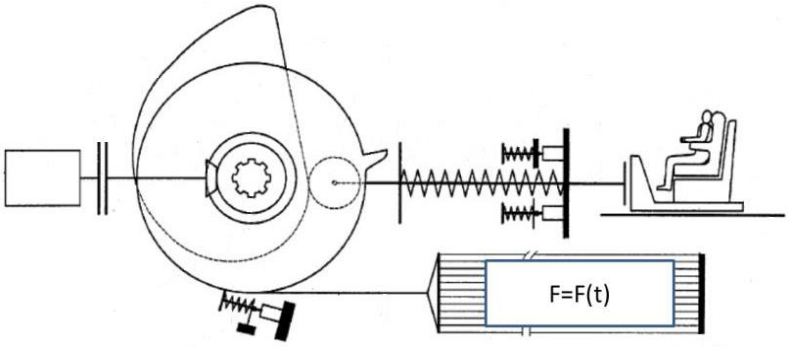

Fig. 1. Acceleration Simulator Vehicles Collisions

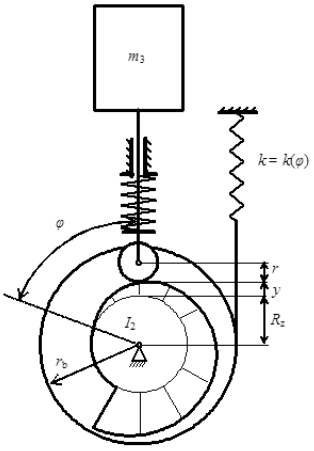

Fig. 2. Mechanical model

Fig. 2 shows a mechanical model of the device. The equation of motion [1] of this model is

$$\left[I_2 + m_3 \left(\frac{\mathrm{d}y}{\mathrm{d}\varphi} \right)^2 \right] \ddot{\varphi} + m_3 \, \frac{\mathrm{d}y}{\mathrm{d}\varphi} \, \frac{\mathrm{d}^2 y}{\mathrm{d}\varphi^2} \dot{\varphi}^2 = F \, r_b \ ,$$

where I_2 is reduced moment of inertia, m_3 is reduced mass, y is momentary lift, φ is angle of cam rotation, F is acting force and r_b is radius of the drum. Regulation [2] defines a corridor for acceleration (Fig 3.), the overall trajectory of the follower (seat) and final velocity of the follower. We suppose angle of cam rotation as a function of time

$$\varphi = \chi(\mathrm{e}^{\alpha t} - 1) \ ,$$

where α and χ are constants, so $\dot{\varphi} = \chi\alpha \, \mathrm{e}^{\alpha t}$, $\ddot{\varphi} = \chi\alpha^2 \, \mathrm{e}^{\alpha t}$ and $t = \frac{1}{\alpha} \ln\left(\frac{\varphi}{\chi} + 1 \right)$.

Cam lifting dependency is then

$$y = C_2 + a_2(t) = C_2 + a_2\left[\frac{1}{\alpha}\ln\left(\frac{\varphi}{\chi}+1\right)\right]$$

with prescribed follower trajectory $a_2(t)$ and integration constant C_2 . Successively can be now expressed

$$\frac{\mathrm{d}y}{\mathrm{d}\varphi},\ \frac{\mathrm{d}^2y}{\mathrm{d}\varphi^2},\ \dot{y} = \frac{\mathrm{d}y}{\mathrm{d}t} = \frac{\mathrm{d}y}{\mathrm{d}\varphi}\frac{\mathrm{d}\varphi}{\mathrm{d}t} \text{ and } \ddot{y} = \frac{\mathrm{d}y}{\mathrm{d}\varphi}\ddot{\varphi} + \frac{\mathrm{d}^2y}{\mathrm{d}\varphi^2}\dot{\varphi}^2.$$

Substituting into the equations of motion we obtain

$$I_2\chi\alpha^2\,\mathrm{e}^{\alpha t} + m_3\frac{a_1\left[\frac{1}{\alpha}\ln\left(\frac{\varphi}{\chi}+1\right)\right]\ a\left[\frac{1}{\alpha}\ln\left(\frac{\varphi}{\chi}+1\right)\right]}{\chi\alpha\,\mathrm{e}^{\alpha t}} = F\,r_b\ ,$$

where $a_1(t)$ is prescribed follower velocity and $a(t)$ is prescribed follower acceleration.

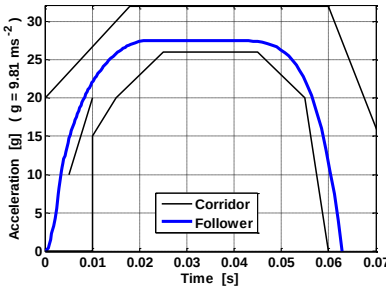

Fig. 3. Prescribed acceleration

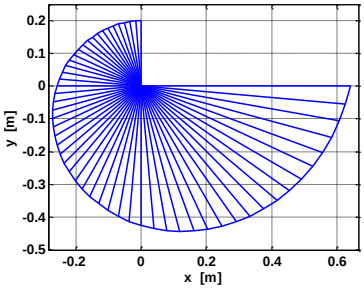

Fig. 4. Resulting cam profile

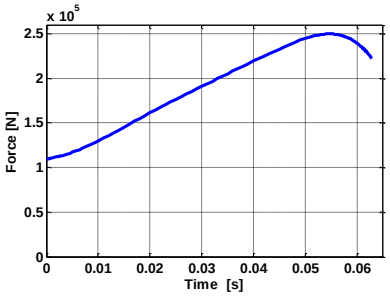

Fig. 5. Required force

For the required force then we obtained

$$F = \frac{1}{r_b}\left\{I_2\chi\alpha^2\,\mathrm{e}^{\alpha t} + m_3\frac{a_1\left[\frac{1}{\alpha}\ln\left(\frac{\varphi}{\chi}+1\right)\right]\ a\left[\frac{1}{\alpha}\ln\left(\frac{\varphi}{\chi}+1\right)\right]}{\chi\alpha\,\mathrm{e}^{\alpha t}}\right\}.$$

This approach enables analytic synthesis of theoretical cam profile for given motion of the follower, when the angular velocity of the cam isn't constant and also computation of required force. Both results are function of selected constants α and χ and it allows theirs optimization.

Acknowledgements

The authors acknowledge the support by the grant project TA03030221 Acceleration Simulator Vehicles Collisions.

References

[1] Stejskal, V., Valášek, M., Kinematics and dynamics of machinery, Marcel Dekker, New York, 1996.
[2] Regulation ECE No. 16/04, Safety belts and restraint systems.

COMPUTATIONAL MECHANICS 2015
31st conference with international participation
Špičák
November 9 - 11, 2015

Kinematic analysis of possible concepts of multi-level mechanisms combining active structures and cable-driven mechanisms

P. Beneš [a], Z. Šika [a], P. Polach [b], M. Valášek [a], J. Zavřel [a], J. Volech [a]

[a] *Faculty of Mechanical Engineering, CTU in Prague, Technická 4,160 00 Praha 6, Czech Republic*
[b] *Faculty of Applied Sciences, University of West Bohemia, Univerzitní 8, 306 14 Plzeň, Czech Republic*

Cable-driven manipulators are based on principles of parallel kinematics combining with the use of cables as links. Such a combination has several advantages – the mass and inertia properties are reduced due to lightweight cables, mechanisms are capable to cover large workspace and usually they are less expensive and easy to built or reconfigure. On the other hand the nature and flexibility of the cables limits the performance mainly to the field of low frequencies. The multi-level mechanism consists of the basic cable-driven manipulator and structure superimposed to its platform that further extends motion capabilities. The superimposed active structure could be driven by cables similarly to the main motion platform, see Fig. 1 – a), b), or by different types of actuators (e.g. piezo elements), Fig. 1- c). In that case the active structure could ensure small but rapid motions, vibration suppression, precise positioning etc. The end-effector of the manipulator is usually assumed as a part of the superimposed active structure but the inverse concept, when the end-effector is identical with the original cable-driven platform, is interesting as well - mainly for vibration suppression and stabilization tasks. The kinematic analysis of possible concepts was focused especially on the size of the reachable workspace, the dexterity and possible collisions within the workspace.

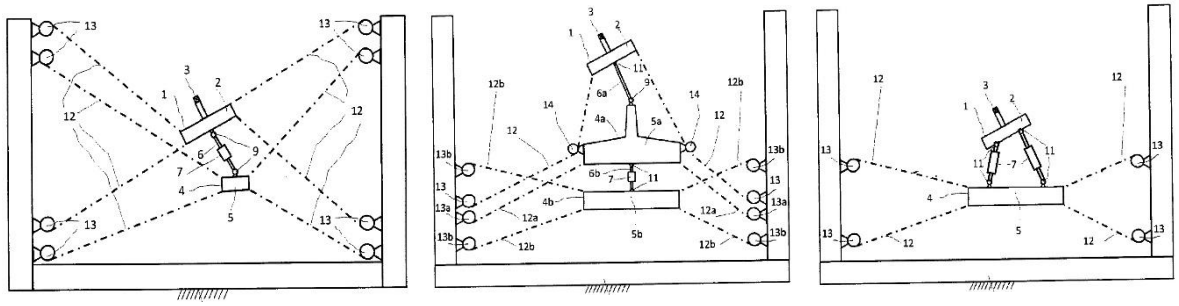

Fig. 1. Examples of structure variants: a) multi-level structure controlled by cables [4], b) modification with cables outside the operational workspace [4], c) cable structure with superimposed active platform

There are two main groups of cable-driven parallel manipulators. The first group are suspended manipulators. They use gravity to ensure that the cables are under tension. Therefore all the cables are in the top part of the workspace and for control we need as many cables as the number of degrees of freedom (DOF). The second group are overconstrained manipulators. Their cables are running in all directions from the platform and as the cables cannot push the platform these manipulators require more cables than DOFs in order to operate. In this paper we are focused on overconstrained manipulators with 6 DOFs and 8 driven cables.

The overconstrained 6 DOF cable-driven parallel manipulator is always in configuration where at most 6 cables are under tension [3]. However for a given pose there could be more than one set of 6 cables that is valid. The basic calculation of reachable workspace is based on a static force analysis [2]. Assuming that cables are perfectly stiff straight lines with ideal spherical joints at the end the equilibrium equation can be formulated as

$$\boldsymbol{f} = -\boldsymbol{J}\boldsymbol{\tau},$$

where $\boldsymbol{f}$ is the vector of external load applied to the platform, $\boldsymbol{J}$ is the Jacobian matrix of cables and $\boldsymbol{\tau}$ is the vector of cable tensions. The workspace of manipulator is the set of poses that can be reached with non-negative tension in all cables and with full rank of $\boldsymbol{J}$ (singularity condition).

The second set of restrictions that limits workspace is the collision avoidance. The cables cannot intersect with each other, with the platform, the mainframe or the superimposed active structure. Therefore all reachable poses that fulfill cable tension condition were checked for possible collisions.

The last parameter for comparison between different variants of manipulator was the dexterity [1]. The criterion was defined as a maximal value of average dexterity with minimal deviation throughout the workspace. All the simulations were performed using the MATLAB software. One of the simulation models is in Fig. 2.

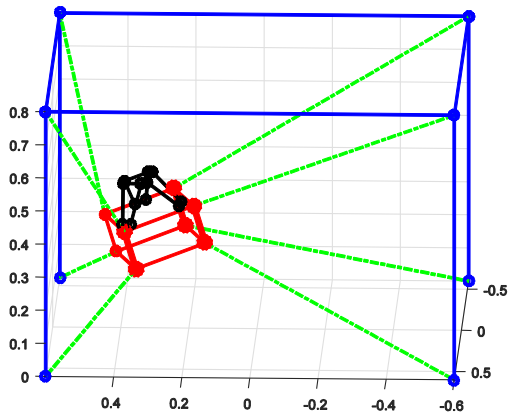

Fig. 2. Simulation model of the parallel cable-driven platform with superimposed active structure

The kinematic analysis is just a first step. The resulting configuration of the platform controlled by 8 cables with superimposed active hexapod structure will be further analysed in terms of dynamics and cable deformation.

Acknowledgements

The work has been supported by the Czech Science Foundation project GA15-20134S - Multi-Level Light Mechanisms with Active Structures.

References

[1] Bauma, V., Šika, Z., Valášek, M., Optimization of stiffness and dexterity of fiber driven parallel kinematical structure, Bulletin of Applied Mechanics 7 (28) (2011) 81-84.

[2] Florián, M., Valášek, M., Efficient computation of antibacklash space for redundant PKM. Proceedings Interaction and Feedbacks 2006, Prague, Institute of Thermomechanics AS CR, 2006, pp. 13-20.

[3] Merlet, J. P., On the redundancy of cable-driven parallel robots, New Trends in Mechanism and Machine Science 24 (2015) 31-39.

[4] Valášek, M., Bauma, V., Šika, Z., Svatoš, P., A method and a device for change of rigidity of a serial or parallel basic movable mechanism, especially of industrial robots and machine tools, Patent, Industrial Property Office, 304673, 2014. (in Czech)

COMPUTATIONAL MECHANICS 2015
31st conference with international participation
Špičák
November 9 - 11, 2015

Verification of algorithm for automatic chute motion control

J. Blekta [a]

[a] *Department of Applied Mechanics, Technical university of Liberec, Studentská 2, 461 17 Liberec, Czech Republic*

Conveyors are very important equipments in surface mines. They transport coal and rocks from one side of mine to another. This paper is focused on conveyors used in the first four levels (floors) of mines. They are used for transportation of rocks (overburden) mostly. Total length of conveyer's line is about 8 km and it consists from several conveyor belts, usually of the 1 km length. The rock is poured from one belt to another. This fact can cause problem with wearing out of the belt. Therefore it was necessary to suggest solution how to reduce a kinetic energy of the falling mass.

Two nearest conveyors are connected in station, where transported material is poured from one belt to another. The first solution, how to minimize kinetic energy of falling rocks, was suggested by changing of station's construction. This suggestion was repeatedly discussed with the designer and finally was rejected. The reason was shortage of construction place necessary for this modification. From above mentioned idea another solution was suggested. The principle of this one is to insert steel chute (wedge) between incoming and outgoing belt. The chute is inserted in the place where are the falling rocks in the contact with outgoing belt. The advantage of this conception is a significant reduction of the impact energy of the falling material, the disadvantage is the danger of clogging of the hopper's area, when the adhesive material is transported. Therefore it was decided, that the chute must be movable.

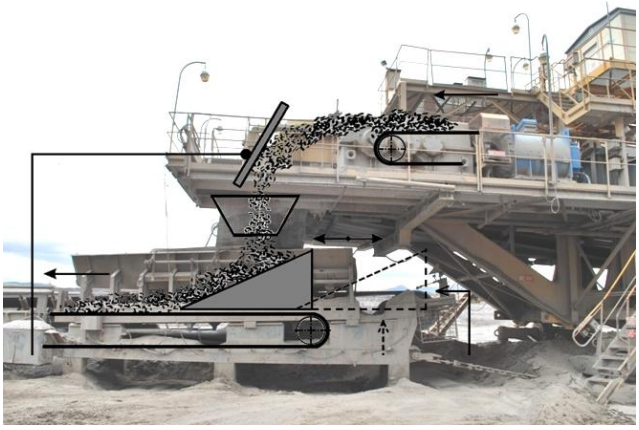

Fig. 1. Scheme of suggested change

It was necessary to suggest suitable algorithm for chute movement control. This algorithm should be based on correct criterion of harness and lumpiness of transported material. Totaly three possibilities were considered to obtain correct criterion [1]:

- Laser sensor: Scanning of the circumference of transported material cross-section area by laser sensor (laser weight). This measure should recognize smoothness of circumference's curve cross-section area of transported materials. The advantage of this method is that this sensor is still used for measuring of quantity of transported material. But this method brings an important disadvantage - method is unsuitable for measuring of material lumpiness and

hardness, because lumpiness material doesn´t automatically means hard material and in advance, big parts of materials can be hidden inside of material mass.

- Manually: by wheel-excavator operator intervention. Operator of wheel-excavator can directly see structure of mined material. Therefore operator is one of the best indicators to say, whether to chute slide in or not. But, instead of this advantage, this possibility is unreliable, because it depends on operator experiences at the first and on operator tiredness secondly.
- The last possibility is based on knowledge that transported material is in contact with the steel shield during falling from incoming belt to outgoing one. This steel shield has a function of directing of transported material to the center of outgoing belt. Consequently it has to be in contact with falling rocks. This shield is placed between both belts. After a many of measures was decided to identify hardness and lumpiness of transported material by the excitation of this steel shield eigenfrequencies. By impact of the hard material, eigenfrequencies are excited with much greater intensity than in the case of the soft adhesive material.

To verify relationship between transported material hardness and intensity of exited shield eigenfrequencies suitable measuring algorithm was suggested. Measuring chain consists from 1D vibration sensor, real-time PC, comparator and software for shield's vibrations evaluation. Sensor is mounted to shield in the place, which was chosen on the base of eigenfrequencies measurement. Suggested algorithm consists from this steps:

- measured signal is split by set time constant to separate signals,
- for each separated signal FFT analysis is computed,
- to highlight fields with eigenfrequencies the results of FFT analysis are multiplied by function of weight coefficients. This function consists of given number of sin waves of different amplitudes, which are 20 Hz wide. Each wave corresponds with one eigenfrequency only. Frequencies below 150 Hz and above 800 Hz are suppressed. Multiplication by weight function gives better sensitivity to vibration effect in the field of shield eigenfrequencies.
- The area under result curve gets from multiplying FFT analysis and weight function is computed.
- This value is stored to matrix of defined length. Its length is user adjustable and depends on required time sensitivity of criterion. When matrix is full, the last element is forgotten.
- Criterion (the result value) is computed as average value of matrix elements.

Specially software in LabView environment was developed to real-time PC control. Suggested algorithm was tested by four series of measures with different properties of transported material. These measures were used to set a proper values of user adjustable constants. Algorithm good functionality was verified by 9 series of measures. Each series contained 10 measures for specific type of transported material. Algorithm right functionality were observe.

Acknowledgements

This work has been supported by the grant project FR-TI4/310 of the Ministry of Industry and Trade.

References

[1] Blekta, J., et al., Algorithm for automatic chute motion control, Book of Extended Abstracts, Experimental Stress Analysis 2015, Český Krumlov, CTU in Prague, 2015, pp. 11-12.

[2] Bocko, P., Petrikova, I., Kraus, V., Marvalova, B., Blekta, J., Skarolek, A., Increasing of working life of conveyor belts affected by shocks, Proceedings of the International Journal of Transport and Logistics, 2012.

COMPUTATIONAL MECHANICS 2015
31st conference with international participation
Špičák
November 9 - 11, 2015

Contact forces on motorcycle rider overall during high speed low side sliding accident

T. Bońkowski [a], M. Hajžman [a], R. Kottner [a], T. Görner [b], L. Hubík [c], J. Vychytil [d], L. Hynčík [d]

[a] New Technologies for the Information Society, University of West Bohemia, Univerzitní 8, 306 14 Plzeň, Czech Republic
[b] Faculty of Mechanical Engineering, University of West Bohemia, Univerzitní 8, 306 14 Plzeň, Czech Republic
[c] PSi Hubík, s.r.o., Daimlerova 3, 301 00 Plzeň, Czech Republic
[d] New Technologies – Research Centre, University of West Bohemia, Univerzitní 8, 306 14 Plzeň, Czech Republic

According to MAIDS [1], single vehicle accidents have around 16 % share of all motorcycle crashes. The low side is a type of the single motorcycle accident which is caused by a loss of traction. In connection with high velocity, this accident can result in ejection of a driver from the seat. The only protection of the driver body from friction of a road during the low side event is a proper protective clothing. Such situation occurred during a Moto GP racing competition in 2011 on the TT Circuit Assen. On the 17th turn, the Czech driver Karel Abraham started to slide on a road after the low side crash. This event became a model example for the research team to prepare the low side high speed accident simulation. Main aim of the simulation is obtaining realistic values of the contact forces between the rider body and the ground. In future those values will be used for the optimization of a personal protecting equipment (PPE).

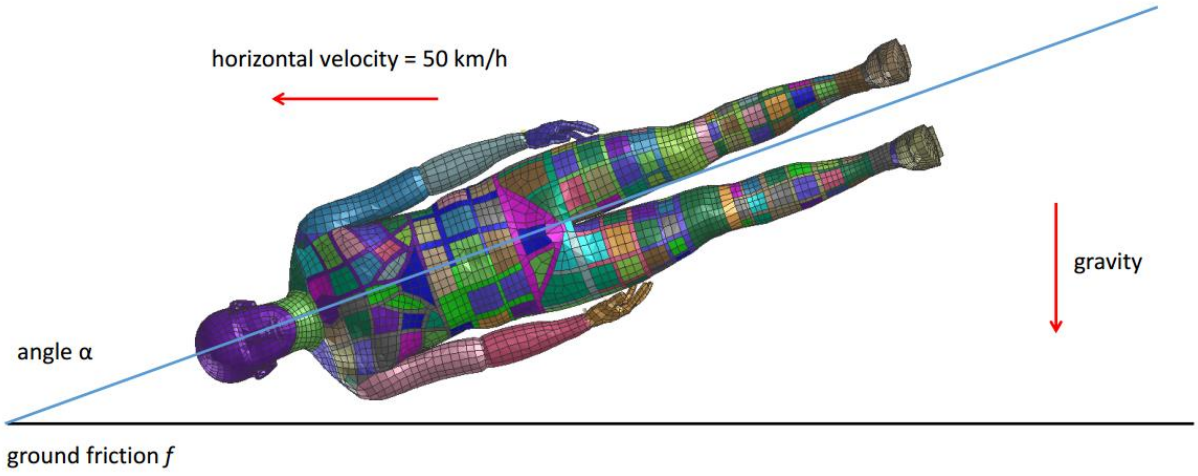

Fig. 1. Virtual experiment setup

For assessing the realistic response of the human body during the accident, the VPS Explicit Virthuman [2] model was used. The model has been scaled to the Karel Abraham body mass and dimensions. Due to lack of experimental data related to the friction coefficient, the sensitivity analysis was made. The Virthuman had been positioned in the way showed in the Fig. 1. The Simulation was carried out 9 times with 3 values of the friction coefficient (0.1, 0.5, and 0.9) and with 3 different alpha angles. Each of the alpha angle was representing

situation with the different first contact point (110° - the shoulder impact first, 115° - the head impact and the shoulder impact together, 135° - the head impact first). During the simulation, 3 main outputs were monitored: the head injury criteria, the head contact force, and the right arm contact force (Fig. 2).

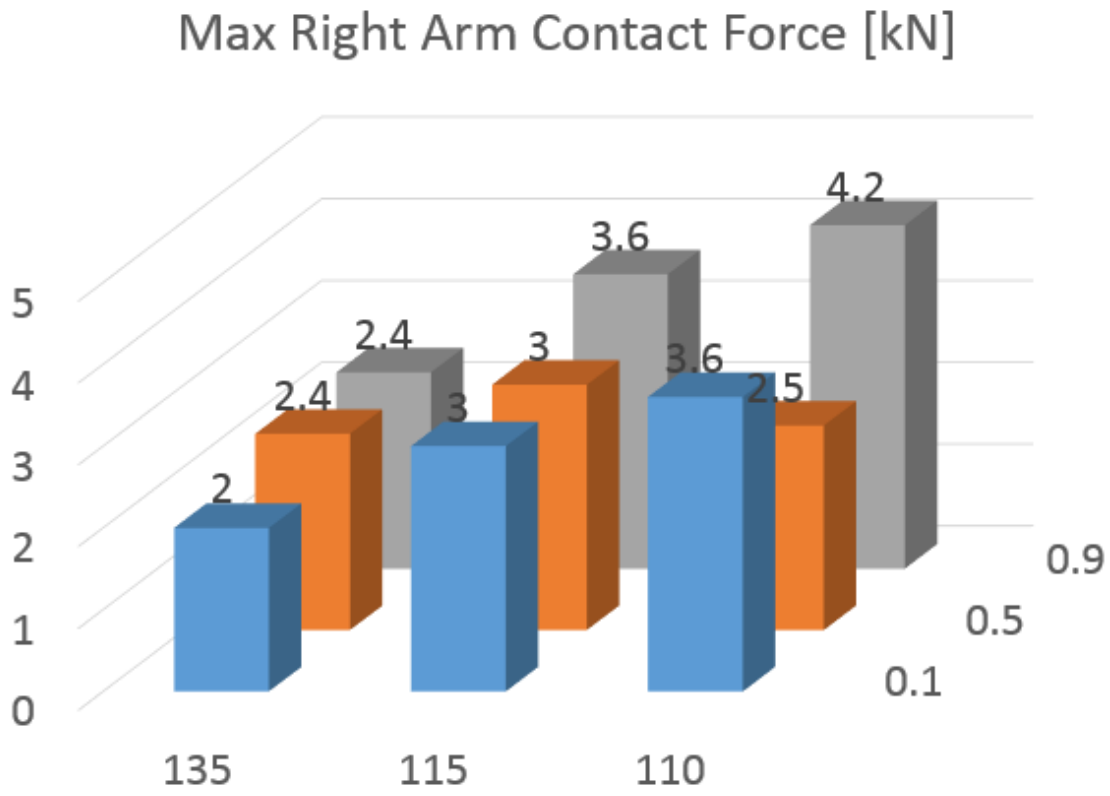

Fig. 2. Maximum values of contact force on right arm

The head injury criteria during the simulations was in range 710 - 14417 (the lowest for CoF = 0.1 and alpha = 135°, the highest for CoF = 0.9 and alpha = 110°). The contact force on the right arm was in range 2 - 4.2 kN (Fig. 2). In the further research simulation will serve for the PPE optimization.

Acknowledgements

The work is co-financed by the ITN network project "MOTORIST" of the 7th FP People of the EU under the contract number FP7-PEOPLE-2013-ITN-608092 and by the internal research project SGS-2013-026. The authors would like to thank PSi Hubík s.r.o. for providing the experimental data.

References

[1] ACEM, MAIDS: In-depth investigation of accidents involving powered two wheelers, Brussels, 2009.

[2] Hyncik, L., Cechova, H., Kovar, L., Blaha, P., On Scaling Virtual Human Models, SAE Technical Paper 2013-01-0074, 2013, doi:10.4271/2013-01-0074.

COMPUTATIONAL MECHANICS 2015
31st conference with international participation
Špičák
November 9 - 11, 2015

Modelling of a blade couple with contact in shrouding by means of Rayleigh beam finite elements

J. Brůha [a], V. Zeman [a]

[a] *Faculty of Applied Sciences, University of West Bohemia, Univerzitní 8, 306 14 Plzeň, Czech Republic*

With more powerful and effective coal-fired and nuclear power plants, demands on today's high-performance steam turbine blades are rising. Mathematical modelling and dynamic behaviour simulations are very important parts of the design theory. However, in cases of design parameters optimization or contact problems of bladed disks, using of complex 3D finite element models of the blades with high number of degrees of freedom can be disadvantageous because of time-consuming computation [2]. In these cases, modelling of the turbine blades by means of various types of beam finite elements [3, 5] can be perceived as a basic tool for dynamic behaviour investigation.

Presented work, continuing to contribution [1], deals with modelling of a couple of twisted blades with rhombic shrouds (that are considered to be rigid). This blade couple is clamped into a rigid disk rotating with constant angular velocity ω_0 around the Y-axis (Fig. 1). Either of the blades is divided into $N-1$ Rayleigh beam finite elements (blade finite elements) with varying cross-sectional parameters along each element and six degrees of freedom in each of the nodes $i = 1, \ldots, N$: longitudinal displacement u_i, transversal displacements v_i, w_i and three angular displacements φ_i, ϑ_i and ψ_i of the cross-section (see Fig. 1).

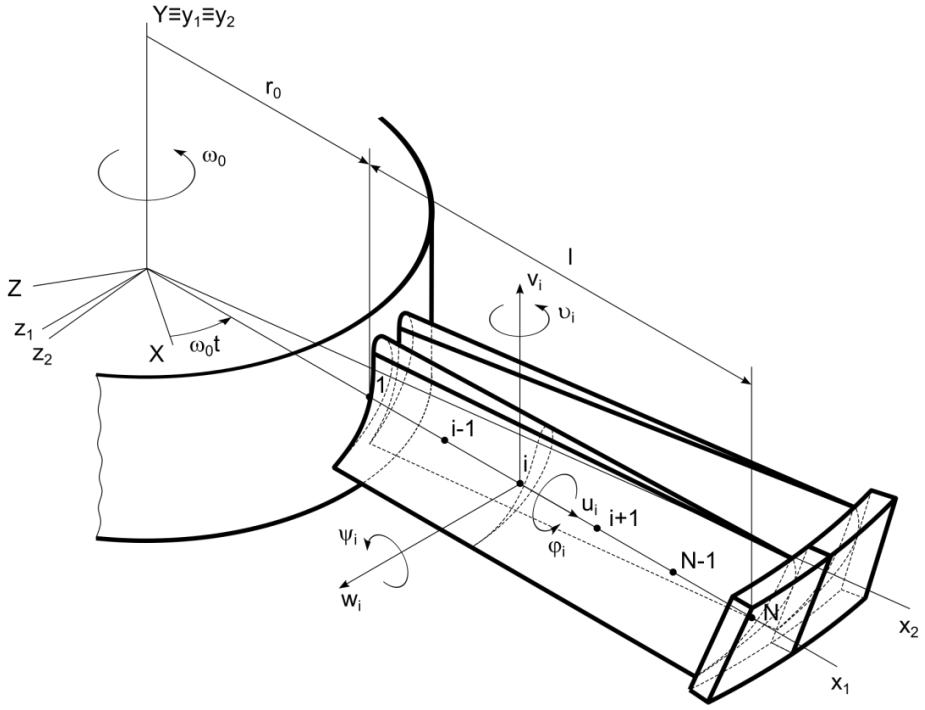

Fig. 1. Rotating blade couple clamped into a disk

Since the finite element models based on the Rayleigh beam theory tend to slightly overrate natural frequencies and underrate deflections in comparison with finite element models including shear deformation effects [3], parameters E_e, ν_e and $J_{T,e}$ representing the Young's modulus, the Poisson's ratio and the torsion resistance of every blade finite element e were being tuned [1]. Using configuration space of the blades written in the form [4]

$$\boldsymbol{q}_{B_j} = [\ldots \quad u_i \quad v_i \quad w_i \quad \varphi_i \quad \vartheta_i \quad \psi_i \quad \ldots]_j^T , \quad j = 1,2 \text{ (blades)} , \tag{1}$$

equations of motion of the rotating blade couple with smooth contact surfaces (without friction) can be expressed in the form

$$\begin{bmatrix} \boldsymbol{M}_B & \boldsymbol{0} \\ \boldsymbol{0} & \boldsymbol{M}_B \end{bmatrix} \begin{bmatrix} \ddot{\boldsymbol{q}}_{B_1} \\ \ddot{\boldsymbol{q}}_{B_2} \end{bmatrix} + \left\{ \begin{bmatrix} \boldsymbol{B}_B & \boldsymbol{0} \\ \boldsymbol{0} & \boldsymbol{B}_B \end{bmatrix} + \omega_0 \begin{bmatrix} \boldsymbol{G}_B & \boldsymbol{0} \\ \boldsymbol{0} & \boldsymbol{G}_B \end{bmatrix} \right\} \begin{bmatrix} \dot{\boldsymbol{q}}_{B_1} \\ \dot{\boldsymbol{q}}_{B_2} \end{bmatrix} +$$

$$+ \left\{ \begin{bmatrix} \boldsymbol{K}_{s,B} + \omega_0^2 \left(\boldsymbol{K}_{stiff,B} - \boldsymbol{K}_{\omega,B} \right) & \boldsymbol{0} \\ \boldsymbol{0} & \boldsymbol{K}_{s,B} + \omega_0^2 \left(\boldsymbol{K}_{stiff,B} - \boldsymbol{K}_{\omega,B} \right) \end{bmatrix} + \boldsymbol{K}_C \right\} \begin{bmatrix} \boldsymbol{q}_{B_1} \\ \boldsymbol{q}_{B_2} \end{bmatrix} = \boldsymbol{0} , \tag{2}$$

where the symmetric matrices $\boldsymbol{M}_B$, $\boldsymbol{B}_B$, $\boldsymbol{K}_{s,B}$, $\omega_0^2 \boldsymbol{K}_{stiff,B}$, $-\omega_0^2 \boldsymbol{K}_{\omega,B}$ and $\boldsymbol{K}_C$ represent mass, material damping, static stiffness, bending stiffening under rotation, softening due to blade modelling in the rotating coordinate system and contact stiffness, respectively. The skew-symmetric matrix $\omega_0 \boldsymbol{G}_B$ represents gyroscopic effects. Then, a modal analysis of the rotating blade couple described by (2) is performed and comparison of calculated natural frequencies in dependence on rotational speed and contact stiffness between blade shrouds is shown.

Presented work deals with modelling of a rotating blade couple by means of Rayleigh beam finite elements and analysis of a contact stiffness impact on natural frequencies. In this paper, contact surfaces of the blade shrouds are considered to be smooth. Described method, which is a useful alternative to large 3D finite element models with high number of degrees of freedom, can find application, for example, in design parameters optimization of bladed disks with contact in shrouding.

Acknowledgement

This work was supported by the project LO1506 of the Ministry of Education, Youth and Sports of the Czech Republic and by the project TE01020068 "Centre of research and experimental development of reliable energy production" of the Technology Agency of the Czech Republic.

References

[1] Brůha, J., Rychecký, D., Modelling of rotating twisted blades as 1D continuum, Extended abstracts of the 21st international conference Engineering Mechanics 2015, Institute of Theoretical and Applied Mechanics AS CR, Prague, 2015, pp. 32-33.

[2] Hajžman, M., Byrtus, M., Zeman, V., Solution of the mutual contact in the finite element analysis of twisted blades, Colloquium Dynamics of Machines 2012, Prague, pp. 51-58.

[3] Han, S. M., Benaroya, H., Wei, T., Dynamics of transversely vibrating beams using four engineering theories, Journal of Sound and Vibration 225 (1999) 935-988.

[4] Kellner, J., Vibration of turbine blades and bladed disks, Ph.D. Thesis, University of West Bohemia, Pilsen, 2009.

[5] Yokoyama, T., Free vibration characteristic of rotating Timoshenko beams, International Journal of Mechanical Sciences 30 (1988) 743-755.

COMPUTATIONAL MECHANICS 2015
31st conference with international participation
Špičák
November 9 - 11, 2015

A parallel implementation of the implicit discontinuous Galerkin finite element method for fluid flow problems

O. Bublík[a], J. Vimmr[a], A. Pecka[a], A. Jonášová[a]

[a] *NTIS – New Technologies for the Information Society, Faculty of Applied Sciences, University of West Bohemia, Univerzitní 8, 306 14 Plzeň, Czech Republic*

The discontinuous Galerkin finite element method (DGFEM) [3, 5] is currently the most rapidly developing method in the field of computational fluid dynamics. The growing popularity is mainly due to its ability to achieve high-order spatial accuracy, low artificial damping, robustness and stability. DGFEM contains a large number of degrees of freedom compared to the finite element method or even more so to the finite volume method. This increases the computational demands of the DGFEM. The papers [1, 2] marginally deals with this drawback and compare different time integration methods, namely explicit local time stepping and implicit methods. This study also tries to overcome the high computational demands using parallel computing.

We consider the 2D compressible viscous fluid flow, which is traditionally modelled by the nonlinear system of Navier-Stokes equations (NSEs). Let $\Omega \in \mathbb{R}^2$ be the computational domain and $\mathcal{T}_h$ its triangulation. The DGFEM is based on seeking the solution in $\boldsymbol{V} = V_h \times V_h \times V_h \times V_h$, where $V_h = \{v_h \in \mathcal{L}^2(\Omega) : v_h|_E \in \mathcal{P}^q(E), E \in \mathcal{T}_h\}$ and $\mathcal{P}^q$ is the space of polynomials up to degree q. Expressing the solution of NSEs as a linear combination of basis functions of $\boldsymbol{V}$, inserting it into the weak formulation [4] and substituting the test function $\boldsymbol{v} \in \boldsymbol{V}$ for the basis functions, we obtain the following system of first-order ordinary differential equations, unknowns of which are coefficients of the linear combinations,

$$\boldsymbol{M}\frac{\mathrm{d}\boldsymbol{u}}{\mathrm{d}t} = \boldsymbol{R}(\boldsymbol{u}), \tag{1}$$

where $\boldsymbol{M}$ is the mass matrix. Discretising the time variable by the backward Euler method and consequently linearising Eq. (1), we obtain a system of linear algebraic equations. In the following, we will be focus on the parallelisation of the iterative GMRES method applied to the resultant linear system and the efficiency of the parallelisation.

We present a parallel implementation based on the original Schwarz method [6]. The principle of the method is to divide the computational domain Ω into a set of overlapping subdomains Ω_i, $\bigcup \Omega_i = \Omega$. The computation is performed for each subdomain separately. The detailed description of the algorithm will be given at the conference.

The algorithm was implemented with the aid of JAVA, a modern object-oriented programming language. The communication between computers (nodes) is performed by the *remote method invocation technology*, which is able to call JAVA methods on remote virtual machines.

Figs. 1 and 2 show the results of a numerical experiment carried out for fluid flow around the NACA 0012 airfoil. Increasing the number of threads Fig. 1 (right) leads to the reduction of computational time, however the computational efficiency drops rapidly. On the other side increasing the number of nodes provides almost linear speedup of calculation, see Fig. 2 (left).

CPU [s]	# of nodes		
# of cores	1	2	3
1	2750	1467	1032
2	1468	796	647
4	921	542	413
8	767	437	313

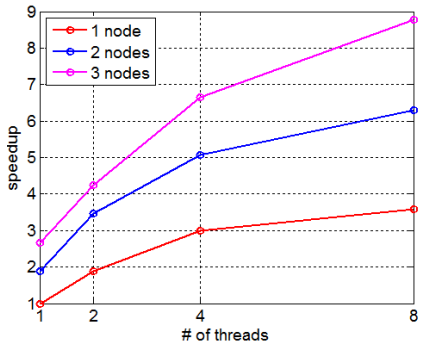

Fig. 1. Computational time required to reach 1000 iterations (*left*), computation speedup depending on the number of threads plotted for various number of nodes (*right*)

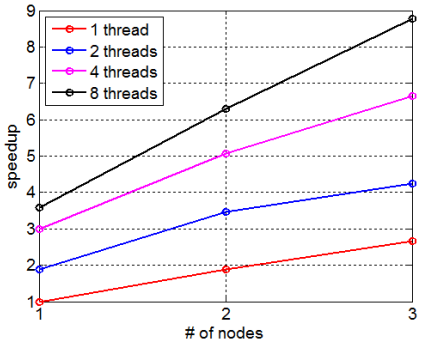

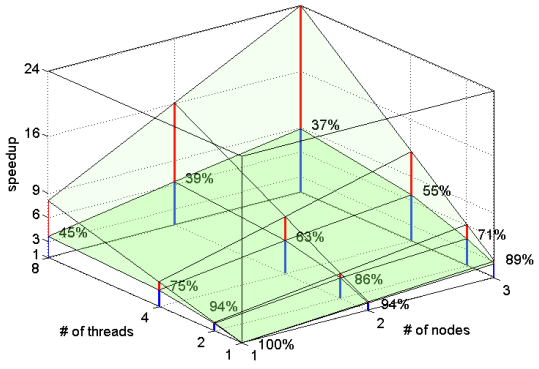

Fig. 2. Computation speedup depending on the number of nodes plotted for various numbers of threads (*left*), efficiency of parallel computing (*right*)

Acknowledgements

This work was supported by the project LO1506 of the Czech Ministry of Education, Youth and Sports and by the project TE01020068 "Centre of research and experimental development of reliable energy production" of the Technology Agency of the Czech Republic.

References

[1] Birken, P., Gassner, G., Haas, M., Munz, C.-D., Efficient time integration for discontinuous Galerkin method for the unsteady 3D Navier-Stokes equations, Proceedings of ECCOMAS 2012, Vienna, 2012, pp. 4334-4353.

[2] Bublík, O., Vimmr, J., Jonášová, A., Comparison of discontinuous Galerkin time integration schemes for the solution of flow problems with deformable domains, Applied Mathematics and Computation (267) (2015) 329-340.

[3] Cockburn, B., Shu, C.-W., The local discontinuous Galerkin method for time-dependent convection-diffusion systems, SIAM Journal on Numerical Analysis (35) (1998) 2440-2463.

[4] Dolejší, V., On the discontinuous Galerkin method for the numerical solution of the Navier-Stokes equations, International Journal for Numerical Methods in Fluids (35) (2004) 1083-1106.

[5] Reed, W. H., Hill, T. R., Triangular mesh methods for the neutron transport equations, Los Alamos Scientific Laboratory Report LA-UR-73-479, 1973. (unpublished)

[6] Schwarz, H. A., Ueber einen Grenzübergang durch alternirendes Verfahren, Vierteljahrsschrift der Naturforschenden Gesellschaft in Zürich (15) (1870) 272-286. (in German)

COMPUTATIONAL MECHANICS 2015
31st conference with international participation
Špičák
November 9 - 11, 2015

Constitutive models of materials showing large elastic strains

J. Burša [a]

[a] *Faculty of Mechanical Engineering, Brno University of Technology, Technická 2, 616 69 Brno, Czech Republic*

After a comprehensive overview of constitutive models of materials [1], a more detailed information on materials showing large elastic strains is presented. The paper presents a brief overview of basic formulations of stress and strain (or deformation) tensors to be distinguished under large deformations and the definition of hyperelastic materials. The theory of hyperelasticity is based on various formulations of the strain energy density (SED) function being a scalar function of all components of deformation tensor. By differentiation of the SED function with respect to components of deformation tensor, the corresponding components of the conjugated stress tensor can be calculated, e.g.

$$S_{ij} = \frac{\partial W}{\partial E_{ij}} = 2\frac{\partial W}{\partial C_{ij}}, \tag{1}$$

where W is a specific SED function, S represents 2nd Piola-Kirchhoff stress tensor, E is Green-Lagrange strain tensor and C is right Cauchy-Green deformation tensor.

Among the phenomenological models, polynomial forms of SED function are the most frequent; the most general form for isotropic materials is as follows:

$$W = \sum_{i+j=1}^{N} c_{ij}\left(\bar{I}_1 - 3\right)^i \left(\bar{I}_2 - 3\right)^j + \sum_{k=1}^{M} \frac{1}{d_k}\left(J-1\right)^{2k}, \tag{2}$$

where the first member describes the deviatoric part of SED by means of $\bar{I}_1$ and $\bar{I}_2$ representing the first and second invariant of deviatoric right Cauchy-Green deformation tensor, respectively; the second member describes the volumetric part of SED by means of the 3rd invariant J of deformation gradient tensor, representing the relative volume change. Number of material parameters c_{ij} and d_k depends on the degrees N and M of the polynomial model, respectively. When omitting the volume related member, an incompressible variant of the model can be obtained; this variant requires introduction of an additional Lagrange multiplier with physical meaning of hydrostatic pressure. For N = 1, 2, or 3, we obtain different forms of Mooney-Rivlin models. When we set N = 1 and j = 0, Eq. (2) reduces to the Neo-Hooke model and the sole material parameter receives a clear physical meaning $c_{10} = G/2$, with G being shear modulus.

Anisotropic hyperelastic models can be formulated either as SED functions of individual components of a strain (deformation) tensor, or as a sum of isotropic and anisotropic (fibre-related) part of SED. The anisotropic parts of SED functions are mostly formulated by means of pseudoinvariants I_4 and I_5 of the right Cauchy-Green deformation tensor and structure tensor A [3]. The structure tensor is defined as the tensor product of unit vector of fibre direction with himself, so we obtain the following double dot contraction formulas for the pseudoinvariants:

$$I_4 = C:A \quad \text{and} \quad I_5 = C^2:A. \tag{3}$$

The invariants I_4 and I_5 represent powered fibre stretches λ_f^2 and λ_f^4, respectively, and the specific forms of anisotropic parts of SED functions are mostly polynomial or exponential (these dominate in soft tissue biomechanics). This approach is sufficient for materials with one family of fibres, showing transversal isotropy; for more fibre families more additional pseudoinvariants are to be formulated. As the fibres mostly cannot bear compressive load, their contribution to the strain energy should be limited to their elongation (stretches $\lambda_f > 1$).

If the fibres in the material are not perfectly aligned but show some dispersion of directions, some dispersion or concentration parameter is needed to specify the orientation probability distribution of fibres. The best known model of this type was formulated in [2] in the form:

$$W = \frac{\mu}{2}(I_1 - 3) + \frac{k_1}{k_2}\left\{e^{\left[k_2(\kappa I_1 + (1-3\kappa)I_4 - 1)^2\right]} - 1\right\}, \tag{4}$$

where dispersion parameter κ is between 0 (perfectly aligned fibres) and 1/3 (perfect isotropic distribution of fibres), while μ, k_1 and k_2 are other material-related parameters of the model. Significant dispersion of fibres is typical e.g. for collagen fibres in soft tissues.

Collagen fibres in arterial wall, however, are not only dispersed in their directions but undulated as well; this fact contributes substantially to the basic feature of these tissues ─ high strain stiffening related to straightening of the collagen fibres. As an example of models taking the undulation of fibres into consideration, the model published in [4] is presented. This model applies a triangular probability distribution function for the undulation of fibres, specified by the range of stretch values under which the fibres become straight and start to bear load.

The structure based models taking directions (including their dispersion) of fibres and/or their undulation into consideration are very promising for description of passive mechanical response of many soft tissues. However, they require thorough information on the internal structure of the tissues, specifically on directions and undulation of collagen fibres in the tissue. During the last decade, this information is growing substantially due to new methods for automated analyses of histological figures [5]. The most actual problem how to distinguish between directional dispersion and undulation of fibres, i.e. between their local and global directions, is analysed in the presentation. In the end limitations related to the assumption of zero bending stiffness (i.e. zero diameter) of the fibres will be mentioned, including a possible way how to introduce the bending stiffness of fibres into the constitutive models.

Acknowledgements

The work has been supported by Czech Science Foundation, grant project No. 13-16304S.

References

[1] Burša, J., Janíček, P., Systemic approach to modelling of constitutive behaviour of various types of matter, Engineering Mechanics 16 (4) (2009) 1-15.

[2] Gasser, T. C., Ogden, R. W., Holzapfel, G. A., Hyperelastic modelling of arterial layers with distributed collagen fibre orientations, Journal of The Royal Society Interface 3 (2006) 15-35.

[3] Holzapfel, G. A., Gasser, T. C., Ogden, R. W., A new constitutive framework for arterial wall mechanics and a comparative study of material models, Journal of Elasticity 61 (2000) 1-48.

[4] Martuffi, G., Gasser, T. C., A constitutive model for vascular tissue that integrates fibril, fiber and continuum levels with application to the isotropic and passive properties of the infrarenal aorta, Journal of Biomechanics 44 (14) (2011) 2544-2550.

[5] Novak, K., Polzer, S., Tichy, M., Bursa, J., Automatic evaluation of collagen fibre directions from polarized light microscopy images, Microscopy and Microanalysis 21 (4) (2015) 863-875.

COMPUTATIONAL MECHANICS 2015
31st conference with international participation
Špičák
November 9 - 11, 2015

Real-space ab-initio electronic structure calculations using SfePy

R. Cimrman[a], M. Novák[b], R. Kolman[c], J. Vackář[b]

[a] *New Technologies Research Centre, University of West Bohemia, Univerzitní 8, 306 14 Plzeň, Czech Republic*
[b] *Institute of Physics, Academy of Sciences of the Czech Republic, Na Slovance 2, 182 21 Praha 8, Czech Republic*
[c] *Institute of Thermomechanics, Academy of Sciences of the Czech Republic, Dolejškova 5, 182 00 Praha, Czech Republic*

We present the recent developments of our code for ab-initio calculations of electronic states within the framework of density-functional theory, cf. [5, 6, 7, 8] and environment-reflecting pseudopotentials [9], based on the open source finite element package SfePy (Simple Finite Elements in Python, http://sfepy.org) [2, 3]. The code brings a new quality to DFT calculations of total energy, Hellmann-Feynman forces and material properties particularly for non-crystalline, non-periodic structures [10].

In electronic structure calculations, various material properties can be obtained by means of computing the total energy of a system as well as derivatives of the total energy w.r.t. atomic positions. The derivatives, also known as Hellman-Feynman forces, require, because of practical computational reasons, the discretized charge density and wave functions having continuous second derivatives in the whole solution domain. In the contribution, we show our use of isogeometric analysis [1, 4] a spline modification of the finite element method, to achieve the required continuity, as well as numerical examples of electronic structure calculations of various systems. We also present the overall structure of our code that allows computing both the primary quantities coming directly from the Schrödinger equation: the charge density ρ and the orbitals Ψ_i (see Fig. 1 for an illustration), and the derived quantities, such as the total energy.

Acknowledgments

The work was supported by the Grant Agency of the Czech Republic, project P108/11/0853. R. Kolman's work was supported by the grant project of the Czech Science Foundation (GACR), No. GAP 101/12/2315, within the institutional support RVO:61388998.

References

[1] Borden, M.J., Scott, M.A., Evans, J.A., Hughes, T.J.R., Isogeometric finite element data structures based on Bezier extraction of NURBS, International Journal for Numerical Methods in Engineering 87 (1-5) (2011) 15-47.

[2] Cimrman, R., Enhancing SfePy with isogeometric analysis, Proceedings of the 7th European Conference on Python in Science (EuroSciPy 2014), Cambridge, UK, 2014, pp. 65-72.

[3] Cimrman, R., SfePy – write your own FE application, Proceedings of the 6th European Conference on Python in Science (EuroSciPy 2013), Brussels, 2013, pp. 65-70.

[4] Cottrell, J.A., Hughes, T.J.R., Bazilevs, Y., Isogeometric analysis: Toward integration of CAD and FEA, John Wiley & Sons, 2009.

[5] Dreizler, R.M., Gross, E.K.U., Density functional theory, Springer-Verlag, 1990.

[6] Martin, R.M., Electronic structure: Basic theory and practical methods, Cambridge University Press, 2005.

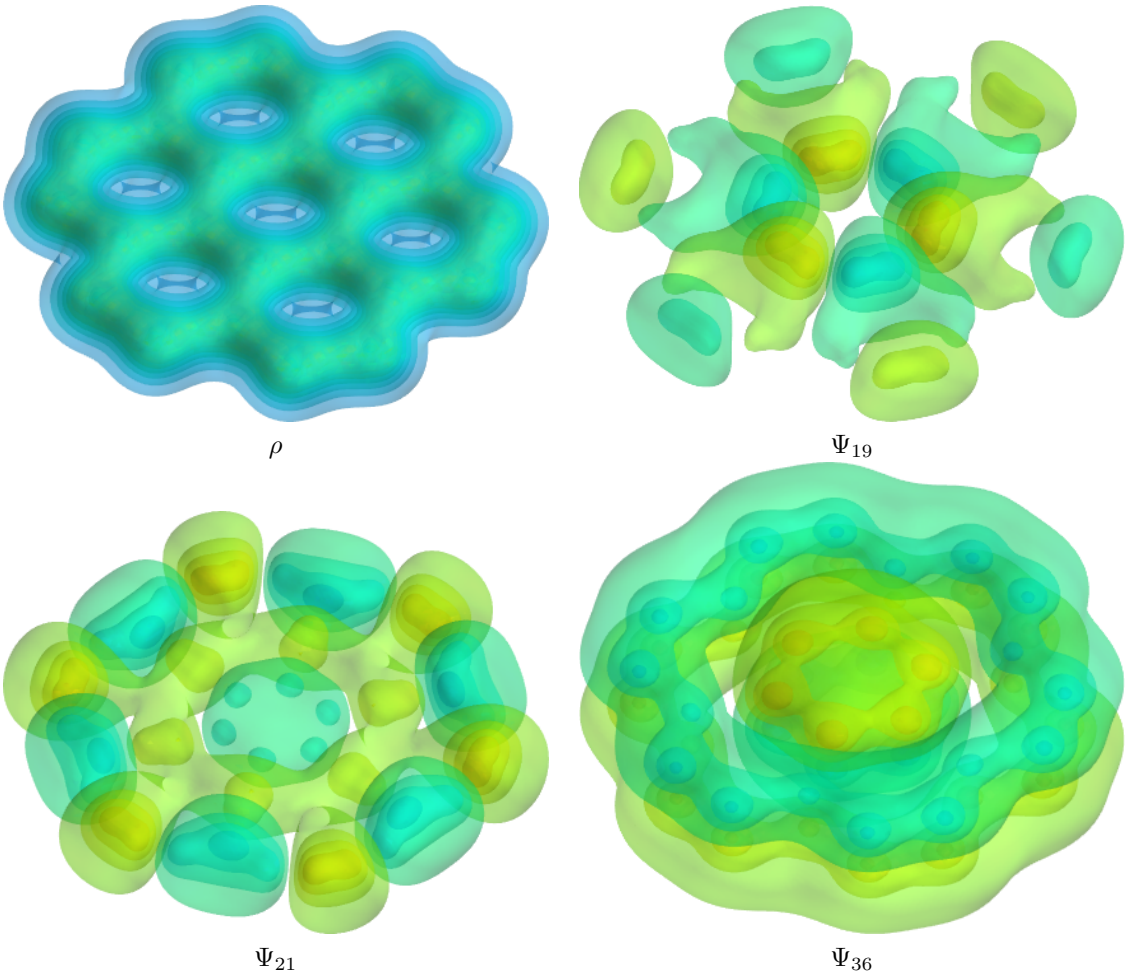

Fig. 1. Electronic structure calculation example: charge density ρ and several orbitals Ψ_i of a graphene "flower"

[7] Parr, R.G., Weitao, Y., Density-functional theory of atoms and molecules, Oxford University Press, USA, 1994.

[8] Pickett, W.E., Pseudopotential methods in condensed matter applications, Computer Physics Reports 9 (3) (1989) 115-198.

[9] Vackář, J., Šimůnek, A., Adaptability and accuracy of all-electron pseudopotentials, Physical Review B 67 (2003) 125113.

[10] Vackář, J., Čertík, O., Cimrman, R., Novák, M., Šipr, O., Plešek, J., Finite element method in density functional theory electronic structure calculations, In: Advances in the theory of quantum systems in chemistry – Volume 22 of the series Progress in Theoretical Chemistry and Physics, editors: P.E. Hoggan, E.J. Brändas, J. Maruani, P. Piecuch, G. Delgado-Barrio, Springer, 2011, pp. 199-217.

COMPUTATIONAL MECHANICS 2015
31st conference with international participation
Špičák
November 9 - 11, 2015

Discretization and parameterization of route description for velocity profile optimization of vehicle

P. Denk [a], P. Steinbauer [a], Z. Šika [a], J. Macek [b] J. Morkus [b]

[a] *CTU in Prague, Faculty of Mechanical engineering, Department of mechanics, biomechanics and mechatronic, Technická 4, 160 00 Praha, Czech Republic*
[b] *CTU in Prague, Faculty of Mechanical engineering, Department of automotive, combustion engine and Railway engineering, Technická 4, 160 00 Praha, Czech Republic*

Nowadays the electric power consumption and its optimization is main topic in development of electric vehicle. The first study of vehicle dynamics shows that the energy power consumption is the most depend on the shape and slope of driving trajectory, value of acceleration and deceleration and the efficiency of vehicle charging system (in the cases of regeneration charging), but in general the most energy consumption affect the driver by the driving behavior. For example, if the driver passes an unknown route, the driver controls the vehicle by predictive control based on the information of the roadway, which are obtain at the visible distance or from traffic sign. The control process is thus limited to the partial section, where driving interventions are restricted to ensure the stability of the vehicle motion. This control process cannot be considered as optimal, because the missing knowledge about necessary following maneuvers depend on route properties causes next energy inefficient maneuver, for example sharp deceleration.

In the case, if we want to optimize total energy consumption, it is necessary to optimize riding behavior based on energy flowing in the internal units of electric vehicle, in general depend on current vehicle velocity and route trajectory shape. The efficiency of charging unit is difficult to optimize, but it is preferable to optimize the vehicle dynamics behavior, which depend on prior route description knowledge and knowledge of energy flow in other interior electric units. Initial studies of the electric vehicle energy consumption indicate that the choice of optimal driving strategy along the prescribed path can reduce energy consumption up to 15% or more [1]. The energy consumption optimization brings benefits for individual passes the trajectory, but more benefits brings using the strategy for a many repeats of driving along the prescribe route (for example in case of delivery vehicles, vehicles distribute newspapers, pastries etc.). Primary and decisive element in optimization energy consumption is becoming the route description knowledge and it is dedicated to following paper.

The first and the most important part of route description is the real trajectory shape. The inputs for the route description are data from one of commercial navigation software, like Nokia Here etc. which plane the route trajectory between chosen beginning and ending points. The data from navigation software contain GPS coordinates of navigation points, the slope and the values of legal velocity limits in those points. In the first step, it is necessary to transformed input data from GPS coordinates into the Cartesian coordinates, based on haversin formula and great cycle distance [2]. The center point of Cartesian coordinates is chosen beginning point of navigation data. In the second step, the obtained points in Cartesian coordinates are necessary to fit by approximating curve and in the third step is solved current value of curvature radius for all navigation points. That is obtained the mathematic model of trajectory shape.

Then it is necessary to create a real velocity limit in each navigation point. The velocity limit value for each point is create from values of legal velocity limit and from physical bounds, depend on adhesion limit and chosen comfortable parameter. In this case, the comfortable parameter means the chosen bounds for lateral acceleration of vehicle, based on the curvature radius knowledge.

The trajectory description extended about real velocity limit allows dividing whole prescribe trajectory into small consecutive section. The section is defined by following set of constant parameters:

a) constant velocity limit,
b) constant slope,
c) constant vehicle load,
d) constant curvature radius.

Each such section can be further divided into smaller phases, defined on the basis of possible driving mode of vehicle. The possible driving mode are following mode:

a) mode with acceleration,
b) mode with constant velocity,
c) coasting mode with deceleration caused only by riding resistances,
d) mode with deceleration caused by vehicle break system.

These possible modes can be used only one time in each section and the sequence of modes is given and unchanged (see Fig. 1).

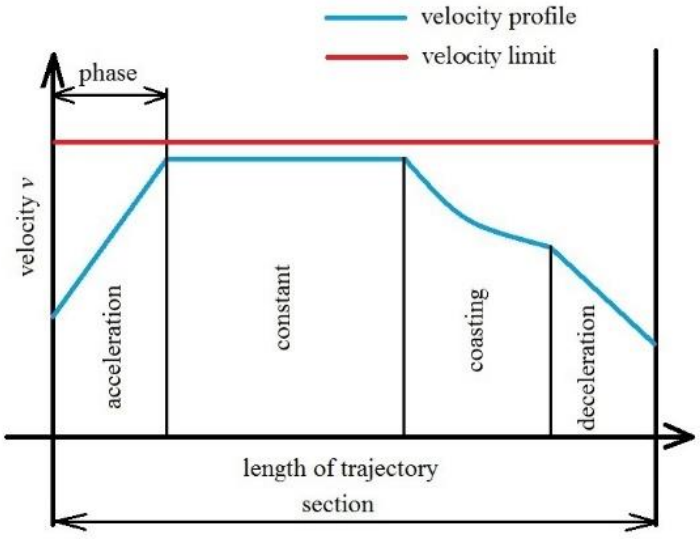

Fig. 1. Dividing one of section into phases with defined riding mode

The route trajectory description by the set of parameters based on mode dividing can be very varied and it will be discussed.

Acknowledgements

This research has been realized using the support of project Improve EP FP7-ICT – Integration and Management of Performance and Road Efficiency of Electric Vehicle Electronics.

References

[1] Fuel Economy Guide, U. S. Department of Energy, www.fueleconomy.gov, Updated September 25, 2015.
[2] The Haversine Formula, www.longitudestore.com/haversine-formula.html, September 24, 2014.

COMPUTATIONAL MECHANICS 2015
31st conference with international participation
Špičák
November 9 - 11, 2015

Methodology of behaviour simulation of cable-driven manipulators with varying cable lengths

J. Dupal [a], M. Byrtus [a]

[a] *New Technologies for the Information Society, European Centre of Excellence, Faculty of Applied Sciences, University of West Bohemia, Univerzitní 8, 306 14 Plzeň, Czech Republic*

The paper deals with methodology and modelling of the cable mechanisms consisting of N cables whose one end rolls pulleys and so called end effector which is taken into account as a rigid body driven by prescribed motion of pulleys. Let suppose that j-th cable is subdivided into n_j parts having length L_j/n_j end discretized into n_j-1 points having mass $m_j = \rho l_j$. $L_j(t)$ (j=1, 2, …, N) is given time dependent length of the j-th cable and ρ is linear density of the unstretched cable. We suppose ρ is common for all cables. For the reason that $L_j(t)$ is time dependent, m_j and l_j are time dependent, too [1]. Since the n_j is constant for each cable, the DOF number of each cable and the total model remains formally constant.

For this moment we omit the superscript in brackets marking the number of the cable. Equilibrium condition of the infinitesimal element of the cable in the tangent direction can be written in form

$$\rho \frac{d^2\mathbf{r}}{dt} = \frac{\partial}{\partial s}\left[EA\varepsilon(s,t)\mathbf{b}(s,t)\right] + \mathbf{a}(s,t)\ , \tag{1}$$

where $\mathbf{b}(s,t)$ and $\mathbf{a}(s,t)$ are the unit vector tangent to the cable and vector of external load, respectively. Length coordinate of the cable is labeled by s. By substituting finite spatial differences instead of derivatives in discretization points into the Eq. (1)

$$\frac{\partial \mathbf{r}_i}{\partial s} \doteq \frac{\mathbf{r}_{i+1} - \mathbf{r}_{i-1}}{2l},\quad \frac{\partial^2 \mathbf{r}_i}{\partial s^2} \doteq \frac{\mathbf{r}_{i+1} - 2\mathbf{r}_i + \mathbf{r}_{i-1}}{l^2}, \tag{2}$$

we can come to the equation of motion of the j-th cable in form

$$\mathbf{m}_j(t)\ddot{\mathbf{x}}_j(t) + \mathbf{c}_j(t)\dot{\mathbf{x}}_j(t) + \mathbf{k}_j(\mathbf{x}_j, t)\mathbf{x}_j(t) = \mathbf{f}^{(j)}(\mathbf{h}, \boldsymbol{\varphi}, \mathbf{x}_j), \qquad j = 1, 2, ..., n_c, \tag{3}$$

where n_c is number of cables, $\mathbf{h}$ and $\boldsymbol{\varphi}$ is radius-vector of end-effector gravity center and Euler's angle vector of end-effector, respectively. The other symbols mean

$$\mathbf{x}_j(t) = \begin{bmatrix} \mathbf{r}_1^{(j)}(t) \\ \mathbf{r}_2^{(j)}(t) \\ \vdots \\ \mathbf{r}_{n_j-1}^{(j)}(t) \end{bmatrix} \in \mathbf{R}^{3(n_j-1)}, \quad \mathbf{m}_j(t) = \begin{bmatrix} \rho l_j(t)\mathbf{I} & & & \\ & \rho l_j(t)\mathbf{I} & & \\ & & \ddots & \\ & & & \rho l_j(t)\mathbf{I} \end{bmatrix} \in \mathbf{R}^{3(n_j-1),3(n_j-1)}, \tag{4}$$

$\mathbf{r}_i^{(j)}$ is radius-vector of the i-th point of the j-th cable,

$$\mathbf{c}_j(t)=\begin{bmatrix} \mathbf{0} & -c_1^{(j)}\mathbf{I} & & & & \\ c_2^{(j)}\mathbf{I} & \mathbf{0} & -c_2^{(j)}\mathbf{I} & & & \\ \mathbf{0} & c_3^{(j)}\mathbf{I} & \mathbf{0} & -c_3^{(j)}\mathbf{I} & & \\ \vdots & \mathbf{0} & \ddots & \ddots & \ddots & \\ \vdots & \vdots & \vdots & c_{n_j-2}^{(j)}\mathbf{I} & \mathbf{0} & -c_{n_j-2}^{(j)}\mathbf{I} \\ \mathbf{0} & \mathbf{0} & \mathbf{0} & \cdots & c_{n_j-1}^{(j)}\mathbf{I} & \mathbf{0} \end{bmatrix}, \quad \mathbf{R}^{3(n_j-1),3(n_j-1)} \quad c_i^{(j)}=-\rho\dot{s}_i^{(j)}(t), \qquad (5)$$

where $s_i^{(j)}(t)=i\dfrac{L_j(t)}{n_j}$, $\dot{s}_i^{(j)}(t)=i\dfrac{\dot{L}_j(t)}{n_j}$. Matrix $\mathbf{k}_j(\mathbf{x}_j,t)$ takes a form

$$\mathbf{k}_j(\mathbf{x}_j,t)=\begin{bmatrix} k_{11}^{(j)}\mathbf{I} & k_{12}^{(j)}\mathbf{I} & \mathbf{0} & \cdots & \cdots & \cdots & \mathbf{0} \\ k_{21}^{(j)}\mathbf{I} & k_{22}^{(j)}\mathbf{I} & k_{23}^{(j)}\mathbf{I} & \mathbf{0} & \cdots & \cdots & \mathbf{0} \\ \mathbf{0} & k_{32}^{(j)}\mathbf{I} & k_{33}^{(j)}\mathbf{I} & k_{34}^{(j)}\mathbf{I} & \mathbf{0} & & \vdots \\ \vdots & \mathbf{0} & k_{43}^{(j)}\mathbf{I} & \ddots & \ddots & \ddots & \vdots \\ \vdots & \vdots & & \ddots & \ddots & \ddots & \mathbf{0} \\ \vdots & \vdots & & & k_{(n_j-2)(n_j-3)}^{(j)} & k_{(n_j-2)(n_j-2)}^{(j)} & k_{(n_j-2)(n_j-1)}^{(j)} \\ \mathbf{0} & \mathbf{0} & \mathbf{0} & \cdots & \mathbf{0} & k_{(n_j-1)(n_j-2)}^{(j)} & k_{(n_j-1)(n_j-1)}^{(j)} \end{bmatrix} \in \mathbf{R}^{3(n_j-1),3(n_j-1)}, \qquad (6)$$

where coefficients $k_{\alpha\beta}^{(j)}$ depend on strain of individual cables and thus on $\mathbf{x}_j$. The right hand side of Eq. (3) corresponds to the force vector which depends on position and velocities of end-effector, cable points and pulleys. The joint displacements and velocities of cable ends and end-effector are described by boundary conditions which performs the couplings between end-effector and individual cable equation of motion. Motion of end-effector is represented by means of system of 6 nonlinear ordinary differential equations (ODE). The total system of cable mechanism is described by $6+3\sum_{j=1}^{n_c}(n_j-1)$ ODE.

Acnowledgements

The paper has originated in the framework of solving No. 15-20134S project of the Czech Science Foundation entitled “Multi-level Light Mechanisms with Active Structures”.

References

[1] Du, J., Bao, H., Cui, Ch., Yang, D., Dynamic analysis of cable-driven parallel manipulators with time-varying cable lengths, Finite elements in analysis and design 48 (2012) 1392-1399.

COMPUTATIONAL MECHANICS 2015
31st conference with international participation
Špičák
November 9 - 11, 2015

Novel limiting process of the discontinuous Galerkin method applied to shallow water equations

M. Fišer[a,b], O. Bublík[b], J. Vimmr[b]

[a] Department of Mechanics, Faculty of Applied Sciences, University of West Bohemia (UWB), Univerzitní 8, 306 14 Plzeň, Czech Republic
[b] NTIS – New Technologies for the Information Society, Faculty of Applied Sciences, UWB, Univerzitní 8, 306 14 Plzeň, Czech Republic

Shallow Water Equations are suitable for the modeling of the free surface flow when the horizontal scales of a liquid mass are much bigger than the vertical scale and vertical flows are negligible. Mathematical model of Shalow Water Equations (SWE) was described by Berre Saint-Venant in 1872 and one of its forms written in 1D is

$$\frac{\partial}{\partial t}\underbrace{\begin{bmatrix} h \\ hu \end{bmatrix}}_{\mathbf{W}} + \frac{\partial}{\partial x}\underbrace{\begin{bmatrix} hu \\ hu^2 + \frac{1}{2}\mathrm{g}h^2 \end{bmatrix}}_{\mathbf{F}(\mathbf{W})} = \begin{bmatrix} 0 \\ 0 \end{bmatrix}, \tag{1}$$

where $\mathbf{W} = [W_1, W_2]^T = [h, hu]^T$ is the vector of conservative variables represented by the water depth $h(x,t)$, and the flow velocity $u(x,t)$, $\mathbf{F}(\mathbf{W})$ is the inviscid flux and g represents gravitational acceleration.

In this work, the mathematical model (1) is solved by the discontinuos Galerkin method (DGFEM). Within DGFEM, the computational area Ω is divided into non-overlapping finite element cells Ω_i and the conservative variables $W_{i,k}$ in the ith finite element cell are expressed as a linear combination

$$W_{i,k}(x,t) = \sum_{j=1}^{nb} w_{i,k}^j(t)\varphi_i^j(x), \quad k = 1,2, \tag{2}$$

where nb means the number of the basis functions, $w_{i,k}^j$ are time dependent coefficients of the linear combination and $\varphi^j(x)$ are basis functions (Legendre polynomials within this work). In the following the parameters t and x are omitted.

Application of DGFEM to (1) yields

$$\mathbf{M}_i \frac{d}{dt}\mathbf{w}_{i,k} + \left[\Phi_k \cdot \varphi_i^j\right]_{x_{i-\frac{1}{2}}}^{x_{i+\frac{1}{2}}} - \int_{\Omega_i} F_k \frac{\partial \varphi_i^j}{\partial x}\, d\Omega = \mathbf{0}, \quad j = 1,2,\dots nb, \quad k = 1,2, \tag{3}$$

where $\mathbf{M}_i = [M_{i_j,l}] = \left[\int_{\Omega_i} \varphi_i^j \varphi_i^l d\Omega\right]$ is mass matrix, Φ_k is k^{th} component of the numerical approximation of the inviscid flux across the cell edge, F_k is is k^{th} component of the inviscid flux and $\mathbf{w}_{i,k} = [w_{i,k}^1, w_{i,k}^2, \dots, w_{i,k}^{nb}]$ is vector of the time dependent coefficients.

As a testing benchmark 2D dam break was chosen. The initial condition of the water depth is $h_0 = 0.6$ and position of the dam is $l_0 = 0.6$. Computational domain was discretized by ten finite element cells. DGFEM can produce non-physical negative values around the wet/dry interface as shown in Fig. 1. In these cases the solution has to be limited.

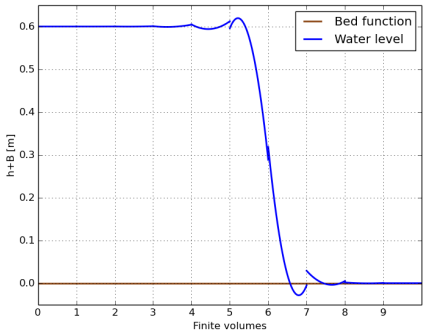

Fig. 1. Non-limited solution of DGFEM in time 0.015 s

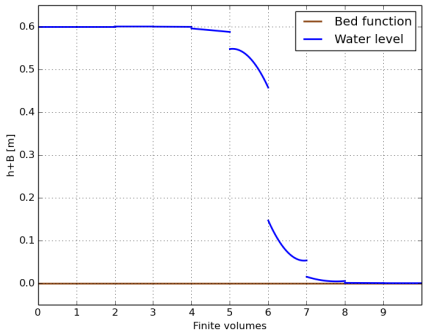

Fig. 2. Limited solution of DGFEM in time 0.015 s

The solution is limited only in cells which are defined as 'troubled' cells. There are many criteria defining this 'troubled' cells, but some of them fails in case of appearance of the wet/dry interface or do not work within high-order approximation. In this work we propose novel criterion for defining 'troubled' cells and also suggest the limiting method, which works in case of high-order approximation, appearance of the wet/dry interface and can be also used for limiting of the solution around the shocks.

The cell is defined as 'troubled' in the time level t^n if

$$\begin{gathered} W_{i,k}(x_i,t^n) \le W_{i,k}(x_{i-\frac{1}{2}},t^n) \quad \text{and} \quad W_{i,k}(x_i,t^n) \le W_{i,k}(x_{i+\frac{1}{2}},t^n) \\ \text{or} \\ W_{i,k}(x_i,t^n) \ge W_{i,k}(x_{i-\frac{1}{2}},t^n) \quad \text{and} \quad W_{i,k}(x_i,t^n) \ge W_{i,k}(x_{i+\frac{1}{2}},t^n), \end{gathered} \tag{4}$$

where $x_{i\pm\frac{1}{2}}$ are positions at the edge of the finite element and x_i is position of the cell centre. If the cell is defined as 'troubled' then the approximating function is reduced to the linear function, second coefficient $w^2_{i,k}$ is computed by minmod limiter

$$w^2_{i,k} = minmod(\ (w^1_{i+1,k} - w^1_{i,k})/(|x_{i+1} - x_i|), \quad (w^1_{i,k} - w^1_{i-1,k})/|(x_i - x_{i-1}|)\ ) \tag{5}$$

and higher coefficients of the linear combination (2) are set to zero.

In case of the water depth limiting, it is important to guarantee non-negative values. To achieve this goal, the modification proposed in [1] is adopted

$$w^2_{i,1} = \begin{cases} 2w^1_{i,1}/\Delta x & \text{if} \quad h(x_{i-\frac{1}{2}},t^n) < 0, \\ -2w^1_{i,1}/\Delta x & \text{if} \quad h(x_{i+\frac{1}{2}},t^n) < 0, \end{cases} \tag{6}$$

where Δx is the finite element cell width. The limited solution can be seen in Fig. 2.

This criterion is simple, computationally not demanding and can be used for variety of problems (hydrodynamics, air flows, etc.). The criterion can be also easily extended for 2D problems.

Acknowledgements

This work was supported by the project LO1506 of the Czech Ministry of Education, Youth and Sports and by the student grant project SGS-2013-036 of the University of West Bohemia.

References

[1] Kurganov, A., Petrova, G., A second-order well-balanced positivity preserving central-upwind scheme for the Saint-Venant system, Communications in Mathematical Sciences 5 (1) (2007) 133–160.

COMPUTATIONAL MECHANICS 2015
31st conference with international participation
Špičák
November 9 - 11, 2015

On the unbalance estimation for large turbine dynamic models from a run-down

M. Hajžman[a], O. Červená[a], J. Mrštík[a], M. Balda[a]

[a]*Research and Testing Institute Plzeň Ltd., Tylova 1581/46, 301 00 Plzeň, Czech Republic*

Rotor dynamics is one of the most important branches of mechanics of many real industrial problems [1]. Prediction of possible rotor vibration is necessary for design engineers and therefore suitable modelling tools should be developed. Another topic is the troubleshooting during turbine operations. Such tasks are related to the knowledge of imposed excitation, which si usually caused by rotor unbalance. The paper deals with the mathematical modelling of turbine rotors including foundation and estimation of their excitation parameters from a measured run-down.

The whole mathematical model is composed of a rotor train (described by vector of generalized coordinates $\mathbf{q}_R$) and a non-rotating foundation part (described by $\mathbf{q}_F$, see Fig. 1)

$$\begin{aligned}\begin{bmatrix} \mathbf{M}_F & \mathbf{0} \\ \mathbf{0} & \mathbf{M}_R \end{bmatrix} \begin{bmatrix} \ddot{\mathbf{q}}_F \\ \ddot{\mathbf{q}}_R \end{bmatrix} + \left(\begin{bmatrix} \mathbf{B}_F + \mathbf{B}_G & \mathbf{0} \\ \mathbf{0} & \mathbf{B}_R + \omega_0 \mathbf{G}_R \end{bmatrix} + \mathbf{B}_B \right) \begin{bmatrix} \dot{\mathbf{q}}_F \\ \dot{\mathbf{q}}_R \end{bmatrix} + \\ + \left(\begin{bmatrix} \mathbf{K}_F & \mathbf{0} \\ \mathbf{0} & \mathbf{K}_R \end{bmatrix} + \mathbf{K}_B \right) \begin{bmatrix} \mathbf{q}_F \\ \mathbf{q}_R \end{bmatrix} = \begin{bmatrix} \mathbf{f}_F \\ \mathbf{f}_R \end{bmatrix},\end{aligned} \tag{1}$$

where $\mathbf{M}_F$ and $\mathbf{M}_R$ are mass matrices of the foundation and the rotor, $\mathbf{B}_F$ and $\mathbf{B}_R$ are material damping matrices, $\mathbf{K}_F$ and $\mathbf{K}_R$ are stiffness matrices of the foundation and the rotor, $\mathbf{B}_G$ is

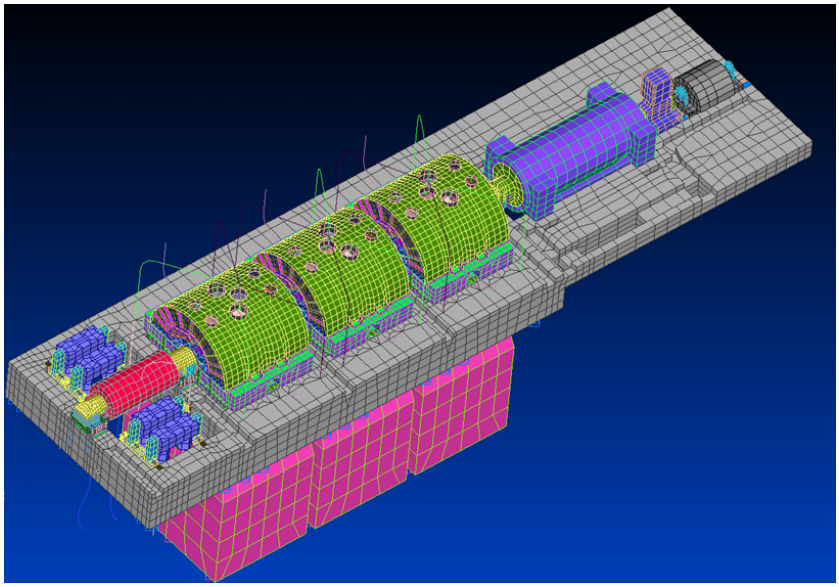

Fig. 1. Finite element model of a turbine stator with foundation

damping matrix representing GERB elements between the foundation and the ground, $\omega_0 \mathbf{G}_R$ is matrix of gyroscopic effects, $\mathbf{B}_B$ and $\mathbf{K}_B$ are damping and stiffness of the bearings (generally dependent on rotor angular velocity ω_0) and $\mathbf{f}_F$ and $\mathbf{f}_R$ are vectors of possible external excitation.

It is suitable to reduce model (1) using a modal transformation [2] in order to have an efficient mathematical model of the whole system and to employ advantages related to usage of various software combination. Steady state vibration (frequency response) of the turbine can be obtained after the definition of excitation by unbalance in vector $\mathbf{f}_R$ [2, 3].

An in-house software for solution of rotor dynamics was created based on the presented methodology and a real turbine model was implemented in this software. Measured (see Fig. 2) and calculated frequency responses from a single run-down were then used for the formulation of suitable objective functions and identification of rotor residual unbalance. Various objective functions were formulated using correlation coefficients, using weighted relative errors of the curves etc. Different numerical procedures for the solution of defined optimization problem were employed.

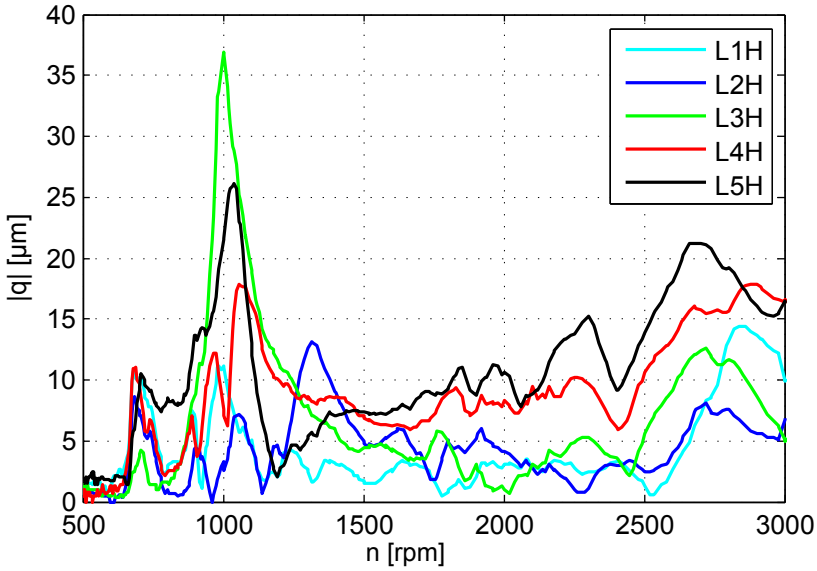

Fig. 2. Measured amplitudes of rotor vibration in horizontal directions for five bearing pedestals

Acknowledgements

The paper has been originated in the framework of institutional support for the long-time conception development of the research institution provided by Ministry of Industry and Trade of the Czech Republic. Authors thank to colleagues from the Noise and vibration department for providing experimental results.

References

[1] Adams, M.L., Rotating machinery vibration: From analysis to troubleshooting, Marcel Dekker, New York, 2001.

[2] Byrtus, M., Hajžman, M., Zeman, V., Dynamics of rotating systems, University of West Bohemia, Plzeň, 2010. (in Czech)

[3] Slavík, J., Stejskal, V., Zeman, V., Basics of machine dynamics, Vydavatelství ČVUT, Praha, 1997. (in Czech)

COMPUTATIONAL MECHANICS 2015
31st conference with international participation
Špičák
November 9 - 11, 2015

Modelling fatigue damage using finite elements and time homogenization

J. Heczko[a], R. Kottner[b]

[a] *Department of Mechanics, Faculty of Applied Sciences, University of West Bohemia, Univerzitní 8, 306 14 Plzeň, Czech Republic*

[b] *NTIS – New Technoloiges for the Information Society, Faculty of Applied Sciences, University of West Bohemia, Univerzitní 8, 306 14 Plzeň, Czech Republic*

Simulations of damage evolution and fatigue are crucial in the design process of various parts. In most situations, linear models can be used, and the superposition principle allows description of different loading states and quantification of accumulation of damage. Should material nonlinearity be considered (either in form of stress-strain relation or the rule for damage accumulation), the framework of continuum damage mechanics (CDM) is suitable for description of damage evolution and changes in mechanical properties of the material. The relations used in CDM are formulated in time domain, which, together with the above mentioned nonlinearity, leads to transient simulations. Computation in time domain is time-consuming in the case of high-cycle loading. Various authors proposed to use time averaging to overcome this obstacle.

The same model of damage as in [1] is used here. It accounts for isotropic damage in small-strain framework. The time-average operator is applied to the evolution equation over one period of loading. Thus the homogenized model is obtained.

The finite element discretization was implemented using the FEniCS project [2]. For spatial discretization, tetrahedral elements with linear approximation of displacement and piecewise constant approximation of the damage variable were used (see Fig. 1). An explicit time-stepping scheme was used.

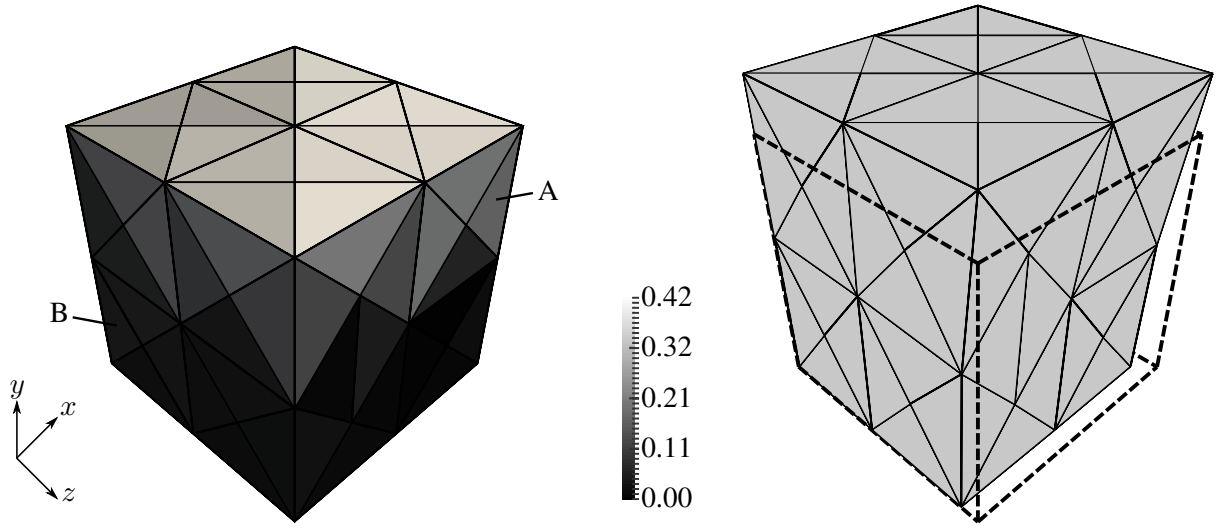

Fig. 1. Left: Distribution of damage parameter D at the end of the simulation. Right: Deformed shape at maximum deformation and the original volume depicted by the dashed line (displacement scaled by 10^4)

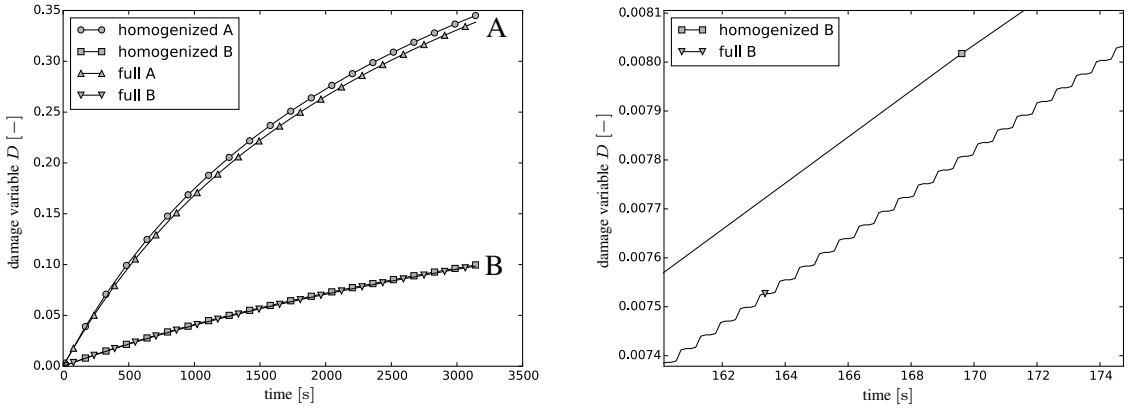

Fig. 2. Evolution of the damage variable over time – left: whole simulation, right: detail with cycles visible in the results of full simulation

The fully relaxing cyclic loading in tension was prescribed. Since stress and strain were inhomogeneously distributed, so was the damage variable. Fig. 2 shows evolution of the damage variable in time for two different elements (denoted A and B, their position is given in Fig. 1). The difference in results (when comparing full simulation and the homogenized model) depends strongly on the length of the time step. Moreover, the steps at the beginning of the simulation need to be smaller, since the value of $\partial D/\partial t$ is higher here. In more complex simulations, an adaptive time-stepping procedure would probably be used so that this problem would not occur.

The main conclusion, however, is that if the frequency of loading is high enough, the homogenized model is much faster than the full simulation.

Acknowledgements

Jan Heczko was supported by the Student Grant System SGS-2013-36. Radek Kottner was supported by the project LO1506 of the Czech Ministry of Education, Youth, and Sports.

References

[1] Devulder, A., Aubry, D., Puel, G., Two-time scale fatigue modelling: Application to damage, Computational Mechanics 45 (6) (2010) 637-646.

[2] Logg, A., Mardal, K.-A., Wells, G.N., Automated solution of differential equations by the finite element method, Springer, Berlin, 2012.

COMPUTATIONAL MECHANICS 2015
31st conference with international participation
Špičák
November 9 - 11, 2015

Comparison of suitability of selected material models of concrete for inverse identification of parameters with the aid of optimization algorithms

F. Hokeš [a]

[a] *Faculty of Civil Engineering, Brno University of Technology, Veveří 95, 602 00 Brno, Czech Republic*

The application of complex non-linear material models at numerical analyses using the finite element method can be considered as bringing the mathematical modelling methods nearer to the real actions of structures [1]. However, this approach at numerical calculations has several pitfalls. One of the problems is a large number of unknown parameters occurring in the constitutive relation definition that represent mechanical-physical or fracture-mechanical parameters of a given construction material. Moreover, values of this relatively extensive range of the parameters are not tabularized in most of the cases. Inappropriateness of the selected material model for the given type of the solved task can be another problem.

The inverse analyses methods can be applied advantageously on the issue of the ignorance of the material models parameters. Currently, several procedures are used for the inverse identification of the parameters of non-linear material models of concrete. One of the procedures is based on the application of optimization algorithms, at which the difference between the load dependence curve vs. deformation obtained from the experiment and the curve representing the output of the computational solution of the problem using the non-linear constitutive law is minimized. The objective function is thus defined by the above-mentioned manner. The design vector for the optimization is made by a set of the previously unknown parameters. Necessary design constraints arise from assumptions in which the selected material model was derived, or from the requirements on securing the solvability and smooth convergence. Using an appropriate model that can express the modelled problem is decisive factor that as a consequence ensures obtaining correct values of the parameters at the inverse identification.

Within the executed study, a commercial database of elasto-plastic material models multiPlas [5] that also disposes of several models for the concrete was used for the simulation of the non-linear behaviour of the materials in the ANSYS system [4]. The aim of the study was to verify the suitability of two selected models of the concrete for a potential inverse identification of the parameters from an experimental curve derived from a 3-point bending test. The first of the applied material models called Menétrey-Willam [2] and specified LAW14 is based on the Willam-Warnke yield surface [3] and belongs to a group of the material models that cannot express the strain rate effect on the state of stress. The second of the applied material models with the LAW9 Concrete specification is based on the combination of two models of the Drucker-Prager type within the multi-surface plasticity concept. Within this concept, two cones of the Drucker-Prager surface describing failure in a tensile and compressive domain are mutually combined. Both of the mentioned models belong to a group of the models with a non-associated law of the plastic flow which generally enables more realistic description of the concrete dilatancy.

Verification of the suitability of the mentioned material models from the multiPlas library was executed on 8 numerical simulations in total of the 3-point bending test of a concrete specimen with a notch in the ANSYS system. The computational model with dimensions of 360 x 120 mm was covered with a mesh of 4-node plane PLANE182 elements that enable the solution of the problem of the plane stress. All the model elements were assigned the thickness of 58 mm. Within the individual simulations possible dependency on the size of the finite element mesh was also monitored next to the suitability of the model for fitting of the predetermined loading curve. For each type of the material model computations on the meshes of the sizes of 1 mm, 2 mm, 3 mm and 6 mm were carried out.

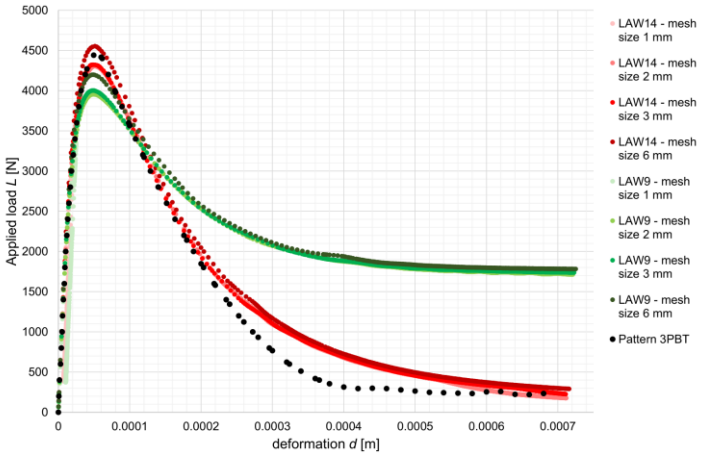

Fig. 1. Comparison of suitability of different mesh sizes

From the resulting loading curves shown in Fig. 1 follows that for the simulations of the bending test on the concrete beam with the notch the LAW14 material model is more suitable. This one is able to describe the area of the concrete post-critical behaviour more accurately. The computations with the LAW9 material model showed that the necessary approximation would not be possible to achieve at the optimization and consequently the correct parameters would be impossible to be identified. However, this conclusion does not exclude the application of this model in analyses with a different type of the stress than the bending tension. For all the finite element meshes, no significant dependence of the results on the size of this mesh was proved. However, there was a collapse of the computational solution at the both models with the mesh of the size of 1 mm, the cause of which has not been clarified for now.

Acknowledgements

The contribution has been created with the financial support of the project FAST-J-15-2875 "The Influence of the Strain Rate on the Parameters of Non-linear Material Models of Concrete" of the specific university research of Brno University of Technology.

References

[1] Hokeš, F., Selected aspects of modelling of non-linear behavior of concrete using multiPlas library, Proceedings of the 13th International Conference Modelling in Mechanics, Ostrava, VŠB-Technical University of Ostrava, 2015, pp. 31-32.
[2] Menétrey, P. G., Numerical analysis of punching failure in reinforced concrete structures, Ph.D. Thesis, École polytechnique fédérale de Lausane EPFL, Lausane, 2014.
[3] Willam, K. J., Warnke, E. P., Consitutive models of triaxial behavior of concrete, Proceedings of the International Association for Bridge and Structural Engineering, Bergamo, vol. 19, pp. 1-30.
[4] ANSYS, Inc., ANSYS Mechanical theory reference, Release 15.0, 2014.
[5] Dynardo GmBH, MultiPlas user's manual release 5.1.0 for ANSYS 15.0, Weimar, Germany, 2014.

COMPUTATIONAL MECHANICS 2015
31st conference with international participation
Špičák
November 9 - 11, 2015

The root-finding of dispersion curves in a bar impact problem

P. Hora[a]

[a] *Institute of Thermomechanics, Czech Academy of Sciences, Veleslavínova 11, 301 14 Plzeň, Czech Republic*

To calculate the stress wave propagation in a bar impact problem it is used the integration along the dispersion curves. This dispersion relations $f(x, \gamma a)$ is defined as

$$\left(2-x^2\right)^2 \mathrm{J}_0\left(\gamma a A\right) \mathrm{J}_1\left(\gamma a B\right) + 4AB\mathrm{J}_1\left(\gamma a A\right) \mathrm{J}_0\left(\gamma a B\right) - \frac{2x^2}{\gamma a} A\mathrm{J}_1\left(\gamma a A\right) \mathrm{J}_1\left(\gamma a B\right) = 0,$$

where a is radius of the semi-infinite bar, γ is wavenumber, x is the ratio of the phase velocity and the shear wave velocity, κ means the ratio of the squares of the phase velocities for the bar's material, $A = \sqrt{\kappa x^2 - 1}$, $B = \sqrt{x^2 - 1}$ and J is the Bessel function of the first kind.

Summary of the Chebyshev expansion algorithm [1]:

1. Choose the following:

   (i) γa.

   (ii) Search interval, $x \in [a, b]$.
   The search interval must be chosen by physical and mathematical analysis of the individual problem. The choice of the search interval $[a, b]$ depends on the user's knowledge of the physics of his/her problem, and no general rules are possible.

   (iii) The number of grid points, N.
   N may be chosen by setting $N = 1 + 2^m$ and the increasing N until the Chebyshev series displays satisfactory convergence. To determine when N is sufficiently high, we can examine the Chebyshev coefficients a_j, which decrease exponentially fast with j.

2. Compute a Chebyshev series, including terms up to and including T_N, on the interval $x \in [a, b]$.

   (i) Create the interpolation points (Lobatto grid):

   $$x_k \equiv \frac{b-a}{2} \cos\left(\pi \frac{k}{N}\right) + \frac{b+a}{2}, \quad k = 0, 1, 2, \ldots, N.$$

   (ii) Compute the elements of the $(N+1) \times (N+1)$ interpolation matrix.
   Define $p_j = 2$ if $j = 0$ or $j = N$ and $p_j = 1, j \in [1, N-1]$. Then the elements of the interpolation matrix are

   $$I_{jk} = \frac{2}{p_j p_k N} \cos\left(j\pi \frac{k}{N}\right).$$

(iii) Compute the grid-point values of $f(x)$, the function to be approximated:

$$f_k \equiv f(x_k), \quad k = 0, 1, \ldots, N.$$

(iv) Compute the coefficients through a vector-matrix multiply:

$$a_j = \sum_{k=0}^{N} I_{jk} f_k, \quad j = 0, 1, 2, \ldots ..., N.$$

The approximation is

$$f_N \approx \sum_{j=0}^{N} a_j T_j \left(\frac{2x - (b+a)}{b-a} \right) = \sum_{j=0}^{N} a_j \cos \left\{ j \arccos \left(\frac{2x - (b+a)}{b-a} \right) \right\}.$$

3. Compute the roots of f_N as eigenvalues of the ChebyshevFrobenius matrix.

   Frobenius showed that the roots of a polynomial in monomial form are also the eigenvalues of the matrix which is now called the *Frobenius companion matrix*. Day and Romero [2] developed a general formalism for deriving the *Frobenius matrix* for any set of orthogonal polynomials.

4. Refine the roots by a Newton iteration with $f(x)$ itself.

   Once a good approximation to a root is known, it is common to *polish* the root to close to machine precision by one or two Newton iterations.

Computations were performed with the normalized Bessel functions that eliminate the large fluctuations in magnitude. For numerical experiments we used the MATLAB's toolbox CHEBFUN [3] and the Julia's package ApproxFun [4].

Acknowledgement

The work was supported by the institutional support RVO:61388998.

References

[1] Boyd, J.P., A Chebyshev polynomial interval-searching method ("Lanczos economization") for solving a nonlinear equation with application to the nonlinear eigenvalue problem, Journal of Computational Physics 118 (1995) 1-8.

[2] Day, D.M., Romero, L., Roots of polynomials expressed in terms of orthogonal polynomials, SIAM Journal on Numerical Analysis 43 (2005) 1969-1987.

[3] Driscoll, T.A., Hale, N., Trefethen, L.N., Chebfun guide, Pafnuty Publications, Oxford, 2014.

[4] Julia package for function approximation, https://github.com/ApproxFun/ApproxFun.jl

COMPUTATIONAL MECHANICS 2015
31st conference with international participation
Špičák
November 9 - 11, 2015

Numerical modelling of flutter instability of the NACA 0012 profile in turbulent and laminar flow

J. Horáček[a], M. Feistauer[b], P. Sváček[c]

[a]Institute of Thermomechanics, Academy of Sciences of the Czech Republic, Dolejškova 5, 182 00 Prague 8, Czech Republic
[b]Charles University Prague, Faculty of Mathematics and Physics Sokolovska 83, 186 75 Praha 8, Czech Republic
[c]Czech Technical University Prague, Faculty of Mechanical Engineering, Karlovo nam. 13, 121 35 Praha 2, Czech Republic

The paper compares the numerical results obtained by the developed finite element solution for flutter instability of the profile with a flap vibrating in the laminar and turbulent flow. The profile motion is described by the nonlinear ordinary differential equations for large vibration amplitudes. The two-dimensional incompressible flow is modelled by the Navier-Stokes equations for the laminar flow and by the RANS equations for the turbulent flow. The flutter behaviour of the profile is numerically simulated in time domain.

Viscous incompressible turbulent flow can be described by the mean velocity vector $\mathbf{u} = \mathbf{u}(x,t)$ and the mean part of kinematic pressure $p = p(x,t)$ (i.e. mean aerodynamic pressure divided by the constant fluid density ρ) depending on $x \in \bar{\Omega}_t$ and $t \in [0,T]$, where $\bar{\Omega}_t$ is the closure of the 2D time domain Ω_t. The boundary $\partial\Omega_t$ consists of mutually disjoint parts: Γ_D is the inlet part, Γ_O is the outlet boundary, and Γ_{Wt} is the moving surface of the profile, $\partial\Omega_t = \Gamma_D \cup \Gamma_O \cup \Gamma_{Wt}$. Usage of the Reynolds decomposition of the flow velocity and the kinematic pressure into the mean parts and their turbulent fluctuations results in the RANS equations [1]:

$$\frac{\partial u_i}{\partial t} + (\mathbf{u}\cdot\nabla)u_i + \frac{\partial p}{\partial x_i} - \sum_{j=1}^{2}\frac{\partial}{\partial x_j}\left((\nu+\nu_T)\left(\frac{\partial u_i}{\partial x_j}+\frac{\partial u_j}{\partial x_i}\right)\right) = 0,\ i=1,2, \qquad \nabla\cdot\mathbf{u} = 0 \quad \text{in } \Omega_t,$$

where $\mathbf{u} = (u_1, u_2)$, u_1 and u_2 are the components of the velocity in the directions of the Cartesian coordinates x_1 and x_2, ν is the kinematic fluid viscosity and the turbulent eddy viscosity coefficient $\nu_T = \nu_T(x,t)$ is an unknown function, which requires further modelling. If $\nu_T = 0$, the flow is considered as laminar.

System of equations is equipped with the initial condition: $\mathbf{u}(x,0) = \mathbf{u}_0(x),\ x \in \Omega_0$,
and the boundary conditions

$$\mathbf{u}(x,t)\big|_{\Gamma_D} = \mathbf{u}_D,\ \mathbf{u}\big|_{\Gamma_{W_T}} = \mathbf{w}_D(x,t)\big|_{\Gamma_{W_T}},\ -(p-p_{ref})n_i + (\nu+\nu_T)\sum_{j=1}^{2}\left(\frac{\partial u_i}{\partial x_j}+\frac{\partial u_j}{\partial x_i}\right)n_j = 0 \text{ on } \Gamma_O,\ i=1,2.$$

Here $\mathbf{n} = (n_1, n_2)$ is the unit outer normal to the boundary $\partial\Omega_t$ of the domain Ω_t, $\mathbf{u}_D = (U_\infty, 0)$ is a prescribed far field velocity on the inlet Γ_D and $\mathbf{w}_D(x,t)$ is the velocity of the moving profile.

The nonlinear equations of motion of the profile for vibrations with large amplitudes are given as

$$m\ddot{h} + \left[(S_\alpha - S_\beta)\cos\alpha + S_\beta\cos(\alpha+\beta)\right]\ddot{\alpha} + S_\beta\ddot{\beta}\cos(\alpha+\beta) - (S_a - S_\beta)\dot{\alpha}^2\sin\alpha$$
$$- S_\beta(\dot{\alpha}+\dot{\beta})^2\sin(\alpha+\beta) + D_{hh}\dot{h} + k_{hh}h = L,$$

$$\left[\left(S_\alpha - S_\beta\right)\cos\alpha + S_\beta\cos\left(\alpha+\beta\right)\right]\ddot{h} + \left[\left(I_a - 2d_{PF}S_\beta\right) + 2d_{PF}S_\beta\cos\beta\right]\ddot{\alpha} + \left[I_\beta + d_{PF}S_\beta\cos\beta\right]\ddot{\beta}$$
$$- d_{PF}S_\beta\dot{\beta}^2\sin\beta - 2d_{PF}S_\beta\dot{\alpha}\dot{\beta}\sin\beta + D_{\alpha\alpha}\dot{\alpha} + k_{\alpha a}\alpha = M_\alpha,$$
$$S_\beta\cos\left(\alpha+\beta\right)\ddot{h} + \left[I_\beta + d_{PF}S_\beta\cos\beta\right]\ddot{\alpha} + I_\beta\ddot{\beta} + d_{PF}S_\beta\dot{\alpha}^2\sin\beta + D_{\beta\beta}\dot{\beta} + k_{\beta\beta}\beta = M_\beta,$$

where L denotes the component of the force acting on the whole profile in the vertical direction, M_α is the torsional moment acting on the whole profile with respect to the elastic axis EA, M_β is the torsional moment acting on the flap with respect to the rotary axis EF, D_{hh}, $D_{\alpha\alpha}$, $D_{\beta\beta}$ are coefficients of a structural damping, S_α, I_α and m denote the static moment of the whole profile around the axis EA, the moment of inertia of the whole profile around the axis EA and the mass of the whole profile, respectively. The coefficient S_β is the static moment of the flap around the rotary axis EF and I_β is the moment of inertia of the flap around the axis EF. Constants k_{hh}, $k_{\alpha\alpha}$, $k_{\beta\beta}$ denote the spring stiffness of the flexible support of the profile and d_{PF} is the distance between the elastic axis EA and the axis EF.

The interaction between the flow and the profile is given by the force component L and the moments M_α and M_β defined by

$$L = -l\rho\int_{P_t\cup F_t}\sum_{j=1}^{2}T_{2j}n_j\,ds, M_\alpha = -l\rho\int_{P_t\cup F_t}\sum_{i,j=1}^{2}T_{ij}n_j\left(-1\right)^i\left(x_{1+\delta_{1i}} - x_{1+\delta_{1i}}^{EA}\right)ds, M_\beta = -l\rho\int_{F_t}\sum_{i,j=1}^{2}T_{ij}n_j\left(-1\right)^i\left(x_{1+\delta_{1i}} - x_{1+\delta_{1i}}^{EF}\right)ds,$$

where l is the depth of the considered profile typical section, $\mathbf{n} = \left(n_1, n_2\right)$ is the outer unit normal to $\partial\Omega_t$ on Γ_{Wt}, δ_{ij} is the Kronecker symbol, x_1 and x_2 are the coordinates of the point on Γ_{Wt}, x_i^{EA} (i=1,2) are coordinates of the current location of the elastic axis EA and x_i^{EF} (i=1,2) are the coordinates of the current location of the flap rotary axis EF. The stress tensor is computed from the flow velocity and the pressure as

$$T_{ij} = -p\delta_{ij} + \left(\nu + \nu_T\right)\left(\partial u_i/\partial x_j + \partial u_j/\partial x_i\right).$$

The results of the numerical simulations of the airfoil vibrations show a slight stabilizing effect of the turbulent flow model in comparison to the laminar model, see Fig. 1. The flutter stability boundary, given by the Reynolds number $\mathrm{Re}_\infty \cong 2\,\mathrm{x}10^5$. However, the results are not too different and the solution of the turbulent flow is much more complicated and computer time demanding. Therefore within a certain allowed tolerance it is possible to use the laminar flow model even for higher Reynolds numbers.

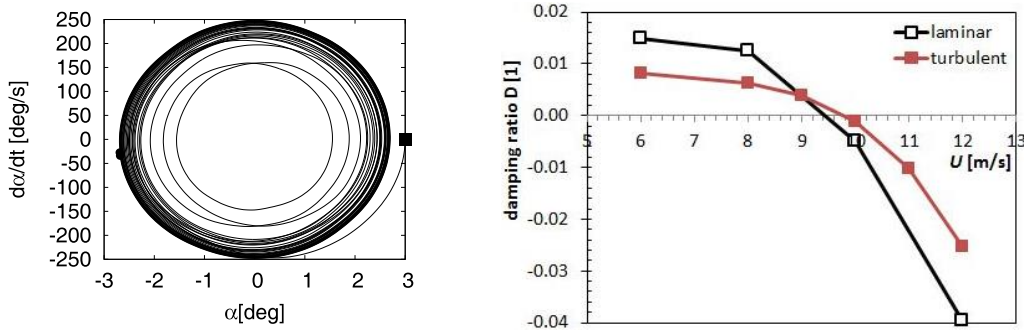

Fig. 1. Example of the phase diagram for rotation α in a post flutter regime for the laminar flow (velocity $U_\infty = 10$ m/s), and the evaluated aerodynamic damping versus the flow velocity for turbulent and laminar flow

Acknowledgment

The work has been supported by the grant project GACR P101/11/0207.

References

[1] Feistauer, M., Horáček, J., Sváček, P., Numerical simulation of vibrations of an airfoil with three degrees of freedom induced by turbulent flow, Communications in Computational Physics 17 (1) (2015) 146-188.

COMPUTATIONAL MECHANICS 2015
31st conference with international participation
Špičák
November 9 - 11, 2015

Combined effect of passive damping element and soil-structure interaction on dynamic behaviour of tall slender structure

S. Hračov[a], M. Macháček[a]

[a] *Institute of Theoretical and Applied Mechanics AS CR, v.v.i.,Prosecká 76, 19000, Prague, Czech Republic*

The problem of soil-structure interaction (SSI) has become a very important subject of investigation in the last decades in the field of structural dynamics. SSI could highly influence the response of structure on various type of dynamic excitation such a seismic, wind or transient cyclic loading, see e.g. [1, 4]. A significant part of the vibration energy is dissipated not only by structure itself but also by a hysteretic material damping of the soil and in particular by radiation damping. Considering the influence of subsoil instead of commonly used assumption of the fixed base also leads to the increase in natural periods of the structure. This fact could be crucial when tuned mass damper (TMD) is required for suppressing e.g., excessive wind-induced vibrations [2], since its efficiency depends mainly on ratio of its designed frequency to the natural frequency of the controlled structure.

The presented paper is focused on the investigation of dynamic behaviour of tall slender structure taking into account SSI and a presence of TMD. The main aim was to qualitatively and quantitatively assess effect of both phenomena on changes in basic dynamic properties in relation to classically damped fixed-base structure. In particular, the differences in resonant frequencies, in the effective damping and in the character of the dynamic response were studied.

An existing 191 meter tall tower as a typical example of slender structure having well separated natural frequencies was chosen and analysed. Its lower part is made of reinforced concrete, the middle part represents steel cylinders with variable cross-section, and the top section is laminate extension. The foundation has the form of square footing with a side of length 18 m. The pendulum absorber supplemented with viscous dampers is installed into laminate extension to suppress excessive vibrations induced by a vortex-shedding, that are related with the second and the third natural frequencies of the fixed-base tower. A two dimensional discrete numerical model of the tower was created in CALFEM (MATLAB FEM toolbox). The model without absorber was built using beam elements, had 192 nodes and 576 dofs. The absorber was subsequently modelled as a concentrated mass connected to the top of the tower with the Kelvin-Voigt element having one degree of freedom in the horizontal direction. The optimal damping ratio of TMD was calculated and set equal to value 20 %, while the damping ratio of the structure was experimentally determined by low value equal 0.5 %. The frequency-dependent stiffness and viscous damping characteristics of soil-foundation interaction were calculated according [3]. The harmonic load representing vortex-shedding effect at steel cylinder with the smallest diameter was applied. The analysis of the vortex-induced vibrations was performed for a set of various soil shear wave velocities V_s ranges from $200\,\mathrm{ms}^{-1}$ to $800\,\mathrm{ms}^{-1}$ and soil hysteretic damping ζ_g from 1% to 5%, while mass density ϱ equal to $2\,000$ kgm^3 and Poisson's ratio of the soil ν equal to 0.3 were kept constant. Also several depths of the foundation embedment D were considered in the numerical calculations.

The comparison of the results from analysis of the structure without TMD on deformable soil and from analysis of the similar fixed-base structure revealed the decrease in the resonant frequencies, in the corresponding deformations and internal forces due to SSI effect. The reduction of these quantities as well as the effective damping of whole system were increasing with the decrease in velocity V_s and in the depth D and with the increase in hysteretic damping ζ_g, see Fig. 1. The complex character of the response of both systems was for resonant oscillation minimal. All points on the structure were vibrating almost with the same or opposite phase. The significant influence of non-classical damping of the system originated from SSI was not observed.

Completely different complex character of the dynamic behaviour was determined for the tower with TMD. The significant difference in the phase shift between structural parts confirmed the assumption of TMD being a relevant source of non-classical damping even for fixed-base structure. The substantial reduction of the dynamic response caused by activity of TMD was determined and is shown in Fig. 1. The effect of the vibration mitigation due to presence of TMD was significantly higher than due to SSI. Nevertheless, the greater bending moments for structure with TMD on deformable soil than for similar fixed-base structure leads to conclusion, that TMD should be tuned into the fundamental frequency of the soil-structure system instead of fixed-base structure in order to optimize its performance.

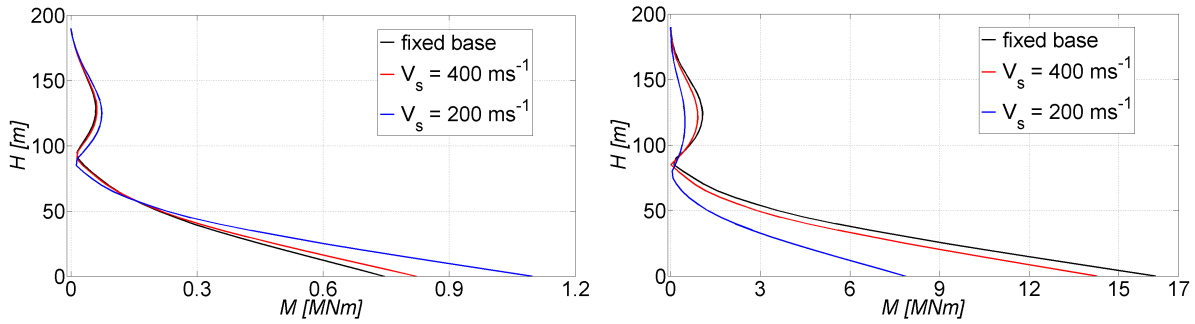

Fig. 1. Envelope of bending moments corresponding to the second resonant frequency of tower with (*left*) and without (*right*) TMD for fixed base and for footing embedded in soils with various velocities V_s ($\zeta_g = 1\%$, $D = 4\,\mathrm{m}$)

Acknowledgements

The kind support of the Czech Science Foundation projects No. 13-41574P and of the RVO 68378297 institutional support are gratefully acknowledged.

References

[1] Chowdhury, I., Dasgupta, S.P., Dynamics of structure and foundation - A unified approach: 2. Applications, Taylor & Francis Group, London, UK, 2009.

[2] Liu, M.Y., Chiang, W.L., Hwang, J.H., Chu, C.R., Wind-induced vibration of high-rise building with tuned mass damper including soil-structure interaction, Journal of Wind Engineering and Industrial Aerodynamics 96 (6-7) (2008) 1092-1102.

[3] Pais, A., Kausel, E., Approximate formulas for dynamic stiffness of rigid foundations, Soil Dynamics and Earthquake Engineering 7 (4) (1988) 213-227.

[4] Pour, N.S., Chowdhury, I., Dynamic soil-structure interaction analysis of tall multi-flue chimneys under aerodynamic and seismic force, Proceedings of the 12th International Conference of International Association for Computer Methods and Advances in Geomechanics, Goa, India, 2008, pp. 2696-2703.

COMPUTATIONAL MECHANICS 2015
31st conference with international participation
Špičák
November 9 - 11, 2015

Numerical analysis of the process of repairing defects in lamellar flange and its influence on the local stress state

P. Hrubý [a], F. Hokeš [a], O. Krňávek [a], A. Nevařil [a]

[a] *Faculty of Civil Engineering, Brno University of Technology, Veveří 95, 602 00 Brno, Czech Republic*

During the operation of every structure it is necessary to pay attention to its current operational state. This care should, at the first, include periodical inspections of the structure, at the second, corresponding actions connected to the repairs of incidental defects. Owing to the previous statement in the civil engineering is particular attention paid to the traffic structures such as bridge works. The design of steel-concrete coupled bridges of long spans due to the production reasons often uses lamellar flanges made of individual steel flanges welded together on their perimeter by sealing welds. Present paper describes numerical analysis of repair process of fictitious defect in the sealing weld of lamellar flange. Local stress state in the vicinity of the repair area is also analysed.

In the analysed study is simulated process of fictitious defect repair. The defect is assumed to be a crack of circular shape having diameter of 5 mm situated on the lower surface of sealing butt weld. The analysed sealing weld connects two flange plates in the transverse direction and directly adjoins load carrying assembly filling weld (see Fig.1). Because the discussed defect is located within the flange, in order to repair it, it is necessary to create a bore hole (see Fig. 1) from the lower surface of the lamella. This bore hole will be in the final phase of repair process again re-welded [1]. In this case it is assumed that whole repair process will be carried out under the condition of load in the lamellar flange (only traffic loads are excluded from the bridge). Thus it is assumed that during the repair process local stress reallocation will arise in the vicinity of the bore hole.

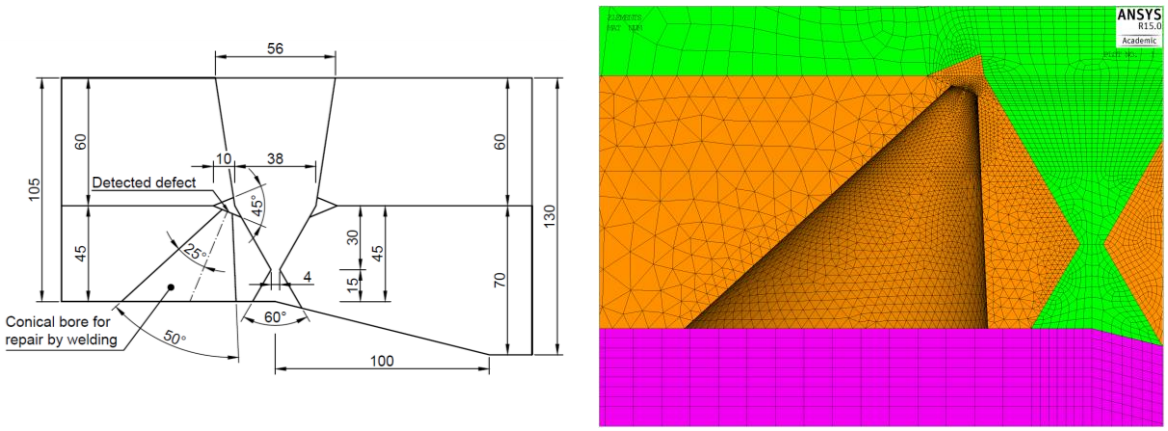

Fig. 1. Schema of repair of sealing weld defected defect (left), FEM model of conical bore hole used for defect repair by welding (right)

The numerical analysis is maintained in the ANSYS system environment [4], using the technique of sub-modelling [2]. Discussed technique requires assembly of two FEM models.

First, less detailed one, includes the whole bridge where global behaviour of the structure is analysed and also boundary conditions for the second, more detailed model, are found out. This second model describes only the detail of interest and its surrounding. This detailed model also includes the above cited conical bore hole.

First step of the analysis describes the global behaviour of the bridge such that it corresponds to the results of experimentally obtained data [3]. Primary target of the analysis is to obtain relevant stress state in the vicinity of the analysed detail before the repair procedure. Further it is necessary to simulate the weakening of the lower lamella by its conical bore in the global model. This is used afterwards for the evaluation of correct boundary conditions in the sub-model. Such simulation was realized using the killed and alive finite elements. For the completeness of the problem it is suitable using the global model to simulate also the stress state after the defect repair thus achieving complete set of boundary conditions for the sub-model analysis.

In response to above described ensuring of boundary conditions it is possible to detail analysis of repair process which also contains three steps. First step models the pre-repair state of the seal weld. In this step are finite elements of the bore active (alive) and fully participate of the load bearing process. There are also contact elements applied on the surfaces of the crack that will be in the next step simulating friction between both surfaces. In the second step are finite elements in the bore killed also the contact is inactive and second set of boundary conditions from the global model is applied. It is possible to examine stress reallocation in this step. As was mentioned above it is suitable to process also the third step where killed elements of the bore hole are made alive again and the contact is activated in order to fully bond the surfaces of the repaired crack (currently area of the bore) together and the third set of global model boundary conditions is applied.

The target of the performed analyses was simulation of the repair process of the fictitious defect in the sealing weld of the lamellar flange. During the dealing with the problem it was found out that using the above described method of sub-models in order to obtain correct reallocation of the stress it is necessary to simulate also decrease of lower lamella stiffness in the global model. Indispensable assumption for the achieving of correct results is also correct evaluation of the stress state before the defect repair which can for some more complex cases exhibit substantial problems. For further development of this analysis procedure it would be relevant to include into analyses also the thermal effects due to the welding. The mechanical properties of the metal in the heat affected zone are highly affected by this effect and so the stress state is. This phenomenon is far beyond the scope of this article and enables the use of even more advanced mathematical and numerical procedures.

Acknowledgements

The work has been supported by the research project FR-TI4/430 under the financial support of the Ministry of Industry and Trade of Czech Republic.

References

[1] Hokeš, F., Krňávek, O., Hrubý, P., Nevařil, A., Probability of joint flange plate weld failure with indication identified by progressive non-destructive methods. Subsection: Influence of repairing defects in the mounting weld to state of stress of surrounding welds, Brno, VUT FAST, 2015. (in Czech)

[2] Hrubý, P., Krňávek, O., Nevařil, A., Totková, L., Submodelling technique and the detail structural analysis, Proceeding of 2nd International Scientific Conference: Structural and Physical Aspects of Civil Engineering, Štrbské Pleso, Technical University of Kosice, 2013, pp. 10

[3] Mackerle, Z., Vejvoda S., Mathematical simulation of stress of weld joint: Measured stress in the area of welds of lamellar flange, Brno, Vítkovice ÚAM a.s., 2012. (in Czech)

[4] ANSYS, Inc. ANSYS 15.0 Help, Release 15.0, USA, Canonsburg, 2013.

COMPUTATIONAL MECHANICS 2015
31st conference with international participation
Špičák
November 9 - 11, 2015

Discrete element method for simulation of dynamical behaviour of crowd of people reacting on external loading

L. Hynčík[a], J. Špička[a], P. Baierl[a]

[a] *New Technologies - Research Centre, University of West Bohemia, Univerzitní 8, 306 14 Plzeň, Czech Republic*

The description of behaviour of a crowd of people is in high interest today taking into account not only public spaces or transport safety optimization [3], but also security reasons such as evacuation dynamics [1], or investigation of historical aspects of motion of crowd of humans such as mapping a medieval battlefield dynamical behaviour in order to provide hints for an archaeological exploration to find artefacts. The numerical simulation describing the behaviour of the crowd of people under the external loading plays an important role here.

The paper provides a preliminary study on dynamical behaviour of a crowd of people moved under external mechanical loading. The discrete element method (DEM) is introduced [5], where the individuals are modelled by particles, which interacts one to another based on the continuous contact model [4]. Considering n particles with masses m_i and inertia $\boldsymbol{I}_i$, $i \in \{1, \ldots, n\}$, one can write the equations of motion (EOM) as

$$m_i \frac{d\boldsymbol{v}_i}{dt} = \boldsymbol{F}_{ij}^c + \boldsymbol{F}_i^c + \boldsymbol{F}_i^g, \tag{1}$$

$$\boldsymbol{I}_i \frac{d\boldsymbol{\omega}_i}{dt} = \boldsymbol{M}_{ij}^c, \tag{2}$$

where $\boldsymbol{F}_{ij}^c$ denotes the mutual contact forces between particles i and j, $\boldsymbol{F}_i^c$ denotes external forces like contact from the external objects, $\boldsymbol{F}_i^g$ denotes gravitational forces and $\boldsymbol{M}_i j^c$ denotes the mutual contact moments caused by tangential forces such as friction. The contact model comes from the linear spring-dashpot model [2] as

$$\boldsymbol{F}_{ij}^c = -K_n \delta_n \boldsymbol{n}_c - C_n \left(\boldsymbol{v}_c \boldsymbol{n}_c\right) \boldsymbol{n}_c + \boldsymbol{F}_{ij}^t, \tag{3}$$

where K_n is the normal contact stiffness, δ_n is the perforation and $\boldsymbol{n}_c$ is the contact normal vector. The damping term is added, where C_n is the normal damping coefficient and $\boldsymbol{v}_c$ is the tangential contact vector. Tangential force

$$\boldsymbol{F}_{ij}^t = -K_t \boldsymbol{v}_c^t + C_t \left(\boldsymbol{v}_c \times \boldsymbol{n}_c\right) \times \boldsymbol{n}_c \tag{4}$$

introduces friction forces with stiffness K_t and damping C_t and applies to the moment

$$\boldsymbol{M}_{ij}^c = \boldsymbol{R}_{ij} \times \boldsymbol{F}_{ij}^t. \tag{5}$$

Here $\boldsymbol{R}_{ij}$ is the distance between the centres of gravity of the contacting particles.

The preliminary study is addressed, so several assumptions are taken into account. Firstly, for easy implementation of mutual contacts, all particles are modelled as spheres. Each particle

has its own mass and the mass distribution is managed by three principal moments of inertia. For n particles defined by their initial positions and initial velocities, the system (1) and (2) introduces $6n$ EOMs. Those EOMs are linked via mutual contact.

For the contact modelling, the planar contact is expected. In each time step, the mutual position of each pair of particles is checked. When the indentation between particles i and j is detected, the continuous contact force based on Eqs (3) and (4) is applied as action and reaction. The contact with external objects (like ground or walls) is added in the same manner, where the external objects are modelled by rigid triangular facets.

Typical example addressed is the crowd of people moving through the narrowing corridor. The situation described in Fig. 1, where red arrows indicate the crowd flow by a given velocity, will be discussed during the conference assessing also the suitability of the proposed method and tests also various contact models, that are developed from the basic Eqs (3) and (4).

The numerical simulation shows the crowd of people dynamics, when the individuals are pushed to fit to the narrowing corridor. The mutual forces can be also evaluated in order to assess the potential injury risk due to the compression.

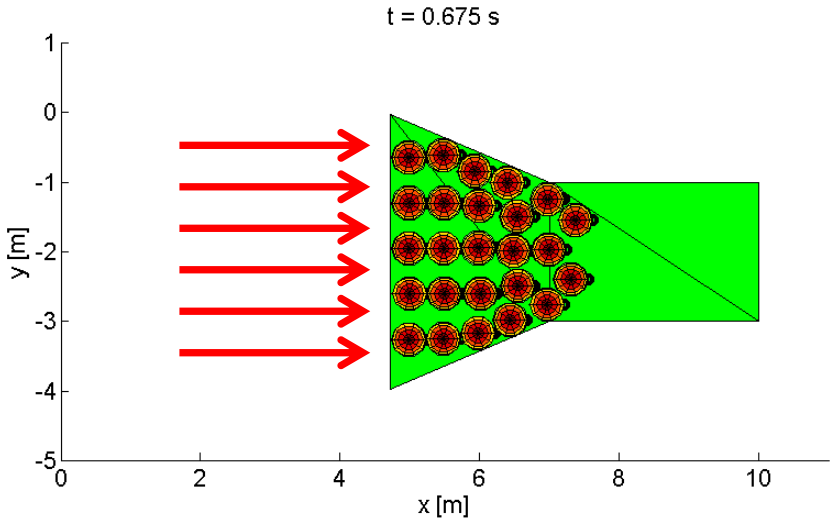

Fig. 1. Flow of a crowd of people

Acknowledgement

This work has been supported by the internal project SGS-2014-017.

References

[1] Jo, A., Sano, T., Ikehata, Y., Ohmiya, Y., Analysis of crowd flow capacity through a door connected to a crowded corridor, Transportation Research Procedia 2 (2014) 10-18.

[2] Lankarani, H. M., Nikravesh, P. E., A contact force model with hysteresis damping for impact analysis of multibody systems, Journal of Mechanical Design 112 (1990) 369-376.

[3] Liao, W., Seyfried, A., Zhang, J., Boltes, M., Zheng, X., Zhao, Y., Experimental study on pedestrian flow through wide bottleneck, Transportation Research Procedia 2 (2014) 26-33.

[4] Pfeiffer, F., On non-smooth dynamics, Meccanica 43 (2008) 533-554.

[5] Zhu, H.P., Zhou, Z.Y., Yang, R.Y., Yu, A.B., Discrete particle simulation of particulate systems: Theoretical developments, Chemical Engineering Science 62 (2007) 3378-3396.

COMPUTATIONAL MECHANICS 2015
31st conference with international participation
Špičák
November 9 - 11, 2015

Cyclic softening of tempered ferritic-martensitic steel P91

J. Janoušek [a], S. Holmström [b], R. Pohja [c]

[a] Research Centre Rez, Hlavní 130, 250 68 Husinec-Řež, Czech Republic
[b] Joint Research Centre, Westerduinweg 3, NL-1755 LE Petten, The Netherlands
[c] VTT Technical Research Centre of Finland Ltd, Vuorimiehentie 3, FI-02044, Espoo, Finland

For the ferritic-martensitic steel P91 cyclic softening has been identified as important factor in the assessments of creep-fatigue in nuclear components. Better understanding of the cyclic softening is needed as it is believed to be the main contributor for the complex material behavior encountered in creep-fatigue testing. In fast reactor components the main life shortening load cycles are from thermal fluctuations causing through-wall stress gradients. The main objective of this work (as a Task in the European project MATISSE) is to perform tailored experiments and to develop models for understanding and predicting the cyclic-softening of P91. The supporting experimental program produces data for calibration and validations of the developed models. An existing elasto-viscoplasticity model simulates the key mechanisms such as decrease in dislocation density, increase in sub-grain size and recovering phenomena. The model will be modified to also incorporate the effect of hold time on the cyclic softening.

The supporting test effort will be focused on strain controlled low cycle fatigue tests with different tension, compression and tension-compression hold times. Especially long hold times are targeted. The evolving change of time-dependent inelastic strains (relaxed strain) during these tests is related to softening and the corresponding creep behavior (strain rates) and creep-fatigue life is directly affected [1, 2].

The cyclic stress-strain curves (as a function of softening) will be compared with the corresponding monotonic stress-strain curves. It is foreseen that new useful information regarding the cyclic stability of a material can be acquired. For example, will hardness, yield strength, ultimate strength, strain-hardening exponent, Norton creep exponent increase, or remain unchanged as a function of cyclic life or softening ratio [3].

The test program has three stages: Complementary tests providing missing data required for the identification of the model parameters (stage I), qualitative and quantitative characterization of the effect of hold time on the cyclic softening of P91 (stage II) and impact of softening on relaxation response (stage III). The work presented here is situated in stage II and III. Several round robin tests will be performed independently between international laboratories Joint Research Centre (NL), VTT Technical Research Centre of Finland Ltd and Research Centre Rez. The tests will be carried out on tempered ferritic-martensitic steel P91 (9Cr1MoVNb type) [4]. This material together with steel 316L and 316L(N) are the main candidates for the construction of the planned research reactor concepts Myrrha, Astrid, Alfred and Allegro.

The cutting plan of the P91 test material block (150x150x60 mm) is shown in Fig. 1 together with shape of fatigue and creep crack growth specimen. The arrow on the block indicates the rolling direction. The chemical composition is defined in Tab. 1. Tensile properties are as follows: yield strength at 20°C $\geq$ 445 MPa, ultimate tensile strength at 20°C = [580 – 760] MPa, elongation at 20°C $\geq$ 20%. Plate properties were measured at several

locations and for two thermal states. The first corresponding to “As-delivered” product (state A) : 1060°C – 4Hrs + Water Quenching + 760°C – 3Hrs20min – Air Cooling The second corresponding to “Simulated PWHT” product (state B) : idem State A +Stress relieving 750°C – 12Hrs.

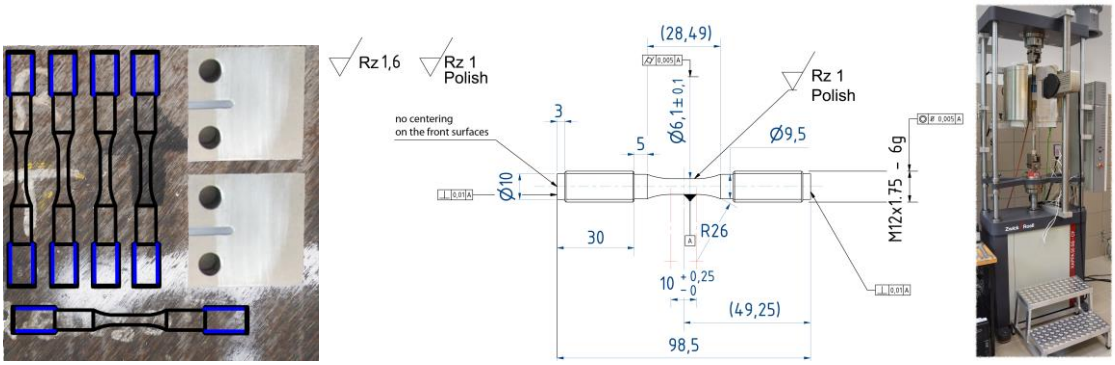

Fig. 1. Cutting plan of block P91, the shape and dimensions of specimen and testing machine Kappa SS-CF

Tests will be performed on electromechanical creep testing machine Kappa SS-CF which offers a wide range of applications especially creep-fatigue tests through-zero (see Fig. 1). Load capacity is up to 50 kN and speed range is 1 μm/h to 100 mm/min. The machine is equipped with 3-zone furnace to 1200°C and non-contacting high resolution video extensometer.

Table 1. Chemical composition of the test material

Elements	C	Mn	Si	Ni	Cr	Mo	Cu	Al	S	P
unit [%]	0.12	0.41	0.24	0.10	8.32	1.02	0.05	0.006	0.001	0.009
Elements	V	Nb	N	As	Sb	Ti	B	W	Zr	O
unit [%]	0.235	0.084	0.041	0.005	0.001	0.002	0.0009	0.001	0.001	15 ppm

The type of tests according asymmetry will be symmetrical reversed strain i.e. strain ratio R = -1. Intended test matrix corresponds with one softening test with 9 relaxation periods in different locations of the softening curve (at 1st, 3rd, 10th, 30th, 100th, 300th, 1000th, $N_f/2$ and 3000th) with strain range $\Delta\varepsilon$ = 0.7%, tensile hold time 72 hours. Next 6 creep fatigue tests will have tensile hold time in every cycle. First 3 tests with 12 hours hold time for strain range $\Delta\varepsilon$ = 0.9%, 0.7% and 0.5% will be stopped after 50 cycles. Others with 1 hour hold time for same strain ranges will be stopped after 1000 cycles, max 1500 cycles or if a failure will occur. The cycle will have shape of triangle and temperature all tests is 600°C. The strain rate in cycling will be 6 % per minute.

Acknowledgements

This research work has been supported by the SUSEN Project CZ.1.05/2.1.00/03.0108 realized in the framework of the European Regional Development Fund (ERDF) and MatISSE project, contract nr. 604862.

References

[1] ASTM E606-92, Standard practice for strain-controlled fatigue testing.
[2] ASTM E2714 – 13, Standard test method for creep-fatigue testing.
[3] Mitchell, M. R., Fundamentals of modern fatigue analysis for design, fatigue and microstructures, ASM Symp., St. Louis, MO, 1978, pp. 385-437.
[4] Technical note, Production of plates (P91 and 316LNmod material) for MATTER FP7 Project, ArcelorMittal, 2013.

COMPUTATIONAL MECHANICS 2015
31st conference with international participation
Špičák
November 9 - 11, 2015

Fatigue life calculation and testing in Regional Technological Institute – current state and vision

M. Kepka [a], M. Kepka jr. [a], L. Bartoň [a], P. Žlábek[a]

[a] *Regional Technological Institute, Faculty of Mechanical Engineering, University of West Bohemia, Univerzitní 8, 306 14 Plzeň, Czech Republic*

RTI – Regional Technological Institute is a new research centre affiliated with the Faculty of Mechanical Engineering of the University of West Bohemia in Pilsen. RTI's research teams and infrastructure are prepared for dealing with comprehensive research tasks ranging from materials research through manufacturing processes to computational and engineering design problems, including experimental verification. One of the totals of four research programmes at RTI involves investigation into the fatigue life of structures operating under time-varying loads. It is pursued in collaboration with the Department of Machine Design and the Department of Material Science and Technology of the University. The RTI's portion of research and development tasks is carried out primarily at the Strength and Fatigue Life Testing Laboratory with some assignments completed by the Mechanical Testing Shop and the Virtual Prototyping Laboratory. Service load characteristics are measured by the Laboratory of Experimental Methods for Mechanical Engineering.

RTI can also provide support for courses taught in this field. For instance, the course Service Strength and Life of Transport Equipment aims to teach students to coordinate the collaboration between engineering designers, computation specialists and testing engineers in their dealing with service strength and fatigue life of vehicles. The students are guided to be aware of the current legislative requirements and codes, to understand the procedures for theoretical assessment of service strength and fatigue life, to be able to suggest the main parameters of laboratory and field tests, and to have an understanding of the methodology and evaluation of such tests.

The RTI department which focuses on matters related to fatigue life is the Strength and Fatigue Life Testing Laboratory shown in Fig. 1.

Fig. 1. Service Strength and Fatigue Life Testing Laboratory

The laboratory houses experimental equipment supplied by INOVA. Its core is a multi-channel electrohydraulic loading system which enables various tests to be set up in a universal test stand using loading cylinders with the force range of 10 kN to 160 kN. In addition,

a biaxial testing machine (tension/compression – torsion) is available, together with a biaxial rig for combined loading of small-size machine components and assemblies. Mechanical Testing Shop is also equipped with a high-frequency vibrophore of a capacity up to 50 kN. Service load characteristics (force, displacement, stress, strain, acceleration and temperature) are measured at the Laboratory of Experimental Methods for Mechanical Engineering which houses a number of measuring instruments.

The main computational tool employed at RTI is the nCode software [1]. A commercial licence of nCode GlyphWorks and a research licence of nCode DesignLife are available. The first is predominantly a tool for analysing measured data and computing fatigue life, while the latter is a fatigue FEM postprocessor. Software nCode offers nominal stress approach and local approach, as well as a large materials data base.

One of the processing and computational routes used by nCode software for structural parts on the basis of measured data and materials properties is illustrated in Fig. 2.

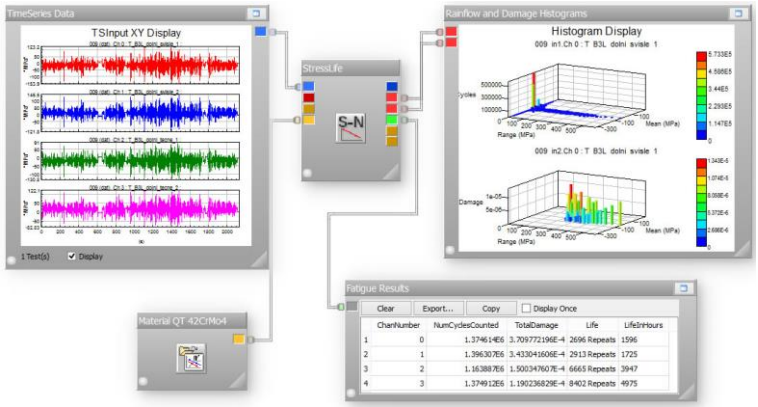

Fig. 2. One of the computation routes for life of structures in nCode software

The first computations were carried out in collaboration with industrial company. Their primary purpose was to explore the flexibility and potential of nCode software computational modules. An interesting tool is the reverse engineering module which enables the designer to determine the maximum permissible notch for the required service life on the basis of a known time-varying load on the part and the chosen material.

In the future, materials databases MATDAT [2] and WIAM METALLINFO [3] are planned to be procured. The latter should be very useful for RTI, as it has been developed and maintained by IMA Dresden, a well-known German research and development institution, along with computational programs that implement procedures set out in the widely-used and accepted FKM-Richtlinien regulations [4].

Besides collaboration with industry, RTI departments will pursue basic research in this field. Attention will be devoted to the effects of exceptional loads (overload cycles) on the fatigue life of machine components and to the design and evaluation of machine component operating under variable loads.

Acknowledgements

The work has been supported by the research project Development of Regional Technological Institute, Nr. LO1502, Ministry of Education, Youth and Sports.

References

[1] nCode, www.ncode.com
[2] MatDat-Material properties database, www.matdat.com
[3] IMA Dresden, www.wiam.de
[4] FKM Forschung im VDMA, www.fkm-net.de

COMPUTATIONAL MECHANICS 2015
31st conference with international participation
Špičák
November 9 - 11, 2015

Mass and heat transfer in the wheel of desiccant cooling system using solar energy

Y. Kerkoub [a,b], L. Merabti[a], A. Benzaoui [b]

[a] *Unité De Développement Des Equipement Solaire UDES , Centre De Développement Des Energies Renouvelables CDER, Bou-Ismail, Tipaza*
[b] *Laboratoire de Thermodynamique et des Systèmes Energétiques, Faculté de Physique-USTHB, Bp N° 32 El Alia- Bab Ezzouar 16111, Alger.*

The desiccant wheel is the key component in a solid desiccant cooling system. Its performance is crucial to the capacity, size and cost of the rotary desiccant cooling system. A desiccant wheel consists of a large number of air flow passages whose walls are constituted by matrix material (supporting material) and are coated or impregnated with desiccant material (adsorbent). Its cross-section is divided into two parts by the external flow sections which are adhering to the wheel: one for process air and another for regeneration air. Water vapor is adsorbed by the adsorbent when moist air is passing through the process air side. Meanwhile in the regeneration side, the water vapor is desorbed from the desiccant by the hot regeneration air.

Several investigations have been performed to build mathematical models for predicting the performance of rotary desiccant wheels.

In this work a three dimensional model is constructed to simulate with more accuracy the mass and energy phenomena over a channel of desiccant wheel in order to better predict the performance of this kind of compound and analyze the effect of some, important structural and operating parameters. A CFD model which is based on conservation of mass, momentum, energy and species equations is used in this study. The channel is divided on two parts, the flow channel is governed by standard fluid flow equations and desiccant material part which is treated as porous media. The interaction between them is described by new source terms added is standard equations. The source term of porous media is composed of two parts: a viscous loss term Darcy, and an inertial loss term

The source terms of conservation of energy equation composed of two part: convection heat transfer between flow channel and desiccant material, and heat generation produced from sorption of water vapor inside desiccant material.

Simulations have been conducted for a desiccant wheel of width 0.2m with wall thickness (c) 0.15 mm. The geometry of the channels in the wheel is sinusoidal with a width of 3.5 mm and a height of 1.75 mm. The air velocity is 2 m/s in both the adsorption and regeneration periods ceramic porous fibre paper, impregnated with silica gel. The honeycomb structure contains 70–80% of type a silica gel. Geometry and operating conditions used in this study is corresponding of [1]. The convective heat transfer coefficient and hydraulic diameter is calculated from the Nusselt number in the sinusoidal shaped channels [2] and the mass transfer coefficient is obtained on the assumption of Le = 1.

The sets of equations governed transfer phenomena were solved by means of finite volume method using Fluent 6.3 with some modification by user defined function.

The parametric analysis of the process air conditions is explained in this way (Fig. 1 and 2). If the process air temperature decreases the relative humidity (at constant humidity ratio)

becomes higher and the dehumidification capacity increases. This effect is due to the higher capacity of sorption substances of keeping water at high relative humidity. As a consequence a pre-cooling of process air can be a good way to increase moisture removal capacity of a desiccant wheel.

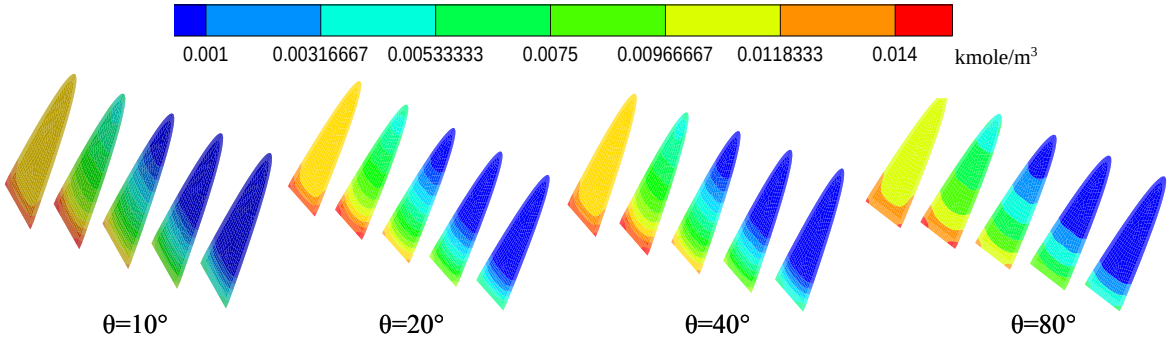

Fig. 1. Distribution of molar concentration a long of the channel for difrent angular position θ

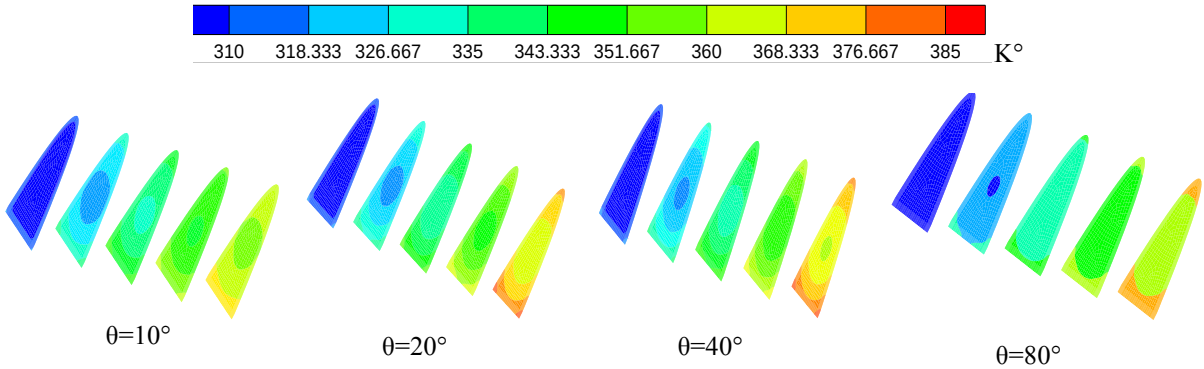

Fig. 2. Distribution of temperature a long of the channel for difrent angular position θ

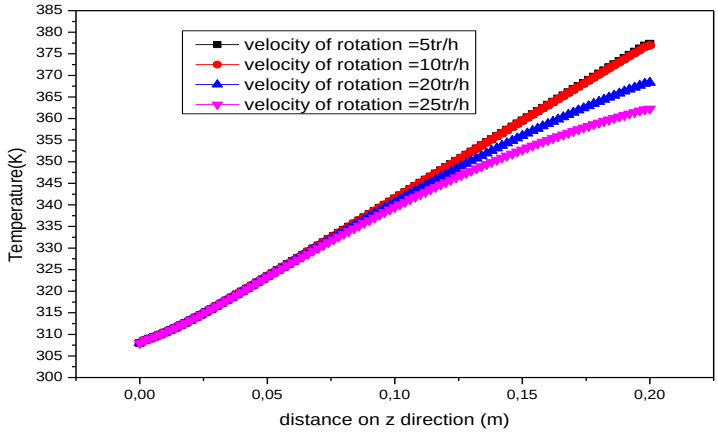

Fig. 3. Profile of temperature a long of the channel for difrent rotation speed

References

[1] Kakac, S., Shah, R. K., Aung, W., Handbook of single-phase convective heat transfer, John Wiley & Sons, New York, 1987.

[2] Kodama, A., Goto, M., Hirose, T., Kuma, T., Temperature profile and optimal rotational speed of a honeycomb rotor adsorber operated with thermal swing, Journal of Chemical Engineering of Japan 27 (1994) 644– 649.

COMPUTATIONAL MECHANICS 2015
31st conference with international participation
Špičák
November 9 - 11, 2015

Control of hydraulic hexapod with 6 DOF

V. Klouček [a]

[a] Center of Engineering Research Development, VÚTS, a.s., Svárovská 619, Liberec XI – Růžodol I, 460 01 Liberec, Czech Republic

The article describes the hexapod with six linear hydraulic motors and six degrees of freedom. In the first part of the article is resolved hexapod kinematics using matrix methods of investigation of spatial multibody systems. Hexapod is used for laboratory motion excitation equivalent to motion measured during real part operation. The second part of the article describes the synthesis of control signal from the measured positions of points on investigated body. There are two cases described. The first, there are three measured points on the investigated body. In this case the solution of the control signal synthesis is a nonlinear problem. In second case there are four measured points. In this case the solution is a linear problem.

The object of study is a laboratory hydraulic hexapod used for dynamic testing of mechanical components and subassemblies, e.g. car seats. Dimensions of hexapod described herein are known from drawing documentation.

Essence of the experiments performed on the hexapod is mounting investigated object to the movable platform and excite the desired movement or vibration by hydraulic motors of the hexapod. Each experiment should best possible to simulate real operation conditions of components. Therefore the desired movement is measured in real operation by accelerometers.

So the aim of the work is accelerometers' signals conversion to control signals for hydraulic motors of hexapod. Because it is a processing of large amounts of measured data, it requires the conversion is simple and fast.

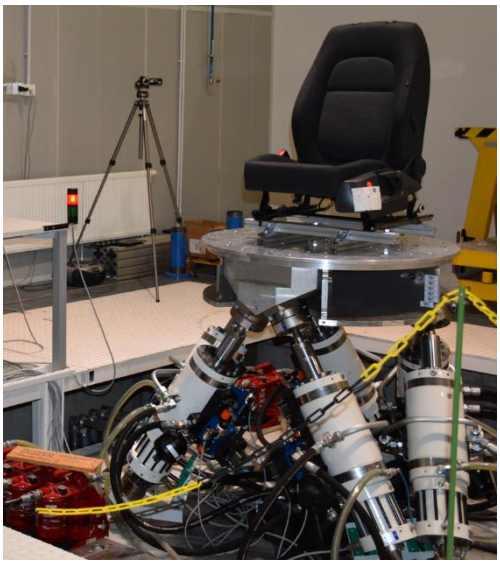

Fig. 1. Laboratory hydraulic with a car seat

For kinematic solution, there are two coordinate systems: Fixed $a: A x_a\, y_a\, z_a$ (rigid fixed with the base plate of hexapod) and movable $b: B x_b\, y_b\, z_b$ (rigid fixed with the movable platform). At the default position of movable platform both of coordinate systems coincide and they are at midpoint of platform. Kinematics is solved using matrix methods of investigation of multibody systems. Transformation matrix of motion $b:a$ denoted $\mathbf{T}_{ab}$. If the transformation matrix components are known, the stroke of i-th hydraulic motor is

$$z_i = \sqrt{\left(\mathbf{u}_{aBi} - \mathbf{u}_{aAi}\right)\left(\mathbf{u}_{aBi} - \mathbf{u}_{aAi}\right)} - L_0,$$

where $\mathbf{u}_{aAi}$ and $\mathbf{u}_{aBi}$ are coordinates of hexapod ball joints in coordinate system a.

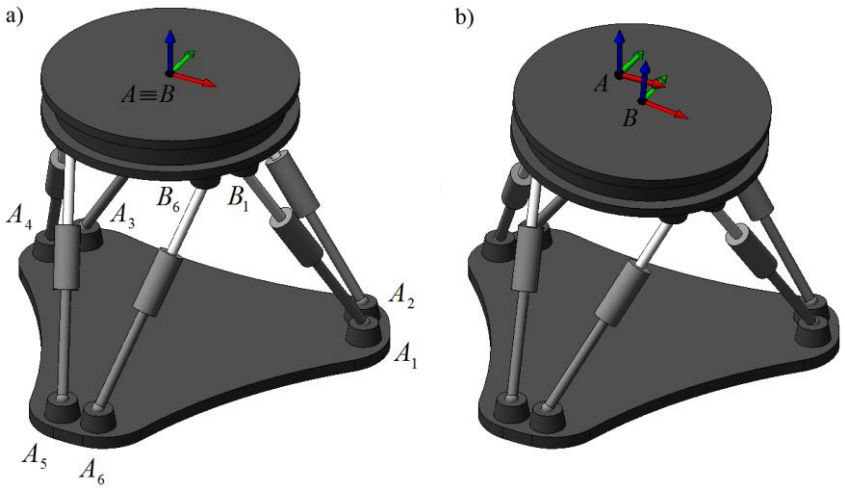

Fig. 2. Coordinate systems: a) hexapod in default position, b) hexapod in general position

Position of body in 3D space is definitely determined by the coordinates of its three points which do not lie in a straight line. Of these nine coordinates are independent only six because the assumption of a rigid body implies three conditions of constant mutual distances of these points.

When using three accelerometers, it is necessary to solve system of non-linear equations for determination of transformation matrix components at each measured time.

When using four accelerometers, the same task requires solving of linear equations system. If the signal is measured with high sampling frequency, the solution is significantly faster and easier.

Acknowledgements

The research was made possible by Technical university of Liberec, Faculty of Mechanical Engineering, Department of Machine Design, and .Center of Engineering Research Development, VUTS, a. s. Liberec.

References

[1] Fliegel, V., Martonka, R., Electro-dynamic measuring equipment, Proceedings of the Conference MMa MS, Technická univerzita v Košiciach, 2011, pp. 101-103.

[2] Fliegel, V., Martonka, R., Hexapod-the platform with 6DOF, Proceedings of 54th International Conference of Machine Design Departments, Technická univerzita v Liberci, 2013, pp. 111-116.

[3] Martonka, R., Petřík, J., Measuring platform for seat testing, Proceedings of 52th International Conference of Machine Design Departments, VŠ TU Ostrava, 2011, pp. 184-187.

COMPUTATIONAL MECHANICS 2015
31st conference with international participation
Špičák
November 9 - 11, 2015

Comparison of finite difference method, finite element method, isogeometric analysis and finite volume method in one-dimensional discontinuous elastic wave propagation

R. Kolman[a], A. Berezovski[b], S.S. Cho[c], O. Okrouhlík[a], J. Kopačka[a], D. Gabriel[a], K. Tamm[b], J. Plešek[a], K.C. Park[d]

[a] *Institute of Thermomechanics, Academy of Sciences of the Czech Republic, Dolejškova 1402/5, Prague 8, Czech Republic*
[b] *Centre for Nonlinear Studies, Institute of Cybernetics at Tallinn University of Technology, Akadeemia tee 21, 12618 Tallinn, Estonia*
[c] *Korea Atomic Energy Research Institute, 999-111 Daedeok-Daero, Yuseong-gu, Daejeon 305-353, Korea*
[d] *Department of Aerospace Engineering Sciences, University of Colorado, Boulder, CO 80309-429, USA*

In the contribution, the finite difference method [7], the finite element method [5], isogeometric analysis [3] and finite volume method [1] are compared among each other in one-dimensional discontinous wave propagation in an elastic bar. For the spatial discretization, lower and higher-order discretizations based on Lagrangian and spline shape function are used. For the time integration, several direct time integration methods are utilized, as the central difference method or the generalized-α method. The special attention is paid to comparison of front- and post-shock spurious oscillations occurring in the stress distribution along the shock loaded bar.

As the benchmark problem, we consider wave propagation in an one-dimensional elastic 'thin' free-fixed bar under shock loading (see the scheme on Fig. 1). Wave motion in an elastic bar in small strain approximation is governed by the wave equation [4]

$$\frac{\partial^2 u}{\partial t^2} - c_0^2 \frac{\partial^2 u}{\partial x^2} = 0 \quad \text{on} \quad [0, L] \times [0, T] \,, \tag{1}$$

where $u(x,t)$ is the axial displacement, $x \in \Omega = [0, L]$ is the axial coordinate, $t \leq T$ denotes the time, L is the length of the bar, c_0 is the wave speed in an elastic bar of the mass density ρ and the Young modulus E. Wave speed c_0 in the elastic bar is defined by $c_0 = \sqrt{E/\rho}$, see [4]. The analytical solution of the benchmark problem can be found in [4].

On Figs. 2-4, the dimensionless stress distributions σ/σ_0 along the elastic bar under the shock loading computed by several numerical methods are presented for the time $t = 0.7L/c_0$. Results are computed for $N = 100$ finite elements or finite cells. The time step size is set as $\Delta t = 0.5h/c_0$, where $h = L/N$, thus the Courant number is $Co = 0.5$.

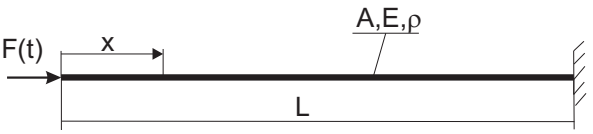

Fig. 1. Scheme of a free-fixed bar under shock force loading

Acknowledgements

The support of the projects GACR No. GAP101/12/2315 within institutional support RVO: 61388998 and No. ETA-15-03 (the Estonian-Czech bilateral mobility project) is acknowledged.

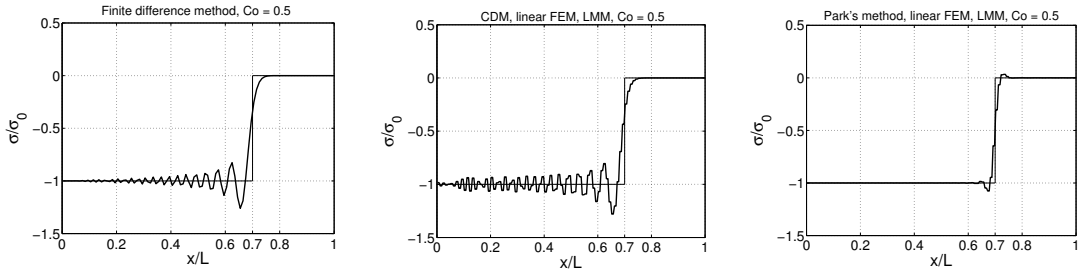

Fig. 2. Results for the explicit finite difference method in space and time [7] (left); the central difference method in time [5], linear finite element method (FEM) [5] in space and diagonal mass matrix (DMM)[5] (middle); the Park's method [6], linear FEM and DMM (right)

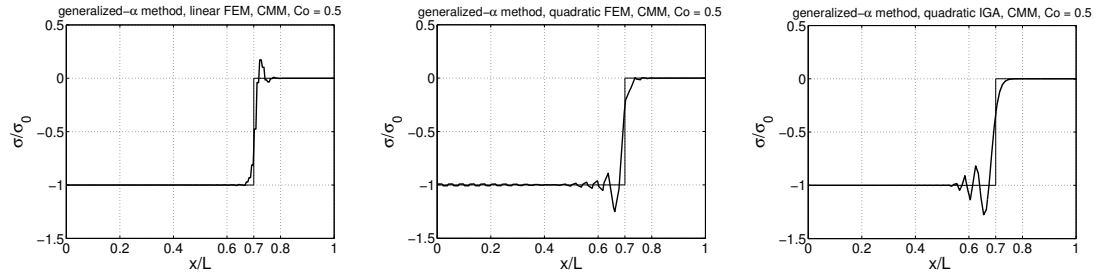

Fig. 3. Results for the generalized-α method [2], linear FEM and consistent mass matrix (CMM) (left); the generalized-α method, quadratic FEM and CMM (middle); the generalized-α method, quadratic Isogeometric Analysis (IGA) [3] and CMM (right)

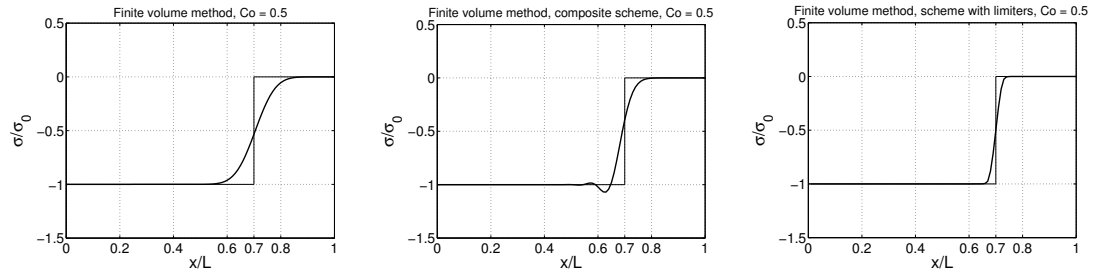

Fig. 4. Results for the first order finite volume Godunov method [1] (left), the FV composite scheme [1] (middle), the second-order FV scheme with the minmod limiter (right).

References

[1] Berezovski, A., Maugin, G.A., Simulation of thermoelastic wave propagation by means of a composite wave-propagation algorithm, Journal of Computational Physics 168(1) (2001) 249-264.

[2] Chung, J., Hulbert, G.M., A time integration algorithm for structural dynamics with improved numerical dissipation: The generalized-α method, J. Applied Mechanics 60 (1993) 371-375.

[3] Cottrell, J.A, Hughes, T.J.R., Bazilevs, Y., Isogeometric analysis: Toward integration of CAD and FEA, John Wiley & Sons, New York, 2009.

[4] Graff, K.F, Wave motion in elastic solids, Oxford University Press, 1975.

[5] Hughes, T.J.R., The Finite element method: Linear and dynamic finite element analysis, New York: Prentice-Hall, Englewood Cliffs, 1983.

[6] Park, K.C., Lim, S.J., Huh, H., A method for computation of discontinuous wave propagation in heterogeneous solids: Basic algorithm description and application to one-dimensional problems, International Journal for Numerical Methods in Engineering 91(6) (2012) 622-643.

[7] von Neuman, J., Richtmeyer, R., A method for numerical calculation of hydrodynamic shocks, Journal of Applied Physics 21 (1950) 232-237.

COMPUTATIONAL MECHANICS 2015
31st conference with international participation
Špičák
November 9 - 11, 2015

Finite element solution of the nonlinear 2DOFs dynamic system under random Gaussian excitation using the Fokker-Planck equation

R. Král[a], J. Náprstek[a]

[a] *Institute of Theoretical and Applied Mechanics, v.v.i., Czech Academy of Sciences, Prosecká 76, 190 00 Prague, Czech Republic*

The problems that often appear in stochastic dynamics can be investigated using the Fokker-Planck (FP) equation provided that random excitation processes of the system are of the Wiener type. Thus, the response being in general of deterministic and random character is described by the probability density function (PDF) that is taken as a natural extension of a deterministic results enabling to deduce additional special attributes of the response in time. Accepting the fact that random effects are introduced separately, the general formulation of the problem can be expressed as follows:

$$\frac{\mathrm{d}x_j(t)}{\mathrm{d}t} = f_j(\mathbf{x},t) + g_{jr}(\mathbf{x},t)w_r(t)\ , \quad j=1,...,2n, \quad n - \text{dynamic degrees of freedom}, \quad (1)$$

$\mathbf{x} = [x_1, x_2, .., x_{2n}]^T$ - response components:
(i) x_{2j-1} - displacements; (ii) x_{2j} - velocities,
$w_r(t)$ - Gaussian white noises, $r = 1, m$ (number of acting noises),
$f_j(\mathbf{x},t), g_{jr}(\mathbf{x},t)$ - deterministic functions of state variables $\mathbf{x}$ and time t.

The respective FP equation for the PDF $p(\mathbf{x},t)$ in variables $\mathbf{x}, t$ can be associated to Eq. (1):

$$\frac{\partial p(\mathbf{x},t)}{\partial t} = -\frac{\partial}{\partial x_j}\left(\kappa_j(\mathbf{x},t)\cdot p(\mathbf{x},t)\right) + \frac{1}{2}\frac{\partial^2}{\partial x_j \partial x_k}(\kappa_{jk}(\mathbf{x},t)\cdot p(\mathbf{x},t)), \quad (2)$$

$\kappa_j(\mathbf{x},t)$ - drift coefficients; $\kappa_{jk}(\mathbf{x},t)$ - diffusion coefficients.

Many methods for the solution of dynamic systems subjected to an external excitation with random character have been developed. Numerical methods and namely Finite Element Method (FEM) represent very effective solution possibility for Eq. (2) particularly when transition processes are investigated or more detailed solution is needed. A series of relevant papers dealing with FEM employed to FP equation has been published by Bergman, Spencer and co-authors, see for instance [1] and later also by authors of this study [3].

Papers published until now are dealing with single degree of freedom (SDOF) systems. So the respective FP equation includes two independent space variables only (x_1, x_2). Nevertheless stepping over this limit and entering into a true multi-dimensionality a number of specific problems must be overcome. While in usual FEM practice the number of space variables is two or three, investigating FP equation, so $2n$ independent space variables emerges. It means for instance 12 space variables when random motion of a rigid body in space with six degrees of freedom is studied. Many requirements should be respected which are out of a conventional practice of Finite Element employment.

The further specific problem is the generation of finite element mesh for which an advanced method of the triangulation has to be proposed. With respect to the order of the differential equation, the multi-dimensional simplex elements with nodal unknowns approximated by the linear shape functions are employed. Unlike earlier studies it is coming to light that the simplex elements are the most appropriate and rectangular (multi-brick) elements should be abandoned for many reason. Also elements with intermediate nodes on edges should be avoided. The triangulation of a set of points in multidimensional space is based on the iterative method where the Delaunay procedure for higher dimensions is applied to the initial distribution of point coordinates and iteratively adapted with respect to the pre-defined distance functions. Basically it means that the points are rearranged in each iterative step towards satisfying required mesh density. It includes, among others, eliminating the redundant points or moving them back to the boundary when they occur outside the computation domain. Since domain decomposition method using multi-processing computation is used, the point coordinates on interface boundaries are mutually compared and modified correspondingly to achieve the identical point position.

As a computational environment for executing the finite element assembly together with time step solution of the given non-stationary problem, the Matlab software is used. The computational domain in the shape of a hyper-block is generated in the multi-dimensional half-space concurrently on a final number of computational sub-tasks and consequently mirrored onto the entire domain. This way of the meshing benefits fully the symmetry of the problem and considerably reduces the computational time. In conjunction with that an effective implementation of the finite element assembly is proposed. Using the process of vectorization working with array operations, the global stiffness and mass matrices are generated very fast while maintaining an optimal memory requirements for the total storage. The integral terms arising from the Galerkin-Petrov method are solved in the closed form over a volume of each polyhedron. Alternatively, the Gauss quadrature of degree 2 can be employed that gives exact integration using affinely symmetric $2n + 1$ points integration formulae [2].

After the spatial discretization the boundary value problem results in the set of ordinary differential equations which is solved by an iterative time integral method for large systems. As a demonstrative example, the two-degree-of-freedom system is investigated. A combination of Rayleigh or Van der Pol with Duffing types of differential equations are assumed characterized by the nonlinear behavior both in the stiffness and damping. This system is subjected to the additive and the multiplicative Gaussian white noise which represents a part of non-linear aeroelastic effects in the system.

Acknowledgments

The kind support of the Czech Scientific Foundation No. 14-34467P and RVO 68378297 institutional support are gratefully acknowledged.

References

[1] Bergman, L.A., Spencer, B.F., Wojtkiewicz, S.F., Johnson, E.A, Robust numerical solution of the Fokker-Planck equation for second order dynamical system under parametric and external white noise excitation, Nonlinear Dynamics and Stochastic Mechanics, American Mathematical Society, Providence, USA, 1996, pp. 23-27.

[2] Hammer, P.C., Marlowe, O.J., Stroud, A.H., Numerical Integration over Simplexes and Cones 10 (55) (1956) 130-137.

[3] Náprstek, J., Král, R., Finite element method analysis of Fokker-Planck equation in stationary and evolutionary versions, Advances in Engineering Software 72 (2014) 28-38.

COMPUTATIONAL MECHANICS 2015
31st conference with international participation
Špičák
November 9 - 11, 2015

Load in total hip arthoplasty during a golf swing

M. Jansová[a], J. Křen[a], L. Lobovský[a], P. Votápek[b], K. Koudela[c], L. Hynčík[d]

[a]NTIS - New Technologies for the Information Society, Faculty of Applied Sciences, University of West Bohemia, Technická 8, 306 14 Plzeň, Czech Republic
[b]Department of Machine Design, Faculty of Mechanical Engineering, University of West Bohemia, Univerzitní 22, 306 14 Plzeň, Czech Republic
[c]Clinic for Orthopaedics and Traumathology of Locomotive organs, The University Hospital in Pilsen, alej Svobody 80, 304 60 Plzeň, Czech Republic
[d]New Technologies - Research Centre, University of West Bohemia, Univerzitní 8, 306 14 Plzeň, Czech Republic

Hip arthoplasty is currently the most common orthopaedic surgical procedure. During a total hip arthroplasty (THA) both the acetabulum and the femoral head are replaced with prosthesis. To stay physically active, the patients with THA are adviced to prefer sporting activities such as golf.

The aim of this study is to assess the influence of increased load on the neck of Metha® Short Hip Stem prosthesis (Aesculap AG, Tuttlingen, Germany) during a golf swing using a finite element model. The results will help the specialists to establish whether playing golf is a risky activity for patients with this femoral prosthesis.

The geometry of femur was taken from study by Křen et al. [1]. The outer layer of bones is composed of hard compact tissue and the interior is filled in by porous trabecular tissue. As the layer of compact tissue varies over the femur, it is modelled by tetrahedral solid elements to obtain realistic distribution. The trabecular bone is modelled by tetrahedral elements. The material properties of compact and trabecular bone are taken from [1].

The surface geometry of the prosthesis is based on 3D laser scan. The stem and the head are used in the model and modelled by tetrahedral elements. The stem is placed in femur as shown in Fig. 1.

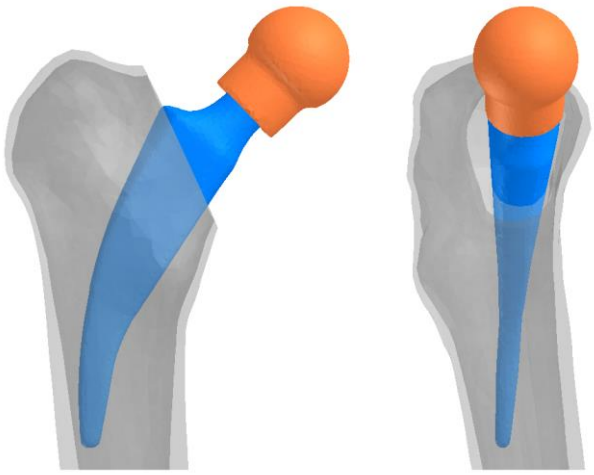

Fig. 1. A finite element model of Metha® prosthesis in the femur - compact bone (light gray), trabecular bone (dark gray), stem (blue) and head (orange)

The stem is made of titanium forged alloy (Ti6Al4V/ISO 5832-3). The head is made of cobalt-chromium forged alloy (CoCrMo/ISO 5832-12). Their material parameters are listed at [2] and [3] respectively.

Fixation of stem in the trabecular bone by cement is replaced by a special coating and an additional 20 μm calcium phosphate layer on the stem that supports integration of the bone into the stem. This is modelled by shared boundary nodes - the geometry is continuous without any gaps.

Two locations of nodes fixed in all degrees of freedom in order to fix the femur in space are tested [4] - the distal end and the mid-diaphysis.

The joint contact force is applied on the head and the force of gluteus medius muscle is applied on its insertion area on the lateral surface of the greater trochanter. The forces correspond to standing upright position and are adjusted to model dimensions. The load during the golf swing is simulated by an additional force applied on the head in the horizontal plane.

The maximal values of von Mises stress in the prosthesis neck are listed in Table 1. With fixed distal end of femur, the maximal value of von Mises stress on the medial side of the neck increased by 10% during the golf swing and its location moved anteriorly. The maximal value of von Mises stress on the lateral side of the neck increased by 22% during the golf swing and its location moved posteriorly.

With fixed mid-diaphysis, the maximal value of von Mises stress on the medial side of the neck increased by 9% during the golf swing and its location moved anteriorly. The maximal value of von Mises stress on the lateral side of the neck increased by 17% and both when standing and during the golf swing was located posteriorly from mid axis of the stem.

Table 1. Maximal von Mises stress values on the prosthesis neck [MPa]

	fixed distal end		fixed mid-diaphysis	
	medial side	lateral side	medial side	lateral side
standing	147	126	140	120
golf swing	161	154	153	140

The ultimate tensile strength of CoCrMo alloy is 660 to 1280 MPa [3] which is at least 4-times higher than the values reached in the neck in presented model. Therefore it is unlikely that it would break during the golf swing.

Acknowledgements

This publication was supported by the project LO1506 of the Czech Ministry of Education, Youth and Sports.

References

[1] Křen, J., Hynčík, L., Řehounek, L., Modelling of interaction between femur and PFN, Proceeding of Computational Mechanics 2001, Plzeň, pp. 141-146.

[2] http://asm.matweb.com/search/SpecificMaterial.asp?bassnum=MTP641

[3] http://www.makeitfrom.com/material-properties/UNS-R30075-ASTM-F75-ISO-5832-4-Co-Cr-Mo-Alloy

[4] Speirs, A. D., Heller, M. O., Taylor, W. R., Duda, G. N., Physiologically based boundary conditions in finite element modelling, Journal of Biomechanics 40 (10) (2007) 2318-2323.

COMPUTATIONAL MECHANICS 2015
31st conference with international participation
Špičák
November 9 - 11, 2015

Modelling of composite spindle rams

V. Kulíšek [a], M. Růžička[a], T. Kašpárková [a], R. Poul[b]

[a] *Department of Mechanics, Biomechanics and Mechatronics, Faculty of Mechanical Engineering, Czech Technical University in Prague; Technická 4, 166 07 Prague, Czech Republic*
[b] *Compo Tech Plus s.r.o., Nová 1316, 342 01 Sušice, Czech Republic*

A global goal for the machine tools' industry is to increase a productivity and precision of machining. One of the ways how to achieve these goals is in designing new machine tools with increased dynamic stiffness and reduced mass of its movable components, which are nowadays made from steel or a cast iron. A replacement of these materials with materials with a higher damping, stiffness and lower density can provide the increase of the significant mechanical properties. A lot of these demands can be fulfilled by composites based on carbon fibres, although care must be taken when designing a thick-walled component from orthotropic materials, as the components have large demands on the rigidity, while mostly loaded by bending, transverse shearing and torque. According to Mohring [1], hybrid structures made of sheet metal or CFRP with cores appear to be a future technology in the machine tools' design, however, systematic design and optimization methods still have to be developed.

A case study was performed with aim on modelling a newly developed composite spindle ram, comparison of the modelling approaches and comparison with a steel reference spindle ram. The composite ram was built as a hybrid structure; composed from carbon/epoxy composite (mostly from ultra-high modulus carbon fibres); damping layers and steel inserts. The geometry of the ram, together with the results of experimental comparison was published by Uher [2]. The composite ram achieved 15 times better dynamic stiffness while having 2.5 times lower mass. The internal structure of the ram is in Fig. 1.

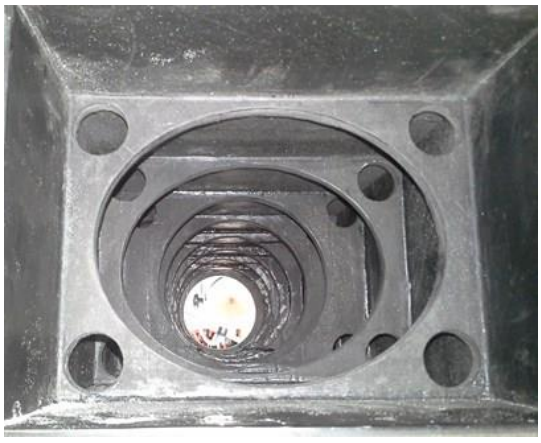

Fig. 1. Internal structure of composite spindle ram

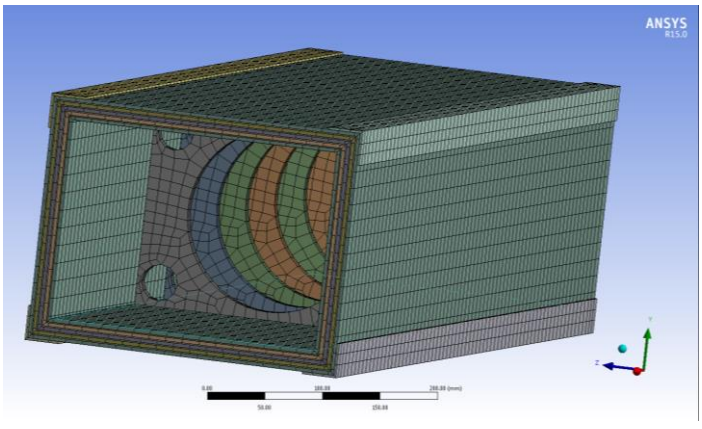

Fig. 2. Finite element model of composite spindle ram

The ram's skins were created from combination of 3 mm thick composite layers, which were separated by thin layers. In the corners, the thin layers were from carbon/epoxy composite; while in central areas these thin layers were created from a damping material with

significantly higher compliance (Young's modulus approximately 50 MPa in comparison with composite layers – in-plane up to 400 000 MPa, out-plane about 3 000 MPa). Between the layers, epoxy adhesive, with modulus about 2 800 MPa, was placed.

The goal of the case study was to select the best approach for modelling the ram to obtain the stiffness and modal properties. The following sources of uncertainties were entering the model: material properties of layers (determined from assumed fibre volume fraction in the layer and nominal matrix and fibre material properties with several unknown parameters); simplifications of geometry and material (for example neglecting the adhesive layers); boundary conditions. The additional errors could be caused by selecting the inappropriate approach of modelling. As the hybrid structure was composed from materials with significantly different stiffness, the usage of shell elements could have led to wrong results. The most feasible approaches were to use models from continuum shell elements (ANSYS – SOLSH190 element) or models based on solid elements with homogenized material properties. In both cases, the ram's models had to be made with several elements per the ram's thickness (see Fig. 2).

The best matching results between the simulation and experiment were obtained using the model with continuum shell element; where the lay-up was specified for each element and the damping layers were separated from the elements of the composite lay-up. The difference between the FEA model and experimental results – the value of the first bending mode shape frequency is given in Table 1. In the comparison, the spindle ram was connected to the ground using two pairs of simplified housings and additional mass as a simplified spindle was connected to the spindle ram's front panel. These boundary conditions were used for experiments with the reference steel spindle ram.

Table 1. Comparison of experimental and numerical results for clamped composite and steel spindle ram

	Composite-exp.	Composite – FEA	Steel – exp.	Steel – FEA
1st bending [Hz]	249	230	203	215
Static stiffness – X [N/μm]		95		110

The variation between the experimental and FE model is approximately 6% for the steel model and 8% for the composite spindle ram. The difference in steel specimen is partially caused by boundary conditions in experiment (clamping of the housings with non-zero compliance). The similar mistake can be assumed in the composite spindle ram.

Overall, the approach with continuum shell elements (including the geometry and material simplifications and large assumptions in material properties of layers) was verified, as the model predicted the most important structural mode shapes (in bending) with a variation to the experiment under 10%.

The FE model predicted the static stiffness of the composite ram slightly lower than for the steel coupon (higher by 15%). Although the static stiffness decreased, due to the increased damping of the new ram's material, the dynamic stiffness of the composite ram was determined from experiment [2] significantly higher than for the steel specimen.

Acknowledgements

The authors would like to thank the Technology Agency of the Czech Republic for supporting this research in the framework of project no. TA02010543.

References

[1] Mohring, H. C., Advanced materials in machine tool structures, Proceedings of the 16th International Machine Tool Engineer's Conference, Tokyo, Japan Machine Tool Builders' Association, 2014, pp. 76-88.

[2] Uher, O., et al., Composites in machine tool applications, Proceedings of the 16th International Machine Tool Engineer's Conference, Tokyo, Japan Machine Tool Builders' Association, 2014, pp. 109-118.

COMPUTATIONAL MECHANICS 2015
31st conference with international participation
Špičák
November 9 - 11, 2015

On the stability of Taylor vortex flow in a cylindrical annulus for different working fluids

A. Lalaoua [a], Z. Chaieb [b], M. Aouli [a]

[a] *Faculty of Physics, Thermodynamic and Energetic Systems Laboratory, USTHB, BP 32 El Alia , Algiers, Algeria*
[b] *Faculty of Physics, Solid Solutions Laboratory, USTHB, BP 32 El Alia , Algiers, Algeria*

The Taylor-Couette system, which consists of a fluid between two independently rotating concentric cylinders, is among the most investigated problems in fluid mechanics, its hydrogen atom, owing to its direct connection with engineering applications (tribology, waste water treatment, mixing processes and biomedical), as well as to its relevance as prototypical flow in the study of laminar-turbulent transition. In this work, the fluid motion in a confined cylindrical gap is investigated numerically. The inner cylinder rotates freely about a vertical axis through its center while the outer one, the bottom and the upper surfaces are held stationary. The basic system is characterized by a height H = 150mm, an annular gap d = 5mm, a ratio of the inner to the outer cylinders radii η = 0.909, an aspect ratio corresponding to the cylinders height reported to the gap length Γ = 30 and a ratio of the gap to the radius of the inner cylinder δ = 0.1. The main goal of this work is to show how operates the change in the structure of the Taylor vortices when changing the working fluid by analyzing three kinds of liquid: Hydrogen, Water and Lithium. Particular attention is given to the onset of Taylor vortices in the vicinity of the threshold of transition, i.e., from the laminar Couette flow to the appearance of Taylor vortex flow. The 3D geometry is meshed with hexahedral cells (structured mesh). The computational domain is divided into a number of grids in the radial (r), azimuthal (θ) and axial (z) directions, respectively. The mesh size is uniform in the axial and azimuthal directions, but it is stretched near both walls in the radial direction where there is a high shear. The outer element, the upper and the bottom plates are modeled as fixed walls with no-slip boundary conditions; while the moving wall boundary condition is applied for inner cylinder with no-slip condition is imposed. Three working fluids are tested during this numerical simulation to highlight the effect of fluid nature on flow behavior. It is found that the nature of working fluid deeply affect the flow patterns. The critical Taylor number (Ta_{c1}), characterizing the onset of Taylor vortex flow (TVF), and the number of Taylor vortices occurring in the annulus and their wavelength are varied from one fluid to another, as shown in Fig. 1. For Water, 13 axisymmetric toroidal rolls are appeared, whereas 12 and 14 rolls are observed for Hydrogen and Lithium respectively. In addition, the numerical results obtained here show significant topological changes on the structure and form of Ekman cell. For the Hydrogen liquid, the Ekman vortices are substantially elongated to about 1.6d and the Taylor vortices are also elongated, so that their height is 1.2d (wavelength Λ=2.4d), which is substantially superior to the height of 1.001d expected in the case of Water. However, for the Lithium liquid, the Ekman cells are compressed to about 1.1d thereby compressing the Taylor vortices, their wavelength decreases up to Λ = 1.6d. We also note that the skin friction coefficient (C_f) of the Lithium increases considerably compared to Water and Hydrogen.

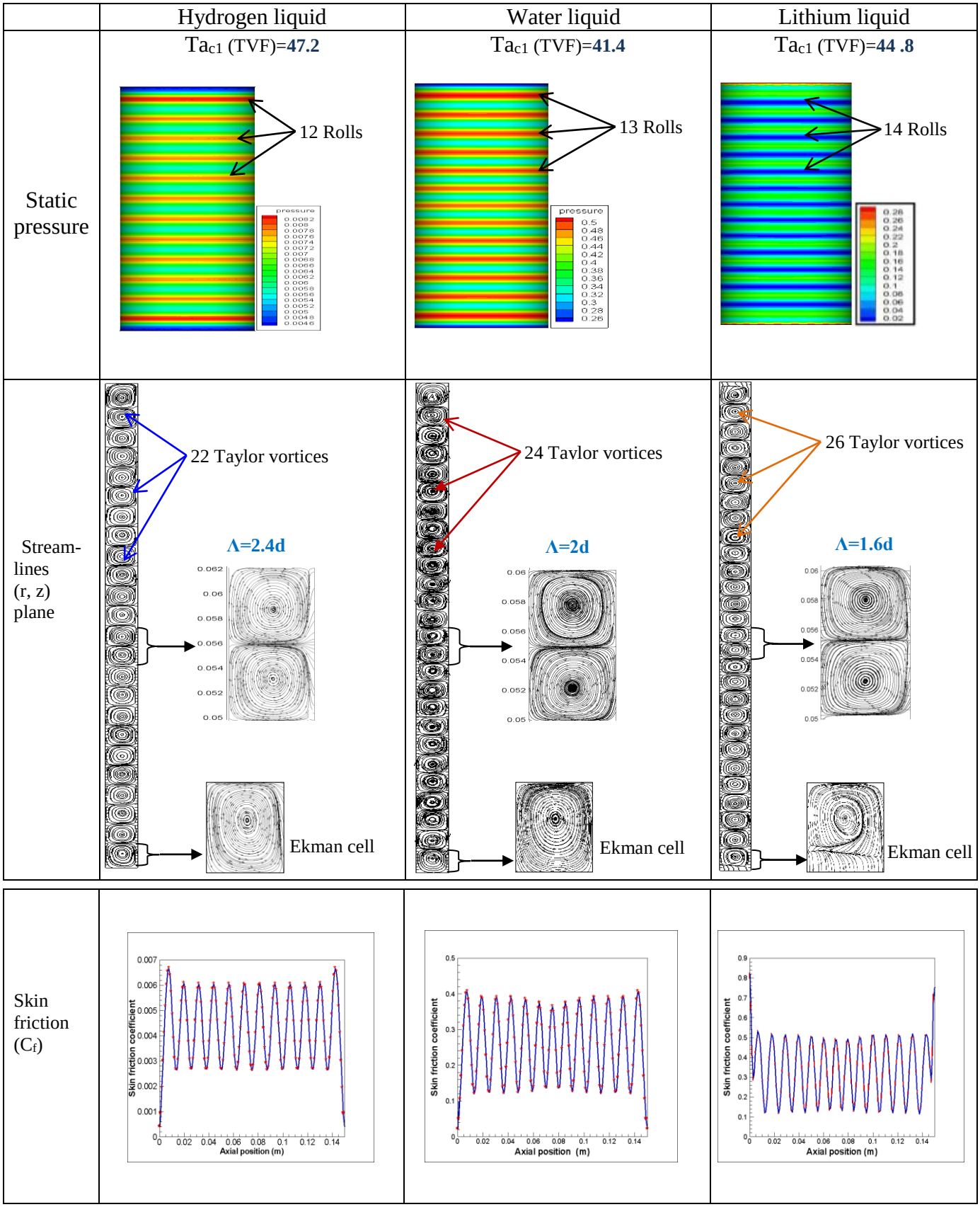

Fig 1. Taylor vortex flow between two rotating cylinders for different fluids

COMPUTATIONAL MECHANICS 2015
31st conference with international participation
Špičák
November 9 - 11, 2015

Comparison of sacral bone fixation techniques

L. Lobovský[a], J. Hartlová[b], M. Salášek[a,c], J. Krystek[a], M. Jansová[a], P. Votápek[d], R. Tupý[e], J. Ferda[e], T. Pavelka[c], J. Křen[a]

[a] *NTIS – New Technologies for the Information Society, Faculty of Applied Sciences, University of West Bohemia (UWB), Univerzitní 8, 306 14 Plzeň, Czech Republic*
[b] *Department of Mechanics, Faculty of Applied Sciences, UWB, Univerzitní 8, 306 14 Plzeň, Czech Republic*
[c] *Clinic for Orthopaedics and Traumatology of Locomotive Organs, University Hospital Plzeň, alej Svobody 80, 304 60 Plzeň, Czech Republic*
[d] *Department of Machine Design, Faculty of Mechanical Engineering, UWB, Univerzitní 8, 306 14 Plzeň, Czech Republic*
[e] *Clinic for Radiology, University Hospital Plzeň, alej Svobody 80, 304 60 Plzeň, Czech Republic*

The study focuses on experimental investigation of deformations in pelvic region after orthopaedic treatment of sacral bone injuries. An attention is paid to stabilisation of unilateral transforaminal sacral fracture. This type of pelvic injuries occur among patients after severe motor vehicle accidents and among polytraumatized patients. Four types of orthopaedic fixators (namely iliosacral screws [2], transiliac internal fixator [1], transiliac plate [5] and sacral bars [3]) and several variations of their application are examined from the mechanical point of view. In order to stabilise the pelvic ring well and to shorten the process of healing, the fixator must prevent large relative displacements of the fractured bone parts.

There is a number of studies focused on various pelvic ring fixation techniques so far. However, no direct comparison of several techniques under the same conditions is provided. The aim of this study is to make an extensive experimental research which compares a number of fixation techniques mentioned above.

The stability of the applied fixation techniques is tested using orthopaedic plastic models of male pelvis made of solid foam [6]. Relative displacements of the bone parts are measured using a non-invasive optical method. A suitable method for photogrammetric measurements of pelvic ring deformations is assessed and its accuracy is determined. Due to the complexity of the pelvic bones surface geometry, a multi-camera digital image correlation (DIC) system is applied.

The orthopaedic model of intact male pelvis is mounted on a dedicated metal stand that is designed and manufactured in order to provide a rigid support to pelvis in acetabula such that the position of pelvis is fixed in space and its rotations in the sagittal plane are prevented. The model is subjected to well defined mechanical loading applied by the mechanical testing device at the base of sacrum. The displacements of selected points are analysed using synchronous images from four cameras by means of DIC. In addition, these data are correlated with the extensometer recordings. In order to analyse the stability of the fixators, the displacements of the selected points at the dorsal surface of the sacrum are quantified.

The best results in terms of stability and relative displacement of the fractured parts are achieved when two sacral bars are applied. However, application of sacral bars provided the least amount of control over the compression of the fracture in the tests performed.

The resulting comparison of all tested fixation technigues is applicable in the decision making process prior to the surgical treatment of the pelvic injuries. However, in the patient specific

cases a wide range of surgical complications (such as vascular injuries, thromboembolic complications or risk of infections) as well as the difficulties in application of the selected fixator must be considered.

The experimental data also serve as a reference for validation of the computational model of the pelvic ring [4]. The study is considered as a starting point for future computational analysis which aims at addressing real physiological conditions in human pelvis, incorporating the real material properties of pelvic bones and implementation of models for cartilage and ligamentous tissues.

Acknowledgement

This publication was supported by the project LO1506 of the Czech Ministry of Education, Youth and Sports.

References

[1] Dienstknecht, T., Berner, A., Lenich, A., Zellner, J., Mueller, M., Nerlich, M., Fuechtmeier, B., Biomechanical analysis of a transiliac internal fixator, International Orthopaedics 35 (12) (2011) 1863-1868.

[2] Giráldez-Sánchez, M.A., Lázaro-Gonzálvez, Á., Martínez-Reina, J., Serrano-Toledano, D., Navarro-Robles, A., Cano-Luis, P., Fragkakis, E.M., Giannoudis, P.V., Percutaneous iliosacral fixation in external rotational pelvic fractures. A biomechanical analysis, Injury 46 (2) (2015) 327-332.

[3] Gorczyca, J.T., Varga, E., Woodside, T., Hearn, T., Powell, J., Tile, M., The strength of iliosacral lag screws and transiliac bars in the fixation of vertically unstable pelvic injuries with sacral fractures, Injury 27 (8) (1996) 561-564.

[4] Salášek, M., Jansová, M., Křen, J., Pavelka, T., Weisová, D., Comparison of methods of pelvic ring fracture fixation using finite element model, Proceedings of the 29th conference Computational Mechanics, Špičák, 2013.

[5] Suzuki, T., Hak, D.J., Ziran, B.H., Adams, S.A., Stahel, P.F., Morgan, S.J., Smith, W.R., Outcome and complications of posterior transiliac plating for vertically unstable sacral fractures, Injury 40 (4) (2009) 405-409.

[6] Model of full male pelvis, Sawbones: http://www.sawbones.com/Catalog/Orthopaedic Models/Pelvis-Full/1301

COMPUTATIONAL MECHANICS 2015
31st conference with international participation
Špičák
November 9 - 11, 2015

Optimization of perforated structures based on two-scale homogenization

V. Lukeš[a], E. Rohan[a]

[a] *NTIS – New Technologies for the Information Society, Faculty of Applied Sciences, University of West Bohemia, Univerzitní 8, 306 14 Plzeň, Czech Republic*

This paper deals with optimization of perforated layer interacting with acoustic field in a domain which is subdivided by the layer in two disjoint subdomains, see Fig. 1 (left). The homogenization approach is used to formulate the computational model of acoustic transmission on periodic perforated layers and the sensitivity analysis is employed in order to solve the optimization problem of perforation design.

The "direct" numerical simulation of acoustic wave propagation, described by the Helmholtz equation, through a perforated structure is computationally expensive therefore we used the reduced model of the acoustic transmission based on the two-scale method of homogenization, see [2, 3]. This approach leads to the global problem describing the waves in an acoustic domain and to the local (microscopic) problem which gives the homogenized coefficients reflecting geometrical arrangement of the perforation. The coefficients are employed in the homogenized transmission condition that governs coupling of acoustic waves in the disjoint domains.

Acoustic wave propagation can be characterized by the transmission loss function and is influenced by design of the perforated layer. The optimization problem can be formulated as to minimize/maximize the transmission loss by changing the geometry of layer perforations. The sensitivity analysis of the homogenized coefficients and objective function with respect to the change of perforation design was developed in [4].

The multiscale optimization procedure is implemented in the Python programming language using *IPOPT* package for large-scale nonlinear constrained optimization [5] and the numerical solution of the local and global acoustic subproblems are solved by *SfePy* – Simple Finite Elements in Python [1]. The overall optimization process involves the following steps:

- solution of the local problem and evaluation of the homogenized coefficients and their sensitivity w.r.t. the change of perforation design,
- solution of the state and adjoint problems for the "global" acoustic fields,
- evaluation of the objective function and its sensitivity w.r.t. the homogenized coefficients.

Optimization of the acoustic field in a waveguide is illustrated in Fig. 2 where the perforated interface is divided into three regions in which the shape of perforations can be changed independently.

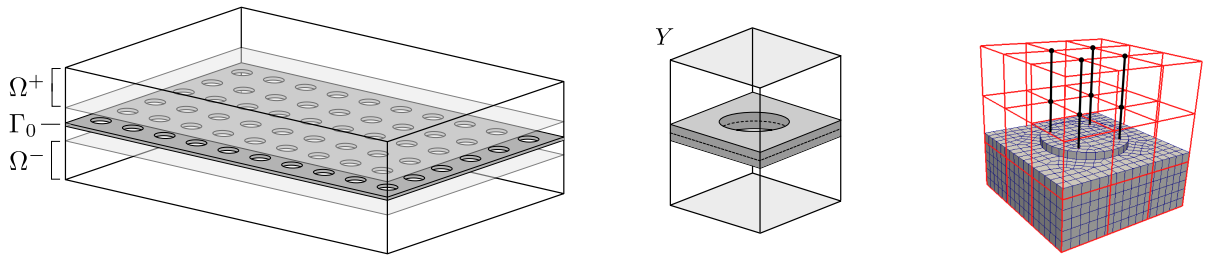

Fig. 1. *Left:* the acoustic domain decomposition in two subdomains separated by the perforated interface; *center:* periodic cell representing the layer perforation; *right:* FE mesh of the periodic cell and its shape parametrization (B-spline)

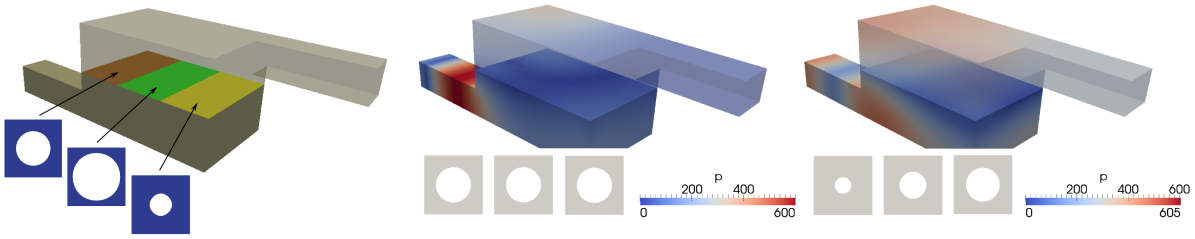

Fig. 2. *Left:* the acoustic domain and perforated layer with three different perforations; *center and right:* the acoustic fields for the initial and optimized perforation designs

Acknowledgements

This work was support by the Czech Scientific Foundation project GACR P101/12/2315. V. Lukeš was supported by the project LO1506 of the Czech Ministry of Education,Youth and Sports.

References

[1] Cimrman, R., SfePy – write your own FE application ArXiv e-prints, Proceeding of the 6th European Conference on Python in Science (EuroSciPy 2013), http://arxiv.org/abs/1404.6391.

[2] Rohan, E., Lukeš, V., Homogenization of the acoustic transmission through perforated layer, Journal of Computational and Applied Mathematics 234 (6) (2010) 1876-1885.

[3] Rohan, E., Lukeš, V., Homogenized perforated interface in acoustic wave propagation – modeling and optimization, Proceedings of ICOVP 2013, Lisbon, Portugal, 2013, pp. 1-10.

[4] Rohan, E., Lukeš, V., Sensitivity analysis for optimal design of perforated plates in vibro-acoustics: Homogenization approach, Proceedings of ISMA 2012 – USD 2012, KU Leuven, 2012, pp. 4201-4214.

[5] Wächter, A., Short tutorial: Getting started with Ipopt in 90 minutes, Combinatorial Scientific Computing, Dagstuhl Seminar Proceedings, Dagstuhl, Germany, 2009.

COMPUTATIONAL MECHANICS 2015
31st conference with international participation
Špičák
November 9 - 11, 2015

Study of a pump based on the pulsatile flow principle

T. Machů [a], S. Fialová [a], Z. Říha [b], F. Pochylý [a]

[a] *Victor Kaplan department of fluids engineering, Brno university of technology, Technická 2896/2, 616 69 Brno, Czech Republic*
[b] *Institute of Geonics, Academy of Sciences, Drobného 28, 602 00 Brno, Czech Republic*

Displacement pumps that use a piston or a membrane for liquid transport are known. Their unsteady movement causes pulsatile flow. The pumping principle is only possible by the opening and closing of the intake and discharge valves. The operation of these valves often limits the lifetime of the device and significantly contributes to hydraulic losses of the aggregate. Pumping of the liquids, either onmicro or macro scale, requires a pump without the use of mechanical valves. Therefore, an idea arose to replace the valves by vortex structures, which would take over their function. This function can be twofold:

a) Vortex structures provide hydraulic closing of the suction and discharge valves
b) Vortex structures will be designed so that in the moment of discharge, the dissipation function in the discharge branch is negligible but maximum possible in the suction branch and vice versa during suction time.

The mathematical model is based on a new form of the unsteady term and right side of the Navier- Stokes equations. According to (Pochylý et al, 2014 - [4]), for an incompressible fluid using the summation convention, the following relation can be written for the unsteady term:

$$\frac{\partial v_i}{\partial \mathrm{t}} = \frac{\partial}{\partial x_j}\left(\frac{\partial v_j}{\partial \mathrm{t}} x_i\right) \quad \text{a} \quad g_i = \rho \frac{\partial}{\partial x_i}\left(g_j x_j\right). \tag{1}$$

This relation is essential for the determination of the force acting on the piston and valves. Analogously, for the velocity vortex $\boldsymbol{\Omega} = rot\mathbf{v}$ can also be deduced, so it holds:

$$\frac{\partial \Omega_i}{\partial \mathrm{t}} = \frac{\partial}{\partial x_j}\left(\frac{\partial \Omega_j}{\partial \mathrm{t}} x_i\right). \tag{2}$$

Integrating the Navier-Stokes equation through the volume of the liquid *V*, the relation for a force acting on the body can be derived in the form:

$$\mathbf{F} = \rho \int_V \frac{\partial \mathbf{v}}{\partial t} dV + \mathbf{F}_\mathrm{i}\,. \tag{3}$$

$\mathbf{F}_\mathrm{i}$ represents the participation of other terms of the equation on the surface $\Theta = S \cup \Gamma$, where the liquid flows in through the surface *S* and out of the region *V* and the region Γ is a solid wall.

Had we not known expression (1) we could not determine the significance of the unsteady term in equation (3), which is essential for the work of the pulsatile pump. Using (1), however, we obtain:

$$\mathbf{F} = \rho \int_{S\cup\Gamma} \left(\frac{\partial \mathbf{v}}{\partial t} \cdot \mathbf{n}\right) \mathbf{x} d\Theta,\ \Theta = S\cup\Gamma, \tag{4}$$

thereby is the effect of the unsteady term converted from volume V onto the boundary Θ, ie on the motion of the piston and valves, or on the vortex structures in place of the suction and discharge valves. A similar relationship applies to the vortex velocity. For example:

$$\frac{\partial \mathbf{\Omega}}{\partial t} + rot(\mathbf{\Omega} \times \mathbf{v}) = \mathbf{0}. \tag{5}$$

Using (2), after integration we obtain (5):

$$\int_V \frac{\partial \mathbf{\Omega}}{\partial t} dV = \int_{S \cup \Gamma} \left(\frac{\partial \mathbf{\Omega}}{\partial t} \cdot \mathbf{n} \right) \mathbf{x} d\Theta + \int_S (\mathbf{\Omega} \times \mathbf{v}) \times \mathbf{n} dS. \tag{6}$$

From here it is already possible to deduce the shape of the vortex structures in place of the suction and discharge valves depending on the shape of the region Γ.

Vortex structures can be very effectively influenced by hydrophilic coating of walls Γ in the area V. The hydrophilic effect causes a slip of the liquid along the wall, so the value of the shear stress can significantly change, according to the equation (Pochylý et al., 2010 - [3]):

$$\boldsymbol{\sigma} = -k\mathbf{v_s}, \tag{7}$$

where $\mathbf{v_s}$ is the velocity of the liquid on the wall and k is the so called adhesion coefficient for ultrahydrophobic surfaces, which takes values $k \in < 0,1; 1 >$ (Fialová & Pochylý, 2015 - [2]).

Using this methodology, the pump has been designed on the principle of non-stationary vortex structures according to the principle set out in paragraph "b)" of the introduction.

Acknowledgement

Grant Agency of Czech Republic GA101/13-20031S is gratefully acknowledged for support of this work.

References

[1] Brdička, M., Samek, L., Sopko, B., Continuum mechanics, Academia, Praha, 2000. (in Czech)

[2] Fialová, S., Pochylý, F., Identification and experimental verification of the adhesive coefficient of hydrophobic materials, Wasserwirtschaft Extra, 2015, pp. 125-129.

[3] Pochylý, F., Fialová, S., Kozubková, M., Zavadil, L., Study of the adhesive coefficient effect on the hydraulic losses and cavitation, International Journal of Fluid Machinery and Systems 3 (4) (2010) 386-395.

[4] Pochylý, F., Fialová, S., Krutil, J., New mathematical model of certain class of continuum mechanics problems, Engineering Mechanics 21 (1) (2014) 61-66.

COMPUTATIONAL MECHANICS 2015
31st conference with international participation
Špičák
November 9 - 11, 2015

Probabilistic assessment of the propeller blade failure based on the fatigue tests and the vibratory stress survey

M. Matyska [a], M. Růžička [b]

[a] *Avia Propeller, Beranových 65/666, 199 00 Praha, Czech Republic*
[b] *Czech Technical University in Prague, Faculty of Mechanical Engineering, Department of Mechanics, Biomechanics and Mechatronics, 166 07 Praha 6, Technická 4, Czech Republic*

Failure of the blade is a primary failure, it means a failure which is not the result of the next failure of another part and Civil Aviation Agencies around the world require very low probability of failure occurrence per propeller flight hour. Assessment is based on the evaluation of the data from blade fatigue tests and vibratory stress survey of the propeller blades. Palmgren-Miner law was used for service life calculation. S-N curve with variable standard deviation and evaluated stress ranges and cycles by Rain Flow Method from blade steady and vibratory stress survey during aircraft ground and flight operation are input variables for probabilistic assessment which is based on Monte Carlo simulation method. The failure probability function is analyzed by using AntHill® software and output in tables and graphs is available.

The total twenty-nine propeller blades were tested in fatigue equipment uses pressure air and blade natural frequency of the blade first flatwise. The blade shank was preloaded by screw to obtain conditions of fixed blade. The equipment was designed and manufactured by Avia especially for blade fatigue testing. Stress level and frequency/cycles was measured by glued strain gages on the blades. The new blades, overhauled blades with approved repairs limits, blades after aircraft service operation (thousands of hours) and blades after operation in the test cells (thousands of hours) were used in the fatigue tests. The goal of the tests was also cover conditions of blade service deterioration [1].

The Finite Element Analysis was used for harmonic analysis to found the blade natural frequencies and places with maximum stress for each natural shape. Campbell diagram is plotted to find the possible resonance regimes based on intersection between natural shape and excitation frequencies caused by engine model or aircraft configuration or flight regimes. Vibratory stress survey of propeller blades during aircraft ground and flight operation was evaluated by Rain Flow Method and loading spectrum was obtained. Stress survey uses strain gages glued on blades and telemetry equipment manufactured by Telemetrie Elektronik Company. Transmitter with battery pack is installed on the propeller hub by means special aluminum fixture and receiver with data recorder is placed and fixed in the aircraft cabin or cargo space [3].

Fatigue characteristics and propeller loading have the random background. These random variables with appropriate distributions can be use for probabilistic modeling to obtain probabilistic assessment of the blade fatigue failure (Fig. 1).

S-N curve with variable standard deviation approximated up to giga cycle fatigue range and steady and vibratory stress histogram from aircraft ground and flight regimes are input to AntHill® software based on Monte Carlo simulation method [2], (Fig 2).

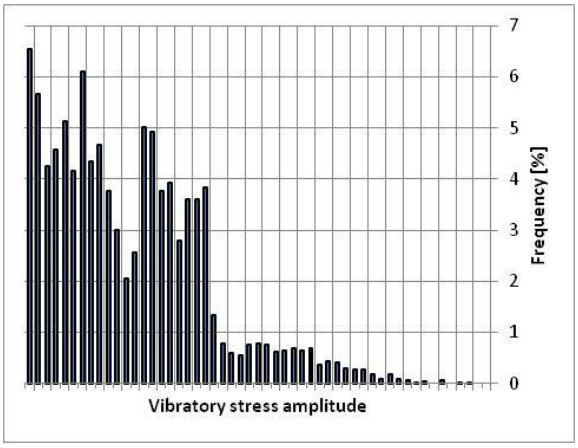

Fig. 1. Vibratory stress histogram from flight

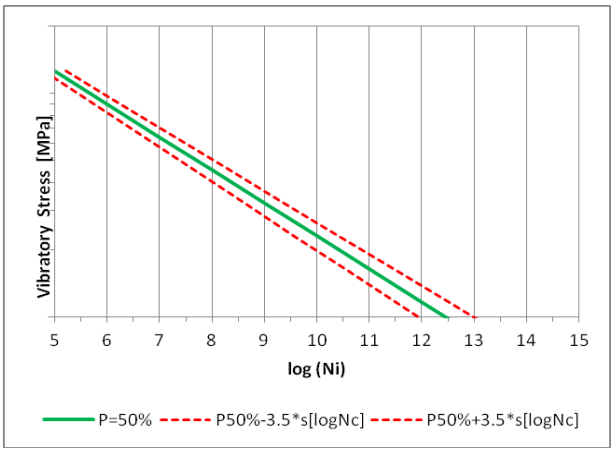

Fig. 2. S-N curve with variable standard deviation

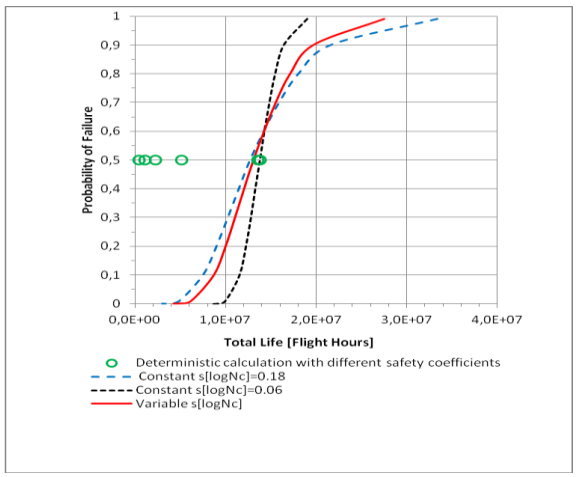

Fig. 3. Probability and deterministic calculation

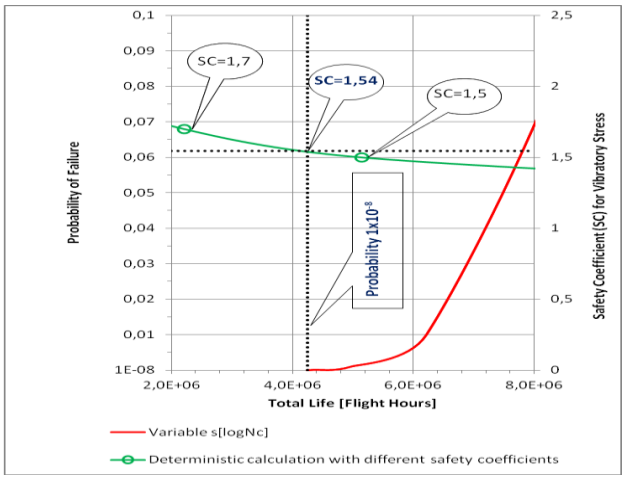

Fig. 4. Safety Coefficient corresponding to probability

Failure probability $1x10^{-8}$ per one flight hour is required for primary failure of the propeller critical parts such as the propeller blades. Fatigue failure probability assessment and deterministic calculation with appropriated safety coefficients was done and relationship between safety coefficients and required failure probability was found (Fig. 3 and Fig 4).

Acknowledgements

This paper was supported by the grant CTU in Prague: SVK 18/15F2/Winter WAM 2015.

References

[1] Burda, C., Fatigue tests of the V508B propeller blades per NLGS-2, Avia, Prague, 1980.
[2] Marek, P., Brozzetti, J., Guštar, M., Tikalsky, P., Probabilistic assessment of structures, TeReCo, Prague, 2003.
[3] Tvrdík, Z., Matyska, M., Test report VJ8.510/KA C90 flight stress survey, Avia Propeller, Prague, 1998.

COMPUTATIONAL MECHANICS 2015
31st conference with international participation
Špičák
November 9 - 11, 2015

Dynamics of beam pair coupled by visco-elastic interlayer

J. Náprstek[a], S. Hračov[a]

[a] *Institute of Theoretical and Applied Mechanics, ASCR v.v.i., Prosecká 76, CZ-190 00 Praha, Czech Republic*

Two parallel slender beams with visco-elastic interlayer can serve as a relevant mathematical model of a number of engineering systems. A typical example is a double skin facade of tall buildings. The outer skin can be considered as a dynamic damper and thus contribute to comfort inside the building. Many applications emerge in power piping when using two coaxial pipes with an interlayer in order to suppress vibration due to flow and structure interaction. Similar inconvenient behavior can exhibit panels which fall into the flutter post-critical state. Further applications can be expected at industrial chimneys, towers, etc. In principle the idea of vibration damping using such a formation is inspired by very well known tuned mass damper. However its internal structure, function, limitations and singular states are incomparably more complicated and therefore adequate applications should be cautious.

From the viewpoint of dynamics linear eigen and forced vibration of two parallel beams with massless visco-elastic interlayer is investigated. Some partial cases have been discussed in literature in the past, see for instance [1, 2]. However mathematical aspects of this problem are still rather limited and should be treated at the level obvious in rational mechanics. Hence in this paper simple Euler-Bernoulli models with prismatic cross section are considered. Thickness of the interlayer is constant. Boundary conditions can be basically adopted in any arbitrary configuration, nevertheless certain frequently used settings are discussed in order to keep some analogy with real structures. So that following differential system can be written:

$$\begin{aligned} EJ_1 u_1'''' + b_1\dot{u}_1 + b(\dot{u}_1 - \dot{u}_2) + c(u_1 - u_2) + \mu_1\ddot{u}_1 &= f(x,t), \\ EJ_2 u_2'''' + b_2\dot{u}_2 + b(\dot{u}_2 - \dot{u}_1) + c(u_2 - u_1) + \mu_2\ddot{u}_2 &= 0, \end{aligned} \tag{1}$$

where geometric and physical parameters of booth beams and interlayer are considered constant independent on the length coordinate. In particular following nomenclature has been adopted: EJ_i - bending stiffness of the i-th beam $(i = 1, 2)$, μ_i - mass/length of the adequate beam, $b_i,\ b$ - viscous damping/length of the adequate beam or interlayer, respectively, c - normal stiffness of the interlayer/length, $f(x,t)$ - excitation force/length (harmonic force in time is considered).

Analytical investigation of the system (1) as a primary procedure has been performed being step by step compared with results obtained by FEM analysis.

Basically the differential operator (1) is positive definite and only harmonic stationary response processes are discussed (eigen- or forced vibration), so time coordinate is eliminated easily by means of commonly known steps using $\exp \omega t$ function. Reduced system of two simultaneous ordinary differential equations in length coordinate is then solved using conventional procedure looking for modal properties or forced vibration response.

Detailed analysis is later performed regarding the general solution which is one of four types depending on the excitation frequency. Each type consists of two parts, where each one is related with: (i) classical static bending of the beam, (ii) bending of the beam on an elastic support,

(iii) conventional dynamic bending of the beam. Variants (i-iii) are combined correspondingly within individual frequency interval, where $\omega_b^2 = c(\mu_1 + \mu_2)/\mu_1\mu_2$:

1. $\omega = 0$, static solution including variants (i) and (ii).
2. $0 < \omega < \omega_b$, "low" frequency cases, dynamic shape combining variants (iii) and (ii).
3. $\omega = \omega_b$, limit separating "low" and "high" frequencies, it combines variants (iii) and (i).
4. $\omega > \omega_b$, "high" frequency cases, both parts correspond to the variant (iii).

Looking for eigenfrequencies, this stratification must be carefully respected.

Boundary conditions corresponding to console (both beams) are introduced to investigate modal properties of the structure for typical parameter configurations applicable in engineering practice. For illustrative purposes a special case of structural parameters has been considered regarding following relation of parameters:

$$EJ_1/EJ_2 \;=\; \mu_1/\mu_2. \tag{2}$$

Fulfilment of this relation provides the identical modal properties of both individual beams. The eigenmodes of the complete system can be divided into two groups, see Fig. 1. In case of odd modes, the corresponding points on both beams have the same amplitude as well as the phase. The odd mode shapes and eigenfrequencies are identical with those of the individual beams. Even modes of the whole system are also composed from the same modes of individual beams. In contrary to the odd modes, the phase between corresponding points on both beams is opposite. The ratio of the amplitudes of the points is constant and equal to a ratio of the stiffness of the beams. The even eigenfrequencies are equal to the eigenfrequencies of the system represented by individual cantilever beam supported by an elastic layer. Its stiffness is a function of the stiffness of the interlayer and of the ratio of the stiffness of the beams.

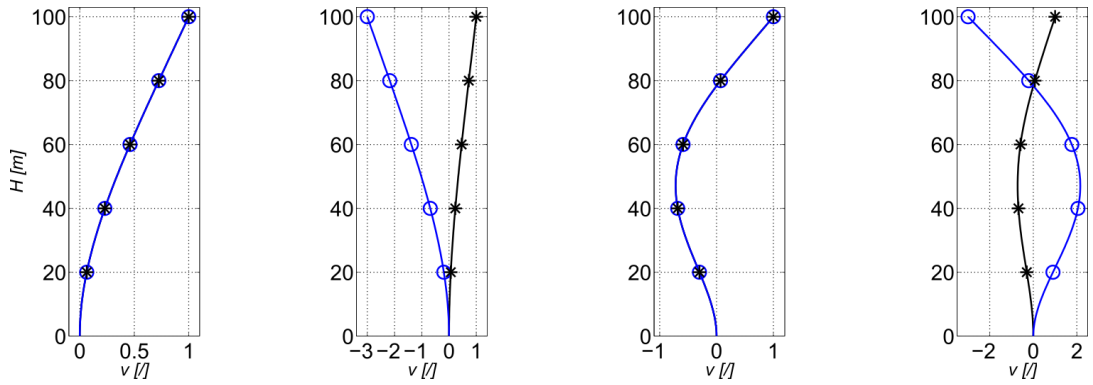

Fig. 1. The first four eigenmodes of the beam pair coupled by visco-elastic interlayer

Acknowledgements

The kind support of the Czech Science Foundation projects No. 13-41574P, 15-01035S and of the RVO 68378297 institutional support are gratefully acknowledged.

References

[1] Kyoung, S.M., Structural design of double skin facades as damping devices for tall buildings, Procedia Engineering 14 (2011) 1351-1358.

[2] Vu, H.V., Ordoñez, A.M., Karnopp, B.H., Vibration of a double-beam system, Journal of Sound and Vibration 229 (4) (2000) 807-822.

COMPUTATIONAL MECHANICS 2015
31st conference with international participation
Špičák
November 9 - 11, 2015

Effect of liquid film on rotor dynamics

N. Nováková [a], L. Dobšáková [a], V. Habán [a], M. Hudec [a]

[a] *Faculty of Mechanical Engineering, Brno University of Technology, Technická 2896/2, 6160 69 Brno, Czech Republic*

Sealing gaps are important constructional components of hydrodynamic machines. Their correct design, including the determination of additional effects, is important for the general dynamic design of the machine. The research was carried out to determine the effects of additives in the sealing gap and was based on the evaluation of the rotor dynamics from the measured radial forces.

The experiment for determining the effects of additional liquid layer in the sealing gap was performed at the Victor Kaplan Department of Fluid Engineering, FME. The purpose of the experiment was to determine the additional effects of the fluid, which acts on the shaft of the test equipment (Fig. 1). [1, 4].

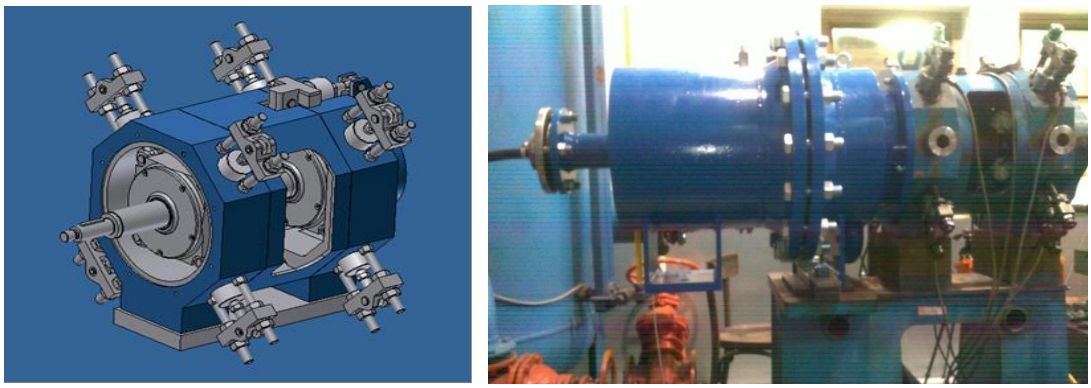

Fig. 1. The test equipment, which were measured additional effects in the sealing gap [2]

The additional rigidity and weight were evaluated in first measurement. In a view of these results it was decided to reduce the bearing stiffness in order to decrease the natural frequency. The natural frequency will be passed at lower speeds, thus the measurements can be performed at the higher relative tuning, [2, 3].

The several variants of the springs were proposed. The final draft was designed with regard to the layout and with respect to the maximum load carrying capacity with minimal stiffness (Fig. 2). The used material was a spring steel, [2].

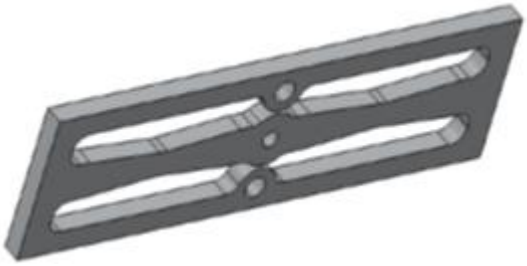

Fig. 2. The final draft [2]

The additional weights in the joint were evaluated after performing a second measurement with a newly designed spring.

Acknowledgements

Presented research was supported by centre of competence of Technology Agency of the Czech Republic TE02000232 “Rotary machines” TA13402001.

References

[1] Gasch, R., Pfützner, H., Rotordynamik, 1st Edition, SNTL, Praha, 1980. (in Czech)
[2] Habán, V., Hudec, M., Pochylý, F., Archalous, J., Nováková, N., Experimental research of the additional effects in hydrodynamic gaps, EÚ-QR-31-12, 2012. (in Czech)
[3] Hu, D., Jia, L., Yang, L., Dimensional analysis on resistance characteristics of labyrinth seals, Journal of Thermal Science 23 (6) (2014) 516-522.
[4] Juliš, K., Brepta, R., Mechanics – Dynamics, 1st Edition, SNTL, Praha, 1987. (in Czech)

COMPUTATIONAL MECHANICS 2015
31st conference with international participation
Špičák
November 9 - 11, 2015

One-dimensional mathematical model of the whole process in a continuous screw press

J. Očenášek [a], J. Voldřich [a]

[a] *New Technologies – Research Centre, UWB in Pilsen, Univerzitní 8, 306 14 Plzeň, Czech Republic*

Within this work, a 1D mathematical model of a continuous screw press incorporating two press parts characterized by significant differences in the physical behavior of a processed oilseed is presented. The first part includes the so called feeding zone and a conveying zone. Herein the oleaginous seeds behave as a compressible mass with a dry friction at the contact with the rotor, the screw or the barrel wall. The dependence of friction forces on pressure brings about an exponential growth of the pressure until the oil point is reached, i.e. the pressure is high enough to release an oil from the seeds. A short transition zone of the gradual oil release is not considered.

In the second part, starting at the position of the oil point, compressed oilseed is modeled as a composite consisting of a solid porous matrix (solid parts of the seed) and an oil filling the matrix pores. Flow of the mixture through the screw press is approximated by a non-Newtonian fluid flow and the Darcy's law is used for a description of the drain of the oil through the porous matrix [1, 2]. The 1D mathematical model of the oil extraction process in a continuous press behind the oil point was presented in the previous year of this conference [3]. Therefore, this work is focused on a model for the situation before the oil point. It should be reminded that the position in the press, where the oil point is reached, depends on the screw press geometry, the actual process parameters of the press as well as material parameters of the oilseed.

Our mode is based on the framework of the classical theory of extrudes [4], which was within this work extended to cover the necessary compressibility of the processed seeds. Based on the experimental analysis (not shown here), it may be accepted that relation between the oilseed density ρ and the pressure p is approximately linear, such that $\rho = \rho_0 + c\,p$. It is also necessary to distinguish the friction coefficient f_s for the screw-oilseed contact and the friction coefficient $f_b = f_b(\theta)$ for the barrel-oilseed contact. Moreover, since the barrel wall is anisotropic (the typical construction has long slits in axial direction), the second frictional coefficient depends on the angle θ given by the direction of the frictional force between the seeds and the barrel wall (see Fig. 1).

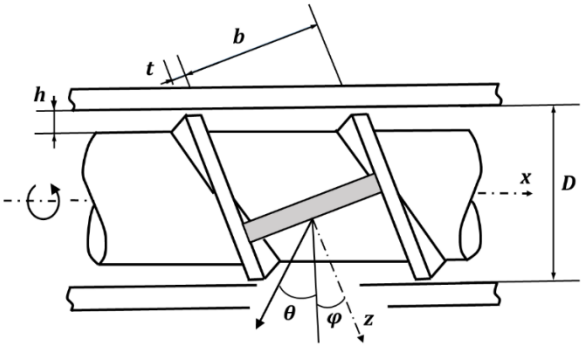

Fig. 1. Screw dimensions

A differential equation for the unknown distribution of pressure $p = p(z)$ along the axial channel coordinate z is derived from the volumetric flow of oilseed and by means of the force equilibrium at an oilseed volume element (see Fig. 1), such that

$$\frac{\mathrm{d}p}{\mathrm{d}z} = F(z,p)p\,.$$

The function F has the form

$$F(z,p) = \frac{1}{hb}\{f_b(\theta)b[\cos(\varphi+\theta) - f_s\sin(\varphi+\theta)] - f_s(2h+b)\},$$

where the angle θ is

$$\theta = \arctan\left(\frac{M}{(\rho_0 + c\,p)Q_{\max} - M}\tan\varphi\right)$$

and the maximum theoretical flow is given by

$$Q_{\max} = \pi NDh\tan\varphi\,(\pi(D-h) - t/\sin\varphi)\,.$$

Here N denotes the number of rotor revolutions per a unit of time and φ is the screw angle. M is the mass flow, which is constant in the first part of the screw press. Geometrical parameters h, b, φ may depend on the axial coordinate z.

Figure 2 presents results of a selected numerical simulation of an oil expelling expressing process in a real screw press for rape seeds. Authors designed the software tool OSLOC_V1 capable to monitor dozens of different quantities. The software, in comparison to finite element based methods, allows rapid analysis of the central quantities such as the pressure or the residual oil content along axial direction in relation to the screw press design parameters and oilseed properties. Authors also designed graphical user interface OSLO_GUI for an effective input of the model parameters and analysis of the results.

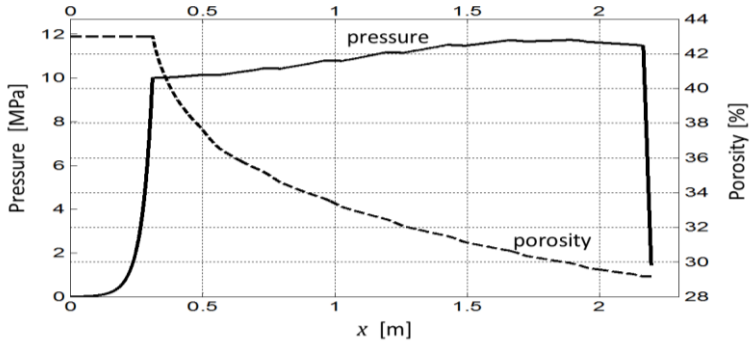

Fig. 2. Case study of the whole process in an actual continuous screw press for rape seeds – the pressure profile and the porosity as the function of the axial distance x

Acknowledgements

The work has been supported by the grant project of the Technology Agency of the Czech Republic number TA04010992.

References

[1] Vadke, V. S., Sosulski, F. W., Shook, C. A., Mathematical simulation of an oilseed press, JAOCS 65 (10) (1988) 1610-1616.

[2] Voldřich, J., OSLO_EXTRUDER - Oddělující šnekové lisování olejnin, Research report NTC-VYZ-12-076, NTC ZČU v Plzni, 2012. (in Czech)

[3] Voldřich, J., Očenášek, J., One-dimensional mathematical model of oil extraction process in a continuous screw press, Extended abstract of the 30th conference Computational Mechanics 2014, Špičák, 2014, pp. 3-5.

[4] Stevens, M. J., Covas, J. A., Extruder principles and operation, Chapman & Hall, London, 1985.

COMPUTATIONAL MECHANICS 2015
31st conference with international participation
Špičák
November 9 - 11, 2015

Computation of thermo-elastic characteristics of plates randomly reinforced with pellets using image processing methods and statistics

Z. Padovec [a], M. Růžička[a], M. Král [a], R. Sedláček [a], P. Růžička [a]

[a] *Faculty of Mechanical Engineering, Czech Technical University in Prague, Technická 4, 166 07 Prague, Czech Republic*

In previous work [2] an approach which leads to computation of thermo-elastic characteristics of randomly reinforced composite was suggested. In [3] a nondestructive experimental method for the estimation of isotropy/anisotropy based on image processing methods was presented (see Fig. 1).

Fig. 1. Image analysis of randomly reinforced plate

The result is histogram for the angle of pellets orientation for each analyzed plate (photography). Each histogram of the angle orientation is then used as an input for classic lamination theory (CLT) and computation of reduced stiffness matrix $\bar{\boldsymbol{Q}}_{ij}$ using Monte Carlo simulation technique. From these matrices $\bar{\boldsymbol{Q}}$ are then computed matrices $\boldsymbol{A}$ (membrane stiffness), $\boldsymbol{B}$ (bending – extension coupling stiffness) and $\boldsymbol{D}$ (bending stiffness) which are used for the computation of stiffness, Eq. (1), and compliance matrices, Eq. (2), for the whole composite

$$C_{ij} = \begin{bmatrix} A_{ij} & B_{ij} \\ B_{ij} & D_{ij} \end{bmatrix} = \begin{bmatrix} A_{11} & A_{12} & A_{16} & B_{11} & B_{12} & B_{16} \\ A_{12} & A_{22} & A_{26} & B_{12} & B_{22} & B_{26} \\ A_{16} & A_{26} & A_{66} & B_{16} & B_{26} & B_{66} \\ B_{11} & B_{12} & B_{16} & D_{11} & D_{12} & D_{16} \\ B_{12} & B_{22} & B_{26} & D_{21} & D_{22} & D_{26} \\ B_{16} & B_{26} & B_{66} & D_{16} & D_{26} & D_{66} \end{bmatrix}, \tag{1}$$

$$C_{ij}{}^{c} = C_{ij}{}^{-1} = \begin{bmatrix} a_{ij} & b_{ij} \\ b_{ij} & d_{ij} \end{bmatrix} = \begin{bmatrix} a_{11} & a_{12} & a_{16} & b_{11} & b_{12} & b_{16} \\ a_{12} & a_{22} & a_{26} & b_{12} & b_{22} & b_{26} \\ a_{16} & a_{26} & a_{66} & b_{16} & b_{26} & b_{66} \\ b_{11} & b_{12} & b_{16} & d_{11} & d_{12} & d_{16} \\ b_{12} & b_{22} & b_{26} & d_{21} & d_{22} & d_{26} \\ b_{16} & b_{26} & b_{66} & d_{16} & d_{26} & d_{66} \end{bmatrix}. \tag{2}$$

Effective elastic properties E_x, E_y, G_{xy} and ν_{xy}, which represent the stiffness of a fictitious, equivalent, orthotropic plate that behaves like the actual laminate under in-plane loads, can be

computed from the $C_{ij}{}^{c}$ matrix as [1]

$$E_x = \frac{1}{ta_{11}}, E_y = \frac{1}{ta_{22}}, G_{xy} = \frac{1}{ta_{66}}, \upsilon_{xy} = \frac{a_{12}}{a_{11}}, \tag{3}$$

where t is thickness of whole composite. Similarly we can assume coefficient of thermal expansion α_x, α_y and α_z or through thickness properties E_z, G_{xz}, G_{yz}, ν_{xz} and ν_{yz}.

27 Monte Carlo simulations were done (3 simulations for each of 9 analyzed photos) and first three from them can be seen in Table 1 with comparison of computation by CLT [2].

Table 1. Comparison of the results

	E_x [MPa]	E_y [MPa]	G_{xy} [MPa]	ν_{xy} [-]	α_x [$10^{-6}K^{-1}$]	α_y [$10^{-6}K^{-1}$]	α_z [$10^{-5}K^{-1}$]
CLT [1]	54 167	54 167	20 785	0,3014	1,84	1,84	3,48
MC_1_1_101	54 123	54 236	20 778	0,3025	1,8401	1,832	3,1453
MC _1_1_121	54 112	54 253	20 777	0,3024	1,834	1,8357	3,1455
MC _1_1_151	54 081	54 232	20 792	0,3027	1,8318	1,8403	3,1458
…	…	…	…	…	…	…	…

	E_z [MPa]	G_{xz} [MPa]	G_{yz} [MPa]	ν_{xz} [-]	ν_{yz} [-]
CLT [1]	15881,8	5454,95	5454,95	0,4471	0,4471
MC_1_1_101	16025	5454,8	5455,1	0,4473	0,4467
MC _1_1_121	16025	5454,9	5455	0,4471	0,4471
MC _1_1_151	16024	5455,2	5454,8	0,447	0,4477
…	…	…	…	…	…

From the results in table above we can assume that developed statistical approach based on image processing methods gives similar values of elastic properties as well as modified CLT [2] for investigated plates manufactured from pellets. This approach is useful for these materials to prove/disprove their isotropy or to detect predominant orientation of composite reinforcement (fibers, pellets, etc…) and computation of elastic properties according to given orientation.

Acknowledgements

This work has been supported by project TA03010209 of the Technological Agency of the Czech Republic and Grant Agency of the Czech Technical University in Prague, grant No. SGS15/188/OHK2/3T/12.

References

[1] Barbero, E. J., Introduction to composite materials design, Second edition, CRC Press, Boca Raton, 2011.
[2] Padovec, Z., Růžička, M., Sedláček, R., Thermo-elastic properties of randomly reinforced composite – A comparison of theories, Proceedings of the 29th conference with international participation Computational Mechanics 2013, Plzeň, Západočeská Univerzita, 2013, pp. 91 – 92.
[3] Padovec, Z., Sedláček, R., Růžička, M., Růžička, P., Chlup, H., Král, M., Stress and strength analysis of flat samples from pellets and their properties prediction, Research report, Praha, ČVUT v Praze, 2014.

COMPUTATIONAL MECHANICS 2015
31st conference with international participation
Špičák
November 9 - 11, 2015

An implicit discontinuous Galerkin scheme for a numerical solution of transonic flow problems

A. Pecka[a,b], O. Bublík[b], J. Vimmr[b]

[a] Department of Mechanics, Faculty of Applied Sciences, University of West Bohemia (UWB), Univerzitní 8, 306 14 Plzeň, Czech Republic
[b] NTIS – New Thechonologies for the Information Society, Faculty of Applied Sciences, UWB, Univerzitní 8, 306 14 Plzeň, Czech Republic

The discontinuous Galerkin finite element method (DGFEM) [2, 3, 4], which is designed for the spatial discretisation of partial differential equations, is still being extensively developed. The DGFEM has received a particular interest in fluid dynamics, where it tents to be thought of as a successor of the still most common method in the field—the finite volume method [5]. The DGFEM employs Galerkin's approach of expanding the solution as a linear combination of chosen basis functions to generalise the finite volume method for higher-order approximations. In contrast with the continuous Galerkin finite element method [3], the basis functions are allowed to be discontinuous on the edges of the grid cells. The DGFEM combines the advantages of both finite volume and finite element methods, namely conservativity, robustness and arbitrary order of accuracy. The drawbacks of the DGFEM are higher memory and computational requirements as well as its implementational and theoretical complexity.

When applying an explicit schemes for the temporal discretisation, i.e. the Runge-Kutta methods [1, 2], the time step is limited by the CFL condition, a necessary criterion for stability. For higher-order polynomials as basis functions, the CFL condition becomes even more restrictive. Thus, it is convenient to use one of the implicit schemes, which have much larger region of stability. The improvement is evident especially for the steady-state problems, in which case we are not interested in the time evolution of the solution, which can be distorted by taking large time steps. For this reason, the main objective of this work is to implement an implicit scheme for transonic flow problems, although this is a more complicated endeavour than to implement an explicit scheme.

We present a combination of the DGFEM and the backward Euler method as a tool for modelling a compressible adiabatic and inviscid flow in two dimensions. Firstly, we discretise the Euler equations by the DGFEM, thereby producing a set of time-dependent ordinary differential equations, which we consequently discretised by the backward Euler method. The resulting linear system needs to be solved by an appropriate sparse-matrix solver. We have implemented the above in the C++ programming language.

We validate the developed implicit DGFEM solver on the GAMM channel. The GAMM channel has become a classical benchmark for testing performance of compressible transonic inviscid flow solvers, as the data produced by various experiments are available. The test problem has a rectangular domain with a cut out circle at the bottom. The left face of the rectangle is the inlet with the stagnation pressure $p_{in} = 1$, stagnation density $\rho_{in} = 1$ and inlet angle $\alpha = 0$. The right-hand side face is the outlet with the static pressure $p_{out} = 0.737$. The rest of the boundary is a solid and impermeable wall. The steady-state solution of the implicit DGFEM solver is shown in Fig. 1 and Fig. 2. This particular computation is second-order accurate in

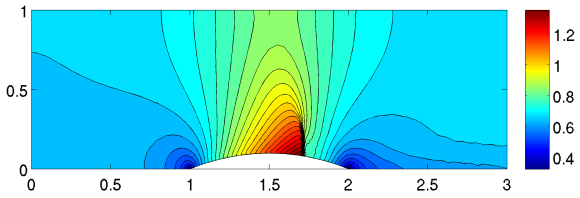

Fig. 1. GAMM channel – Mach contours

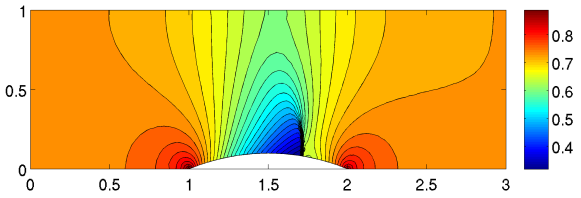

Fig. 2. GAMM channel – pressure contours

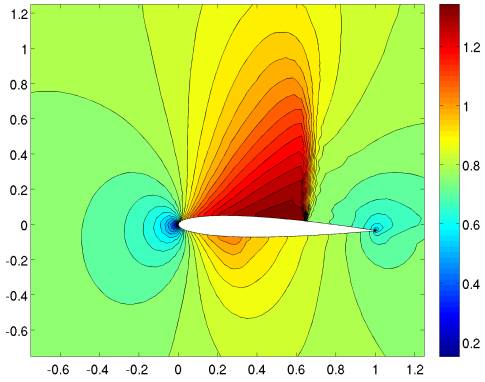

Fig. 3. NACA 0012 – Mach contours

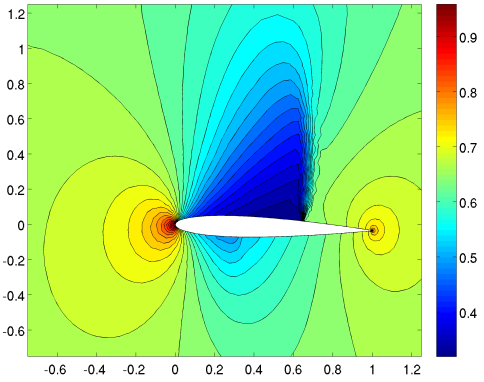

Fig. 4. NACA 0012 – pressure contours

space. In the region above the cut out circle, there is a shock wave, where the exact solution is discontinuous. This region needs to be artificially damped, otherwise it would start to oscillate.

Let us look at another test problem—a transonic and inviscid flow around the NACA aerofoil, which have been used for a number of airplane wings. We preformed the simulation for the NACA 0012 airfoil with the angle of attack $\alpha = 2^\circ$ and the Mach number of the undisturbed flow $M = 0.8$. The steady-state results are shown in Fig. 3 and Fig. 4.

The discontinuous Galerkin method gives us a way of obtaining an arbitrary order of accuracy in space which, along with an appropriate implicit scheme, is an effective tool for solving transonic flow boundary-value problems.

Acknowledgements

This work was supported by the project LO1506 of the Czech Ministry of Education Youth and Sports and by the student grant project SGS-2013-036 of the University of West Bohemia.

References

[1] Cockburn, B., Shu, C.W., Runge-Kutta discontinuous Galerkin methods for convection dominated problems, Journal of Scientific Computing 16 (2001) 173-261.

[2] Cockburn, B., Shu, C.W., TVB Runge-Kutta local projection discontinuous Galerkin finite element method for conservation laws II: General framework, Mathematics of Computation 52 (1989) 411-435.

[3] Feistauer, M., Felcman, J., Straškraba, I., Mathematical and computational methods for compressible flow, Oxford University Press, 2003.

[4] Feistauer, M., Kučera, V., Prokopová, J., Discontinuous Galerkin solution of compressible flow in time-dependent domains, Mathematics and Computers in Simulation 80 (8) (2010) 1612-1623.

[5] Ferziger, J., Peric, M., Computational methods for fluid dynamics, Springer-Verlag, Berlin, 2001.

COMPUTATIONAL MECHANICS 2015
31st conference with international participation
Špičák
November 9 - 11, 2015

Parametric oscillations of the coolant in PWR primary circuit

L. Pečínka [a], M. Švrček [a]

[a] ÚJV Řež a. s., Hlavní 130, 250 68 Husince – Řež, Czech Republic

Exciting forces in PWR volant are of mechanical origin, acoustical origin and from turbulent flow. Theory the parametric oscillations is based on the electromechanical analogy. The capacitance C of the fluid flow is calculated from the equation

$$C = \frac{PD^2L}{4\rho c^2} = \frac{V}{\rho c^2}\,. \tag{1}$$

The speed of sound c is calculated using Gibbs function g (p,t) which depend on the coolant pressure and temperature. Since we are interested in the field of pressure oscillations, equation (1) may be rewritten in the form

$$C = k\frac{V}{p} \quad => \quad C = k_1 * \frac{1}{p}\,, \qquad \frac{\Delta P}{P} = -\frac{\Delta C}{C} \tag{2}$$

and we will suppose that the pressure pulsations of coolant takes the form

$$P = P_0 + \Delta P \sin \omega t\,, \qquad \frac{\Delta P}{P_0} = m\,. \tag{3}$$

Further we will suppose that the amplitude of the flow rate W_v is determined as

$$W_v = \bar{\omega}_r V \tag{4}$$

and if the primary circuit has the acoustic resistance r, than the following equation is valid

$$\Delta P = W_v r\,. \tag{5}$$

Using equations (2) and (3) may be proved that

$$\frac{\cos \omega t}{P_0} = C_0 \tag{6}$$

and using equation (3) as the result we obtain

$$c(t) = \frac{C_0}{1+m \sin \omega t}\,. \tag{7}$$

After application of Newton polynomial to equation (7) one can to write

$$\frac{c(t)}{C_0} = (1 + m \sin \omega t)^{-1} =$$
$$= 1 + \frac{1}{2}m^2 - m\left(1 + \frac{3}{4}m^2\right)\sin \omega t - \frac{1}{2}m^2 \cos 2\omega t + \frac{1}{4}m^2 \sin 3\omega t + \cdots\,. \tag{8}$$

Neglecting higher harmonics, equation (8) can be rewritten in the form (for $m << 1$)

$$-c(t) = \bar{C}_0 - C_1 \sin \omega t\,, \tag{9}$$

where

$$\overline{C_0} = C_0\left(1 + \frac{1}{2}m^2\right) \cong C_0 \quad \text{and} \quad C_1 = C_0 m\left(1 + \frac{3}{4}m^2\right) \cong C_0 m\,.$$

From equation (9) we can obtain

$$\frac{1}{C(t)} = \frac{1}{C_0 - C_1 \sin \omega t} = \frac{1}{C_0(1 - m \sin \omega t)}\,, \qquad m = \frac{C_1}{C_0} \ll 1\,. \tag{10}$$

After simply rearrangement we can written

$$\frac{1}{c(t)} = \frac{1}{C_0}(1 + m \sin \omega t)\,. \tag{11}$$

Using equations (2) and (4) the following relation can be derived

$$P = k\frac{W_{vr}}{C\bar{\omega}_r}, \qquad \Delta P = -\Delta C \frac{W_{vr}}{\bar{\omega}_r C_1^2} k\,. \tag{12}$$

Using equations (9) and (10) we can obtain

$$\Delta C = C_0 m \cos \bar{\omega}_r t = C_1 \cos \bar{\omega}_r t \quad \text{and} \quad \Delta p|t| = -\frac{W_{vr}}{\bar{\omega}_r C_1 k_2} \cos \bar{\omega}_r t\,. \tag{13}$$

Since $C_1 = \frac{C_0}{m \sin \bar{\omega}_r t}$ than equation (13) can be rewritten in the form

$$\Delta p(t) = -\frac{W_{vr}}{\bar{\omega}_r C_0 k_2}\, m \sin \bar{\omega}_r t \cos \bar{\omega}_r t = -\frac{W_{vr}}{2\bar{\omega}_r C_0 k_2}\, m \sin 2\bar{\omega}_r t\,. \tag{14}$$

Since the coolant system has an acoustical resistance r which is related to component frequency $\bar{\omega}_r$ then additive part of coolant flow rate using equation (5) is given as

$$\Delta W_r = -\frac{W_v}{2\bar{\omega}_r C_0 r k_2} m \sin 2\bar{\omega}_r t\,. \tag{15}$$

Additive part of pressure drop due to ΔW_r is given as

$$\Delta p_m = \Delta W_r r = -\frac{W_{vr} m}{2\bar{\omega}_r C_0 k_2}\,. \tag{16}$$

Additive acoustical active resistance r_ related to existence Δp_m can be calculated as

$$r_- = \frac{\Delta p_m}{W_{vr}} = \frac{m}{2}\frac{1}{\bar{\omega}_r C_0 k_2}\,. \tag{17}$$

From previous theory the following can be conclude

- due to the fact that the additive resistance is negative as a result the flow rate W increase,
- the capacitance oscillate with eigenfrequencies of coolant,
- increasing of the modulation factor m result in increasing of r_,
- from equation (17) the critical value of m_{crit} can be derived as

$$\frac{m}{k_2} = m_{crit} = 2\bar{\omega}_r C_o r = 2/Q = 2\delta,$$

where δ is the coefficient of resistance and Q is the quality factor [1].

References:

[1] Pečínka, L., Švrček M., Acoustic frequencies of coolant in primary circuit of NPP Temelín and possibility of resonances with fuel assembly TVSA-T, Engineering Mechanics 2014, Svratka, TU Brno, 2014.

COMPUTATIONAL MECHANICS 2015
31st conference with international participation
Špičák
November 9 - 11, 2015

Microphone arrays and their algorithms - short review

L. Phamová [a]

[a] *Faculty of Mechanical Engineering, CTU in Prague, Technická 4, 166 07 Praha, Czech Republic*

The microphone arrays are used for a localization of sound sources. Many types of arrays exist and so computational algorithms. The article gives short overview of the array types and algorithms and practical example of measurements.

The simplest microphone array is a linear array [2]. This is widely used in laptops or is integrated in computer monitors. The number of microphone is typically two or four. Circular microphone arrays are used in conference room table. These arrays have typically six or eight microphones. They have up to 16 microphones which are placed in concentric circles. Planar arrays are used mostly in industry. They have up to 128 microphones spread in one plane by different ways. The simplest arrangement is that microphones are regularly apart in both directions or microphones form a circle. Microphones pattern can be also irregular square or circle, star, one-spiral and more-spiral. Volumetric arrays have a sphere form. They capture sound source of any direction. Special arrays are used as hearing-aid devices.

The algorithm *Delay-and-Sum Beamformer* (DAS) is the simplest and the fastest of all recently used algorithms [1]. Each microphone signal is delayed and after that all signal are summed. Point or points with the highest power is or are the assumed sound source. The algorithm is suitable for far-field measurement.

The basic idea of the algorithm *Multiple signal classification* (MUSIC) is to divide vector space into two perpendicular spaces – signal space and noise space. MUSIC finds sources via angle maximum between noise space and model of source or via angle minimum between signal space and model of source. This algorithm is used for far-field measurement.

The algorithm Minimum Variance Distorionless Response (MVDR) Beamformer is also known under the name *Capon*. Unlike DAS Beamformer Capon calculates Gain in each computational step and adjusts it according to microphone array geometry and input signals. Contrary to DAS, Capon suppresses significantly more noise.

Near-field Acoustic Holography and *Statistically Optimal Near-field Acoustic Holography* (NAH and SONAH) are both used for near-field measurement. NAH pictured three-dimensional acoustic field from measured two-dimensional hologram scanned above measured source surface. SONAH significantly restricts one of the disadvantage of NAH.

For measurements were used array with 32 microphones “randomly” placed in 800x800mm frame. Microphones are ¼”, omnidirectional with the sensitivity of 30 mV/Pa.

The first described measurement was realized in diffuse acoustic field. Sound sources were two closely located speakers in laptop. The measurement was performed in an office. The different algorithms were used and results were compared, see Fig. 1.

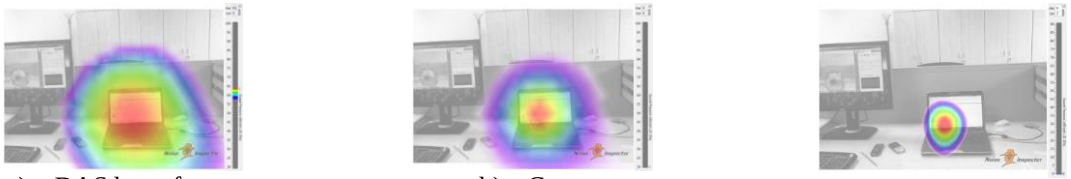

a) DAS beamformer b) Capon c) MUSIC

Fig. 1. Results for two closely located speakers in diffuse field, f 900 Hz

The second measurement was performed under the free field condition. The sound source was moving car. The DAS Beamformer was used. The results for different moments and different frequencies were compared, see Fig. 2 - 3.

a) 9,00-9,25 s b) 9,25-9,50 s c) 9,50-9,75 s

Fig. 2. Results for different moments, f = 800 Hz

a) 9,00-9,25 s b) 9,25-9,50 s c) 9,50-9,75 s

Fig. 3. Results for different moments, f = 2 000 Hz

The third measurement was done again in the free field. The sound source was stationary and very small. It was small loudspeaker. The evaluation was done for different algorithms, see Fig. 4.

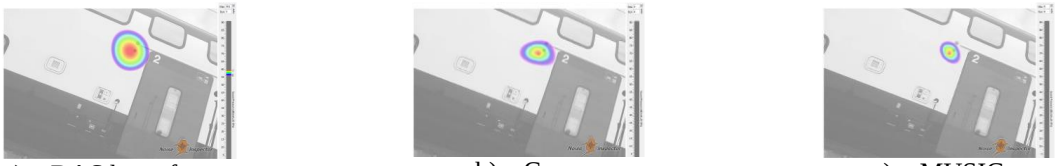

a) DAS beamformer b) Capon c) MUSIC

Fig. 4. Results for small loudspeaker

The measurements under different conditions were performed. For evaluation, different algorithms were used and results were compared.

Acknowledgements

The work has been supported by the grant project Josef Bozek Competence Centre for Automotive, TE01020020.

References

[1] Bai, M., Ih, J.-G., Benesty, J., Acoustic array systems: theory, implementation, and application, John Wiley & Sons, Singapore, 2013.

[2] Tashev, I. J., Sound capture and processing: practical approaches, Wiley, Chichester, 2009.

COMPUTATIONAL MECHANICS 2015
31st conference with international participation
Špičák
November 9 - 11, 2015

Convective flux schemes for numerical solution of two-phase flows

S. Plánička [a], J. Vimmr [a]

[a] *NTIS - New Technologies for the Information Society, Faculty of Applied Sciences, UWB, Univerzitní 8, 306 14 Plzeň, Czech Republic*

The main objective of this paper is the comparison of several numerical schemes for calculation of the convective numerical flux used in two-phase flow modeling and its impact on the quality of obtained numerical results. This text is aimed at the dispersed two-phase flow modeling of immiscible compressible fluids. The averaged Eulerian two fluid model with one pressure field is discussed. The flow is assumed to be inviscid without any interphase interaction. The approach is widely used in petroleum and nuclear industry. The in-house computational software written in Matlab was developed for the solution of the considered aforementioned two-phase flow problem. This software is based on the finite volume method. Only first order accuracy schemes for convective numerical flux are used to overcome nonlinearity of two-phase models. The developed numerical code was validated for the water faucet problem proposed by Ransom [2], which is frequently considered as a standard benchmark in these flow problems.

The mathematical model considered in this paper is based on the common two fluid model expressed by two separated flow equations belonging to the class of Eulerian models. The flow problem is one-dimensional and it can describe, for example, pipe flow of gas and liquid mixture very well. The two fluid model is assembled from the continuity and momentum equations for the first phase (denoted here as gas - *G*) and the second phase (liquid - *L*). The composed vector of conservative variables is expressed as

$$W = [\alpha_G \rho_G \, , \alpha_L \rho_L \, , \alpha_G \rho_G v_G \, , \alpha_L \rho_L v_L]^T, \tag{1}$$

where α is volume fraction of phase, ρ is density and v denotes velocity component. Naturally, the validity of the equation for the volume fractions of gas and liquid components must be ensured

$$\alpha_G + \alpha_L = 1. \tag{2}$$

The suggested model uses only one pressure field supplemented by an algebraic equation of the interface pressure correction. The above described system is closed by two equations of state for the gas and liquid phases. Both equations of state are in a similar simple algebraic form and they correspond to a well compressible gas and a poorly compressible liquid.

The mathematical model mentioned above can be written in one dimension as

$$\frac{\partial W}{\partial t} + \frac{\partial F_W}{\partial x} + (p - p_{corr}^{INT}) \frac{\partial A}{\partial x} + A \frac{\partial p}{\partial x} = A \, S_{ource} \, , \tag{3}$$

where the flux term was split into convective and pressure parts. The finite volume method was used for the spatial discretization of Eq. (3).

The convective numerical flux was approximated by the various suitable first order schemes in order to damp instabilities, which can occur by using two-phase flow models. A simple central space scheme was used for the third term in Eq. (3) with interface pressure correction. The fourth term of Eq. (3) was approximated by the Lax-Friedrichs type of scheme, as it is similarly done in [1]. Moreover, it is necessary to deal with the pressure field, description of

which is derived by substituting both equations of state into Eq. (2) – the sum of volume fractions. In our specific case, this leads to a second order polynomial, which is solved by the simple iterative method.

The developed numerical code was tested on the water faucet benchmark. This problem should essentially describe the shape change of water flow from faucet due to gravity. The shape is represented by the liquid volume fraction, which is equivalent to the relative cross-section area of water. The 1D computational domain is formed by a 12 meters high vertical pipe. Four uniform computational grids with different number of cells were used for the numerical solution of this problem. The inlet boundary condition is equal to the initial condition ($\alpha_L = 0{,}8$; $v_L = 10$ *m/s*; $v_G = 0$ *m/s*; $p = 10^5$ *Pa*) in the whole computational domain. Gravity ($g = 9{,}81$ *m/s*^{2}) was included in our model as a source term on the right-hand side of Eq. (3).

This test case was solved by the in-house code, where various numerical schemes for the convective flux (Harten-Lax-van Leer, central, upwind, hybrid central-upwind and composed upwind-central) have been used on grids with different number of cells.

First, the volume fraction of gas was observed and compared with known analytical solution. This was done for two different states – the first one captures the volume fraction shock change at time $T = 0{,}6$ *s* due to ongoing initial condition, the second one shows developed steady shape of water stream. Comparisons of numerical results from different schemes on the finest mesh are shown in Fig.1 for the volume fraction shock change and in Fig.2 for the developed shape.

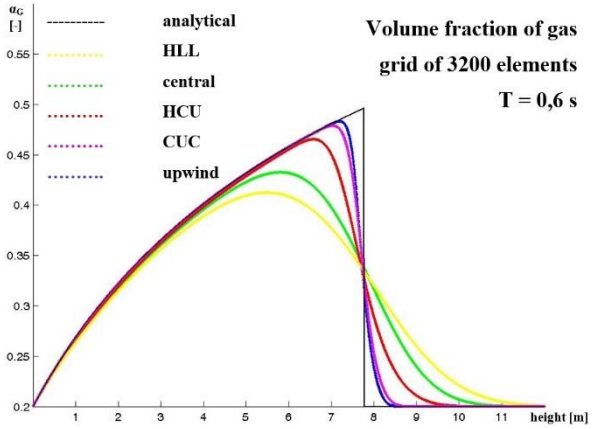

Fig. 1. Dependence of volume fraction of gas on height of the pipe at the time $T = 0{,}6$ *s*

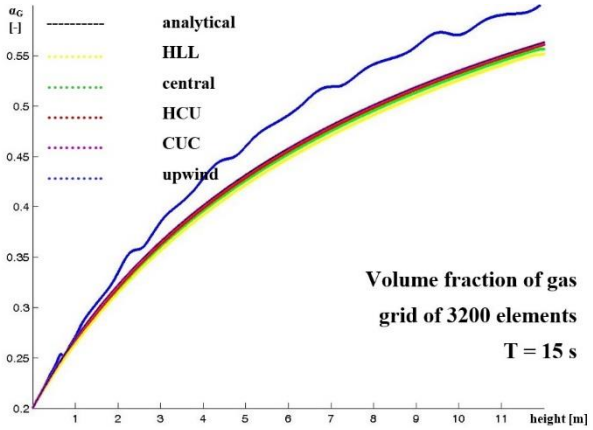

Fig. 2. Dependence of volume fraction of gas on height of the pipe at the time $T = 15$ *s*

Obtained numerical results demonstrate the suitability of chosen method for solving this mathematical model. Steady state results of numerical simulations are in very good agreement with the shape of a developed water stream. The disadvantage of the presented numerical approach is the artificial viscosity of all the tested schemes, which blunts sharpness of shock changes. Although the upwind scheme is able to capture the shock change the best, not all numerical oscillations of the solution are sufficiently damped.

Acknowledgements

This work was supported by the project TA03010990 of the Technology Agency of the Czech Republic and by the project LO1506 of the Czech Ministry of Education, Youth and Sports.

References

[1] Evje, S., Flåtten, T., Hybrid central-upwind schemes for numerical resolution of two-phase flows, ESAIM: Mathematical Modelling and Numerical Analysis 39 (2005) 253-273.

[2] Ransom, V.H., Numerical benchmark test: faucet flow, Multiphase Science and Technology 3 (1987) 465-467.

COMPUTATIONAL MECHANICS 2015
31st conference with international participation
Špičák
November 9 - 11, 2015

A simple method of assessing residual stress distribution in PE pipes

J. Poduška [a,b], P. Hutař [a], J. Kučera [c], J. Sadílek [c], L. Náhlík [a]

[a] Institute of Physics of Materials, Academy of Sciences of the Czech Republic, Žižkova 22, 61662 Brno, Czech Republic
[b] Brno University of Technology, Faculty of Mechanical Engineering, Technická 2896/2, 61669 Brno, Czech Republic
[c] Polymer Institute Brno, Tkalcovská 36/2, 656 49 Brno, Czech Republic

Residual stress in polymer pipes is a result of the cooling phase in the manufacture process of pipe products (Fig. 1). Since the wall of the pipe cools down unevenly after the extrusion, circumferential and axial residual stresses originate in the pipe wall. The significance of residual stress lies in its characteristic distribution and magnitude and its influence on pipe's lifetime. Typically, the distribution has a shape of an exponential line. There are tensile stresses on the inner surface of the pipe with a magnitude of approximately *1.5* MPa and on the outer surface there are compressive stresses with a magnitude of *–4* MPa (Fig. 1), [2, 3].

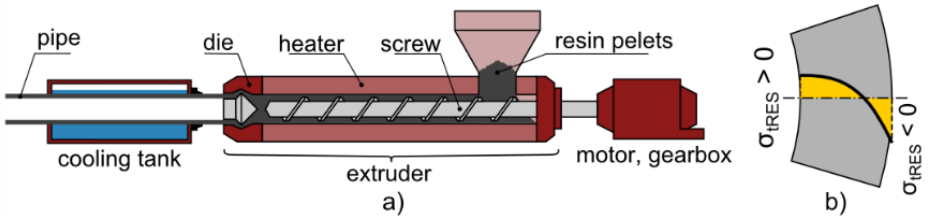

Fig. 1. Scheme of the pipe manufacture process (a) and a characteristic distribution of residual hoop stress (b)

Lifetime of polyethylene pressure pipes is determined by the time that it takes a crack to grow radially through the pipe wall. This process is influenced by many factors, especially by internal and external pressure, initial crack size and also by residual stress. The tensile part of residual hoop stress distribution in the pipe wall increases the total level of hoop stress that makes the crack grow, [2].

It is not necessary to know the exact residual hoop stress distribution and magnitude for lifetime estimation, if the estimation is done by a classic hydrostatic pressure test, as the pipes in these tests remain intact. However, a better and faster way to estimate the lifetime of modern pipe materials is to measure the crack growth rate in the material (using specially made specimens) and calculate the lifetime, using the approach of linear elastic fracture mechanics. The effect of residual stress has to be added to the calculation, [1].

The experimental method for the estimation of the residual hoop stress distribution is based on measuring the deflection of rings that were cut off of the pipe and then slit in the axial direction [5]. The authors of this contribution carried out this experiment on a set of pipes made of polypropylene. The results of this research and the description of the experiment can be found in [4]. The article features a general equation that describes the residual hoop stress distribution in polypropylene and provides a certain estimation of the distribution without the need to carry out an experiment. It has a form $\sigma_{tRES}(x) = c_1 - c_2 \cdot e^{3.2x}$, where σ_{tRES} is the residual hoop stress, x is a relative position in the pipe wall and c_1 and c_2 are constants specific for given pipe and material. For polypropylene pipes $c_1 = 1.559$ and $c_2 = -0.212$.

The same experiment was carried out on a polyethylene pipe 160/4.7 (nominal outside diameter/wall thickness) and the results were similar.

The experimental methods for determining the residual hoop stress needed a quite large amount of specimens – thirteen specimens for every pipe. The amount of specimens can be reduced. If the general equation form is used, it is possible to calculate a more precise estimation of residual hoop stress distribution from one specimen either. From the measured deflection of one ring the total bending moment acting on the ring can be calculated. If we divide the wall into a certain number of discrete layers, then the total bending moment has to be the sum of partial bending moments caused by constant stress in these layers. This gives an equation, where the only two unknown values are the constants of the exponential equation that describes the stress values: $M_t = \sum_{i=1}^{10} (c_1 + c_2 e^{3.2 \cdot i \cdot 0.1}) \cdot t \cdot w \cdot (R - r_i)$, where M_t is the total bending moment, t is the thickness of the layer, w is the axial thickness of the specimen, R is the neutral surface radius and r_i is the position of the layer. To solve this problem, the condition of balance has to be added as the second equation. The comparison of results produced by the simplified method and the more precise method using 13 rings is in Fig. 2.

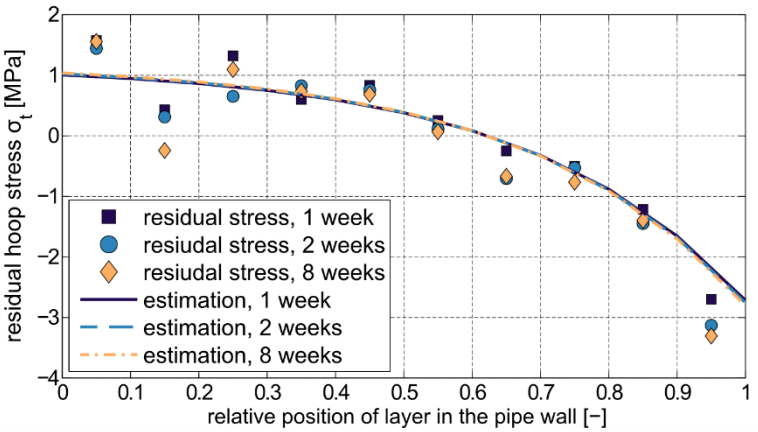

Fig. 2. Comparison of the simplified method and precise results for the PE pipe 160/4.7

The described simplified method of estimating the residual hoop stress distribution makes it possible to reduce the number of specimen needed for the estimation and also revisit and recalculate older results that were calculated with the assumption of linear residual hoop stress distribution.

Acknowledgements

The work was supported through the specific academic research Grant No. FSI-S-14-2311 provided to Brno University of Technology, Faculty of Mechanical Engineering.

References

[1] Hutar, P., Sevcik, M., Frank, A., Nahlik, L., Kucera, J., Pinter, G., The effect of residual stress on polymer pipe lifetime, Engineering Fracture Mechanics 108 (2013) 98-108.
[2] Hutar, P., Sevcik, M., Nahlik, L., Pinter, G., Frank, A., Mitev, I., A numerical methodology for lifetime estimation of HDPE pressure pipes, Engineering Fracture Mechanics 78 (17) (2011) 3049-3058.
[3] Janson, L. E., Plastics pipes for water supply and sewage disposal: 3rd edition, Borealis, Stockholm, 1999.
[4] Poduska, J., Kucera, J., Hutar, P., Sevcik, M., Krivanek, J., Sadilek, J., Nahlik, L., Residual stress distribution in extruded polypropylene pipes, Polymer Testing 40 (2014) 88-98.
[5] Williams, J. G., Hodgkinson, J. M., Gray, A., The determination of residual stresses in plastic pipe and their role in fracture, Polymer Engineering and Science 21 (13) (1981) 822-828.

COMPUTATIONAL MECHANICS 2015
31st conference with international participation
Špičák
November 9 - 11, 2015

Influence of mean stress on residual fatigue lifetime of railway axles

P. Pokorný [a,b], L. Náhlík [a], P. Hutař [a]

[a] Institute of Physics of Materials of the Academy of Sciences of the Czech Republic, Žižkova 22, 616 62 Brno, Czech Republic
[b] Faculty of Mechanical Engineering, Brno University of Technology, Technická 2, 616 69 Brno, Czech Republic

Still the non-destructive testing methods have their limits [1] and presence of small, but even dangerous defects in railway axles could not be excluded. The cyclic loading and potential defect could lead to an initiation of fatigue crack with consequent fatigue crack growth and fatigue failure. For safe operation of trains it is necessary to remove railway axle from service before fatigue crack reaches its critical size (to avoid fatigue failure). Axles are subjected to regular inspections. Nowadays, the frequency of regular inspection intervals could be determined from the residual fatigue lifetime, which could be estimated from numerical calculations. These calculations count number of load cycles necessary for fatigue crack growth from the initial crack size (detectable size of a crack by non-destructive testing methods) to the critical crack size, which leads to consequent fatigue failure. For conservative estimation of residual fatigue lifetime of railway axle, the fatigue crack is assumed at the most severe loaded place. Such place is often at the notch close to press-fitted wheel, see Fig. 1.

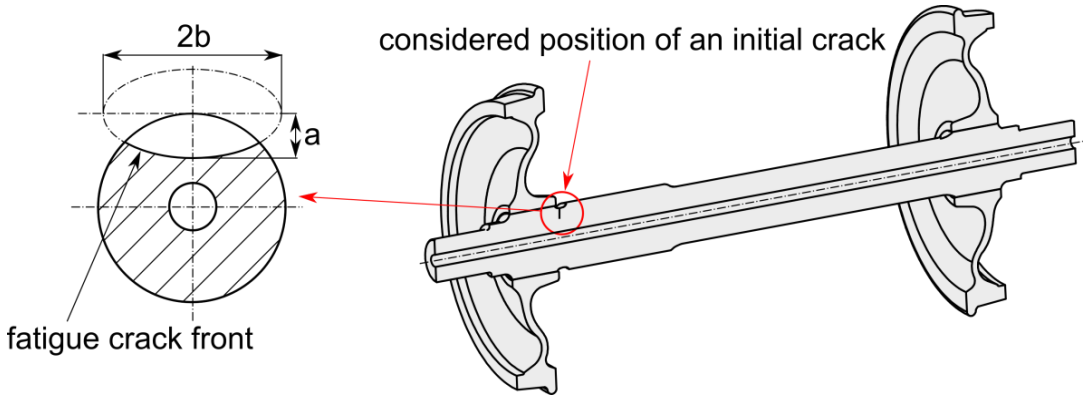

Fig. 1. The scheme of railway axle with highlighted position of the fatigue crack with the shortest lifetime

One of the parameters influencing fatigue crack propagation is mean stress, usually described by stress ratio R. The rotary bending leads to stress ratio R = -1. However, in the case of fatigue crack situated close to press-fitted wheel, the stress ratio is higher [2]. This fact is caused by positive longitudinal stresses (caused by press-fit) at location of considered fatigue crack. The Fig. 2 shows K-calibration functions for loading by weight of train (causes dominant bending loading) and by pure press-fit loading.

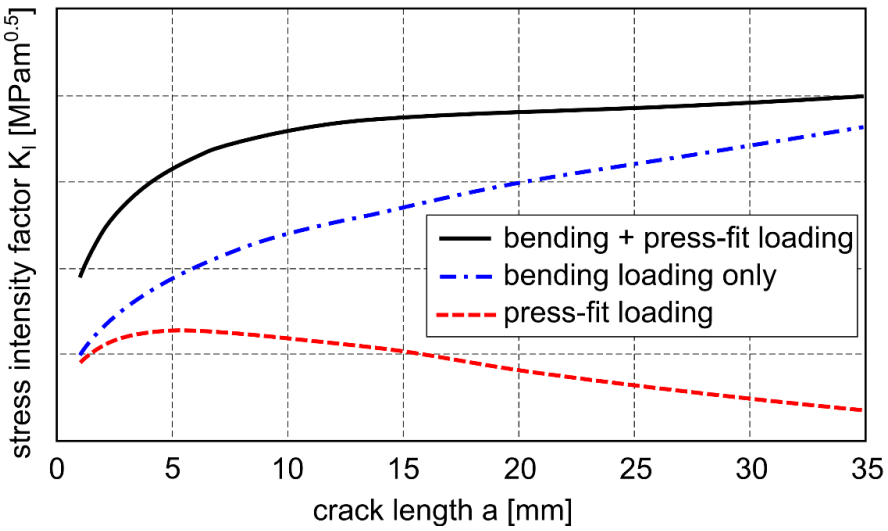

Fig. 2. Evolution of stress intensity factors in dependence on the crack length. The total stress intensity factor is separated into load by weight of the train (pure bending) and load caused by press-fit

The bending part of stress intensity factor in Fig. 2 is determined just for basic level of loading (load by weight of train). Nevertheless, due to different regimes of train operation, the load amplitude is variable. The stress ratio of *i-th* load cycle R_i is given by:

$$R_i = \frac{(K_{I,press-fit,i}(a) - n_i.K_{I,bending}(a))}{(K_{I,press-fit,i}(a) + n_i.K_{I,bending}(a))}, \quad (1)$$

where $K_{I,press-fit,I}(a)$ is stress intensity factor caused by press-fitted wheel in *i-th* cycle, n_i is multiple describing dynamic effect of *i-th* cycle (taken from the load spectrum) and $K_{I,bending}(a)$ is stress intensity factor caused by weight of the train.

From relationship 2 follows that the stress ratio is various in each cycle in general. Nevertheless, it could be declared that the stress ratio is set into interval $R = -1$ and $R = 0$. The procedure used for residual lifetime estimation takes into account *v-K* curves (dependency between stress intensity factor and fatigue crack propagation rate) determined for stress ratios -1, -0.5 and 0.1. The fatigue crack increment in each cycle is determined by interpolation of measured *v-K* curves for acting stress ratios. This procedure leads to more accurate results in comparison with results obtained by classical conservative approaches.

Acknowledgements

This work was supported through the specific academic research grant No. FSI-S-14-2311 provided to Brno University of Technology, Faculty of Mechanical Engineering and grant No. CZ.1.07/2.3.00/20.0214 of the Ministry of Education, Youth and Sports of the Czech Republic.

References

[1] Benyon, J. A, Watson, A. S., The use of Monte-Carlo analysis to increase axle inspection interval, Proceedings of the 13th International Wheelset Congress, Rome, Italy, 2001.

[2] Zerbst, U., Beretta, S., Kohler, G., Lawton, A., Vormwald, M., Beier, H. Th., Klinger, C., Cerny, I., Rudlin, J., Heckel, T., Klingbeil, D., Safe life and damage tolerance aspects of railway axles – A review, Engineering Fracture Mechanics 98 (2013) 214-271.

COMPUTATIONAL MECHANICS 2015
31st conference with international participation
Špičák
November 9 - 11, 2015

Alternative modelling of cables of varying length

P. Polach [a], M. Byrtus [a], J. Dupal [a], M. Hajžman [a], Z. Šika [b]

[a] *New Technologies for the Information Society, European Centre of Excellence, Faculty of Applied Sciences, University of West Bohemia, Univerzitní 8, 306 14 Plzeň, Czech Republic*
[b] *Department of Mechanics, Biomechanics and Mechatronics, Faculty of Mechanical Engineering, Czech Technical University in Prague, Technická 4, 166 07 Praha, Czech Republic*

The paper deals with an alternative description of modelling cables of varying length, which are suitable for involving in dynamics of fibre mechanisms. It is the authors' first introductory paper about this topic. The motivation is the development of a cable model, which could be efficient for the usage in a mechatronic model of a manipulator consisting of cables and an end-effector whose motion is driven by cables – particularly for the usage in the model of QuadroSphere (see Fig. 1) [1]. QuadroSphere is a tilting mechanism with a spherical motion of a platform and an accurate measurement of its position. The platform position is controlled by four fibres; each fibre is guided by a pulley from linear guidance to the platform. The numerical model of QuadroSphere will serve for the investigation of different possible strategies of the control of this active structure superimposed to the end-effector of the cable-driven mechanism in order to improve the end-effector positioning accuracy and the operational speed.

Fig. 1. The QuadroSphere tilting mechanism – central spherical joint with sensors

The fibre and cable modelling should be based on considering the fibre flexibility and the suitable approaches can be based on the flexible multibody dynamics (see e.g. [2]). The branch of the flexible multibody dynamics is a rapidly growing area of computational mechanics and many industrial applications can be solved using newly proposed flexible multibody dynamics approaches. Studied problems are characterized by the general large motion of interconnected rigid and flexible bodies with the possible presence of various non-linear forces and torques. There are many approaches to the modelling of flexible bodies in the framework of multibody systems [3]. Details of multibody formalisms and means of the creation of equations of motion can be found e.g. in [4].

Three different approaches to the cable modelling are considered. The first one is based on the fact that spatial discretization of cables and spatial derivatives of cable lengths are performed by means of difference method using absolute displacement coordinates [5]. The other two approaches use the point-mass discretization where the cable mass is replaced by a

finite number of point masses and the cable stiffness is modelled by discrete springs of corresponding stiffness. The first of the later models is derived in absolute coordinate system and. It is created in MATLAB as well as the above mentioned model. The second one is derived in relative coordinate system and the testing model is created by means of the **alaska** commercial software. All the models are created under assumption that each point of discretization has two degrees of freedom – displacement in horizontal a vertical axes. For this reason the whole model is represented by the system of time dependent non-linear ordinary differential equations.

The all mentioned modelling approaches are tested on the selected simple system and the results are compared. A cable stretched between two rigid points was chosen as a simple model (see Fig. 2), whose parameters are: cross-section area = $1 \cdot 10^{-6}$ m^2, Young's modulus = $2.1 \cdot 10^{11}$ Pa and linear mass density = 1 kg/m. The cable is discretized into 10 segments, i.e. 9 discrete points. The case of non-prestressed cable was simulated, its free length was equal to the distance between supporting points. The cable is loaded by its own weight, which causes its vibration. Equilibrium position is given by the steady-state solution and its shape is a flexible catenary. All the mentioned models give a good agreement of the results (see Fig. 2).

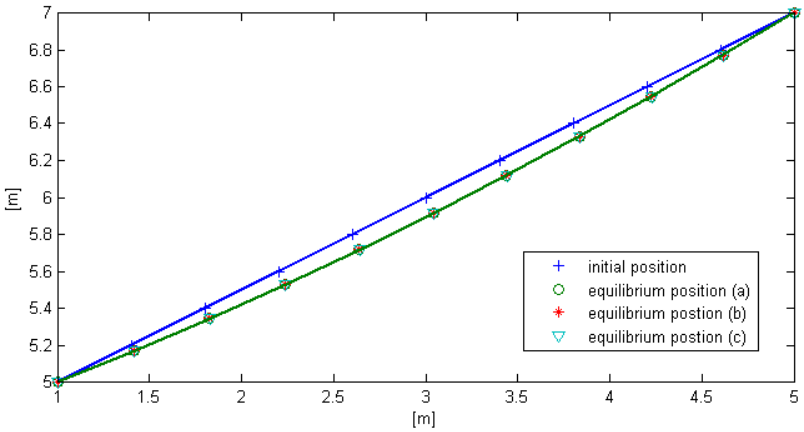

Fig. 2. Comparison of equilibrium position of non-prestressed cable gained by different approaches: (a) continuous model spatially discretized by difference method in absolute coordinate system, (b) point-mass model in absolute coordinate system, (c) multibody model in relative coordinate system created in the **alaska** simulation tool

Development of the approaches to modelling of cables of length varying in time continues. Next step will be simulations with a model consisting at least of two cables and an end-effector.

Acknowledgements

The paper has originated in the framework of solving No. 15-20134S project of the Czech Science Foundation entitled "Multi-level Light Mechanisms with Active Structures".

References

[1] Svatoš, P., Šika, Z., Zicha, J., Valášek, M., Rada, V., Optimization and design of fibre-driven spherical mechanism, Proceedings of Extended Abstract of 29th conference with international participation Computational Mechanics 2013, Špičák, University of West Bohemia, 2013. (CD-ROM)

[2] Shabana, A. A., Flexible multibody dynamics: Review of past and recent developments, Multibody System Dynamics 1 (2) (1997) 189-222.

[3] Hajžman, M., Polach, P., Modelling of flexible bodies in the framework of multibody systems, Proceedings of the 6th International Conference Dynamics of Rigid and Deformable Bodies 2008, Ústí nad Labem, Jan Evangelista Purkyně University in Ústí nad Labem, 2008, pp. 33-42.

[4] Stejskal, V., Valášek, M., Kinematics and dynamics of machinery, Marcel Dekker, Inc., New York, 1996.

[5] Du, J., Bao, H., Cui, C., Yang, D., Dynamic analysis of cable-driven parallel manipulators with time-varying cable lengths, Finite Elements in Analysis and Design 48 (1) (2012) 1392-1399.

COMPUTATIONAL MECHANICS 2015
31st conference with international participation
Špičák
November 9 - 11, 2015

Negative stiffness in gear contact

L. Půst [a], L. Pešek [a], A. Radolfová [a]

[a] *Institute of Thermomechanics, Czech Academy of Sciences, Dolejskova 5, 182 00 Praha, Czech Republic*

The dynamic analysis of multi-mesh planetary gear transmission systems is of fundamental importance for reduction of noise and vibrations of these very often used mechanical devises. Planetary gearboxes have several advantages (e.g. minimizing of weight at given power) against the single parallel-axes gearings, particularly due to splitting of force flow into several planet stages. However, the non-ideal mounting, errors in production etc can cause that the load sharing on all planet stages is very unequal. The application of floating sun gear or of flexible pins of planet gears are the possible ways to achieve better load sharing.

However, application of floating or idle gears causes that the deformations in mesh contact are not only in the direction of tangent to the base circle, but there is a motion component perpendicular to this tangential motion. Restoring forces at displacement in this radial direction are usually not taken into account and are not respected in mathematical modelling.

Presented paper attempts to fulfil this white place and derive the radial stiffness of gears contact both for external and internal tooth systems. Added examples show influence of this radial stiffness on the dynamic behaviour of planet trains and of simple parallel gearings.

The dynamic mathematical model of planetary gearing set with fixed planetary carrier is based on several assumptions:

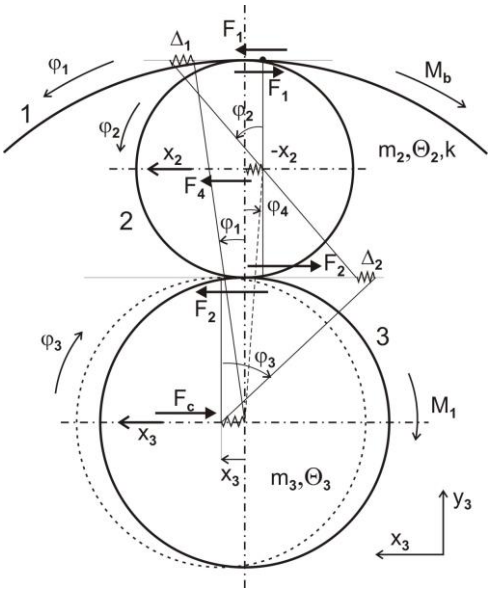

Fig. 1. Kinematical situation in horizontal direction and torsion

a) Plane motion of all gearing wheels.
b) Rigid wheels, with inertia parameters Θ_1, Θ_2, Θ_3, m_2, m_3.
c) Exact gearings.
d) Compliant planet wheels pivot, stiffness k_c.
e) Entire system is un-damped, linear.
f) Axis of the annulus rig wheel is fixed and the wheel can only rotate.

Horizontal motions

Graphical representation of kinematical situation of one planetary wing in horizontal direction and torsion is plotted in Fig. 1. External moments M_1, M_b containing constant component – preload – ascertain forces in gearing's contacts, which influence the radial stiffness at mutual radial motions of wheels.

Vertical motions

The mutual forces in wheels contact at theirs centres approaching Δy are given by the change $\Delta\alpha$ of pressure

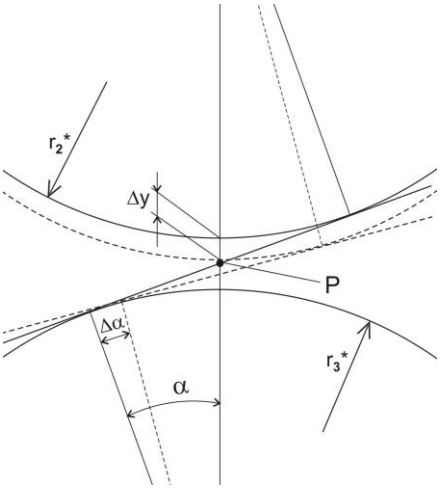

Fig. 2. Kinematical situation in vertical direction

angle α, as shown in Fig. 2 by the dashed lines. The radial component of contact mesh force decreases

$$\Delta F = F(\sin(\alpha - |\Delta\alpha|) - \sin(\alpha)) \cong -F\cos(\alpha)\sin(|\Delta\alpha|).$$

The radial shift Δy is connected with the change of pressure angle $\Delta\alpha$.

$$\Delta y = \frac{r_3^* + r_2^*}{\cos(\alpha)} - \frac{r_3^* + r_2^*}{\cos(\alpha - |\Delta\alpha|)} \cong \frac{(r_3^* + r_2^*)\sin(\alpha)\sin(|\Delta\alpha|)}{\cos^2(\alpha)},$$

where r_3^*, r_2^* are radiuses of base circles.

From these two expressions we get the radial contact stiffness k_r:

$$-k_r = k_{r32} = \frac{\Delta F}{\Delta y} = \frac{-F\cos^3(\alpha)}{(r_3^* + r_2^*)\sin(\alpha)} = \frac{-F\cos^2(\alpha)}{(r_3 + r_2)\sin(\alpha)}.$$

The interesting property of this radial external mesh stiffness is its negative value.

Similar relations are valid also for the radial contact force between ring and planetary wheel, But with the basic difference in the internal gearing of ring wheel. In this tooth system, the pressure angle α increases $\Delta\alpha > 0$ at positive wheels centres approaching Δy and the radial contact stiffness k_r of this internal gearing set is positive as opposed to the external gearing set:

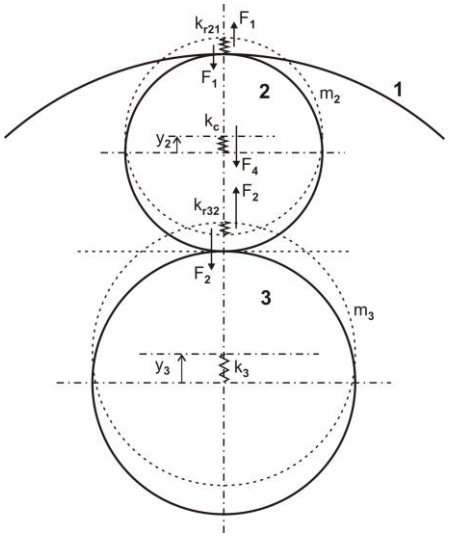

Fig. 3. Vertical motion

$$k_{r21} = \frac{\Delta F}{\Delta y} = \frac{F\cos^3(\alpha)}{(r_1^* - r_2^*)\sin(\alpha)} = \frac{F\cos^2(\alpha)}{(r_1 - r_2)\sin(\alpha)}.$$

As in planetary gearing gilt $r_3 + r_2 = r_1 - r_2$ and contact forces F_1, F_2 acting on satellite are approximately the same, then the radial stiffness in both gear's contacts have the same absolute value, but with opposite sign: $k_{r21} = -k_{r32} = k_r$.

The negative radial mesh stiffness k_{r32} between satellite and free unsupported sun wheel ($k_3 = 0$) causes the gear wings in Fig. 3 unstable. Addition of supporting spring with stiffness $k_3 > 0$ to the sun wheel axis decreases the level of instability. The planetary wing becomes stable with the stronger spring.

The radial stiffness of contacts between gears is a phenomenon, which is nearly always neglected in the literature concerning gearing. It has been shown that this stiffness depends on load of gears, on pressure angle and on base diameters of contacting gears. Its value is negative for external gearings, positive for internal gearings. It has been shown on examples that this radial stiffness is small in comparison to the tangential stiffness, but in some special cases it can cause instability of motion.

Acknowledgements

The work has been supported by the grant project TA04011656.

References

[1] Pust, L., Pesek, L., Radolfova, A., Dynamický model planetové převodovky se zastaveným planetovým unášečem, Research report No. Z-1530/15, IT ASCR, 2015. (in Czech)

COMPUTATIONAL MECHANICS 2015
31st conference with international participation
Špičák
November 9 - 11, 2015

Bifurcation of co-dimension 2 in the Cajal-like cell model dynamics

J. Rosenberg [a], M. Byrtus [b]

[a] Research centre New Technologies, University of West Bohemia, Univerzitní 8, 306 14 Plzeň, Czech Republic
[b] Department of Mechanics, Faculty of Applied Sciences, University of West Bohemia, Univerzitní 8, 306 14 Plzeň, Czech Republic

To model the pathological events in the lower part of urinary tract (LPUT) like the over-active bladder (OAB) and detrusor over-activity (DO), it seems to be necessary to take into account all cellular types present in the detrusor tissue. Besides the smooth muscle cells (SMC) there are the Cajal-like interstitial cells (ICCLC) and urothelium cells. According to the last investigations (see e.g. the survey [1] and [2]), the ICCLC are involved in the spontaneous contractile activity during bladder filling. It seems to be important to prepare the simple as possible model of this cell, to verify it and to analyse its properties. Such relatively simple model based on the current knowledge about these cells was developed. The model of the Cajal-like cell consists from five nonlinear ODE's. The most important variables are the calcium concentration in cytoplasm *cc* and in endoplasmatic reticulum *cer* along with the membrane potential *v*. In the neighbourhood of the physiological parameters the properties of this dynamical system has very interesting properties like spiking or bursting in correspondence with the experimental results [3].

Detailed analyses of the system are performed numerically using continuation approach. The phenomena of bifurcation of co-dimension 2 like Bogdanov-Taken's and generalized Hopf's (Bautin) bifurcation are analysed. The physiological meaning of the bifurcations is explained and demonstrated by changes of Ca2++ concentration in the cytoplasm. To study the spiking and bursting the slow-fast decomposition of the system was used.

The scheme of the ICCLC is presented on the Fig.1 with all channels and pumps and corresponding fluxes. As the control parameters were chosen: the conductivity *GCa* in the formula for *JVOOC* and the equilibrium potential *zNaCa* in the formula for *JNaCa*.

Integrating and analysing the whole system and using the continuation software Matcont the dependence of the different bifurcations can be obtained, see Fig. 2.

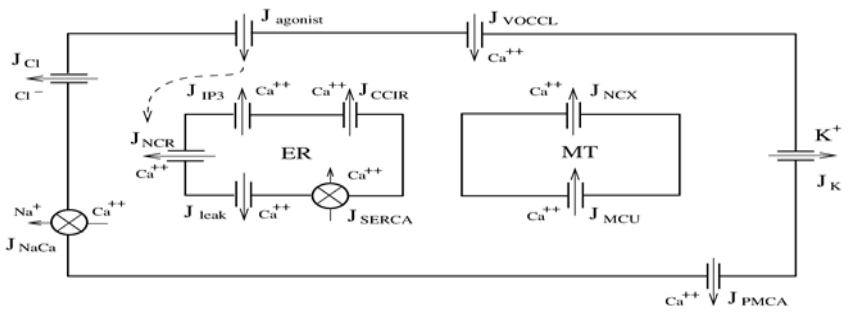

Fig. 1. Scheme of ICCLC with all fluxes. ER is the endoplasmatic reticulum and MT is the mitochondria

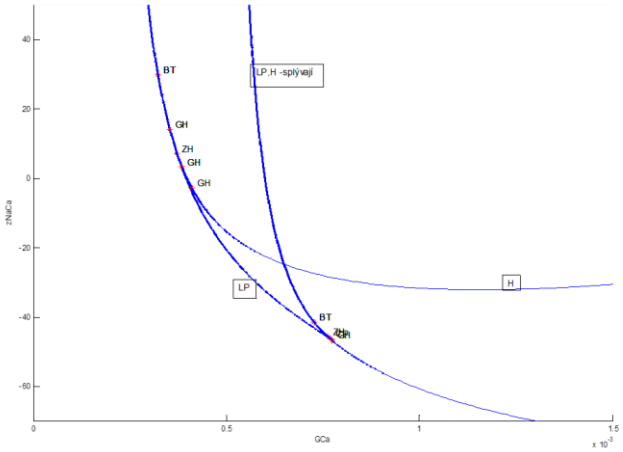

Fig. 2. Continuation curves in the parameter space. On the left from the LP (limit point) curve the variables are in silence. In the narrow neighbourhood of this curve under GH (Boutin) bifurcation the spiking and bursting occur. This corresponds with the results in [8] where the similar analysis for the neurons was done

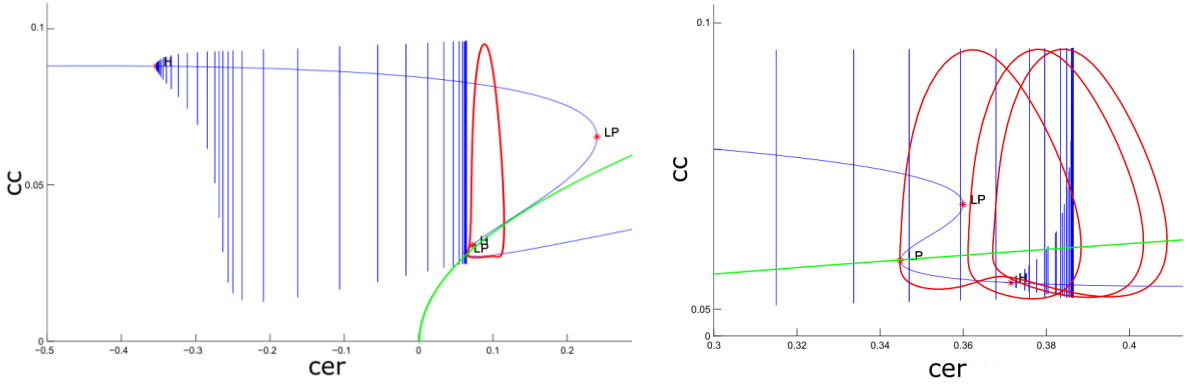

Fig. 3. Spiking (left) and bursting (right) demonstration using fast-slow decomposition. Blue curves is the continuation in the fast system, green is the nullcline for the slow system and red one is the spiking/bursting curve of the whole system

If we take into account the time evolution of *cer*, two frequencies can be observed. Therefore, we can split the system in the slow (*cer*) and fast (rest of variables) systems. We will take the *cer* variable as a parameter for the fast system. The result is shown on Fig. 3.

Acknowledgements

The result was developed within the CENTEM project, reg. no. CZ.1.05/2.1.00/03.0088, cofunded by the ERDF as part of the Ministry of Education, Youth and Sports OP RDI programme and, in the follow-up sustainability stage, supported through CENTEM PLUS (LO1402) under the ”National Sustainability Programme (author a) and by the project LO1506 of the Czech Ministry of Education, Youth and Sports (author b).

References

[1] Andersson, K. E., Arner, A., Urinary bladder contraction and relaxation: Physiology and Pathophysiology, Physiological Reviews. 84 (2004) 935-986.

[2] Drumm, B. T., Koh, S. D., Andersson, K. E., Ward, S. M., Calcium signalling in Cajal-like interstitial cells of the lower urinary tract, Nature Reviews Urology 11 (10) (2014) 555–564.

[3] Kim, S. O., Jeong, H. S., Jang, S., Wu, M. J., Park, J. K., Jiao, H. Y., Jun, J. Y., Park, J. S., Spontaneous electrical activity of cultured interstitial cells of cajal from mouse urinary bladder, The Korean Journal of Physiology & Pharmacology 17 (6) 2013 531-536.

COMPUTATIONAL MECHANICS 2015
31st conference with international participation
Špičák
November 9 - 11, 2015

Experimental identification of modal properties of turbine generator foundations

L. Smolík[a,b], J. Hyrát[a]

[a] *Research and Testing Institute Plzen Ltd., Tylova 1581/46, 301 00 Plzeň, Czech Republic*
[b] *Faculty of Applied Sciences, University of West Bohemia, Univerzitní 8, 306 14 Plzeň, Czech Republic*

Design of turbine generator (TG) foundations can notably impact the configuration, construction and costs of power plants and have also direct influence on TG rotordynamics [1]. Traditionally, TG foundations had been considered *rigid* or *high-tuned* when supported by massive beams and columns. These high tuned systems should have a fundamental frequency greater than the TG operating speed. In reality high-tuned foundation systems are unachievable however massive they are. Larger columns increase system stiffness but also its mass and thus it is virtually impossible to achieve rigid system with the fundamental frequency higher then 30 Hz, much less 50 Hz [2]. All foundation systems are *low-tuned* or *flexible* in reality.

When a flexible foundation is being designed, its impact on TG rotordynamics should be considered and at the same time, foundation response to TG rotor unbalance excitation should be estimated. One of the most common techniques for a response decrease is to design the foundation with no natural frequencies which are close to the TG operating speed, since a prolonged operation in resonant mode generally causes higher vibration levels than desired.

Natural frequencies of a TG foundation system are determined not only by foundation geometry, but also by mass and stiffness of a supported rotor-stator system. Results given by FE analysis are subjected to relatively high errors; errors higher than 20 % at excitation frequencies, which are not close to any natural frequency, are common [4]. Since the operation with such a type of the excitation is desirable, the theoretical results should be verified experimentally.

In accordance with methodology [3], there are usually two experiments performed for each newly built foundation. The first one is carried out at least 30 days after concrete works have been finished. Only a reinforced concrete structure without any additional technology is tested. Results of the test can be used not only for a verification but also for last-minute design changes if there are unexpected differences between the theoretical and experimental analysis. The second test is carried out after all technologies, including rotor, stator, condensers and piping, have been installed and TG rotor can be operated on a turning gear.

Due to high weight of foundation system – a typical system weight is in the thousands of tons [4] – it can be difficult to perform standard experimental modal analysis (EMA), since the excitation force has to be at least in the order of tens of thousands of Newtons so as to foundation response be measurable. Modal exciters which can produce such force are heavy and sometimes need an external cooling system. Also the examined foundation has to be excited in all three directions which can prove to be difficult if a directional force is used for the excitation.

The usage of an exciter with a rotating unbalance can eliminate some of the above-mentioned problems. Such a test is called a *dynamic load test* (DLT). Usually a slow but steady exciter speed sweep within the desired frequency range is employed. A run in the range of 2 000 –

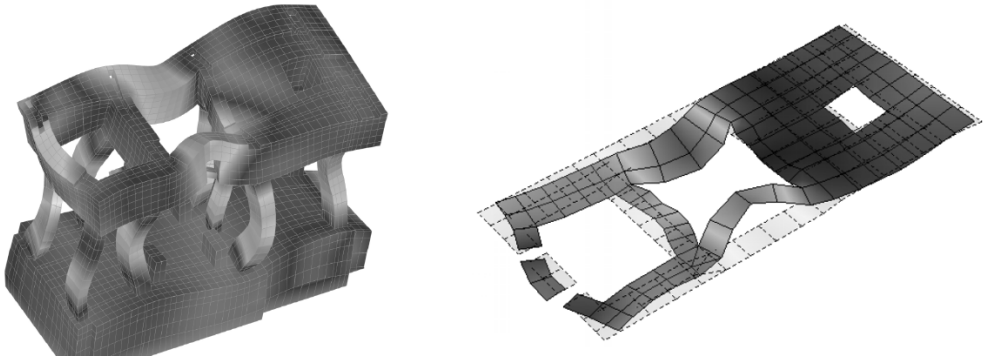

Fig. 1. The comparison of theoretical (53 Hz) and experimentally obtained (55 Hz) mode shape

3 300 RPM lasts roughly 7 minutes and there can be as much as 40 runs per load case and up to 6 load cases per foundation, so the DLT tends to be time-consuming. The number of runs is determined directly by the number of available channels and measurement points.

If the exciter speed is changing slowly enough the foundation response can considered equal to the steady-state response. The only peak in the frequency spectrum of the response is located precisely at the exciter speed (additionally there can be peaks at integer multiples of the exciter speed or minor peaks due to non-linearities). Using the order tracking tracking filter only this peak is sampled at predetermined exciter speeds. Since the standard EMA requires excitation forces with same phase angles and the rotating force can be viewed as two directional harmonic forces with 90° phase angle shift, the responses in different directions are sometimes evaluated separately (e.g., for resonance shape visualisation).

In order foundation response shapes could be visualized, the phase angle of the response in each of the measurement points has to be known. To use one of the measurement points as the reference point, where a vibration transducer is permanently installed during the test, is the common technique. However, triaxial transducers are usually employed. In such a case, the reference transducer blocks three much needed channels.

If the exciter speed is used as the reference signal Y, no other reference transducer is needed. The response is then measured as a so-called phase-assigned (auto)spectrum defined as

$$G_{XX}^{PAS} = G_{XX} \frac{G_{YX}}{|G_{YX}|}, \tag{1}$$

where X is a signal, G_{XX} is the autospectrum for X and G_{YX} is a cross-spectrum of X and Y.

Acknowledgement

The work was supported by TE01020068 project of Technology Agency of the Czech Republic.

References

[1] Ehehalt, U., Lneburg, B., Staubach, R., Daniel, Ch., Strackeljan, J., Woschke, E., Methods to incorporate foundations elasticities in rotordynamic calculations, Proceedings of the 8th SIRM, International Conference on Vibrations in Rotating Machines, Vienna, 2009, Paper-ID 41.

[2] Medearis, K. et al., Dynamics of low-tuned turbine generator foundation systems, EPRI, Palo Alto, 1981.

[3] Pavlík, V., Šafařík, I., LTO dynamic load tests of TG foundations, ČEZ, Praha, 2014. (in Czech)

[4] Štrunc, A., Foundation of a turbine-generator unit of 660 MW in the Ledvice power plant, Stavebnictví 5 (6-7) (2011) 32-35. (in Czech)

COMPUTATIONAL MECHANICS 2015
31st conference with international participation
Špičák
November 9 - 11, 2015

Simulation study of vehicle stream with coordinated control

P. Steinbauer [a], R. Stojan [a], Z. Šika [a]

[a] *Faculty of Mechanical Engineering, CTU in Prague, Technická 4,160 00 Praha 6, Czech Republic*

Current traffic suffers from high intensity leading into interactions between individual vehicles. It causes velocity fluctuations and significant decrease of average vehicle stream velocity. The main reason follows from overacting human drivers. In addition, they have limited perception horizon. The usual drivers thus do not know about obstacles, traffic jams or accidents in advance and cannot adjust their behaviour properly. Only good drivers look ahead and adjust vehicle velocity in optimal way along whole course of driving.

Fortunately, nowadays vehicles are equipped with many sensors and actuators, so that its behaviour can be optimized by sophisticate algorithms. In addition, means of vehicle to vehicle (v2v) communication are becoming available. It enables to use information coming from vehicles ahead and adapt driving strategy.

There are many activities (e.g. SUMO) which model and study vehicle stream behaviour. However, usually quite simple and not calibrated models of vehicle dynamics and adaptive cruise control (ACC) are used, as well as driver models.

Within this contribution, scalable model of vehicle stream consisting of arbitrary number of vehicles is developed. The modelling and control design tool MATLAB/SIMULINK is used. Each vehicle in the stream can be controlled by its individual controller, which uses various sets of available information about traffic with various or controlled in coordination with other vehicles using the infrastructure support. The model based predictive control (MPC) design methods are used to develop ACC algorithm. The results are compared with vehicle stream behaviour similar to current traffic state (optimized PID controller and 1st order dynamics delay dynamics).

The vehicle stream consists of individual vehicles. They are modelled by simple models which maintain important non-linearities (Fig. 1, [1]).

$$(m + m_r)\, a = (M_e\, p_t\, p_f\, \eta_{tf})/\, R_e - R - R_b$$

$$m_r = \left[(I_e + I_t)(p_t p_f)^2 + I_d p_f^2 + I_w\right] 1/R_e^2$$

$$R = \left[mgcos(\alpha) - \frac{1}{2}\rho V^2 S C_z\right](f_0 + KV^2) + \frac{1}{2}\rho V^2 S C_x + mgsin(\alpha)$$

$$M_e = f(\omega_e, u)$$

$$\omega_e = p_t p_f\, V/R_e$$

$$R_b = f(v, u)$$

$$\frac{U}{U_c} = e^{-T_D s}\frac{1}{\tau s + 1}$$

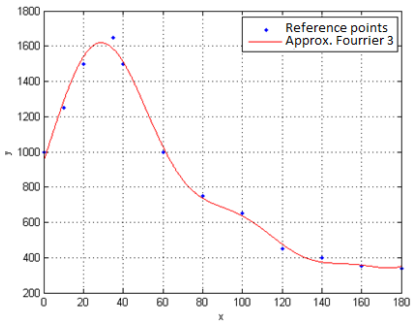

Fig. 1. Vehicle and driver model (a), tractive force with respect to velocity according to ([2]) (b)

The advanced adaptive cruise control (ACC) algorithms based on model based predictive control strategies is developed ([4]). The following finite prediction and control horizon

criterion is used.

$$J = \int_0^T \left(\sum_{i=1}^{n} Q\left(s_i - s_{i_{des}}\right)^2 + \sum_{i=1}^{n} R\left(\frac{u_k - u_{k-1}}{\Delta t}\right)^2 \right) \mathrm{d}t \,.$$

The criterion highlights both safe distance between vehicles and reduced control variable (acceleration/braking) changes. It leads to more efficient operation of the vehicle with the ACC based on MPC.

Safe distance is taken from the selection of available legislatively required minimum safe distance source data in: Czech Rep. (none, recommended 2 s), Germany (1/4 of kph speedometer value), Austria (0,4 s) and USA-California (one length of vehicle increased for every 10 mph), the highest required minimum safe distance is in Germany and USA (22,5 m in case of 90 kph, 4,5m), summarized in ([3]).

Investigation of ACC control was done on vehicle stream, which follows leading vehicle with sudden changes of its velocity (Fig. 2a).

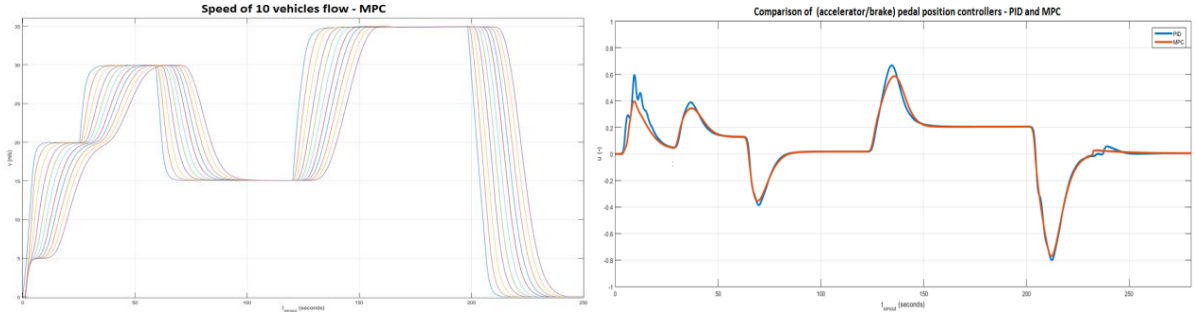

Fig. 2. Vehicle stream velocity profile (a) Required action (torque/braking) for original PID and MPC versions of ACC

Velocity profiles of vehicles in the stream controlled by MPC ACC and original ACC based on optimized PID controllers differ only a little bit. However, the resulting actions of selected vehicle in the stream show, that MPC driven ACC provides much better behaviour then ACC with PID (Fig. 2b).

Simulation experiments with MPC control strategy within ACC shows that the smoothly working controller can be obtained by much more straightforward way, comparing to older approaches ([2]). In addition, the control actions (both acceleration and braking) are reduced. It may enable to achieve more environmentally friendly vehicle behaviour in traffic.

Acknowledgements

This research has been realized using the support of EU Regional Development Fund in OP R&D for Innovations (OP VaVpI) and The Ministry of Education, Youth and Sports, Czech Republic, project # CZ.1.05/2.1.00/03.0125 Acquisition of Technology for Vehicle Center of Sustainable Mobility and The Ministry of Education, Youth and Sports program NPU I (LO), project # LO1311 Development of Vehicle Centre of Sustainable Mobility. This support is gratefully acknowledged.

References

[1] Gillespie, T. D., Fundamentals of vehicle dynamics, SAE Technical paper, Warrendale, 1992.
[2] Ioannou, A. P., Chien, Ch.-Ch., Autonomous intelligent cruise control, IEEE Transactions on Vehicular Technology 42 (4) (1993) 657-672.
[3] Safe distance, In.: NEHODA.EU, cit. 2015-10-16, Available on: http://www.nehoda.eu/?p=41. (in Czech)
[4] Valášek, M., Šika, Z., Florián, M., Macek, J., Polášek, M., Model based predictive control of combustion engine with constraints, Review of Automotive Engineering of Japan SAE 26 (3) (2005) 349-356.

COMPUTATIONAL MECHANICS 2015
31st conference with international participation
Špičák
November 9 - 11, 2015

Initial evaluation of possible resonance vibration consequences due to parametric flow oscillation

P. Stulík [a], J. Hanuš [a], M. Bém [a]

[a] *ÚJV Řež a. s., Hlavní 130, 250 68 Husince – Řež, Czech Republic*

At one of our operational measurement stay in NPP Dukovany we had been observing unusual reactor dynamic behaviour. Measuring instruments of MCP supply current in unit control room had exhibiting random current fluctuations in 150A range with maximum of 30A amplitude swing instead of usual 3 – 5 A. Video from the start of 5th cycle of Unit #4 in 22.10.1992 will show this situation. There were operational consequences afterwards, i.e. growth of average reactor output temperature asymmetries and increase of number of thermocouples with these asymmetries. We have later confirmed that this unacceptable situation started exactly on above mentioned date (Fig. 1).

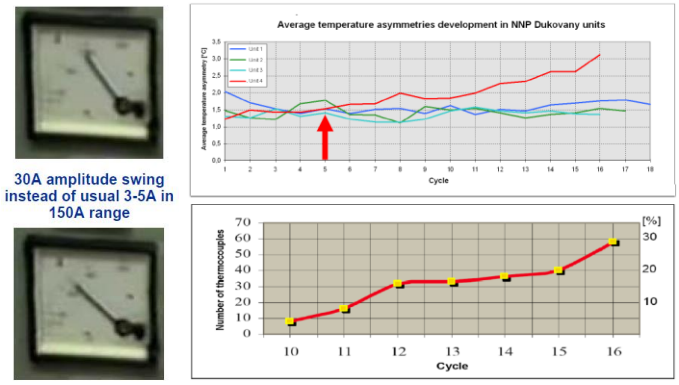

Fig. 1. NPP Dukovany Unit #4 MCP supply current fluctuations and longterm consequences

From the view of many realized operational measurements, their processing, evaluating and comparing with computational models ([5]) the origin of that phenomena has been becoming more clear. There is a need to know more about coolant flow behaviour. Standard flow measurement is usually based on the measurement of pressure drop and characteristic of the main circulation pump. Different solution based on the measurement of MCP supply electrical current was developed and resulted in the estimation of pressure fluctuations which can lead to an evaluation of flow changes ([1], [2], [4]). With regard to the fact that MCP motors are asynchronous type with inherent slip, then changing hydrodynamic load can cause a different revolutions change of MCP in particular loops. Observed beat effects of reactor vibrations generated by input pressure fluctuations in Fig. 2 at slightly different MCP revolutions can be symptoms of possible parametric flow oscillations. These flow oscillations can be estimated by MCP supply current measuring together with a beat effects evaluation.

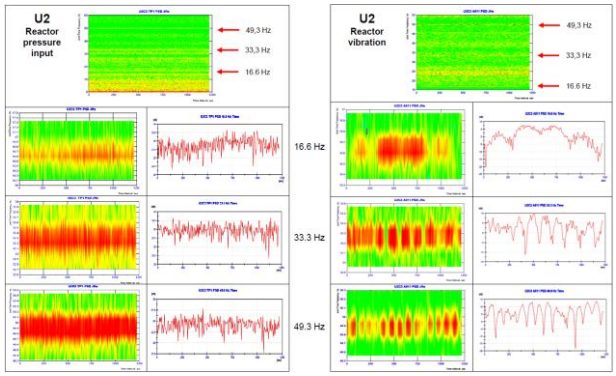

Fig. 2. Beat vibration effects at MCP harmonic frequencies generated by input pressure fluctuations (NPP Temelin, U2C03)

Parametric coolant oscillations in PWR primary circuit are treated on electromechanical analogy in [3]. Assuming that the pressure fluctuations can be written in the form $P=P_0+\Delta P\sin\omega t$, the modulation coefficient m is defined as ratio of pressure fluctuations ΔP and static pressure P_0, i.e $m=\Delta P/P_0$. The critical value m is here derived for acoustic active resistance to be negative i.e. when the coolant flow starts to increase and parametric oscillations are then further developing. Beat pressure fluctuations effects as symptoms of flow parametric oscillation were mentioned before. 2D and 3D pressure fluctuations spectrograms from NPP Temelin are shown in Fig. 3. Beat effects are clearly recognized in the frequency ranges up to 5 Hz, dominating 6.6 Hz, 9.2 Hz, 13.8 Hz and 16.6 with well identified acoustic, mechanical and turbulent flow origin. Possible and unwanted resonance phenomena in these ranges, here described as consequence of excited parametric flow oscillations, should be further studied and refined for diagnostic application in NPP operational environment.

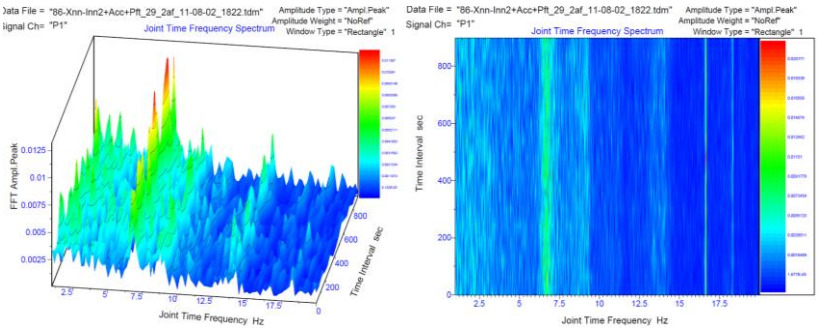

Fig. 3. Beat effects of the 1st loop hot leg pressure fluctuations (NPP Temelin, U2C09)

References

[1] Pečínka, L., Stulík, P., Experimental verification of WWER 1000/320 reactor dynamic response to pressure pulsations generated by the main circulating pumps, Colloquium Dynamics of Machines, Prague, 2008. (in Czech)

[2] Pečínka, L., Stulík, P., Pulsations of coolant flow through reactor V1000/320 generated by the slightly different revolutions of main circulation pumps, Colloquium Dynamics of Machines, Prague, 2012.

[3] Pečínka, L., Švrček, M., Parametric oscillations of the coolant in PWR primary circuit, Computational Mechanics, 31st Conference with international participation, Špičák, Czech Republic, 2015.

[4] Pochylý, F., Habán, V., Study of pressure fluctuations in the WWER 1000/320 primary circuit, Technical University of Brno, Report No VUT-EU13303-QR-14-08, 2008. (in Czech)

[5] Stulík, P., WWER 1000/320 reactor fuel dynamic behaviour in joint time frequency domain, Reactor Noise Knowledge Transfer Meeting UJV Rez, Chalmers University Göteborg, Prague, Czech Republic, 2012, pp. 16-19.

COMPUTATIONAL MECHANICS 2015
31st conference with international participation
Špičák
November 9 - 11, 2015

Extended finite element method for free-surface flows

P. Sváček[a]

[a] *Czech Technical University in Prague, Faculty of Mechanical Engineering, Department of Technical Mathematics, Karlovo nám. 13, Praha 2, 121 35, Czech Republic*

The mathematical modelling of two-phase flows with the consideration of the free surface motion influenced by the surface tension is addressed in various scientific as well as technical applications. Such a problem is important both from the mathematical modelling point of view and also from the technical practice. Particularly, its numerical approximation is very challenging task, see among others [1] or [2]. The approximation of the surface tension naturally can play a key role here.

In this paper, we consider the two-dimensional flow of two immiscible fluids, the problem is mathematically described and the variational formulation is introduced. For the discretization the finite element(FE) method is used. The free surface motion is realized using the level set method, cf. [3]. In the case of high surface tension, a modification of the standard FE method is required to avoid the spurious currents, see [4] or [1]. For the verification of the implemented method a benchmark problem is solved, cf. [2].

We consider the flow of two immiscible fluids (called A and B) in a computational domain $\Omega \subset \mathbb{R}^2$ with the Lipschitz continuous boundary $\partial\Omega$. The boundary $\partial\Omega$ has three mutually disjoint parts Γ_W, Γ_S, Γ_O. The fluids A and B are assumed to occupy subdomains $\Omega^A_{(t)}$) and $\Omega^B_{(t)}$ at any time instant $t \in (0,T)$, respectively. The free surface (interface) between the fluids is denoted by $\hat{\Gamma}_t = \overline{\Omega}^A_{(t)} \cap \overline{\Omega}^B_{(t)}$, whose motion is influenced by the applied surface tension. Each of the fluids (A and B) is characterized by its density (ρ^A and ρ^B) and its viscosity (μ^A and μ^B, respectively).

Mathematical description is given with the aid the density $\rho(x,t)$ and viscosity $\mu(x,t)$ functions, i.e. functions which give the density and viscosity of the fluid particle located at a point $x \in \Omega$ at time $t \in (0,T)$. The pressure and the flow velocity functions are denoted by $p(x,t)$ and $\boldsymbol{u} = \boldsymbol{u}(x,t)$, respectively. Similarly as for the density function, the flow velocity (or pressure) is equal to flow velocity (or pressure) of fluids A and B in the domain $\Omega^A_{(t)}$ and $\Omega^B_{(t)}$, respectively.

Using this notation the flow motion can be formally described by the incompressible Navier-Stokes equations written in the form

$$\rho\frac{\partial \boldsymbol{u}}{\partial t} + \rho(\boldsymbol{u}\cdot\nabla)\boldsymbol{u} - \nabla\cdot\boldsymbol{\sigma} = \rho\boldsymbol{f} + \gamma\kappa\boldsymbol{n}\delta_{\hat{\Gamma}_t}, \tag{1}$$

where $\boldsymbol{\sigma}$ is the Cauchy stress tensor given by $\boldsymbol{\sigma} = -pI + \mu(\nabla\boldsymbol{u} + (\nabla\boldsymbol{u})^T)$, and $\delta_{\hat{\Gamma}_t}$ is the delta function of the interface $\hat{\Gamma}_t$, κ is the interface curvature, γ is the surface tension coefficient and $\boldsymbol{n}$ is the unit normal vector to the interface $\hat{\Gamma}_t$ (oriented into $\Omega^B_{(t)}$). Eq. 1 should be better understand in its integral form, i.e. for any $\boldsymbol{v} \in \boldsymbol{H}^1(\Omega)$ it should hold

$$\int_\Omega \rho\left(\frac{\partial \boldsymbol{u}}{\partial t} + (\boldsymbol{u}\cdot\nabla)\boldsymbol{u}\right)\cdot\boldsymbol{v} + \boldsymbol{\sigma}\cdot(\nabla\boldsymbol{v})\,\mathrm{d}x = \int_{\hat{\Gamma}_t}\gamma\kappa\boldsymbol{n}\cdot\boldsymbol{v}\,\mathrm{d}S + \int_\Omega \rho\boldsymbol{f}\cdot\boldsymbol{v}\,\mathrm{d}x. \tag{2}$$

Here, $\boldsymbol{H}^1(\Omega)$ is the Sobolev's space of square integrable functions together with their first derivatives, see [5]. Further, the system of Eqs. 1 is equipped with initial and boundary conditions.

Furthermore, to treat the motion of the free surface $\hat{\Gamma}_t$ the *level set* method is applied, which means that we solve another equation for the level set function. The level set function is basically the signed distance function being zero on the interface $\hat{\Gamma}_t$ at any time instant t, positive in $\Omega^A_{(t)}$ and negative in $\Omega^B_{(t)}$. In order to treat the surface tension, its weak reformulation is used.

For the spatial discretization the finite element method is used, where the FE spaces $\boldsymbol{V}_h$ and Q_h are defined over an admissible triangulation $\mathcal{T}_h$. For the approximation the well-known Taylor-Hood FE is used. In order to capture the pressure discontinuity across the interface the extended finite element method (XFEM) enlarging the original pressure space is used.

The numerical results will be shown for the case of a rising bubble considered in [2], where the following values were used for the test case I: $\rho^A = 1000\,\mathrm{kg\,m^{-3}}$, $\rho^B = 100\,\mathrm{kg\,m^{-3}}$, $\mu_A = 10\,\mathrm{Pa\,s}$, $\mu_B = 1\,\mathrm{Pa\,s}$, $\boldsymbol{f} = (0, -0.98)\,\mathrm{m\,s^{-2}}$ and the surface tension $\gamma = 24.5\,\mathrm{N/m}$. The height of the computational domain is $H = 2\,\mathrm{m}$ and width is $W = 1\,\mathrm{m}$. The fluid B is originally located in the circle of the diameter $0.5\,\mathrm{m}$, whose center is displaced by $0.5\,\mathrm{m}$ up from the bottom of the domain. Due to the gravity force, the fluid B with the lower density starts to rise, which also leads to a shape deformation. The numerical method was also applied to the second benchmark test (test case II), where the following quantities were used $\rho^A = 1000\,\mathrm{kg\,m^{-3}}$, $\rho^B = 1\,\mathrm{kg\,m^{-3}}$, $\mu_A = 10\,\mathrm{Pa\,s}$, $\mu_B = 0.1\,\mathrm{Pa\,s}$, $\boldsymbol{f} = (0, -0.98)\,\mathrm{m\,s^{-2}}$ and $\gamma = 1.96\,\mathrm{N/m}$.

Acknowledgment

This work was supported by grant No. 13-00522S of the Czech Science Foundation.

References

[1] Barrett, J.W., Garcke, H., Nürnberg, R., Eliminating spurious velocities with a stable approximation of viscous incompressible two-phase Stokes flow, Computer Methods in Applied Mechanics and Engineering 267 (2013) 511-530.

[2] Hysing, S., Turek, S., Kuzmin, D., Parolini, N., Burman, E., Ganesan, S., Tobiska, L., Quantitative benchmark computations of two-dimensional bubble dynamics, International Journal for Numerical Methods in Fluids 60 (11) (2009) 1259-1288.

[3] Sethian, J.A., Level set methods and fast marching methods, Cambridge Monograph on Applied and Computational Mathematics, Cambridge University Press, Cambridge, UK, 1999.

[4] Sauerland, H., Fries, T.-P., The stable XFEM for two-phase flows, Computers & Fluids 87 (2013) 41-49.

[5] Adams, R.A., Sobolev spaces, Academic Press, New York, 1975.

[6] Kuzmin, D., On the design of general-purpose flux limiters for finite element schemes. I. Scalar convection, Journal of Computational Physics 219 (2006) 513-531.

COMPUTATIONAL MECHANICS 2015
31st conference with international participation
Špičák
November 9 - 11, 2015

Vibration tests of 15T tram chassis cover

J. Svoboda [a], V. Kraus [b]

[a] Research Centre Rez, Morseova ul. 1245/6, 301 00 Plzeň, Czech Republic
[b] ŠKODA TRANSPORTATION a.s., Emila Škody 2922/1, 301 00 Plzeň, Czech Republic

The paper describes briefly the vibration test of the 15T tram car chassis cover made with the assistance of ŠKODA TRANSPORTATION workers. The aim of the test was to verify the lifetime of the subject structure in a loading mode that corresponds to 720,000km of trouble-free operation. On the basis of operational measurements of acceleration on the tram car chassis in both vertical and horizontal directions, regression analysis was used for selected frequencies to calculate blocks of harmonic amplitude cycles corresponding to 336km running in the operation mode. Table 1 shows the test program for the respective loading directions.

Table 1. Test program for the loading directions

Vertical direction			Transversal direction			
Number of oscillations per block	Frequency amplitude [mm]		Number of oscillations per block	Frequency amplitude [mm]		
	Frequency [Hz]			Frequency [Hz]		
	12	17.8		6.5	8	10.5
2762	2.6	1.2	2210	9	5.9	3.4
910	3.5	1.6	548	12	7.9	4.6
330	4.4	2	214	15	9.5	5.1
128	5.3	2.4	70	18	11	5.7
50	6.2	2.8	18	21	12.5	6.3
19	7	3.2	14	24	14.5	6.9
8	7.9	3.6	4	-	16.5	7.6
5	8.8	4	10	-	impact	impact
2	10.6	4.8				
1	13.2	6				

To achieve the required lifetime, 2143 loading blocks in total had to be vibrated in either direction with the given frequencies.

Check measurements were made before application in either direction to make sure that the level of simulated loading blocks corresponded to the acceleration values measured in operation. Based on the measurements, minor corrections were then made in the program to take into account the resonance frequency of the fixing grid, for instance. In the transversal loading program, the loading blocks for the 8 and 10.5 Hz frequencies were completed with 10 cycles of rectangular impulses of 3mm amplitude and 0.7 Hz frequency.

The greatest problem to be resolved before taking the test was cover fixing during the test so as to simulate as faithfully as possible in loading in both directions the cover installation

Fig. 1. Cover attachment to the auxiliary structure for oscillation in vertical direction

in operation. It was managed by designing and manufacturing a universal fixing structure that could be readjusted for both loading directions together with the loading cylinder in a simple manner. Fig. 1 shows this arrangement for cover oscillation in a vertical direction.

The cover frame to the 4 brackets of which the cover being tested was attached was connected firmly to the bracket holder with both ends connected flexibly to the bracket attached to the fixing cube mounted on the testing laboratory grid. In its centre, the cover frame was attached to the plate of the upper cross joint of the loading servo-cylinder, which was mounted to the testing laboratory grid by means of the lower cross joint with a plate.

To simulate transversal loading of the cover being tested, the cover fixing structure had to be readjusted. To the upper surface of 2 fixing cubes of 140 mm of total height, see Fig. 2, a bracket was attached, with the bracket holder attached flexibly to the bracket on the fixing cubes being suspended flexibly in a vertical position with its upper ends. The lower ends of the holder were connected to the frame, to which the cover being tested was attached from the outer side. The plate of the upper cross joint of the servo-cylinder mounted horizontally to the supporting cube attached to the grid was fixed laterally in the centre of the auxiliary frame of the cover.

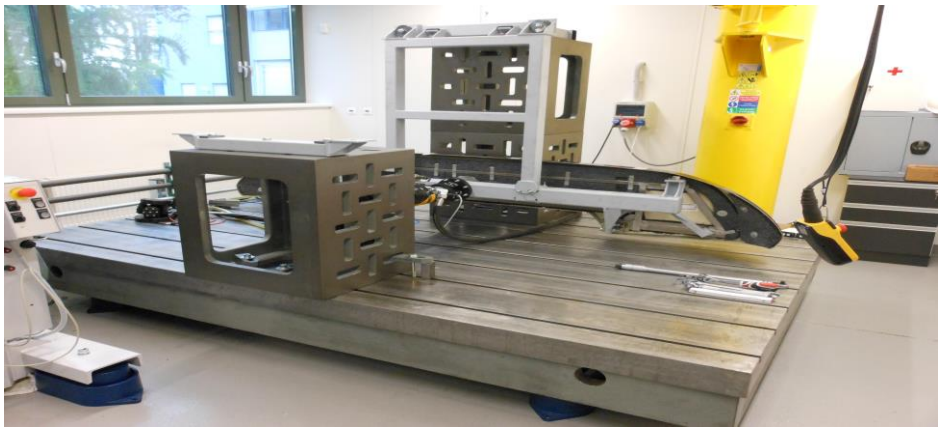

Fig. 2. Cover attachment to the auxiliary structure for oscillation in transversal direction

The tests made on the 15T tram chassis cover proved the lifetime of 720,000km.

Acknowledgements

Publication of this paper was supported by the SUSEN Project CZ 1.05/2.1.00/03.0108 realized in the framework of the European Regional Development Fund (ERDF).

COMPUTATIONAL MECHANICS 2015
31st conference with international participation
Špičák
November 9 - 11, 2015

Data reduction method as an investigation tool in the field of internal aerodynamics

P. Šafařík [a]

[a] Czech Technical University in Prague, Faculty of Mechanical Engineering, Department of Fluid Mechanics and Thermodynamics, Technická 4, 166 07 Prague 6, Czech Republic

Data reduction method originally developed for aerodynamic investigations of blade cascades in wind tunnels is based on integrals of mass flux, axial momentum flux, and circumpherential momentum flux solved from data set flow parameter distributions in the traverse plane. The main aim of the method is to evaluate values of representative parameters and to replace the extensive data set by, which represents functions of the coordinates, by homogeneous values. Homogenous values should be applied for determination further parameters, as for instance aerodynamic forces, loss coefficients, etc. It requires that both data set are equivalent with respect to their physical properties. So that, consequential balances of mass, momentum, and energy fluxes have to be ensured. In the case of an ideal gas. The exact solution of the system of conservation equations supplemented with equation of state for a gas is derived in [1] and flow conditions can be analysed. The analysis proves the existence of two solutions; so experience with the data reduction method is required. The basic algorithm has been developed for reduction of data sets. Available data from aerodynamic investigation of compressible fluid flows are processed by means of the data reduction method. Experimental results or results from numerical simulations are for given traverse plane prepared into data sets and values of representative parameters of flow are solved [3]. The method is a basic equipment of laboratories performing aerodynamic research and is applied namely at investigation of models of flow parts of turbomachines [5]. Further extensions of the data reduction method were performed. The extension of the data reduction system to flow fields with non-constant total temperature was shown by Oldfield et al. [2]. The data reduction method of [1] evaluates parameters of flow fields with the injection of one or more foreign gases. The procedure for the calculation of the thermodynamic properties of gas mixture is applied as well to the local values as to the homogenous values. Another attempt referred to a reduction data from three-dimensional flow fields. Application of the sliding reduction method proved to be an impetus for improvement quality of measurement techniques. The new favourable extension of the data reduction procedure is aimed at the steam flow fields [4]. Real gas thermodynamics has to be applied, namely properties of water and steam according to IAPWS IF-97 are included into evaluation procedure of the data reduction method, and an iterative computational procedure has been developed. Undoubtedly, a very important part of aerodynamic investigations is analysis and detail discussion of results. Application of the data reduction method should be discussed. Limit conditions of input data resulted from analysis of the method, as shown in Figure1. The data reduction method is based on consequential physical principle and has theoretical and numerical system for solution of homogeneous data. It offers significant data for evaluation of aerodynamic parameters describing flow and effects in flow parts. Nevertheless, new topics for further development and applications of this method are in demand.

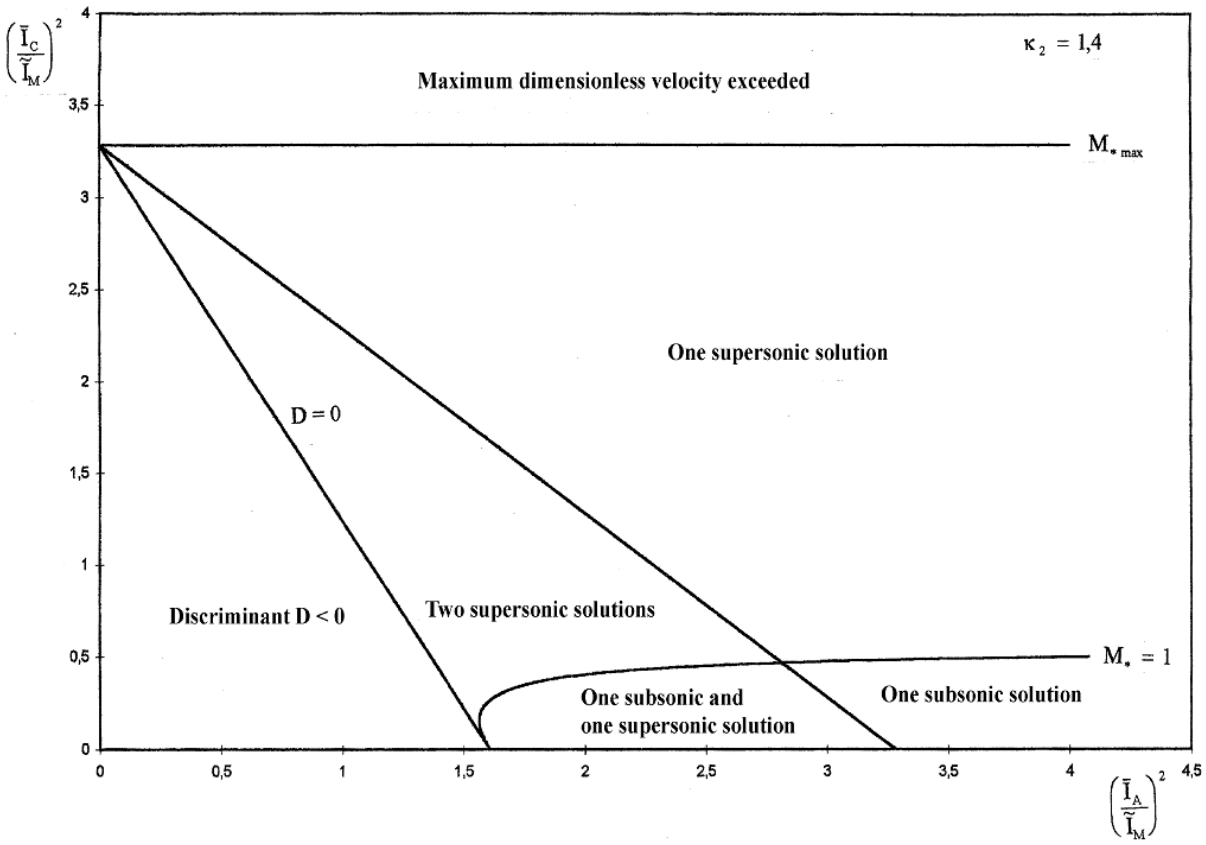

Fig. 1. Range of valid arguments for the solution of the conservation equations

In Fig. 1, a result of analysis of the data reduction method is shown. Squared ratio of integrals of circumferential momentum flux and mass flux is plotted against squared ratio of integrals of axial momentum flux and mass flux. For air (ratio of heat capacities, $\kappa = 1.4$), limits of input data are determined and regions of solutions of the data reduction method are depicted. M_* is non-dimensional velocity.

Acknowledgement

The support by the Technology Agency of the Czech Republic under project No.TE01020036 is acknowledged.

References

[1] Amecke, J., Šafařík, P., Data reduction of wake flow measurements with injection of another gas, DLR-Forschungsbericht No.95-32, Göttingen, 1995.

[2] Olfield, M. L. G., Schultz, D. L., Nicholson, J. H., Loss measurements using a fast traverse in an ILPT transient cascade, Proceedings of 6th Symposium on Measuring Techniques in Transonic and Supersonic Flows in Cascades and Turbomachines, Lyon, 1981.

[3] Straka, P., Numerical simulations to support of the experimental high-speed aerodynamic investigation of flow in the linear turbine cascades, Ph.D. Thesis, Czech Technical University in Prague, Prague, 2010. (in Czech)

[4] Šafařík, P., Nový, A., Hajšman, M., Jícha, D., Range of valid arguments for data reduction method in the steam flow fields, The Application of Experimental and Numerical Methods in Fluid Mechanics and Energy 2014, University of Žilina, Žilina, 2014, pp. 245-248.

[5] Váchová, J., Luxa, M., Příhoda, J., Šimurda, D., Transition model application on mid-section turbine blade cascade, 12th International Symposium on Experimental and Computational Aerothermodynamics of Internal Flows, Lerici, Paper No. ISAIF 12_100, 2015.

COMPUTATIONAL MECHANICS 2015
31st conference with international participation
Špičák
November 9 - 11, 2015

Heterogeneous material modelling via optimized Wang tiles

D. Šedlbauer [a]

[a] *Department of Mechanics, Faculty of Civil Engineering, CTU in Prague, Thákurova 7/2077, 166 29 Prague, Czech Republic*

On the field of random heterogeneous composite material modelling the concept of the Periodic Unit Cell (PUC) is frequently used. Even though each cell has the same statistical information, a reconstructed material sample shows periodicity which is against both random and heterogeneous principles. Therefore the concept of the stochastic Wang tiling is utilized in order to reduce unwanted periodicity artefacts. The main aim of this work is to present an optimized generation of the Wang tile set for 2D material models composed of rigid circular particles within a matrix.

In general, Wang tiling is characterized by a set of tiles where each single tile is represented as a square with codes (colours, letters etc.) on edges. If we consider the stochastic tiling algorithm – the CSHD algorithm [2] and two different codes for both horizontal and vertical edges then the minimal Wang tile set consists of eight tiles, Fig. 1.

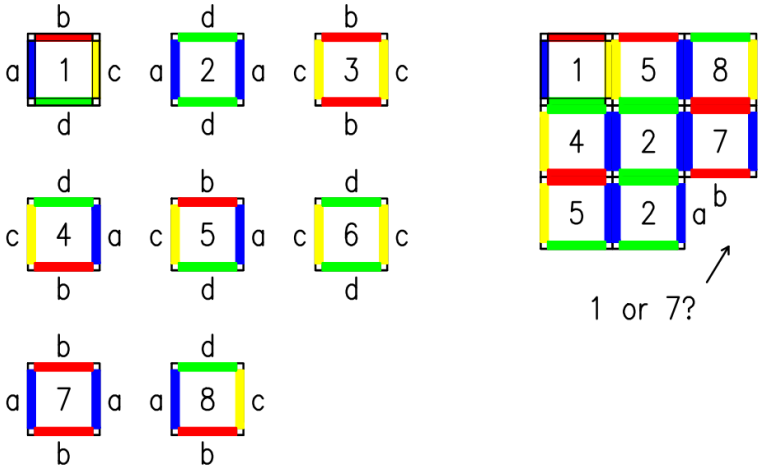

Fig. 1. The minimal set of 2D Wang tiles for stochastic tiling, the principle of stochastic Wang tiling in 2D

The algorithm of the generation is based on the molecular dynamics where the main idea is to let particles grow from the initial zero areas to their final radii and also allow them to move within their zones to ensure compatibility of tiles according to rules of the stochastic tiling. If a particle leaves the cell (with the PUC usage) it appears on the opposite wall and the volume fraction remains the same. Copying particles when they leave Wang tile is a little bit complicated. If a circle during the motion leave any Wang tile through the edge then this particle have to be copied into other tiles with the same edges (with the same code) in order to ensure compatibility of tiling. However, this is unacceptable in terms of changes in the volume fraction of the whole set. Therefore each single tile is divided into four marginal parts (borders) and one central part and disc centres move only within appropriate areas and are not copied.

During the set creation particles grow, move randomly and collide according to their initial random velocities. The final position of particles is controlled only by initial random parameters of a start position, velocity and by the number of time steps which determinate a growth rate. With this procedure we gain a set for Wang tiling that finally forms a random microstructure element. To compare formed microstructures with the reference one a method for statistical microstructure description needs to be introduced. In this work statistical descriptor known as the Radial Distribution Function (RDF) [1] is utilized.

The Particle Swarm Optimization (PSO) [3] as a part of Swarm intelligence techniques is a stochastic method based on behaviour of a bird's flock or fish school. During the flock motion particles share their knowledge to each other so the flock can efficiently find the optimum with updating their velocities. The molecular dynamics for the set generation set of Wang tiles use similar principles as the PSO. The velocities of particles need to be modified in order to minimize objective function which is formed by differences between the radial distribution functions of modelled tilings and the reference medium.

During the algorithm best so far values of the objective function are saved as well as the set of particles forming the basics of a tiling. In Fig. 2 is the convergence of the modified PSO algorithm where after only a few iterations the method converged to the local optima which means that the RDF of modelled sample is close to the RDF of the reference material.

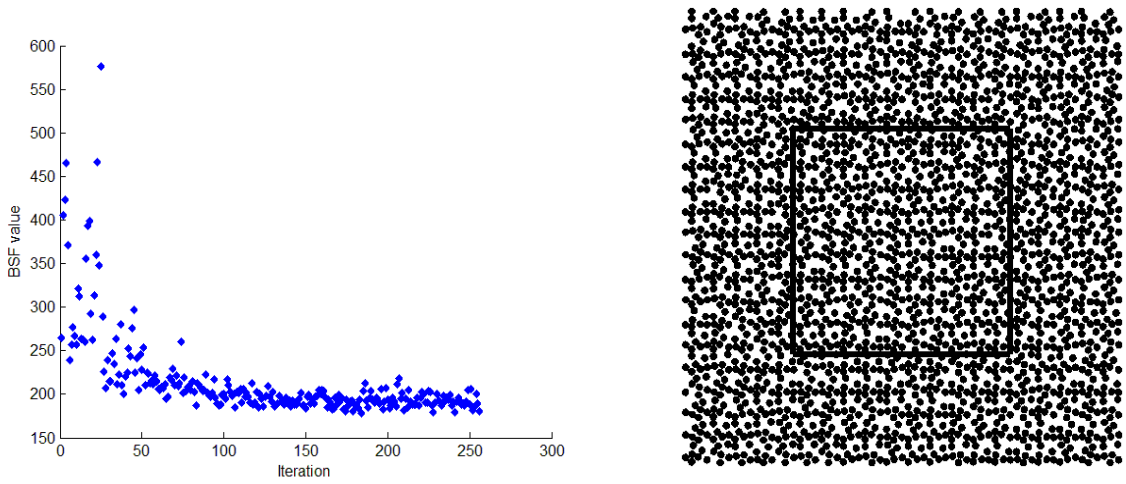

Fig. 2. Convergence of the modified PSO and one of the realizations

With the proposed dynamic algorithm it is possible to generate optimized Wang tile sets. A final set of the Wang tiles meets requirements for the stochastic tiling through which we can stack aperiodic material domains with prescribed material characteristics. The proposed algorithm exhibit potential and should be used in the field of localization tasks.

Acknowledgements

This outcome has been achieved with the financial support of the Grant Agency of the Czech Technical University in Prague, grant No. SGS15/030/OHK1/1T/11.

References

[1] Axelsen, M., Quantitative description of the morphology and microdamage of composite materials, Ph.D. thesis, Aalborg University, 1995.

[2] Cohen, M. F., Shade, J., Hiller, S., Deussen, O., Wang tiles for image and texture generation, ACM Transactions on Graphics 22 (3) (2003) 287-294.

[3] Kennedy, J., Eberhart, R. C., Particle swarm optimization, 1995 IEEE International Conference of Neural Networks Proceedings, 1995, pp. 1942-1948.

COMPUTATIONAL MECHANICS 2015
31st conference with international participation
Špičák
November 9 - 11, 2015

Synthesis of computed torques control of flexible robot with additional sensors

Z. Šika [a], J. Volech [a], J. Plecháček [a], L. Mráz [a], M. Valášek [a], P. Beneš [a]

[a] *CTU in Prague, Faculty of Mechanical Engineering, Department of Mechanics, Biomechanics and Mechatronics, Technická 4, Praha 6, 166 07, Czech Republic*

Many of new concepts of robots have been invented and applied during the last few decades and these robots perform nowadays more and more activities. The demands to their accuracy are rapidly increasing. The robots with parallel structure have undisputable advantages in higher stiffness and better modal properties, but the disadvantages are in the complexity of their control, small workspace and higher price due to multiple actuators and many mechanical components. The robots with serial kinematic have on the other hand advantages of the lower price and significantly larger workspace than the robots with parallel structures. The disadvantages are the lower stiffness due to chain of compliances in the motors, gearboxes and the robot arms. This brings many issues which have to be addressed. Several approaches to compensate these compliances have been analysed in several complex projects [1-3].

The strategy presented in this paper combines the usage of redundant set of sensors and application of the computed torques control method. Sensors in conventional serial robots are placed next to the electrical motors before the gearboxes. The prepared functional model [4] is equipped with additional sensors directly in revolute joints (behind the gearboxes) and also with deformation sensors sensing the arm bending and torsional deformations. Computed torques method realize the linearization of the dynamic system through the inverse dynamics model. The used functional model has four driving torques $\boldsymbol{\tau} = [M_1, M_2, M_3, M_4]^T$ ensuring the requested motion of the arm. The main structure of control strategy is shown in Fig. 1.

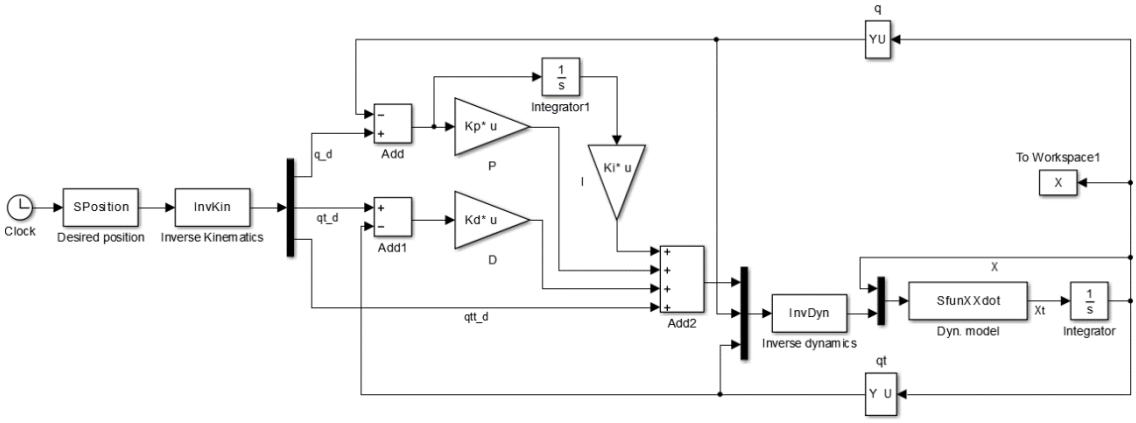

Fig. 1. Computed torque method control structure for robot chain

In order to optimize the accuracy of motion control of end-effector the controllers parameters must be tuned properly. Optimization was executed in three steps. Firstly the PID controllers have been optimized separately. There are 12 optimization parameters because of four PID controllers. Second step takes into account the dynamics of the robot chain, however with robot arms and gearboxes considered as ideally rigid. Any control of the physical system

is influenced by the sources of uncertainties. Here the uncertainties are mainly caused due to unknown payloads on the robot end-effector, modelling errors on the actuators and the unknown robot mass properties. The control law coefficients have been optimized for several randomly disturbed sets of robot parameters used within the inverse dynamics. The optimization is realized for the robot workspace (Fig. 2) using the selected trajectories (Fig. 3).

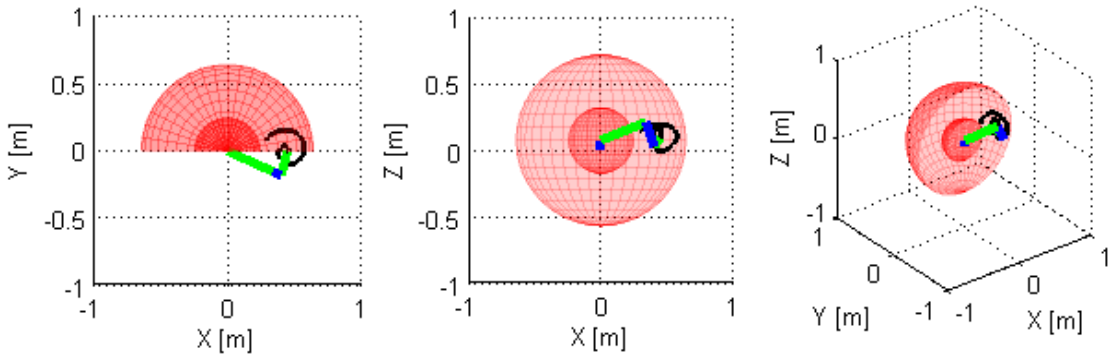

Fig. 2. Workspace of experimental robot chain

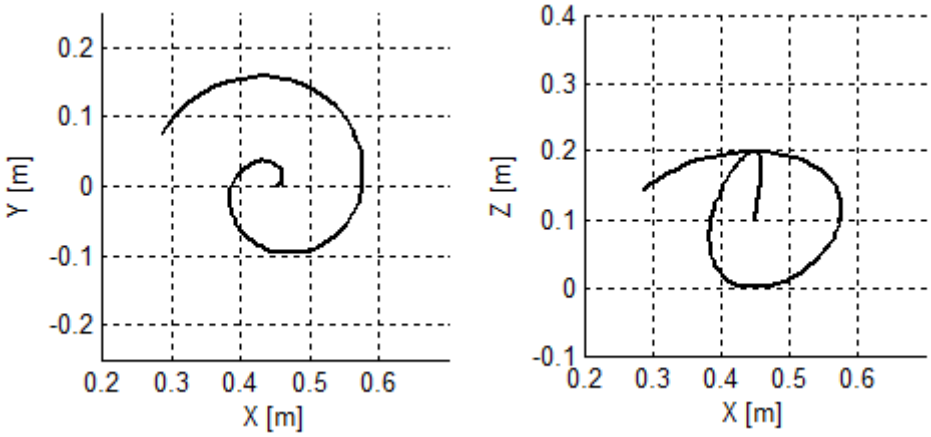

Fig. 3. Example of trajectory used for control law optimization

The final third step of the control law optimization considers the complete flexible dynamic model of the robot chain. The further development will combine the optimized Computed torques regulator with the H-infinity robust control strategy.

Acknowledgements

The authors appreciate the kind support by the grant GA13-39057S "Position Feedback Based Stiffness Increase of Robots by Redundant Measurement" of the Czech Science Foundation.

References

[1] Abele, E., ADVOCUT, Abschlussbericht BMBF – Verbundprojekt, Adaptive vollserielle Werkzeugmaschine mit hochintegriertem mechatronischen Fräsmodul zur HSCBearbeitung, PTW, TU Darmstadt, Darmstadt, 2007.

[2] Lehmann, C., Pellicciari, M., Drust, M., Gunnink, J. W., Machining with industrial robots: the COMET project approach, Communications in Computer and Information Science 371 (2013) 27-36.

[3] Sörnmo, O., Olofsson, B., Schneider, U., Robertsson, A., Johansson, R., Increasing the milling accuracy for industrial robots using a piezo-actuated high dynamic micro manipulator, The 2012 IEEE/ASME International Conference on Advanced Intelligent Mechatronics, Kaohsiung, 2012, pp. 104-110.

[4] Volech, J., Mráz, L., Šika, Z., Valášek, M., Model of flexible robot with deformation detection, Procedia engineering 96 (2014) 510-516.

COMPUTATIONAL MECHANICS 2015
31st conference with international participation
Špičák
November 9 - 11, 2015

Application of Euler parameters for the development of MBS human body model

J. Špička[a]

[a] *New Technologies - Research Centre, University of West Bohemia, Univerzitní 8, 306 14 Plzeň, Czech Republic*

Purpose of this paper is to introduce the principle of the rigid body spatial motion and consequently the modelling of the human body within the multibody approach. The description of the dynamical behaviour of the human body or the body's parts is under high interest of the researches nowadays. This paper deals with the elementary description of the kinematics and dynamics of the rigid body, see Fig. 1a, and tree-like structure of constrained rigid bodies, see Fig. 1b, respectively. This work is focused primarily on the parametrization of the spatial rotations. The standard equation describing the orientation of the rigid body in the space using Euler angles is

$$\mathbf{r}^i = \mathbf{R}^i + \mathbf{A}^i_{pre}(\psi)\ \mathbf{A}^i_{nut}(\vartheta)\ \mathbf{A}^i_{spin}(\varphi), \tag{1}$$

where $\mathbf{r}^i$ are coordinates of any point on the body defined in global coordinate system, $\mathbf{R}^i$ is the global position vector of the origin of the reference (body-fixed) coordinate system and $\mathbf{A}^i_{pre}(\psi)$, $\mathbf{A}^i_{nut}(\vartheta)$ and $\mathbf{A}^i_{spin}(\varphi)$ are the transformation matrices of the precession, nutation and spin motion, respectively. The variables $[\psi, \vartheta, \varphi]^T$ are the well-known Euler angles. However, this concept suffers with some undesirable troubles such as singular positions and consequently the ill-numerical stability. For the sequence of the mutual rotations applied here, the singular positions are close to $\vartheta = 0$ rad and $\vartheta = \pm n\pi$ rad, $n = 1, 2, 3, ...N$.

This paper is closely connected with the work [4], which describes the human body model. Generally, the relative internal motion between bodies are not limited. Thus there always exist time t where the nutation angle ϑ meets such singular position and the process of the numerical integration becomes unstable. There exists some methods, how to avoid such positions [3], but

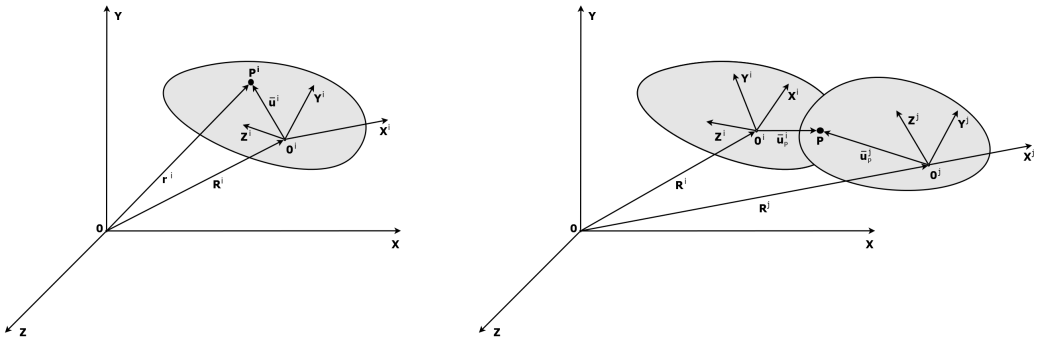

(a) One body (b) Constrained bodies

Fig. 1. Rigid body

generally they are not very precise and close to reality since they do not deal with crossing such values. Since the joints of human body model, which is closely connected with this work, are range-unlimited and thus the nutation angle ϑ always meets such singular values. Consequently the Euler angles are not sufficient tool here.

The rotation motion of the joints is currently unlimited. Hence, the concept of Euler parameters, which is free of these deficiencies, is being investigated in order to solve the problem with the singular positions [1, 2].

The four Euler parameters can be expressed in terms of the components of the unit vector along one axes of rotation (called instantaneous) together with the angle of rotation. The concept of Euler parameters consist of 7 coordinates (3 translational and 4 Euler parameters) but the body in space has only six degree of freedom (3 translations and 3 rotations). Thus the Euler parameters cannot be totally independent since the constraint equation between is

$$\sum_{k=0}^{3}(\beta_k)^2 = 1 \quad \Leftrightarrow \quad \boldsymbol{\beta}^T\boldsymbol{\beta} - 1 = 0 \tag{2}$$

and two-times differentiated of Eq. (2) with respect to the time gives the form

$$\dot{\boldsymbol{\beta}}^T\dot{\boldsymbol{\beta}} + \boldsymbol{\beta}\ddot{\boldsymbol{\beta}} = 0. \tag{3}$$

The Newton-Euler equation of motion for one rigid body expressed in global coordinates with respect to the Euler parameters together with the second derivatives of constraint Eq. (3) gives the form

$$\begin{bmatrix}\mathbf{I}_{\theta\theta}\mathbf{G}\\ \boldsymbol{\beta}^T\end{bmatrix}\ddot{\boldsymbol{\beta}} + \begin{bmatrix}\mathbf{I}_{\theta\theta}\dot{\mathbf{G}} + \dot{\mathbf{G}}\mathbf{G}^T\mathbf{I}_{\theta\theta}\mathbf{G}\\ \dot{\boldsymbol{\beta}}^T\end{bmatrix}\dot{\boldsymbol{\beta}} = \begin{bmatrix}\sum \mathbf{u}_k^j \times \mathbf{F}_k^j\\ 0\end{bmatrix}, \tag{4}$$

where $\mathbf{I}_{\theta\theta}$ is the 3x3 symmetric inertia matrix defined in global coordinate system, $\mathbf{F}_k^j$ is vector of external forces loading the body at point $\mathbf{u}_k^j$ and $\mathbf{G}$ is the matrix defining the relationship between vector of angular velocities $\boldsymbol{\omega}$ and derivatives of Euler parameters $\dot{\boldsymbol{\beta}}$ as

$$\boldsymbol{\omega} = \mathbf{G}\dot{\boldsymbol{\beta}}. \tag{5}$$

The concept of Euler parameters application for unlimited range of rotation is introduced here. Eq. (4) can solve the problem with the singular positions, however it is still need to improved for the purpose of human body model.

Acknowledgement

This work was supported by internal grant project SGS-2014-017.

References

[1] Nicravesh, P. E., Computer-aided analysis of mechanical system, Prentice-Hall Inc., 1988.

[2] Shabana, A. A., Computational dynamics, John Wiley & Son, 2009.

[3] Singla, P., Mortari, D., Junkins, J. L., How to avoid singularity for Euler angle set, Proceedings of the AAS Space Flight Mechanics Conference, Hawaii, 2014.

[4] Špička, J., Hynčík, L., Hajžman, M., Multibody model of a human body, Proceeding of the 30th Computational Mechanics, Špičák, Czech Republic, 2014, pp. 137-138.

COMPUTATIONAL MECHANICS 2015
31st conference with international participation
Špičák
November 9 - 11, 2015

Crack propagation study in layered alumina-zirconia ceramic composite

K. Štegnerová [a,b], L. Náhlík [a,b], P. Hutař [a]

[a] CEITEC IPM, Institute of Physics of Materials, Academy of Science of the Czech Republic, Žižkova 22, 616 62 Brno, Czech Republic
[b] Institute of Solid Mechanics, Mechatronics and Biomechanics, Faculty of Mechanical Engineering, Brno University of Technology, Technická 2896/2, 616 69 Brno, Czech Republic

The contribution is focused on the crack behaviour in layered ceramic composites with strong interfaces based on alumina-zirconia. Layered design of ceramics helps to improve a resistance to crack propagation in comparison with monolithic ceramics. Material interfaces and internal residual stresses can significantly influence crack propagation direction; they can cause deflection of crack from its original direction and/or crack bifurcation, which was observed during experiments [1, 3, 5].

Residual stresses are developed during the sintering process, when the material is cooling down from the stress free temperature 1200°C to the room temperature. This occurs due to the different coefficients of thermal expansion of the individual constituents.

Crack propagation through the laminate body was estimated using finite elements method (FEM) to obtain the stress distribution field and criterion derived on the base of the strain energy density factor S [4]:

$$S = a_{11}K_I^2 + 2a_{12}K_IK_{II} + a_{22}K_{II}^2, \tag{1}$$

where a_{ij} are functions of elastic constants and polar coordinates, K_I and K_{II} are stress intensity factors corresponding to mode *I* and *II*. The crack will propagate if the value of S reaches its critical value S_{cr}, i.e. for $S = S_{cr}$. The critical value can be correlated with fracture toughness of the material. The angle of next crack propagation direction θ_0 can be determined from the following conditions:

$$\left(\frac{\partial S}{\partial \theta}\right)_{\theta=\theta_0} = 0 \ \wedge \left(\frac{\partial^2 S}{\partial \theta^2}\right)_{\theta=\theta_0} > 0. \tag{2}$$

Two-dimensional numerical model was developed according to [2]. The model consists of 9 layers: 5 made of ATZ (alumina with tetragonal zirconia) with thickness 0.5170 mm and 4 layers made of AMZ (alumina with monoclinic zirconia) with thickness 0.1038 mm. Simulations were focused on the description of crack propagation through the second (AMZ) layer with compressive residual stresses. Fracture toughness of AMZ layer is 2.6 MPa.m$^{0.5}$.

Boundary conditions corresponded to four-point-bending. The laminate was subjected to the thermal load (ΔT = 1180°C). The value of residual stresses due to the thermal load was 109.8 MPa in ATZ layers and -683.6 MPa in AMZ layers.

The propagating crack was modelled perpendicularly to the first interface (thought the ATZ layer) and terminated just behind the ATZ/AMZ interface. All calculations were performed assuming the linear elastic fracture mechanics, under small scale yielding condition and plane strain condition. In each step, the mechanical loading force increases until the condition $S = S_{cr}$ isn´t fulfilled. Then the angle θ_0 of further crack propagation is estimated

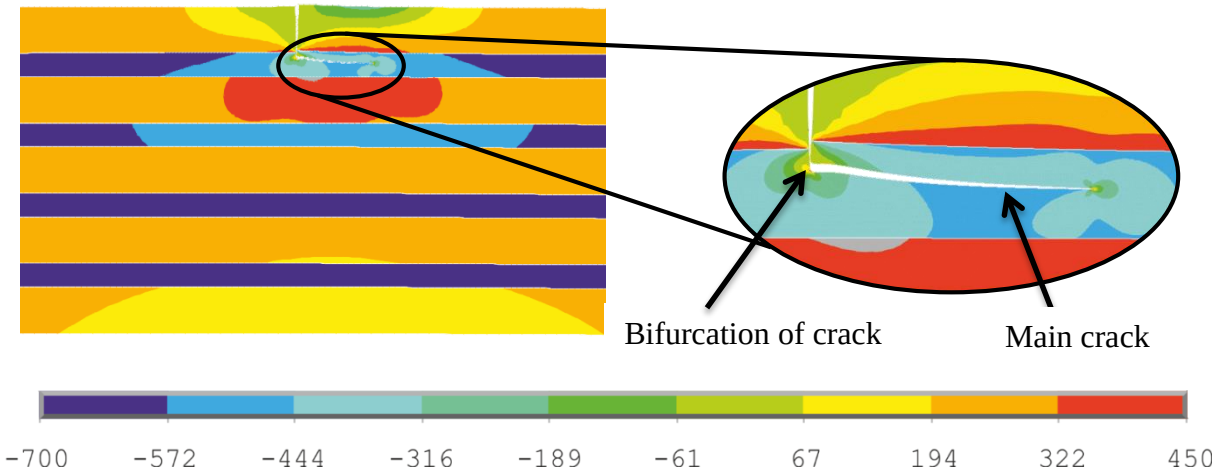

Fig. 1. Stress distribution in the ceramic laminate in longitudinal direction [MPa] with detail of crack path in the layer with compressive residual stresses

and the crack is extended by the increment 1 μm. Hundreds of calculations were performed to obtained realistic crack path in compressive AMZ layer during the simulation, see Fig.1.

Propagation of the crack was stopped after few steps of simulation due to presence of high compressive residual stresses which cause strong decrease of *S* factor under its critical value. For further crack propagation the external force was necessary to add. After that the crack was strongly deflected from the original direction and then the crack started to propagate in new direction almost parallel with material interface.

A new small stress concentrator was created in the location of the crack deflection. The main crack was progressively extended and fracture parameters at the new stress concentrator tip were determined. Favourable conditions for crack bifurcation (extension of the second crack tip from the stress concentrator) appeared for the certain depth of the main crack.

More energy is absorbed to create a new fracture surfaces in this case. This fact leads to the better fracture behaviour (higher fracture toughness) of the ceramic composite in comparison to the monolithic one.

The procedure suggested and the resulted data contribute to better understanding of fracture behavior and damage mechanism of ceramic composites.

Acknowledgements

This work was supported through the Grant No. 15-09347S of the Czech Science Foundation and the specific academic research grant No. FSI-S-14-2311 provided to Brno University of Technology, Faculty of Mechanical Engineering.

References

[1] Bermejo, R., Danzer, R., High failure resistance layered ceramics using crack bifurcation and interface delamination as reinforcement mechanisms, Engineering Fracture Mechanics 77 (2010) 2126–2135.
[2] Bermejo, R., Pascual, J., Lube, T., Danzer, R., Optimal strength and toughness of Al2O3-ZrO2 laminates designed with external or internal compressive layers, Journal of the European Ceramic Society 28 (2008) 1575-1583.
[3] Náhlík, L., Šestáková, L., Hutař, P., Bermejo, R., Prediction of crack propagation in layered ceramics with strong interfaces, Engineering Fracture Mechanics 77 (2010) 2192–2199.
[4] Sih, G. C., Methods of analysis and solutions of the crack problems, Noordhoff Intern. Publishing, Leyden, 1973.
[5] Ševeček, O., Bermejo, R., Kotoul, M., Prediction of the crack bifurcation in layered ceramics with high residual stresses, Engineering Fracture Mechanics 108 (2013) 120–138.

COMPUTATIONAL MECHANICS 2015
31st conference with international participation
Špičák
November 9 - 11, 2015

Improved formula for fully developed mean flow velocity profile for both laminar and turbulent flow in tube

J. Štigler [a]

[a] *Victor Kaplan's Department of Fluid Engineering, Brno University of Technology, Faculty of Mechanical Engineering, Technická 2, 616 69 Brno, Czech Republic*

The velocity profile in a tube for fully developed mean flow has been in a center of an interest for a long time. In the case of the laminar flow it is well known parabolical profile.

In the case of the turbulent flow it is quite difficult to find some simple expression for the fully developed mean flow velocity profile. Many different expressions are listed in the literature [1]. It is difficult to say which of them is better because it is not so easy to find an experimental data to verify them. Probably the most popularly known formula is the Power law formula taken from [4] or [1].

$$\frac{v}{v_{(avg)}} = (n+1)\left(1-\frac{r}{R}\right)^{1/n}. \tag{1}$$

This formula has some discrepancies. Therefore another improved variation of power law velocity profile formula is introduced it is also taken from [1].

$$\frac{v}{v_{(avg)}} = (n+1)\left(1-\frac{r^2}{R^2}\right)^{1/n}. \tag{2}$$

The coefficient n is a function of Reynolds number (Re).

$$\frac{1}{n} = 1+\sqrt[6]{\frac{\mathrm{Re}}{50}}. \tag{3}$$

Another formula, also mentioned in the [1], is the formula introduced by Štigler in [2].

$$\frac{v}{v_{(avg)}} = \frac{(N+3)}{(N+1)}\left(1-\frac{r^{N+1}}{R^{N+1}}\right). \tag{4}$$

The coefficient N can be expressed from the pressure drop in tube.

$$N = \lambda.\frac{Re}{16.}-3. \tag{5}$$

This formula is not so precise. The velocity profiles are too flat. It means that the curvature radius of profile is infinite in the centerline of tube. But this formula can be improved and this is the aim of this paper. The improved velocity profile for the turbulent flow has been derived by applying the same ideas as the profile in [2]. The basic idea is to express velocity induced by a vorticity which is continuously distributed over the pipe cross-section this idea is presented in [2]. The unknown coefficients are derived from these known parameters a pipe flow rate, a centerline velocity and a pressure drop. The improved formula for velocity profile has a form

$$\frac{v}{v_{(avg)}} = 2.\left(1-\frac{r^2}{R^2}\right)+\frac{(1-g)}{(N-1)}.\left[(N+3).\left(1-\frac{r^{N+1}}{R^{N+1}}\right)-2.(N+1).\left(1-\frac{r^2}{R^2}\right)\right], \tag{6}$$

where

$$N = \left(\frac{\lambda . Re}{16} - 4 \right) . \frac{1}{(1-g)} - 1 \tag{7}$$

and

$$g = \frac{v_{(max)} - v_{(avg)}}{v_{(avg)}} . \tag{8}$$

The value of the exponent *N* is derived from the pressure drop. The function *g* expresses normalized velocity difference. Velocity difference is normalized by average velocity. This function *g* is very similar to coefficient *n* in case of Power law velocity profile. The coefficient *N* is a function of a Re (Reynolds number) and a roughness of wall. Function *g* is assumed to be the function only Re.

Zagarola and Smits provided an experiment in which they measured velocity profiles for vide range of Re. This experiment is described in [3]. Their data were used to validate the new formula. The comparison of mean flow velocity profile formulas for two different Reynolds numbers with experimental data taken from [3] is depicted in Fig. 1.

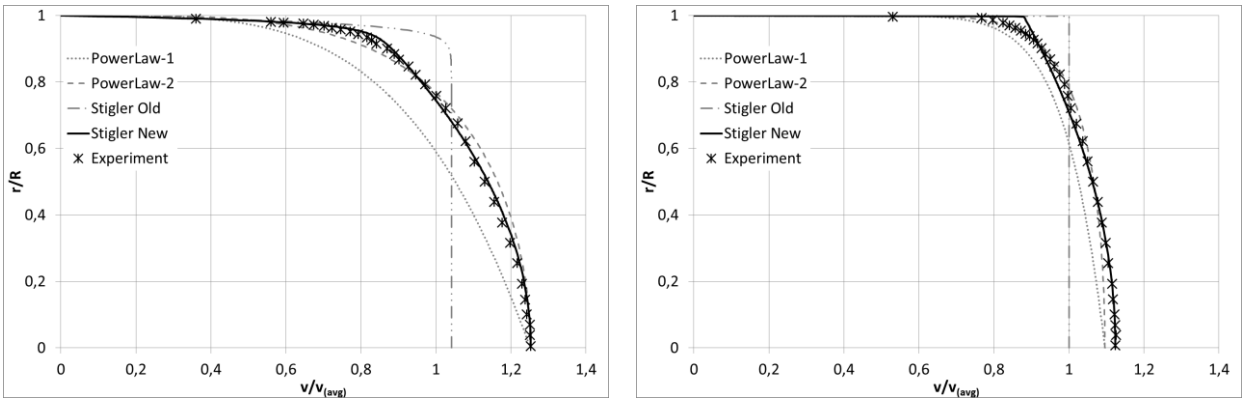

a) Re=35 000 b) Re= 35 000 000

Fig. 1. Comparison of normalized power law velocity profile expression (3) and new formula for velocity profile expression (6) with experimental data presented by Zagarola [4] for different Reynolds number

The new improved formula is in very good agreement with experimental data in case of lower Re (35 000). The comparison of different formulas and experimental data for high Re (35 000 000) is worst and the profile obtained from the new formula is again too flat.

The new formula is also possible to apply for the mean flow velocity profile for a flow of a magnetic fluid through a magnetic field. The function *g* and the exponent N will be then a function of the magnetic induction and the permeability of fluid.

Acknowledgements

This work has been supported by the grant project GA101/15-06621S.

References

[1] Matas, R., Cibera, V., Syka, T., Modelling of flow in pipes and ultrasonic flowmeter bodies, EPJ Web of Conferences 67, 02073 (2014).
[2] Štigler, J., Analytical velocity profile in tube for laminar and turbulent flow, Proceedings of the 31st Setkání kateder mechanicky tekutin a termomechaniky, Mikulov, Czech Republic, 2012.
[3] Zagarola, M. V., Smits, A. J., Mean-flow scaling of turbulent pipe flow, Journal of Fluid Mechanics 373 (1998) 33-79.
[4] Munson, B. R., Young, D. F., Okiishi, T. H., Fundamentals of fluid mechanics, Fifth Edition, John Wiley & Sons, New York, 2006.

COMPUTATIONAL MECHANICS 2015
31st conference with international participation
Špičák
November 9 - 11, 2015

Modelling of ionic transport in cortical bone porous structure

J. Turjanicová[a,b], E. Rohan[a]

[a] NTIS – New Technologies for the Information Society, Faculty of Applied Sciences, University of West Bohemia, Univerzitní 8, 306 14 Plzeň, Czech Republic

[b] Department of Mechanics, Faculty of Applied Sciences, University of West Bohemia, Univerzitní 8, 306 14 Plzeň, Czech Republic

Cortical bone tissue, as well as many others biological tissues, can be considered as porous medium consisting of two phases: rigid collagen-apatite matrix with a small electric charge and pores saturated by a so-called bone fluid. Bone fluid is in our case seen as an electrolyte solution of two species of charged monovalent ions of opposite polarizations (cations Na+ and anions Cl-). The trasport of such electrolyte through a network of small channels with charged surface is controled by coupling between the electric field, Stokes flow and the convection-diffusion transport phenomena [2].

The electrokinetic phenomena, such as the electroosmotic mechanism, can influence fluid flow throught porous media. They occure due to the electric double layer (EDL), which is formed by interaction between charged solid-fluid interface and ionied solution. The EDL is an union of Stern layer formed by imobile ions with thickness of one molecular diameter and diffuse layer where the ions density varies smoothly. Outside this layer, in the remaining bulk fluid, the solvent can be considered as locally electro-neutral [1].

Usually, three levels of porosity are distinguished in the cortical bone tissue: vascular porosity, lacuno-canalicular porosity and porosity in the collagen-apatite matrix. Our present work is focused on the ionic transport at the lacuno-canalicular porosity level with characteristic scale $l \approx 10\,\mathrm{nm}$, further referred to as the microscopic level. Thus, we consider cortical bone tissue as porous medium, occupying domain Ω with pore space denoted by Ω^ε, with superscript ε referring to a ration between the pore size and dimension of the porous medium. Pore surface is charged with small charge σ, thus the ions in the pore filling fluid are subjected to a static electric field $\mathbf{E}$, which corresponds to the exterior potential Ψ^{ext}, $\mathbf{E} = \nabla\Psi^{ext}$.

Following the procedure from the paper [1], we can introduce a decomposed form for following hydrodynamic and electrostatic unknowns: Fluid velocity $\mathbf{u}^\varepsilon$, pressure p^ε, electrostatic potential Ψ^ε and concentration of ith ionic species $n_i^\varepsilon, (i = 1, 2)$, can be written as

$$n_i^\varepsilon = n_i^{0,\varepsilon}(x) + \delta n_i^\varepsilon(x), \qquad \Psi_i^\varepsilon = \Psi_i^{0,\varepsilon}(x) + \delta\Psi_i^\varepsilon(x), \tag{1}$$

$$\mathbf{u}_i^\varepsilon = \mathbf{u}_i^{0,\varepsilon}(x) + \delta\mathbf{u}_i^\varepsilon(x), \qquad p_i^\varepsilon = p_i^{0,\varepsilon}(x) + \delta p_i^\varepsilon(x), \tag{2}$$

where the superscript $\sqcup^0$ designates equilibrium quantities corresponding to zero external body forces and external electric potential. The prefix δ indicates a perturbation.

These forms of unknown and the bulk electroneutrality condition is needed to introduce a mathematical model describing macroscopic ion transport phenomena in porous medium. Such dimensionless linearized model was introduced in [1].

Coupled fluid flow and ionic transport

$$\varepsilon^2 \Delta \mathbf{u}^\varepsilon - \nabla P^\varepsilon = \mathbf{f}^* - \sum_{j=1}^{N=2} z_j n_j^{0,\varepsilon}(x)(\nabla \Psi_j^\varepsilon + \mathbf{E}^*) \quad \text{in } \Omega^\varepsilon, \tag{3}$$

$$\text{div}\mathbf{u}^\varepsilon = 0 \text{ in } \Omega^\varepsilon, \quad \mathbf{u}^\varepsilon = 0 \quad \text{on } \partial\Omega^\varepsilon \setminus \partial\Omega, \tag{4}$$

$$\text{div}\left(n_j^{0,\varepsilon}(x) \left(\nabla \Psi_j^\varepsilon + \mathbf{E}^* + \frac{\text{Pe}_j}{z_j} \mathbf{u}^\varepsilon \right) \right) = 0 \quad \text{in } \Omega^\varepsilon \text{ for } j = 1, 2, \tag{5}$$

$$(\nabla \Psi_j^\varepsilon + \mathbf{E}^*) \cdot \mathbf{n} = 0 \quad \text{on } \partial\Omega^\varepsilon \setminus \partial\Omega \text{ for } j = 1, 2, \tag{6}$$

where z_i is the valency of ith ionic species, Pe_j is Peclet number, $\mathbf{f}^*$ is dimensionless external body force, $\mathbf{E}^*$ is dimensionless electric field and $\mathbf{n}$ is unit normal vector. For convenience, global pressure P^ε was introduced.

Electrostatic field — Poisson-Boltzmann equation

$$-\varepsilon^2 \Delta \Psi^\varepsilon = \left(\frac{l}{\lambda_D} \right)^2 \sum_{j=1}^{N=2} z_j n_j^{0,\varepsilon}(x) \quad \text{in } \Omega^\varepsilon, \tag{7}$$

$$\varepsilon \nabla \Psi^\varepsilon \cdot \mathbf{n} = -\sigma \quad \text{on } \partial\Omega^\varepsilon \setminus \partial\Omega. \tag{8}$$

The homogenization method was applied to derive a macroscopic model, see [1], so that ionic transport problem can be solved on the cubic local representative cell Y composed of solid Y_s and fluid Y_f part. In the homogenized model, the non-linearity occure in the Poisson-Boltzmann cell problem for potential distribution. This problem is treated by means of numerical computation. After finding solution for potential Ψ^0 distribution we can compute the coefficients for cell problems. Local cell problems are solved on geometry representation of periodic cells Y and yield so-called corrector functions. Finally effective coefficients can be evaluated. For numerical simulation we used the FEM based software *SfePy*. We consider a few different representations of microstructure in order to study its influence on potential distribution on microscopic cell and behavior on the macroscopic scale.

Acknowledgments

The research was supported in part by project LO1506 of the Czech Ministry of Education, Youth and Sports. Jana Turjanicová is also grateful for the support of her work by project SGS-2013-026.

References

[1] Allaire, G., Brizzi, R., Dufrêche, J.F., Mikelić, A., Piatnitski, A., Ion transport in porous media: Derivation of the macroscopic equations using upscaling and properties of effective coefficients, Computational Geosciences 17 (3) (2013) 479-495.

[2] Allaire, G., Brizzi, R., Dufrêche, J.F., Mikelić, A., Piatnitski, A., Role of non-ideality for the ion transport in porous media: Derivation of the macroscopic equations using upscaling, Physica D: Nonlinear Phenomena 282 (2014) 39-60.

COMPUTATIONAL MECHANICS 2015
31st conference with international participation
Špičák
November 9 - 11, 2015

Simulation and experimental calibration of mechatronic flexible joint

M. Valášek [a], V. Bauma[a], T. Vampola[a]

[a] *Faculty of Mechanical Engineering, CTU in Prague, Technická 4, 166 07 Praha 6, Czech Republic*

The paper deals with the simulation of self-calibration and experimental calibration and self-calibration of mechatronic flexible joint. The flexible joint is a compliant body fulfilling the function of movable connection of other bodies. The mechatronic flexible joint is a flexible joint that is actuated and measured [1] (Fig. 1). Flexible joints are used in compliant mechanisms. If they are actuated they are called mechatronic flexible joint. However, the examples are compliant arms of traditional robots as well as inflated/deflated smart structures or compliant mechanisms from hyperelastic materials with traditional as well as not traditional actuators (Fig. 2).

The ultimate challenge is the development of methods using computation and efficient measurement for determination of kinematic transformation of the mechatronic flexible joint in order to enable its precise position control under real operation condition (especially loading). If the position of flexible mechatronic joint is measured by an external device and it leads to the determination of the kinematic transformation then it is traditional calibration. If the motion of flexible mechatronic joint is measured by only internal sensors (e.g. by force sensors and strain-gauges in Fig. 1, 2) without an external device and it leads to the determination of the kinematic transformation then it is self-calibration. The self-calibration is typically used for mechanisms with parallel kinematic structures.

The self-calibration concept was developed also for flexible mechatronic joints [1]. Let describe and measure the position of flexible mechatronic joint ([x, y, φ] of the flange in Fig. 1, 2) by at least two sets of sufficient variables s_{kj}, k=1,2 (forces and deformations in Fig. 1, 2). Using these variables efficient regression descriptions were developed [1]. If the

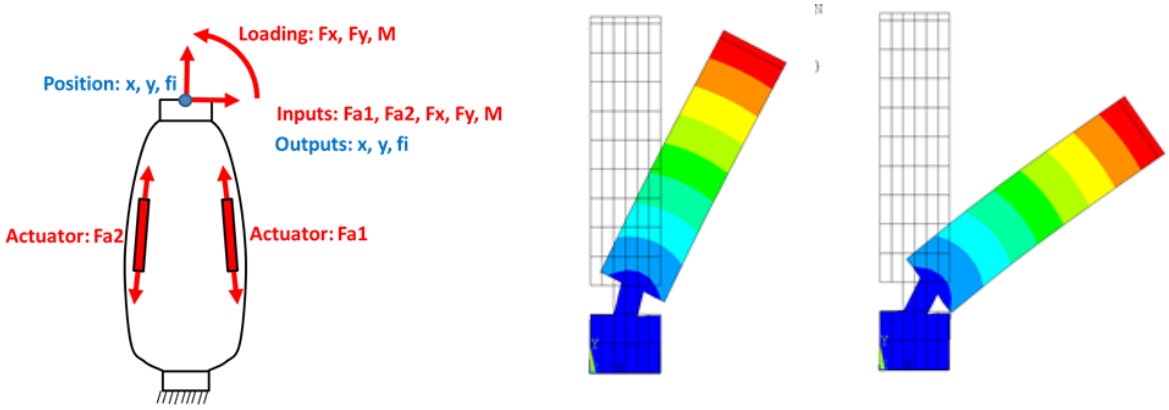

Fig. 1. Mechatronic flexible joint and its FEM model during its motion

regression expression is applied then it holds for the description of the position [x, y, φ] of the upper flange (Fig. 1, 2)

$$\begin{aligned} x &= \sum_i a_{kxi} b_i(s_{kj}) \\ y &= \sum_i a_{kyi} b_i(s_{kj}) \,, \\ \varphi &= \sum_i a_{k\varphi i} b_i(s_{kj}) \end{aligned} \tag{1}$$

where a_{kxi}, a_{kyi}, $a_{k\phi i}$ are regression coefficients for the base regression functions $b_i(s_{kj})$ in measured values s_{kj}. Comparing both set of equations (1) for k=1 and k=2 the following equations for calibration regression can be derived

$$\begin{aligned} \sum_i a_{1xi} b_i(s_{1j}) &= \sum_i a_{2xi} b_i(s_{2j}) \\ \sum_i a_{1yi} b_i(s_{1j}) &= \sum_i a_{2yi} b_i(s_{2j}) \,. \\ \sum_i a_{1\varphi i} b_i(s_{1j}) &= \sum_i a_{2\varphi i} b_i(s_{2j}) \end{aligned} \tag{2}$$

The equations (2) can be solved by regression for the unknown coefficients under the important assumption that within the measurements (sensors) some lengths are included, otherwise some external measurement of absolute positions is necessary. The knowledge of coefficients is enough for the kinematic transformation of flexible mechatronic joint in (1).

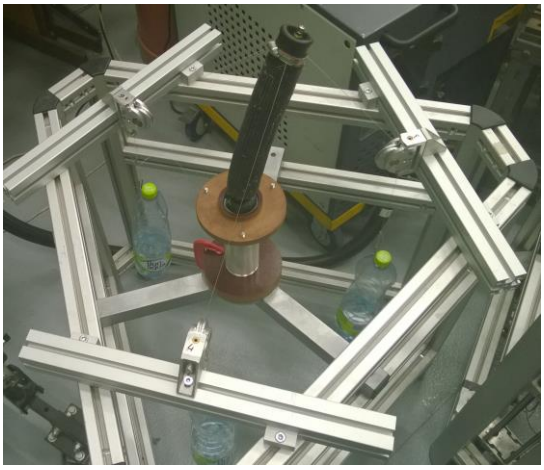

Fig. 2. Experimental set-up of mechatronic flexible joint

The open challenge is whether the redundant measurement would enable to carry out the self-calibration as it is possible for traditional robotic structures with rigid bodies and joints. The paper describes that it is possible. It demonstrates it by simulation and experiment.

Acknowledgements

The authors appreciate the kind support by the research grant P101/13-39100S, Mechatronic flexible joint.

References

[1] Valasek, M., et al., Motion description of mechatronic flexible joint, Proceedings of the 7th Eccomas Thematic Conference on Smart Structures and Materials SMART 2015, IDMEC, Lisbon, 2015, pp. 1-11.

COMPUTATIONAL MECHANICS 2015
31st conference with international participation
Špičák
November 9 - 11, 2015

Numerical reconstruction of the videokymography records – sensitivity of the computational model

T. Vampola [a], J. Horáček[b]

[a] Faculty of Mechanical Engineering, CTU in Prague, Technická 4, 166 00 Prague, Czech Republicc
[b] Institute of Thermomechanics, Czech Academy of Sciences, Dolejškova 1401/5, 182 00 Praha 8, Czech Republic

Voice problems are common especially in professional voice users like teachers, actors and singers. The main reason may be a fatigue because of mechanical loading of the vocal fold tissue during voice production [1]. Design of a model of the human vocal folds, which would enable to model some pathological situations and voice disorders, is becoming an important part of the voice research. With regard to the clinical practice, when basic investigative techniques include video-kymography, the question arises of whether the character of vibration recorded by videographic or the high-speed camera can be used for prediction of the damage to the vocal cords. In this contribution the reconstructed video-kymography records [2] from the numerical simulation of the vocal fold vibration are used for evaluation of the character of vibration of the damage vocal fold.

The 3D complex dynamic FE model of the human larynx was developed by transferring the CT image data from the DICOM format to the FE mesh. The developed fully parameterized 3D FE model enables to vary the thickness and material properties of the individual layers and to take into account longitudinal pretension and adduction of the vocal folds by positioning of the arytenoids and thyroid cartilages – see Fig.1.

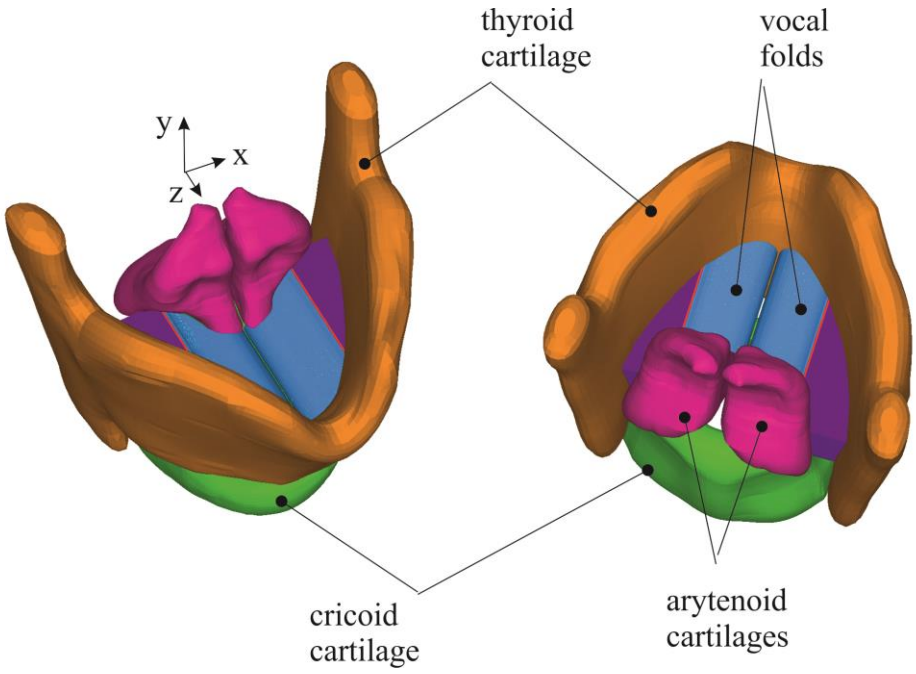

Fig. 1. FE model of the human larynx with the vocal folds between the arytenoids and thyroid cartilages

The geometrical configuration of the cross-section of the vocal fold was taken according to [3] and the CT snaps. Three layers of vocal fold tissue were considered. An additional superficial lamina propria layer formed by incompressible liquid was used and tested for improving character of numerically simulated vibration modes of the vocal fold.

The nonlinear elasticity theory for large-strain deformations with the linear transversal isotropic material model was used for modelling of the vocal fold tissue, where the matrix of the elastic constants in strain-stress relations is defined according [4].

The motion of the vocal folds was numerically simulated for a prescribed intraglottal pressure *p(y,t)* dependent on the vertical coordinate and given by a periodic function in the time domain. The intraglottal pressure signal loading the vocal fold surface was generated by the 2D aero elastic model [5] of the vocal folds during the vocal folds self-sustained vibrations. The computed deformations were used for reconstruction of the video-kymographics records of the human vocal fold vibration. Fig. 2 demonstrates the sensitivity of vibration patterns in video-kimographs for three and four layer model.

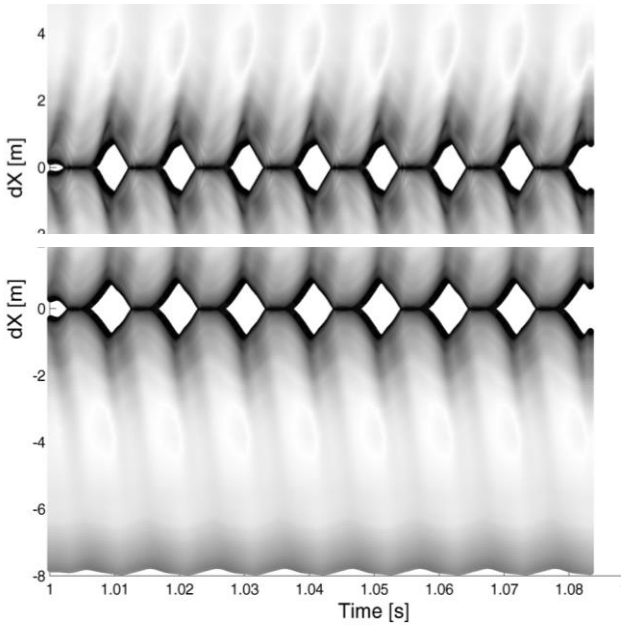

Fig. 2. Reconstruction of the video-kymographic records for the model with and without liquid layer

Acknowledgements

The research is supported by the Grant Agency of the Czech Republic by project No P101/12/1306 “Biomechanical modelling of human voice production - way to artificial vocal folds“.

References

[1] Titze, I. R., Mechanical stress in phonation, Journal of Voice 8(2) (1994) 99-105.
[2] Švec, J. G., Schutte, H. K., Videokymography: high-speed line scanning of vocal fold vibration, Journal of Voice 10 (1996) 201-205.
[3] Hirano, M., Phonosurgery, basic and clinical investigations, The 76th Annular Convention of the Oto-Rhino-Laryngological Society of Japan, 1975.
[4] Luo, H., Mittal, R., Zheng, X., Bielamowicz, S. A., Walsh, R. J., Hahn, J. K., An immersed boundary method for flow-structure interaction in biology systems with application to phonation, Journal of Computational Physics 227 (2008) 9303-9332.
[5] Horáček, J., Laukkanen, A. M., Šidlof, P., Estimation of impact stress using an aeroelastic model of voice production, Logopedics Phoniatrics Vocology 37 (2007) 185-192.

COMPUTATIONAL MECHANICS 2015
31st conference with international participation
Špičák
November 9 - 11, 2015

Adaptive calibration of measurement model of flexible robot end-effector position using internal sensors

J. Volech [a], Z. Šika [a], T. Skopec [a], M. Valášek [a]

[a] *Faculty of Mechanical Engineering, CTU in Prague, Technická 4, Praha 6, 166 07, Czech republic*

The aim of the paper is to present adaptive calibration method for flexible robot arm. The new adaptive calibration method that extends the geometrical calibration of mechanisms from calibration of only dimensions and kinematical joints positions

$$\boldsymbol{f}(\boldsymbol{d},\boldsymbol{s},\boldsymbol{v}) = 0\,, \tag{1}$$

into the calibration of kinematic joint shape imperfections [1]. The aim is to improve the appropriate complexity of the model for the evaluation of the end-effector motion based on the internal sensors including the links deformation sensors. In order to improve overall calibration results the ideal models of kinematical joints are replaced with nonlinear models that adaptively adjust their complexity [3]. After preparing the input data, the logic of adaptive calibration algorithm that is described in [4] can be applied. This approach can be divided to four simplifying steps: Firstly must be created the initial calibration model and choose the validity functions. Then generate a collection of available variants for all available inputs for the given complexity i_c. In this step are also needed to compute validity functions of the given variant [2] and add the new calibration parameters and generate a new form of the constraint equation (3). The third step is to select best available variant (with lowest rank for the current value of the calibration complexity i_c). And the last step is to test the convergence, if the method converges it is logic to increase the value of complexity to $i_c = i_c + 1$ and continue with step 2.

This approach of the adaptive calibration is currently under development for the calibration of the robotic arm equipped with the additional sensors [5].

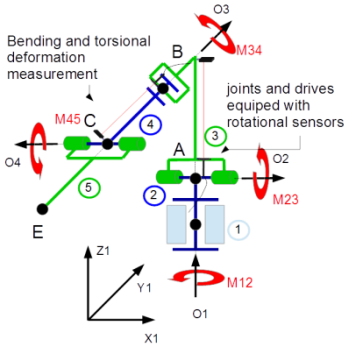

Fig. 1. Simple mechanism scheme with nonlinear kinematical joint

The Fig. 1 showed the simple mechanism scheme, for which the calibration process is need to be done in order to improve the precision of their control synthesis. It consists of two flexible arm (3, 4) and four kinematical joints that consist of compliant gearboxes. These deviations are measured with Renishaw revolute sensors and four quadrant laser diode

detectors. The position of the end-point E $\boldsymbol{E}_i = \left[x_{E_i},\ y_{E_i},\ z_{E_i},\ 1\right]^T$ is determine by the robots kinematical structure (2) in the coordinate system (x_1, y_1, z_1)

$$\boldsymbol{r}_{E_i} = \boldsymbol{T}_{\varphi_y}\left(\varphi_{y_{1_i}}\right)\boldsymbol{T}_y(l_{2_i})\boldsymbol{T}_{\varphi_z}\left(\varphi_{z_{1_i}}\right)\boldsymbol{T}_y(l_{3_i})\boldsymbol{T}_x\left(d_{x_{3_i}}\right)\boldsymbol{T}_z\left(d_{z_{3_i}}\right)$$
$$\boldsymbol{T}_{\varphi_x}\left(-\varphi_{x_{3_i}}\right)\boldsymbol{T}_x(-l_{4_i})\boldsymbol{T}_y\left(d_{y_{4_i}}\right)\boldsymbol{T}_z\left(d_{z_{4_i}}\right)\boldsymbol{T}_{\varphi_z}\left(\varphi_{z_{4_i}}\right)\boldsymbol{T}_x(-l_{5_i})\boldsymbol{r}_{ep_i}\,, \qquad (2)$$

where $d_{x_{3_i}}, d_{z_{3_i}}, d_{y_{4_i}}, d_{z_{4_i}}$ represents the robots arm deviations in their coordinate systems. Calibrated position of end-point E is influenced by considered orientation of the robots joints and the arm deviations. The boundary conditions for kinematical structure of robot arm is than assembled in following form

$$\left(x_{0_i}^I - x_{\boldsymbol{r}_{E_i}}^I\right)^2 + \left(y_{0_i}^I - y_{\boldsymbol{r}_{E_i}}^I\right)^2 + \left(z_{0_i}^I - z_{\boldsymbol{r}_{E_i}}^I\right)^2 - E_i^2 = 0\,. \qquad (3)$$

The individual kinematic pairs and their imperfection has to be described by their absolute LLM parameters of their end points, it also describes their orientations. This must be done specially for the flexible arms, where their deviations are measured. But it's not possible to calibrate all parameters so some of them must be removed from calibration process.

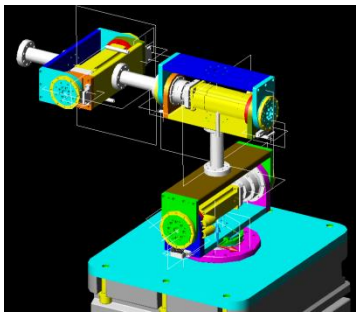

Fig. 2. Model of flexible robotic arm with additional deformation sensors

The adaptive calibration method will use the synchronous measurements from the laser-trackers external sensors for the motion of endpoint E (with mounted reflector) and the data from all sensors mounted on robot arm Fig. 2. With this approach is expected to receive more precise data about kinematical joints position and robots arm deviation and achieve the relatively precise calibration results.

Acknowledgements

The authors appreciate the kind support by the grant GA13-39057S "Position Feedback Based Stiffness Increase of Robots by Redundant Measurement" of the Czech Science Foundation.

References

[1] Nof, S. Y., Handbook of industrial robotics, John Wiley and Sons, New York, 1999.
[2] Nelles, O., Nonlinear system identification: From classical approaches to neural networks and fuzzy models, Springer, Berlin, 2001.
[3] Skopec, T., Šika, Z., Valášek, M., Measurement and improved calibration of parallel machine sliding star, Bulletin of Applied Mechanics 6 (23) 2010 52-56.
[4] Skopec, T., Šika, Z., Valášek, M., Calibration using adaptive model complexity for parallel and fiber-driven mechanisms, Robotica 2015. (article in press)
[5] Volech, J., Mráz, L., Šika, Z., Valášek, M., Model of flexible robot with deformation detection, Procedia Engineering 96 (2014) 510-516.

COMPUTATIONAL MECHANICS 2015
31st conference with international participation
Špičák
November 9 - 11, 2015

Study of wheel geometrical parameters for single-axle suspension by using elasto-kinematic model

T. Vrána [a], J. Bradáč [b], J. Kovanda [c]

[a] Department of Vehicles and Ground Transport, Faculty of Engineering, CULS Prague, Kamýcká 129, 165 21 Praha – Suchdol, Czech Republic
[b] Department of Automotive Technology, ŠKODA AUTO University, Na Karmeli 1457, 293 60 Mladá Boleslav, Czech Republic
[c] Department of Security Technologies and Engineering, Faculty of Transportation Sciences, CTU in Prague, Konviktská 20, 110 00 Praha 1, Czech Republic

This paper deals with constructing the elasto-kinematic computational model Multi-Body-Systems (MBS) type in the HyperWorks system. This computational model is then used for analyzing the geometric parameters such as wheel camber angle and wheel toe by single-axle suspension. These parameters and their changes during the vertical movement of the wheels play important role in the suspension design, because they highly influence the driving dynamics of the vehicle and thus contributing to high driving safety.

There are a lot of kinematic schemes given in [2] which can be effectively used for the implementation. The number of degrees of freedom DOF can be determined according to the equation (1).

$$DOF = 6 \cdot (u - 1) - 5 \cdot (R + T) - 3 \cdot SP \,, \tag{1}$$

where u is number of elements of axle suspension mechanism including the frame, R number of rotational kinematic pairs (KD), T number of sliding KD and SP number of spherical KD.

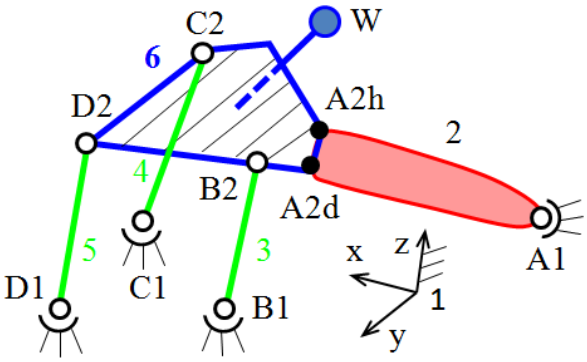

Fig. 1. Kinematical scheme of suspension

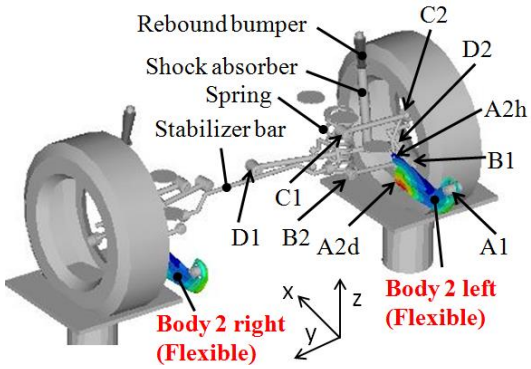

Fig. 2. MBS model

The MBS model of single-axle suspension was made according to kinematic scheme shown in Fig. 1. This mechanism requires for its correct function defined compliancy of the longitudinal arm. The simulation system HyperWorks [1] was used for this purpose. MotionView preprocessor was used for the preparation of the model, MotionSolve calculation tool for simulation analyses and HyperView post-processor and HyperGraph for processing results. MotionSolve numerically solve the equations of motion of the MBS model mechanical system prepared by the method of Lagrange equations, generally written in matrix

form according to equation (2).

$$\frac{\mathrm{d}}{\mathrm{dt}}\left(\frac{\partial \mathrm{E}}{\partial \dot{\mathrm{s}}}\right) - \frac{\partial \mathrm{E}}{\partial \mathrm{s}} = \mathrm{Q} + \frac{\partial \mathrm{f}^{\mathrm{T}}}{\partial \mathrm{s}}\lambda\,, \tag{2}$$

where E is kinetic energy, $\mathrm{s} = \left[\mathrm{s}_1, \mathrm{s}_2, \ldots \mathrm{s}_\mathrm{j}, \ldots \mathrm{s}_\mathrm{m}\right]^\mathrm{T}$ is vector of dependent coordinates, $\mathrm{f} = [\mathrm{f}_1, \mathrm{f}_2, \ldots \mathrm{f}_\mathrm{k}, \ldots \mathrm{f}_\mathrm{r}]^\mathrm{T}$ is vector of holonomic binding conditions, $\mathrm{Q} = \left[\mathrm{Q}_1, \mathrm{Q}_2, \ldots \mathrm{Q}_\mathrm{j}, \ldots \mathrm{Q}_\mathrm{m}\right]^\mathrm{T}$ is vector of generalized forces and $\lambda = [\lambda_1, \lambda_2, \ldots \lambda_\mathrm{k}, \ldots \lambda_\mathrm{r}]^\mathrm{T}$ is vector of Lagrange multipliers.

The introduced model consists of absolutely rigid bodies (transverse arms, knuckle and subframe) which are linked by flexible kinematic pairs representing the rubber-metal beds. Geometric position of kinematic pairs of suspension mechanism for the default variant of the model in the global coordinate system (GCS) is shown in Table 1.

Table 1. Coordinates of kinematic pair of single-axle suspension

Coordinate in GCS	Point of suspension kinematic pair – left side								
	A1	A2d	A2h	B1	B2	C1	C2	D1	D2
x [mm]	2100	2405	2405	2481	2504	2532	2536	2810	2800
y [mm]	-605	-596	-596	-367	-679	-382	-687	-107	-688
z [mm]	37	-33	27	-20	-42	144	126	-12	-50

The model also includes force elements, such as springs, shock absorbers and stabilizer bar. The behavior of each rubber-metal bed is described in the model by six nonlinear strength-deformation characteristics, determined by the experimental measurement.

Longitudinal arm (body 2 - Fig. 1, 2) is on the other hand constructed by the synthesis of modal shapes using Craig-Bampton method. Flexible model of longitudinal arm was generated by FlexPrep tool in MotionView from the standard FEM model in Hypermesh module. The FEM network of the arm is composed of surface elements PSHELL type with defined properties corresponding to the thickness 3 mm and steel material characteristic.

The main output are calculated values of toe angle α and camber angle β (Fig. 3) depending on the wheel rebound Wz in z-axis direction for different positions of kinematic points B1,C1 and D1. These are functions $\alpha = f(W_Z)$ and $\beta = f(W_Z)$ with parameters B1Y+2, B1Y-2, B1Z+2, B1Z-2, where B1Y + 2 e.g. means the movement 2 mm of the kinematic point B1 in positive direction of y-axis.

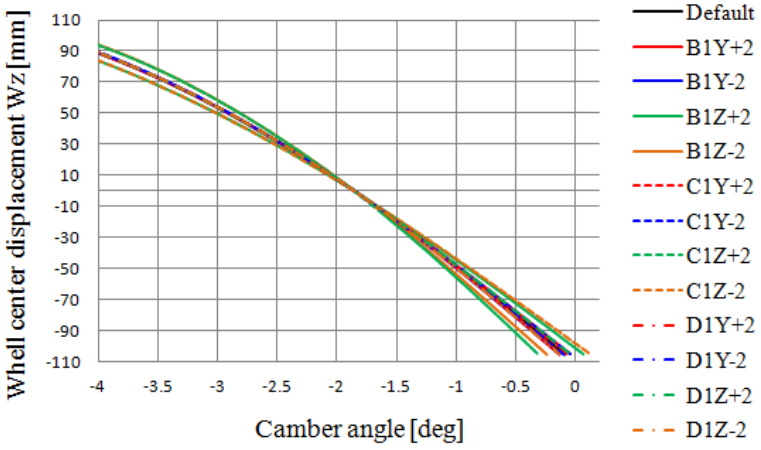

Fig. 3. Wheel camber angle vs. rebound for different positions of kinematic points

References

[1] Altair University, Practical aspect of multi-body simulation with Hyperworks, Michigan, January 2015.

[2] Schramm, D., Hiller, M., Bardini, R., Modellbildung und simulation der dynamik von Kraftfahrzeugen, Springer-Verlag Berlin Heidelberg, Duisburg, 2010.

COMPUTATIONAL MECHANICS 2015
31st conference with international participation
Špičák
November 9 - 11, 2015

Mechanical response of neck in virtual human body model VIRTHUMAN

J. Vychytil[a], H. Čechová[a], J. Maňas[b]

[a] *New Technologies - Research Centre, Univerzitní 8, 306 14 Plzeň, Czech Republic*
[b] *MECAS ESI, s.r.o., Brojova 16, 326 00 Plzeň, Czech Republic*

VIRTHUMAN is a numerical model of a human body developed for applications in traffic safety. In numerical simulations supporting safety systems development or accidents reconstructions of various means of transport, VIRTHUMAN model can be used to represent both pedestrians and passengers. It is formed of multi-body structure representing basic skeleton and deformable segments representing soft tissues.

In this work we developed and validated a new neck model. The goal is to achieve its biofidelity, that is, the mechanical response of the neck should be similar to that of a real human body. Therefore, detailed multi-body structure corresponding precisely to the cervical spine is proposed. It is formed of 7 rigid bodies representing cervical vertebrae (C1 to C7) that are interconnected via 6 kinematic joints. Another two joints are necessary to connect the neck with the head and the torso, see Fig. 1. Each joint has 6 degrees of freedom defined by nonlinear stiffness and damping. Validation of the neck thus represents a challenging task. In fact, it means the proper setting of 48 stiffness and 48 damping curves.

As a basis for material properties of joints, characteristics published in [1, 3] are used. Same authors describe also experimental tests to obtain mechanical response of real human neck. In these tests seated volunteers were exposed to accelerations of 15g frontal and 7g lateral sled tests resulting in a total number of 21 experimental corridors such as head acceleration, neck link rotation, displacement of occipital condyles and many others. These data are used for validation of our model. Numerical simulations of both 15g frontal and 7g lateral sled tests are performed. The aim is to fit mechanical response of the model in terms of accelerations and displacements within experimental corridors. Although a demanding task, modification of joints characteristics leads to a complete validation. Mechanical response of the neck model fits all 21 experimental corridors, see Fig. 2 as an example.

Biofidelity of the neck model is ensured for frontal and lateral impacts in the range of accelerations prescribed by validation tests. This is confirmed also by low-g tests in [2]. However, higher energy level impacts have to be considered as well. Simulations such as pedestrian-vehicle or motorbike rider-wall impact with velocities over 45 km/h exhibit excessive neck deformations, namely the flexion-extension and the axial rotation. To deal with this issue, ranges of motions (ROM) are taken into account [1]. ROM's of cervical joints represent limit values of relative rotations and displacements that can be achieved *in vivo* without causing any injury. We implement these values in our model by modifying stiffness characteristics of individual joints. If displacement or rotation in the model joint exceeds the ROM value, the stiffness increases which prevents excessive deformations. These modifications of joint characteristics in neck model improve its mechanical response; excessive deformations for higher energy level

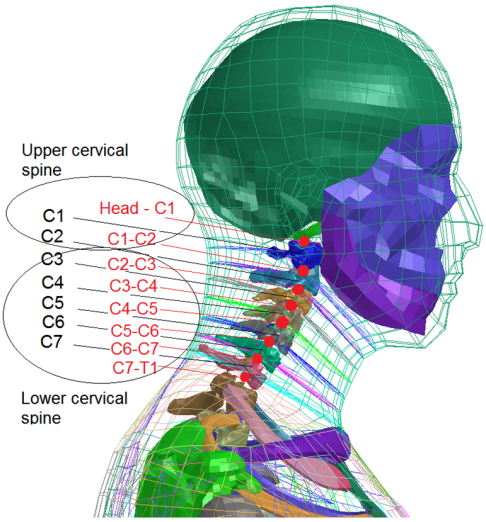

Fig. 1. Head and neck of the VIRTHUMAN model (cervical vertebrae are denoted with black labels, joints with red labels)

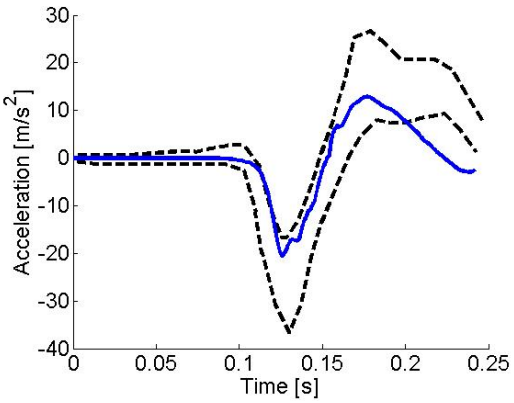

Fig. 2. Acceleration of head in frontal direction for 7g lateral test – model response (blue solid curve) and experimental corridor (black dashed curves)

impacts are reduced. At the same time, validations for 15g frontal and 7g lateral sled tests are not violated.

After the development of the neck model in VIRTHUMAN is completed, its biofidelity is tested on the sled test according to Vezin [4]. Numerical simulation of human body seated in sled and exposed to prescribed acceleration is performed. In fact, prescribed loading represents frontal crash with the impact velocity of 30 km/h. Results of the simulation, such as head acceleration and head injury criterion are in a good agreement with experimental data obtained for post-mortem human surrogates.

Due to the detailed neck model and its proper mechanical response, VIRTHUMAN can be applied also for complex injury analyses including so-called whiplash. First studies in this area are promising for further applications of VIRTHUMAN in virtual prototyping and injury prevention.

Acknowledgement

This work has been supported by the New Technologies - Research Centre.

References

[1] de Jager, M.K.J., Mathematical head-neck models for acceleration impacts, Ph.D. thesis, Eindhoven University of Technology, Eindhoven, 1996.

[2] Špirk, S., Čechová, H., Maňas, J., Hynčík, L., Virtual human model in low-g impact, Proceedings of the 29th conference Computational Mechanics, Špičák, Czech Republic, 2013, pp. 129-130.

[3] van der Horst, M.J., Human head neck response in frontal, lateral and rear end impact loading, Ph.D. thesis, Eindhoven University of Technology, Eindhoven, 2002.

[4] Vezin, P., Garnier, K., Bermond, F., Verriest, J.P., Comparison of Hybrid III, Thor-alfa and PMHS response in frontal sled tests, Stapp Car Crash Journal 46 (2002) 1-26.

COMPUTATIONAL MECHANICS 2015
31st conference with international participation
Špičák
November 9 - 11, 2015

Modelling and investigations of influence of material damping on vibrations of flexible rotors

J. Zapoměl [a], P. Ferfecki [b], V. Dekýš [c], M. Žmindák [c]

[a] *Faculty of Mechanical Engineering, VSB-TU of Ostrava, 17. listopadu 15, 708 33 Ostrava, Czech Republic*
[b] *IT4Innovations National Supercomputing Center, VSB-TU of Ostrava, 17. listopadu 15, 708 33 Ostrava, Czech Republic*
[c] *Faculty of Mechanical Engineering, ZU of Žilina, Universitná 8215/1, 010 26, Slovak Republik*

Material damping strongly influences amplitude of lateral vibrations of turning rotors. During some operating regimes it contributes, together with external damping, to its attenuation. But if the rotor angular speed exceeds a critical value, material damping becomes a source of inducing the rotor self-excited vibrations with monotonously rising amplitude. This implies, determination of the safe speed interval requires good knowledge of the shaft material properties, a proper choice of a material model and relevant setting of its elastic and damping coefficients.

The investigated rotor consists of a shaft made of steel and of one disc. At both its ends it is supported by rolling element bearings. The rotor is loaded by its weight and excited by the disc unbalance. The whole system can be considered as symmetric relative to the disc middle plane. The task is to analyse its principal dynamic characteristics concentrating on determination of the interval in which the rotor vibrations ramain stable.

Dependence of the specific damping capacity of the shaft material on the vibrations frequency was determined experimentally by means of a measurement of the damping ratio [1]. The results are summarized in Table 1.

Table 1. Results of measurements of the damping ratio and specific damping capacity

	Vibration frequency [rad/s]	Damping ratio [-]	Damping capacity [-]
1.	130	0.0008	0.010
2.	160	0.0011	0.014
3.	255	0.0018	0.022
4.	345	0.0017	0.021
5.	470	0.0015	0.019
6.	540	0.0023	0.029

The course of the specific damping capacity on the vibrations frequency was approximated by corresponding dependences derived for three theoretical materials [1]: Kelvin-Voigt, Zener and hysteretic (Fig. 1). Values of the related material coefficients were obtained by application of the least-square method. The sum of deviations referred to the individual theoretical materials takes the values 0.00015, 0.00006, 0.00022, respectively. As evident, the standard Zener material shows the highest agreement with results of the measurements and therefore, it was chosen for modelling the shaft.

In the computational model the rotor was represented by a Jeffcott one and both bearings were considered as absolutely rigid. Then the rotor lateral oscillations are described by a set

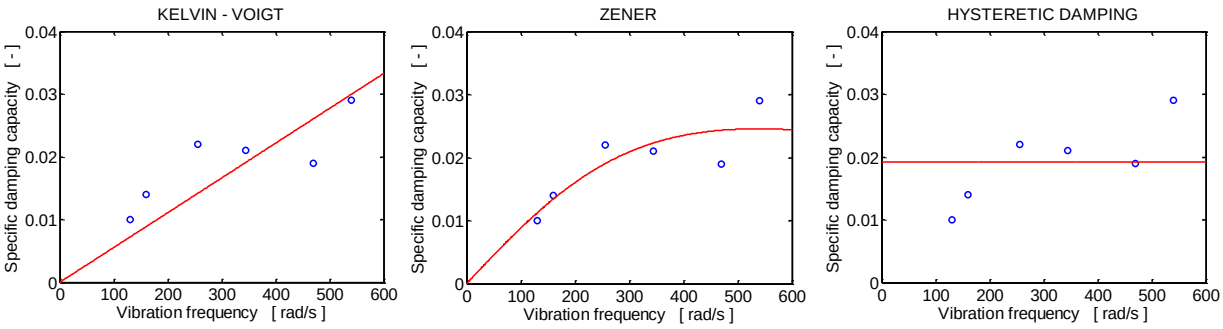

Fig. 1. Dependence of the specific capacity coefficient on the vibration frequency

of differential equations of the first and second orders which can be expressed in a matrix form

$$\begin{bmatrix} \mathbf{M} & \mathbf{O} \\ \mathbf{O} & \mathbf{O} \end{bmatrix} \begin{bmatrix} \ddot{\mathbf{x}} \\ \ddot{\mathbf{q}} \end{bmatrix} + \begin{bmatrix} \mathbf{B}_P + \mathbf{B}_M & -\mathbf{H} \\ -\mathbf{H} & \mathbf{F} \end{bmatrix} \begin{bmatrix} \dot{\mathbf{x}} \\ \dot{\mathbf{q}} \end{bmatrix} + \begin{bmatrix} \mathbf{K} - \omega\mathbf{K}_C & \omega\mathbf{H}_C \\ \omega\mathbf{H}_C & \mathbf{H} - \omega\mathbf{F}_C \end{bmatrix} \begin{bmatrix} \mathbf{x} \\ \mathbf{q} \end{bmatrix} = \begin{bmatrix} \mathbf{f} \\ \mathbf{o} \end{bmatrix}. \quad (1)$$

M, **K** are the mass and stiffness matrices, $\mathbf{B}_P$ is the damping matrix referred to external damping, $\mathbf{K}_C$ is the circulation matrix, $\mathbf{B}_M$, **H**, **F**, $\mathbf{H}_C$, $\mathbf{F}_C$ are the matrices composed of parameters describing material damping related to Zener material, **O**, **o** are the zero matrix and zero vector, **f** is the vector of applied forces acting on the disc, **x** is the vector of displacements of the disc centre, **q** is the vector of additional (internal) coordinates referred to Zener material, ω is the speed of the rotor rotation and $(\dot{\cdot})$, $(\ddot{\cdot})$ denote the first and second derivatives with respect to time.

The scheme of the investigated rotor system is depicted in Fig. 2. The frequency response characteristic and dependence of real parts of the system eigenvalues on speed of the rotor rotation are drawn in Fig. 4 and 5. The results of the carried out simulations show that after exceeding the angular velocity of 323 rad/s the maximum real part of the system eigenvalues starts to take a positive value which implies the vibrations become unstable.

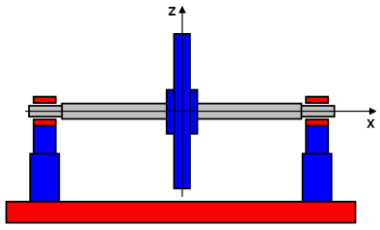

Fig. 2. Investigated rotor system

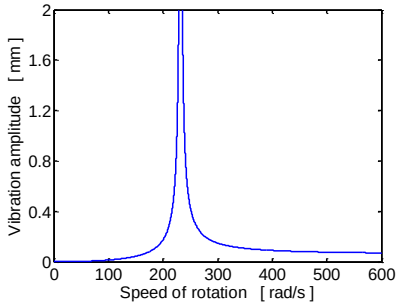

Fig. 3. Frequency response

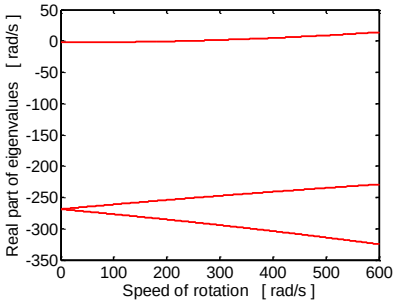

Fig. 4. Eigenvalue analysis

Acknowledgements

This work was supported by the European Regional Development Fund in the IT4Innovations Centre of Excellence (no. CZ.1.05/1.1.00/02.0070), the Slovak Research and Development Agency (contract no. APVV-0736-12) and Slovak Grant Agency (proj. VEGA 1/0983/15).

References

[1] Zapoměl, J., Approaches to implementation of material damping into computer models of mechanical systems, Habilitation thesis, Ostrava, 1998. (in Czech)

COMPUTATIONAL MECHANICS 2015
31st conference with international participation
Špičák
November 9 - 11, 2015

Optimization of mechanical properties of active structure and choice and placement of sensors and actuators

J. Zavřel[a], Z. Šika[a], M. Valášek[a], P. Beneš[a], J. Dupal[b]

[a] *Faculty of Mechanical Engineering, CTU in Prague, Technická 4, 166 07 Praha 6, Czech Republic*
[b] *Faculty of Applied Sciences, University of West Bohemia, Univerzitní 8, 306 14 Plzeň, Czech Republic*

The idea behind this optimization is the hierarchical motion control of the lightweight multi-level mechanisms consisting of the large motion level realized by the cabledriven parallel mechanisms and the small motion levels realized using the active structures.

The aim of the optimization and control design such structures is tuning of frequency bandwidth of the feedback motion control. The active structures can improve an accuracy of the end-effectors of cabledriven parallel mechanisms. The concrete cable driven mechanism (Fig. 1) is considered. It is primarily actuated by eight cables and performs a motion with six degrees of freedom. An active structure with six piezoactuators [3] is integrated between the end-effector platform and auxiliary platform suspended and moved by the cable driven mechanisms (Fig. 1). The target of the optimization is maximization of the controllability of end-effector platform using all available actuators in the given bandwidth. The large lower frequency components of motion are controlled [1] by the servo-drives through the cables, whereas the small high frequency components of motion are controlled by the piezoactuators.

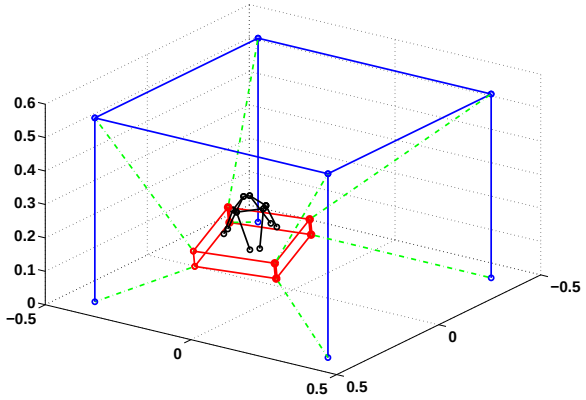

Fig. 1. The considered cable driven mechanism with the active hexapod structure

The task is modeled in the first step as the one-dimensional problem (Fig. 2). The input force F_0 is generated by the drive. The modelled problem consists of the cable, piezoactuator, driven platform and end-effector. Cable is described by its stiffness k_1 and damping constant b_1, even the piezoactuator by its stiffness k_2 and dumping constant b_2 and corresponding masses. The free length l_{piezo} of the piezoactuator is given by dependency on the input voltage v like $l_{piezo} = l_{20} + qv$.

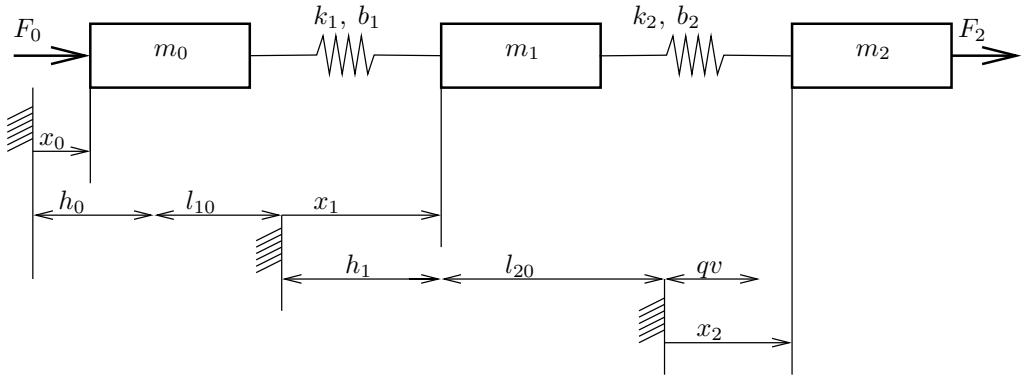

Fig. 2. Scheme of the one dimensional model

The one-dimensional problem with concentrated masses is described by three degrees of freedom model as shown on Fig. 2. The system (Fig. 2) is described by three differential equations:

$$\begin{aligned} m_0\ddot{x}_0 &= F_0 + k_1(x_1 - x_0) + b_1(\dot{x}_1 - \dot{x}_0), \\ m_1\ddot{x}_0 &= -k_1(x_1 - x_0) - b_1(\dot{x}_1 - \dot{x}_0) + k_2(x_2 - x_1 - qu) + b_2(\dot{x}_2 - \dot{x}_1 - q\dot{u}), \\ m_2\ddot{x}_0 &= F_2 - k_2(x_2 - x_1 - qv) - b_2(\dot{x}_2 - \dot{x}_1 - q\dot{u}). \end{aligned} \tag{1}$$

By substitutions, where $z_1 = x_0,\ z_2 = \dot{z}_1,\ z_3 = x_1,\ z_4 = \dot{z}_3,\ z_5 = x_2,\ z_6 = \dot{x}_2$ and $z_7 = v$ is problem (2) transformed into state-space form $\dot{\mathbf{z}} = \mathbf{Az} + \mathbf{Bu},\ \mathbf{y} = \mathbf{Cz} + \mathbf{Du}$ with states $\mathbf{z}$ and outputs $\mathbf{y}$ with the artificial input $w = k_2qv + b_2q\dot{v}$.

The transfer function [2] taken from the state-space description of the system is given like

$$\mathbf{G}(\omega) = \frac{\mathbf{y}}{\mathbf{u}} = [\mathbf{C}(s\mathbf{I} - \mathbf{A})^{-1}\mathbf{B} + \mathbf{D}], \tag{2}$$

where $s = i\omega$.

In optimization procedure there is observed the system and changed the shape of the transfer function $\mathbf{G}(\omega)$.

Described procedures were used to optimization of the singular values of the transfer function matrices. The target of optimization is the widening of the control bandwidth. There were used simple models which will be extended in the future work on the project.

Acknowledgement

This work is supported by the grant GA 15-20134S "Multi-level Light Mechanisms with Active Structures" of the Czech Science Foundation entitled.

References

[1] Duan, X., Qiu, Y., Duan, Q., Du, J., Calibration and motion control of a cable-driven parallel manipulator based triple-level spatial positioner, Advances in Mechanical Engineering 2014 (2014) 1-10.

[2] Gawronski, W., Advanced structural dynamics and active control of structures, Springer-Verlag, New York, 2004.

[3] Svatoš, P., Šika, Z., Valášek, M., Bauma, V., Polach, P., Optimization of anti-backlash fibre driven parallel kinematical structures, Bulletin of Applied Mechanics 8 (31) (2012) 40-44.

COMPUTATIONAL MECHANICS 2015
31st conference with international participation
Špičák
November 9 - 11, 2015

Impact vibrations of guide thimbles in nuclear fuel assembly

V. Zeman[a], Š. Dyk[a]

[a] *NTIS - New Technologies for the Information Society, Faculty of Applied Sciences, University of West Bohemia, Univerzitní 8, 306 14 Plzeň, Czech Republic*

The guide thimbles (GT) in nuclear fuel assembly (FA) are beam-type continua embedded in spacer grid cells and sleeve (SL) with radial clearances. Spacer grid vibrations excited by pressure pulsations of the cooling liquid were investigated still on the linearized FA global model [3, 4]. The aim of this paper is presentation of the original approach to mathematical modelling and simulation analysis of nonlinear GT impact vibrations respecting friction forces described with the "force-velocity-displacement" characteristics [1].

The chosen GT (see Fig. 1) is fixed by means of FA lower and upper tailpieces at the level of the nodal points $L_R^{(s)}$ and $U_R^{(s)}$ into mounting plates in the reactor core. At the level of even nodes $i = 2, 4, \ldots 14$, GT is surrounded in FA skeleton by three spacer grid cells with radial clearance δ_C. At the level of the node $i = 16$, GT passes with the radial clearance δ_{SL} through the sleeve linked with six spacer grid cells. GT vibrations are kinematically excited by spatial motion of both mounting plates [4]. GT is discretized using finite element method for Euler-Bernoulli continua including mass forces on flexure (Rayleigh theory) and the prestress effect by pressure force F_0 [2]. GT nodal points displacements are marked as $u_i, v_i, w_i, \varphi_i, \vartheta_i, \psi_i, i = L_R^{(s)}, 1, 2, \ldots 17, U_R^{(s)}$. SL lateral vibration are described by displacements x, y, φ.

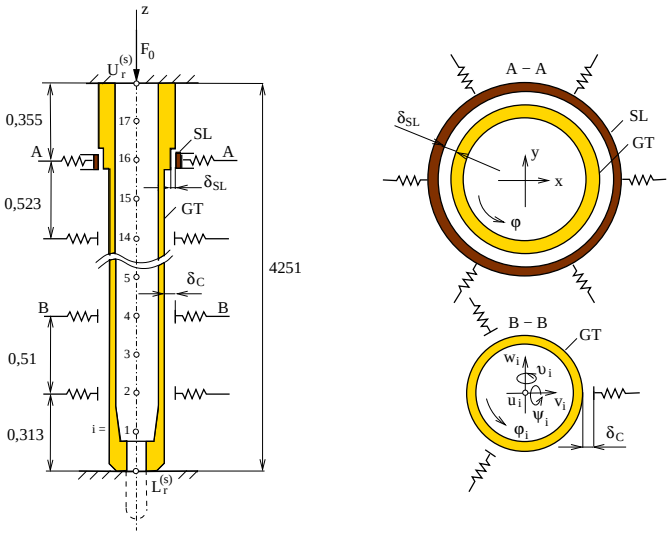

Fig. 1. A scheme of GT with couplings

Every impact of GT with single cell j at the level of spacer grid g ($i = 2g$) generates normal (N) impact force (index g is let out) and friction force with tangential (T) and axial (A) components

$$N_j = k(d_j - \delta_C)\mathcal{H}(d_j - \delta_C), \quad T_j = N_j f(c_j)\frac{c_{j,T}}{c_j}, \quad A_j = N_j f(c_j)\frac{c_{j,A}}{c_j}, \quad j = 1, 2, 3. \quad (1)$$

The normal impact force N_j depends on radial cell stiffness k and radial relative displacement d_j of the corresponding GT even nodal point with respect to cell centre. The Heaviside function $\mathcal{H}(d_j - \delta_C)$ in (1) is zero when contact GT with spacer grid cell does not occur ($d_j < \delta_C$). The

friction coefficient $f(c_j)$ in (1) depending on slip velocity c_j can be approximated by smooth function

$$f(c_j) = \frac{2}{\pi} \arctan \varepsilon c_j \left[f_d + (f_0 - f_d) e^{d|c_j|} \right], \tag{2}$$

where f_0 is static friction coefficient, f_d is dynamic friction coefficient and $\varepsilon, d \gg 1$ are suitable elected parameters.

At the level of spacer grid $g = 8$ ($i = 16$), the impact of GT with SL generates normal (N) impact force and friction force with tangential (T) and axial (N) components in the form

$$N = k_C(e - \delta_{SL})\mathcal{H}(e - \delta_{SL}), \quad T = Nf(c)\frac{c_T}{c}, \quad A = Nf(c)\frac{c_A}{c}. \tag{3}$$

The normal impact force depends on contact stiffness k_c between GT and SL and relative eccentricity $e = \sqrt{(v_{16} - x)^2 + (w_{16} - y)^2}$ (see Fig. 1). The dependence of the friction coefficient $f(c)$ on the slip velocity is approximated similarly to (2).

Equations of motion of the GT and SL subsystems can be written in the standard form

$$\boldsymbol{M}\ddot{\boldsymbol{q}} + \boldsymbol{B}\dot{\boldsymbol{q}} + \boldsymbol{K}\boldsymbol{q} = \boldsymbol{f}_N(\boldsymbol{q}, \dot{\boldsymbol{q}}, t),\ \boldsymbol{q} = [\ldots, u_i, v_i, w_i, \varphi_i, \vartheta_i, \psi_i, \ldots, x, y, \varphi]^T, i = 1, \ldots 17. \tag{4}$$

The kinematic excitation by means of FA mounting plates motion and the nonlinear impact forces with friction in all twenty-two possible contact points are included in the global nonlinear force vector $\boldsymbol{f}_N(\boldsymbol{q}, \dot{\boldsymbol{q}}, t)$. The dynamic response is investigated by integration of Eqs. (4) in time domain.

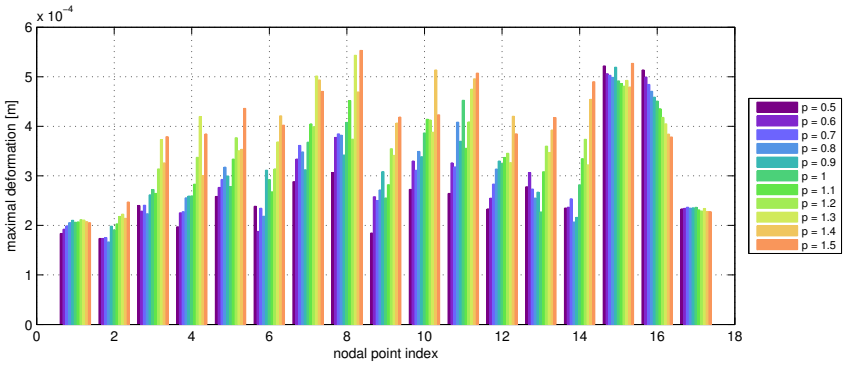

Fig. 2. Maximal lateral deformations of chosen GT in dependence on radial clearances $\delta_X = p\delta_{X,ref}, X = C, SL$, where $\delta_{X,ref}$ are reference values of clearances

The presented method is applied to calculation of the GT lateral deformations and time behaviour of the GT contact forces in TVSA-T fuel assemblies in VVER-1000/320-type reactor operated in NPP Temelín. As an illustration, maximal lateral deformations of the chosen GT are presented in Fig. 2 in dependence on different radial clearances δ_C and δ_{SL}.

Acknowledgements

This publication was supported by the project LO1506 of the Czech Ministry of Education, Youth and Sports and the research project ČEZ – Fuel cycle of NPP coordinated by NRI Řež plc.

References

[1] Blau, P. J., Friction science and technology, CRC Press, Boca Raton, 2008.

[2] Géradin, M., Rixen, D., Mechanical vibrations, John Wiley & Sons, Chichester, 1997.

[3] Hlaváč, Z., Zeman, V., Vibration of nuclear fuel assemblies, LAP Lambert Academic Publishing, Saarbrücken, 2013.

[4] Zeman, V., Hlaváč, Z., Dynamic response of nuclear fuel assembly excited by pressure pulsations, Applied and Computational Mechanics 6 (2) (2012) 219-230.

COMPUTATIONAL MECHANICS 2015
31st conference with international participation
Špičák
November 9 - 11, 2015

Model of binding point in comparison with a real fabric

J. Žák[a], V. Lukášová[a]

[a] VÚTS, a.s. Liberec, Svárovská 619, 460 01 Liberec XI, Czech Republic

In our previous work we faced some difficulties with the estimation of mechanical properties of fabrics. They are mostly influenced by the waviness of yarns and by the value of their crossing angle. To predict the final shape of a fabric we used the methods of classical mechanics. The form of yarns in a binding point was described by means of parametrized shape functions, then by using the principle of minimization of energy a set of values of the said parameters was found [2]. These parameters enable us to draw the theoretic shape of yarns. Once this shape, mainly the crossing angle and waviness are known we can estimate mechanical properties of the fabric.

To evaluate this method we have carried out the comparison of calculated shape of a fabric with its real form. First step consisted in the preparation of sections of the real fabric. A modified method of section preparation developed at Technical University of Liberec was used [1]. Then an image analysis was carried out. Figs. 1 and 2 demonstrate the preparation of the data; the length of pictured section is of about 10 mm.

Fig. 1. Microphotography of the section

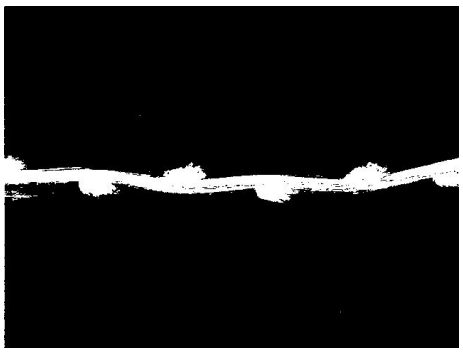

Fig. 2. Binary image of the section

Then a part of digitized image close to its centre must be chosen manually. The reason is to avoid the image margins which may be deformed by perspective, also the limited computational resources are to be taken in consideration. Length of the selected part is given by a multiple of repeat period which is known exactly. This selected part is 'trimmed', i.e. by using linear regression, the constant, linear and parabolic members of regression polynomial are subtracted from the data set, see Fig. 3.

The selected data are analysed by using non linear regression. The regression functions used to fit the cloud of geometric points are of the same form as used to model theoretically the binding point, it is to say a combination of $cosine$ and linear functions. The interval $\langle p_1, p_2 \rangle$ over which the $cosine$ function spans is to be determined, thus a strongly non linear problem

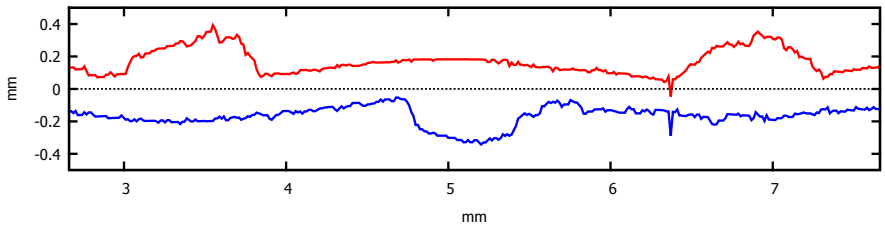

Fig. 3. Trimmed contour of the sectioned fabric over 3 binding points

emerges. The fit functions take the following form (equivalent to the numeric simulation):

$$\mathrm{f}_{\mathrm{lin}}\left(C,x\right)=C_{1,3}\pm C_2\cdot\left(x-p_{1,2}\right)\ \text{in linear and}$$

$$\mathrm{f}_{\mathrm{cosine}}\left(C,x\right)=C_{1,3}-\frac{C_{2,4}\cdot\left(p_2-p_1\right)}{\pi}\cdot\cos\left(\frac{\pi}{p_2-p_1}\cdot\left(x-\frac{p_1+p_2}{2}\right)\right)\ \text{in } \textit{cosine} \text{ intervals.}$$

Parameters p_1 and p_2 are the left and right boundaries, respectively, of *cosine* form section. Outside of this interval, the linear form is assumed. The $\pm$ symbol yields the position of x in the left and right linear interval, indexes 2 and 4 in $C_{2,4}$ term the upper and lower contour in *cosine* interval, respectively, as do the 1 and 3 in $C_{1,3}$. Then, the function to minimize is

$$S=\sum_{k=1}^{N}\left(\mathrm{f}\left(C,X_k\right)-Y_k\right)^2.$$

The unknowns C_i are found by solving the serie of linear problems of form $\frac{\partial S}{\partial C_i}=0$ for given values of p_1 and p_2.

A strategy of interval sectioning makes it possible to evaluate the value of S over an acceptable number of pairs (p_1,p_2) and thus, to find a global minimum of squares S. Then, the corresponding set of $\left(C_i,p_1,p_2\right)|_{S\to min}$ is used to draw the best fitting function $f\left(C,x\right)$. As well, they can be used to compare directly the numeric model with the real fabric.

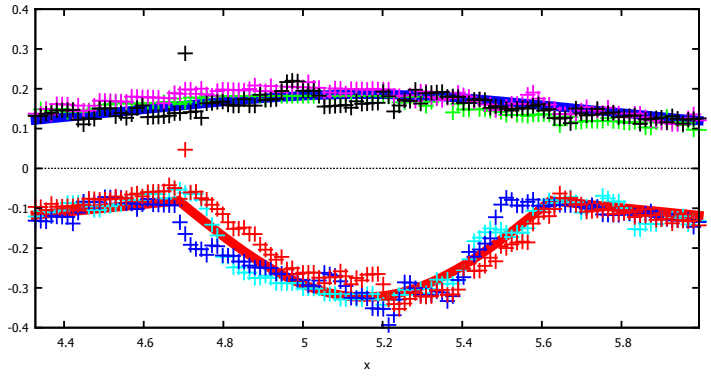

Fig. 4. Data over 3 binding points fitted by the fit function

References

[1] Internal norm IN 46-108-01/01 – Recommended procedure for preparation of samples. Soft and hard sections (slices), Research Centre TEXTIL, Technical University of Liberec, Liberec, 2004. (in Czech)

[2] Žák, J., Modelling of textile structures, Proceedings of the 21st International Conference Engineering Mechanics, Svratka, Czech Republic, 2015, pp. 370-371.